UNIVERSITY OF SOUTHAMPTON

FACULTY OF NATURAL AND ENVIRONMENTAL SCIENCES

Chemistry

Model Inverse Electro-catalyst Investigations of Metal Support Interactions

By

Hugo Jungius

Thesis for the degree of Doctor of Philosophy

January 2017

UNIVERSITY OF SOUTHAMPTON

ABSTRACT

FACULTY OF NATURAL AND ENVIRONMENTAL SCIENCES

Chemistry

Thesis for the degree of Doctor of Philosophy

MODEL INVERSE ELECTRO-CATALYST INVESTIGATIONS OF METAL SUPPORT INTERACTIONS

Hugo David Turquand Jungius

Gold supported titania nano-particle surfaces have been synthesised in order to understand supported electrochemical mechanisms through an inverse catalyst. The catalyst process investigated was the electro-oxidation of CO which is known to be promoted on Au nano-particles on a titania support. Synthesis proceeded via physical vapour deposition (PVD) of titanium onto a gold surface (both polycrystalline and 111 crystal), followed by alloying and oxidation to form discrete particles of titania on the surface, with variations in density of particles achieved by control of the initial titanium coverages.

Scanning tunnelling microscopy (STM) and atomic force microscopy (AFM) measurements indicate these particles develop with consistent triangular and hexagonal shapes, with average diameters of 11.5 and 20 nm observed depending on alloying temperature. The procession of titanium deposition on the gold surface and subsequent alloy formation was followed by X-ray photoelectron spectroscopy (XPS) measurements, with the formation of pure TiO_2 revealed once synthesis was complete, with minimal modification to the final electronic state of the underlying gold.

Electrochemical testing in an acidic environment provides evidence for alteration of the electrooxidation of CO on these modified gold surfaces. A deactivation of the CO oxidation is observed with initial addition of titania, explained by the blocking of CO adsorption on the surface. This is followed by significant subsequent increases in activity with increasing densities of titania particles, with decreasing over-potential and increasing current density observed as the titania coverage increases.

This observed effect on CO oxidation activity with titania coverage in the inverse system provides significant evidence for the action of either reactant spill-over or Ti-Au interface sites as being responsible for the changes in activity observed for titania modified gold systems, whether in the inverse or standard form.

Table of Contents

List of Tables

List of Figures

Declaration of Authorship

I, Hugo Jungius declare that this thesis and the work presented in it are my own and has been generated by me as the result of my own original research.

Model Inverse Electro-catalyst Investigations of Metal Support Interactions

I confirm that:

1. This work was done wholly or mainly while in candidature for a research degree at this University;
2. Where any part of this thesis has previously been submitted for a degree or any other qualification at this University or any other institution, this has been clearly stated;
3. Where I have consulted the published work of others, this is always clearly attributed;
4. Where I have quoted from the work of others, the source is always given. With the exception of such quotations, this thesis is entirely my own work;
5. I have acknowledged all main sources of help;
6. Where the thesis is based on work done by myself jointly with others, I have made clear exactly what was done by others and what I have contributed myself;
7. None of this work has been published before submission

Signed: .....

Date: .....

Acknowledgements

Firstly, and most importantly, I would like to thank Professor Brian Hayden for believing I was capable of tackling and completing a PhD and for offering me the tremendous opportunity to do so in such a great environment, as well as supervising me through my fumbles and encouraging my successes. I appreciate the companionship of Fiona Rodgers, alongside whom I began this trek, as we navigated the requirements and bureaucracy of a PhD at each stage together, sharing the highs and lows as we went. I would also like to extend my thanks to the group members past and present, in particular - Dr. Fiona Mcbride, Dr. Jin Yao, Dr. Sandy Kerr, Dr. Jovine Emmanuel, Jaffar Saleh, Mabkhoot Alsairi, Abdul Alharbi, Carmen Villa-Garcia, Dr. John Kavanagh and any others I may have missed, for all the help given, as well as putting up with my occasional lack of confidence, making the PhD experience as enjoyable as it was.

I would also like to offer my thanks for all the support and advice provided by members of Ilika Plc, in particular Dr. Samuel Guerin, James Barnett and Dr. Audrey Cooper, throughout my PhD. I will always be grateful to all those at Ilika who made my undergraduate industrial placement such a positive experience that inspired me continue exploring the sometimes difficult world that is materials development. I am very appreciative of the patience shown me by the mechanical workshop staff, Alan Glass and Robert Alley, for the numerous occasions when I required and benefitted from their expertise.

I also wish to give thanks for all the love and support of my family: my mother, Kate Jungius, who always encouraged and believed in me, despite self-avowed lack of understanding in just what I was doing, and my brothers James and Toby, despite being as generally uninterested as siblings tend to be in such things, were always there for me. Finally, I want to thank my father Richard Jungius for all he did to raise me into who I am today; sadly he is unable to see me complete this stage of my life, having been taken from us just as I was beginning my PhD journey but I hope he would have been as proud of me as I am thankful to have had him as a father.

Definitions and Abbreviations

Physical Vapour Deposition – PVD

Ultra-High Vacuum – UHV

High Throughput – HT

Scanning Probe Microscopy – SPM

Scanning Tunnelling Microscope/Microscopy – STM

Atomic Force Microscope/Microscopy – AFM

Polymer Electrolyte Membrane Fuel Cell – PEMFC

Membrane Electrode Assembly – MEA

Carbon Monoxide – CO

Fast Entry Chamber – FEC

Low Energy Electron Diffraction – LEED

Bead Crystal Electrochemical Cell – BCEC

X-ray Photo-electron Spectroscopy – XPS

Effective thickness – ET

Reversible Hydrogen Electrode – RHE

Reactive Layer Assisted Deposition – RLAD

Cyclic Voltammetry – CV

1 Introduction

Throughout the course of mankind's history, different fuels have been favoured as technology has developed. Typically, energy production has relied on the combustion of fossil fuels, such as coal, oil and gas. There are a couple of issues with using these as fuels, notably being that, barring new reserves being discovered, they are a finite resource. Another problem comes from the fact that there are pollution concerns associated with the combustion of fossil fuels. A number of pollutants can be produced due to impurities, or incomplete combustion of the fuels, such as carbon monoxide, sulphur dioxide and nitrous oxides, which cause a number of problems. However, even with 100% lean combustion, the fuels produce water and carbon dioxide.

Due to the effect carbon dioxide is believed to have on global climate change, current energy production is one of the largest contributors to CO_2 emission. As such, finding alternative sources of energy that bypass this problem are of utmost importance. As time has passed, fuels have contained greater and greater quantities of hydrogen, as shown in Figure 1.1. Due to the fact that the combustion of hydrogen with oxygen produces only water, the greater the hydrogen content of a fuel source, the less carbon dioxide will be produced by its combustion.

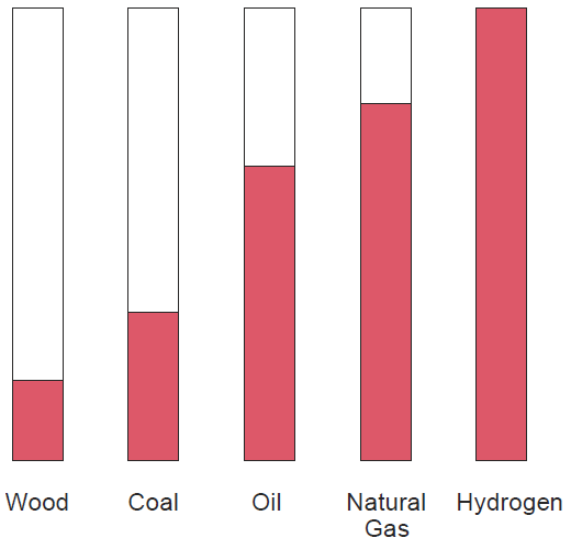

Figure 1.1 Various fuels' hydrogen percentage content[1]

Pure hydrogen would be thus be the ideal fuel, as in theory it should produce no carbon dioxide when combusted. There is, however, a more efficient way to use hydrogen as a fuel: hydrogen fuel cells.

Fuel cells produce power by converting chemical energy directly into electrical energy, and do so considerably more efficiently than current power sources, such as internal combustion engines.[2] The basic reaction between hydrogen and oxygen is shown in Equation 1.

$$2H_2 + O_2 \rightarrow 2H_2O + energy \qquad \textbf{Equation 1}$$

Electrode reactions of hydrogen and oxygen

There are numerous types of fuel cells, besides hydrogen ones, which utilise other energy dense fuels, ranging from the those initially produced by William Grove in 1839[3], through to polymer electrolyte membrane fuel cells (PEMFCs)/Direct Methanol Fuel Cells (DMFCs). These last two fuel cells are of particular interest to us here, as they are the most suitable for transport and personal device applications, so will be discussed in more detail.

1.1 Polymer Electrolyte Membrane Fuel Cells (PEMFCs)

The main section in a PEMFC is the Membrane Electrode Assembly (MEA) shown in Figure 1.2. The MEA consists of two electrodes (often platinum based) separated by a solid polymer electrolyte layer (the membrane). The electrolyte is normally Nafion® (a polymeric sulphonated fluorocarbon material), which prevents crossover of the reactant gases so that the fuel cannot react uncontrollably with the oxidant[4]. The reaction scheme for the reaction of hydrogen and oxygen at the two electrodes is shown below in Equation 2.

$$Anode: H_2 \rightarrow 2H^+ + 2e^- \qquad \textbf{Equation 2}$$

$$Cathode: \tfrac{1}{2}O_2 + 2H^+ + 2e^- \rightarrow H_2O$$

$$\boldsymbol{Overall: H_2 + \tfrac{1}{2}O_2 \rightarrow H_2O}$$

The theoretical equilibrium potential difference for this reaction is 1.23 V, though the kinetics of the reaction even with the best electro-catalysts leads to a lower potential under operating conditions. This is one of the major causes for the limited commercial success with fuel cell technology.

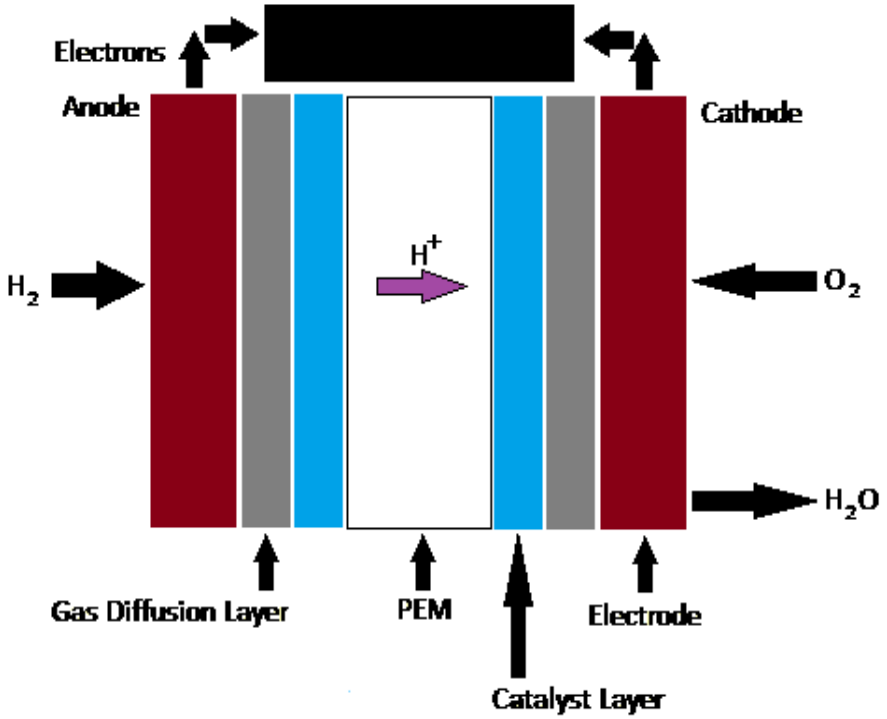

Figure 1.2 Polymer Electrolyte Membrane Fuel Cell schematic

In a hydrogen fuel cell the hydrogen is oxidised at the anode to form protons and electrons. The solid electrolyte membrane is semi-permeable; only the protons can pass through it (leading to the other name for Polymer Exchange Membranes: Proton Exchange Membranes). The electrons, however, are forced to travel through an external circuit, as the membrane/electrolyte is electrically insulating to electrons. It is this movement of electrons that produces useful power, before the electrons move to the cathode. At the cathode the hydrogen ions and electrons react with oxygen molecules, reducing them to form water, which are then removed from the system. The hydrogen and oxygen gas are pumped into the MEA via channels on either side of the MEA.

1.2 Proton Exchange Membrane

The electrolyte of a fuel cell is an ion conducting medium which is able to carry mobile protons, typically a solid, organic polymer. There are a number of properties that PEM materials need in order to perform their function.

- High proton conductivity
- Low electron conductivity
- Low fuel/oxidant permeability
- Thermal and oxidative stability
- Low cost

There are a number of membrane materials available for use as PEMs that fulfil these conditions to varying degrees. The most commonly used membranes (such as Nafion®) are polyperfluorosulphonic acid polymers that consist of a fluorocarbon backbone with pendant side chains that end in ion clusters consisting of sulfonic acid ions ($SO_3^- H^+$).[5]

The sulphonic acid groups are crucial as they form hydrophilic channels in the membrane. These channels absorb water strongly due to the negative charge on the acid groups, allowing for proton transport. The presence of water in the system does, however, limit the temperature that the cell can operate at; if the temperature increases above 100°C the membrane is swiftly dehydrated and rendered useless.

1.3 Issues associated with PEMFCs

Although PEMFCs are very much suitable as a replacement for current power sources, with the final product being water and no CO_2 emissions, there are still some drawbacks that prevent their widespread use. The first of these is that platinum has long been considered the desired catalyst for PEMFCs due to its high efficiency at catalysing oxidation reactions, particularly that of hydrogen. There are, however, a number of issues with using platinum as a catalyst in such a commercially significant product, the most significant being the rarity, and thus cost, of the metal making it unfeasible to use on a large scale.

As such, numerous investigations have been performed to either improve the activity of platinum or to discover cheaper alternatives that give a comparable level of

activity. One method to improve the commercial viability of platinum catalysis is to reduce the absolute quantity (mass) of platinum used. This can be achieved by utilising Pt particles to improve the relative area of platinum per volume, most generally mounted on a support of some kind.

Originally, these catalysts were made from platinum black (a fine platinum powder), giving platinum loadings of 25 mg/cm^2; carbon supported catalysts have reduced this value to 0.4-0.8 mg/cm^2.[6] Further reductions in Pt loading have been achieved by depositing platinum on novel carbon supports, to prevent the reduction of the supports and agglomeration of the catalysts during use, both of which reduce efficiency. This also has the benefit of reducing the quantity of platinum used, thus dropping costs as well as increasing the activity of the catalyst.[7]

As the oxidation of hydrogen on platinum has such fast kinetics, the catalyst platinum loading can be reduced by a reasonable degree without significant reduction in anode performance. However, reducing the Pt loading at the cathode is not feasible; the oxygen reduction reaction is considerably slower than hydrogen reduction (a significantly larger over-potential is required, attributed to strong catalyst surface binding of oxygen[8]). As such, lower platinum loading leads to a loss in performance of the cell as a whole[9], and so other solutions besides Pt loading need to be considered.

Improving the activity of the platinum catalyst has thus become an area of serious investigation with numerous methods having been found to enhance platinum's catalytic abilities. One of the most popular methods consists of alloying platinum with other metals (particularly ruthenium), reducing the relative quantity of platinum in the catalyst and increasing the catalyst's tolerance to Carbon Monoxide (CO)[10].

This is the more pressing concern for these catalyst systems, both gas-phase and electrochemical: the presence of CO in the system, rising from impurities in the stock fuel for the cells. CO acts as a poison for PEMFC fuel systems, as it strongly bonds to the commonly used catalyst materials, thus effectively binding in preference to any reactants and preventing the desired reactions from progressing, with performance significantly reduced even with trace levels of CO.

As such, further investigation has been carried out for further improvement of the catalysis on these systems; notably the use of varying supports for the catalyst material.

1.4 The use of supports in heterogeneous catalysis

At the most basic level, catalysts are materials that increase the rate of a particular reaction without themselves being consumed during the reaction. For heterogeneous catalysts, the catalyst itself is in a different physical state to that of the reactants/products for the relevant reaction. These are the type most commonly found in PEMFCs, generally consisting of a solid catalyst with liquid/gaseous reactants/products; as such, some or all of the reactants will adsorb onto the catalyst surface during the reaction, and, possibly, the support, for the reaction to take place.

One of the most common methods utilised to influence the catalytic activity of metals (both specific activity and mass activity) is by supporting the metal as particles on a support material. In PEMFCs platinum is deposited as particles on a high area carbon surface. The use of a support in such a system allows for a number of benefits to a catalytic material such as platinum or gold: the most immediate being the increased surface area of the catalyst material relative to the quantity of material used. This results in a higher number of active sites being available for the reaction, giving a higher efficiency for the catalyst (an increase in mass activity) and reducing the quantity of material utilised in the catalyst.

This formation as particles also leads to changes in the catalyst material itself, giving different morphologies depending on the size and deposition conditions utilised[11,12]. With such a system, modifying the method for material deposition can result in the effectiveness of the subsequent catalyst system being modified. An example of such an effect from depositing the catalyst material as particles is shown below in Figure 1.3, where platinum particles have been deposited on carbon. It should be noted that these data are for Johnson Matthey produced high-area catalyst material, and thus some differences will be present between this and PVD synthesised materials which are focussed on later.

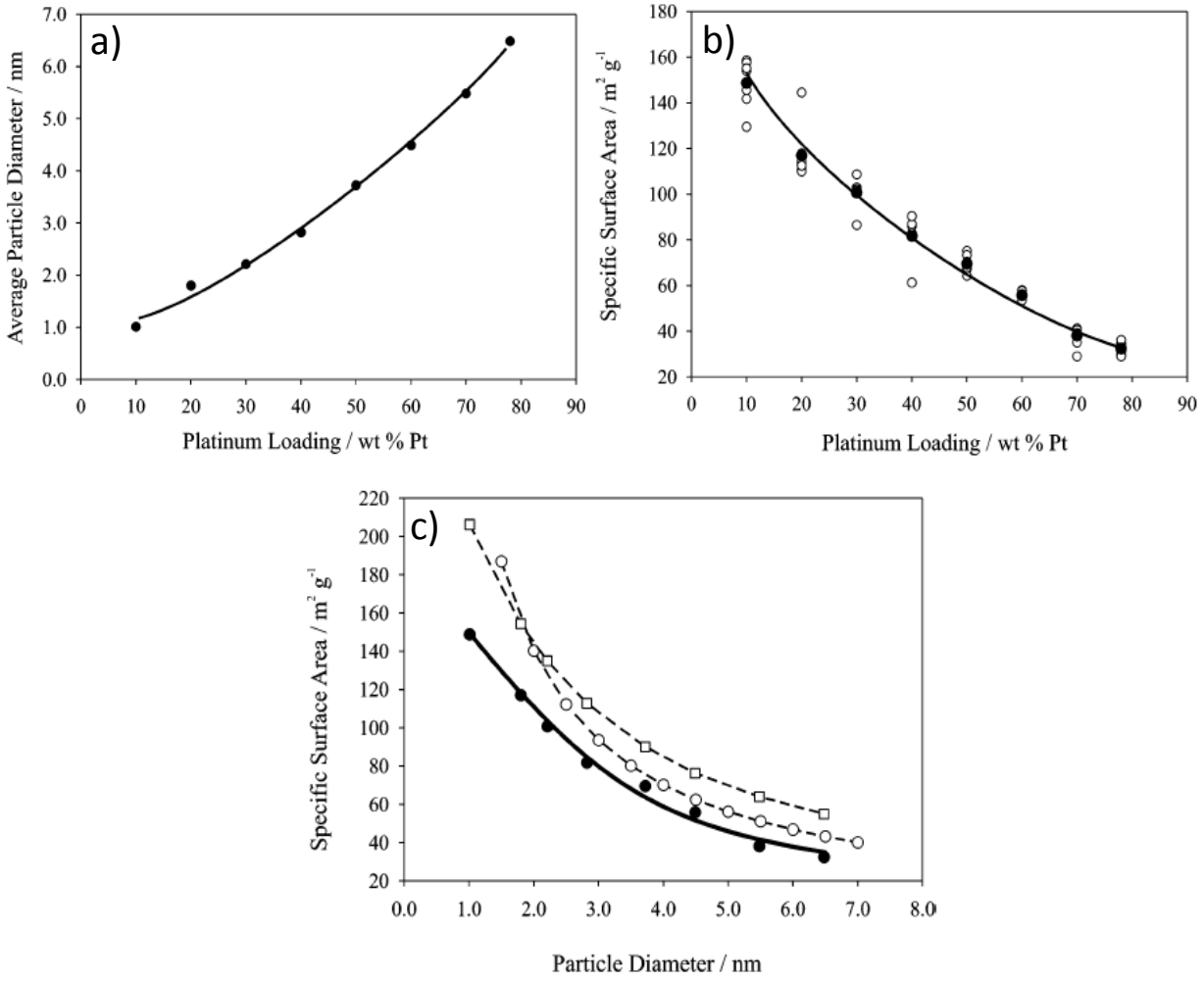

Figure 1.3 Platinum particles deposited on carbon. a) Total platinum weight % vs average particle diameter determined by XRD, b) Total platinum weight % vs specific surface area calculated via electrochemical measurements, unfilled circles show full data collected with filled circles the average values, c) Calculated particle diameter vs determined specific surface area. Filled circles are experimental data, unfilled circles are values calculated assuming spherical particles and unfilled squares are calculated assuming cubooctohedral particles. Graphs reproduced from Guerin *et al.*[13]

In Figure 1.3 c), it can be seen that as the diameter of the deposited particles decreases, the specific surface area of platinum available increases, also corresponding with the lowest platinum loading values. The effects this variation in particle morphology has on the electroreduction of oxygen can be seen below in Figure 1.4.

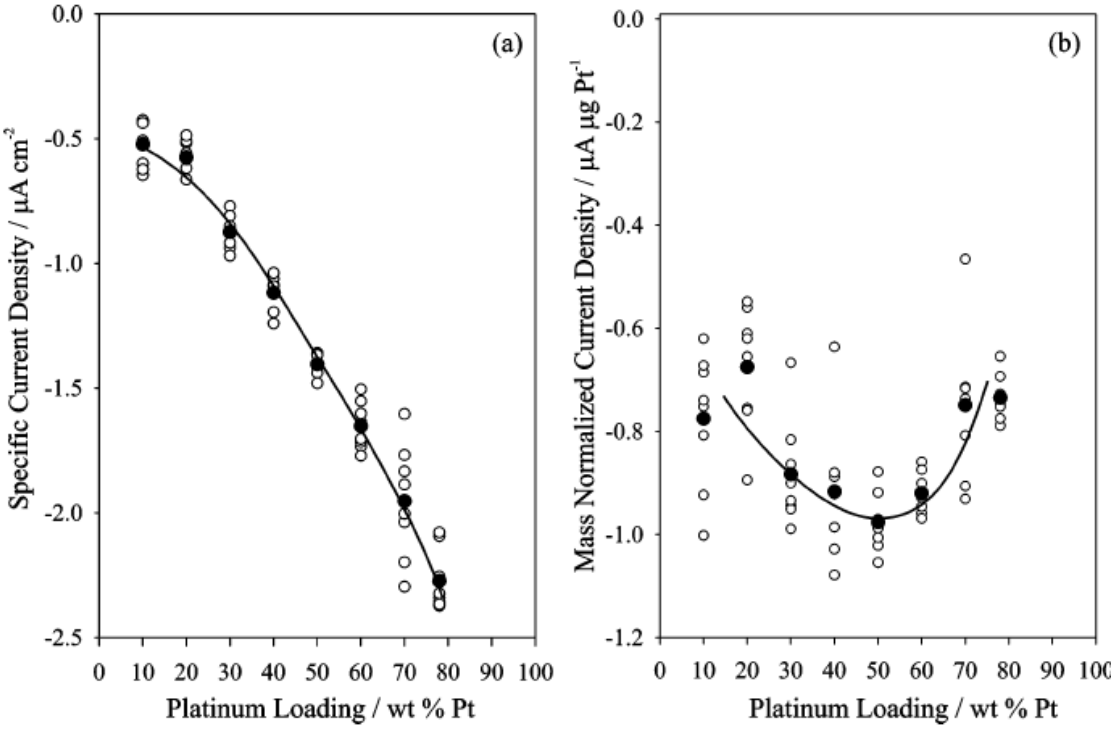

Figure 1.4 Current Densities for the electroreduction of oxygen at 0.85 V vs SHE on carbon supported platinum particles of varying loadings. a) Per Surface area, b) Per Unit mass Pt. Scans taken in O_2 saturated 0.5 M H_2SO_4. Unfilled circles represent full data, filled circles are average values. Reproduced from Guerin *et al.*[13]

It can be seen that as the loading of platinum decreases, the recorded current density (and thus activity) decreases, as might be expected with a lower overall quantity of platinum. However, when the current density is normalized against the utilised platinum mass, a different pattern emerges, showing a maximum at ~50% Pt loading, or particles with a diameter of 2-3 nm. This effect has also been directly linked to particle size in the model system.[14]

1.4.1 Metal oxide supported Gold Nanoparticles

The most common support used for platinum and gold catalysts in PEMFCs is carbon. However, the use of different supports can change the specific effect on the catalysts, as well as how they behave with differing particle sizes; investigations into the effects of differing supports have been performed for many years.[15,16] Of particular note is the use of metal oxides, as they are often used as supports for metal catalysts for a

variety of reactions.[17,18,19] An notable example of such effect metal oxide supports for metal particles can have is that of the oxidation of CO and other hydrocarbons on gold particles.

Gold has historically been considered to be a poor catalyst[20,21,22,23,24], but in 1987 Haruta *et al.* showed, in a number of papers, that gold could have a very high activity for the gas – phase activation of the oxidation of CO[25,26,27], along with a number of other reactions, ranging from the partial oxidation of hydrocarbons to the reduction of various nitrogen oxides[28], if supported as nanoparticles on specific metal oxides.

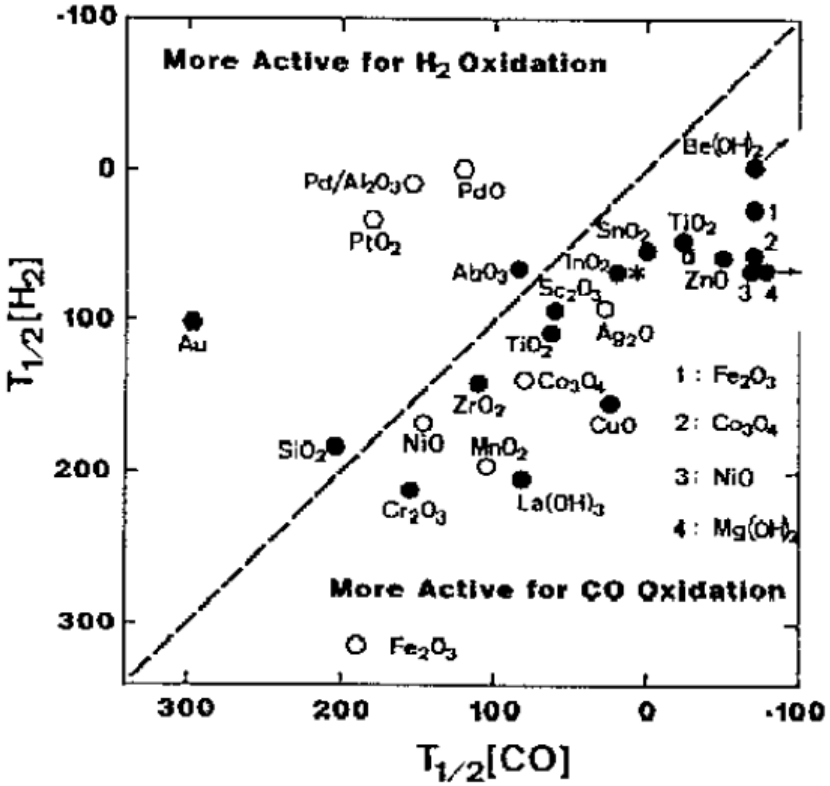

Figure 1.5 Temperature required for 50% catalytic conversion of H_2 and CO over noble metals and metal oxide catalysts. (•) supported gold catalysts calcined at 200-400°C, with metal loadings of 2-5 atom% Au, (*) Au(3 .8 wt%)/Al2O, (O) metal oxides without Au deposition ; (⌀) Pd/A12O3(Pd 0 .5 wt%) and oxides of Pt and Pd, (⬢) gold powder prepared from colloidal metal particles with diameters around 20 nm. Reproduced from Haruta *et al.*[27]

Figure 1.5 shows numerous examples of the benefit of metal oxide supports for the catalytic activity of the conversion of hydrogen and carbon monoxide, specifically the temperature required to give a 50% conversion rate of the material. Unsupported gold and platinum/palladium metals and oxides have a higher activity towards H_2 oxidation, but supported gold and simple metal oxides show a higher preference towards carbon

monoxide oxidation. It can also be seen that the specific variation of support utilised can affect the activity, with oxides such as TiO_2, Co_3O_4 and Fe_2O_3 requiring the lowest temperature for CO conversion.

Additionally, it has also been found that the specific dispersion and size that the particles take has a distinct effect on the activity of the gold; this can be clearly seen in Figure 1.6 with a comparison of turnover frequency for CO oxidation against varying gold particle size on differing metal oxide supports.

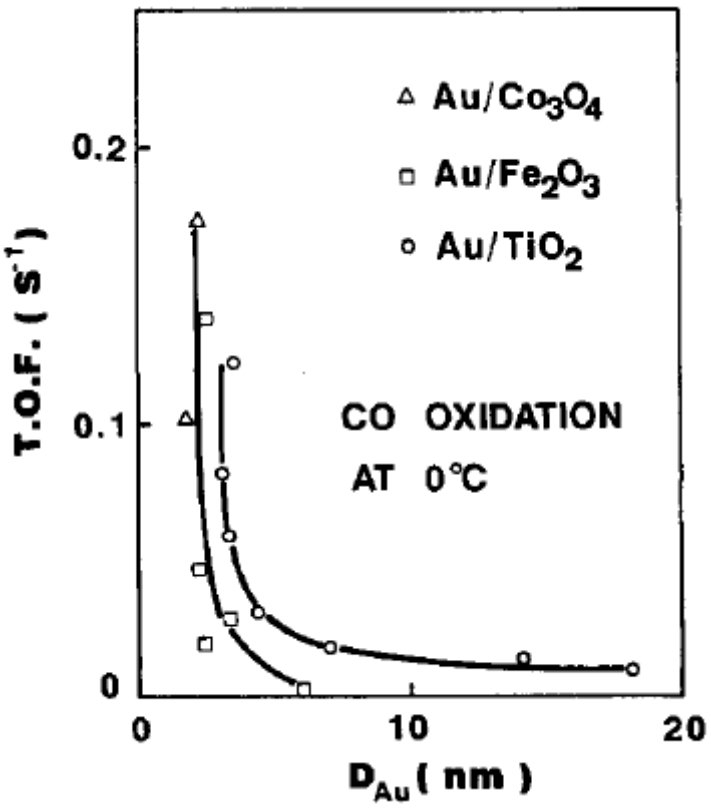

Figure 1.6 CO oxidation turnover frequency at 0 °C for supported varying gold catalyst systems. Based on exposed gold atoms compared to mean particle diameter of gold. Reproduced from Haruta[28]

This figure also once more illustrates the effect support choice can have on the catalytic activity, with Fe_2O_3 and Co_3O_4 showing higher activities than TiO_2. The specific effects of particle size on activity will be discussed in more detail elsewhere. This discovery of such a significant increase in activity for metal oxide gold led to a resurgence of interest in using gold for gas-phase and electro-catalysis for various reactions, as well as investigating the effect of these metal oxides as supports for other catalysts, such as platinum.

The reasons behind this observed increase in activity due to support choice is under much discussion. Tauster *et al*[19] coined the phrase "Strong Metal Support Interaction" (SMSI) to describe the effect of metal oxides on the activity of supported metal particles. Specifically, it was used to describe the effect seen whereby reducing TiO_2 supported metals such as Pt and Ru in H_2 at 500°C led to a significant decrease in the adsorption of H_2 and CO on the surface that is not seen with other supports. It is now accepted that the cause for this particular change in activity for group 8-10 metals supported on transition metal oxides with heating is due to encapsulation of the metal particle by the support.[29] Encapsulation only occurs when the catalyst system is heated and subsequently reduced, and as such is unlikely to be in effect when such heating is not performed, as is the case for a number of the reactions described above.

Of particular interest is the increase in activity for heterogeneously catalysed CO oxidation over titania supported gold particles: especially the observed change of activity with particle size, with a maximum often seen at mean particle diameters of ~3 nm.[30,31] This particle size effect is seen in both gas-phase and electro-catalytic CO oxidation[32], despite the differences between the two systems: most notably the oxidant is provided by the activation of water in the case of the electro-catalytic oxidation, compared to oxygen for heterogeneous catalysis. As such, considerations for this shared increase in activity despite differing conditions must be considered, and the proposed theories can be broadly grouped into three areas:

1. Low coordinated gold atoms stabilised by Titania support[33]

The number of Au atoms at kink/edge sites becomes more and more prevalent as the size of particles on a support is decreased. A progression of the structure these particles take can be seen in Figure 1.7, where the size of the clusters is compared to the ratio of edge atoms to total atoms. The figure represents both the ratio of overall step atoms as well as the ratio of atoms that are not in direct contact with the support. The overall step ratio increases until only a single monolayer of atoms forms the cluster, as to be expected.

However, of more interest is the fact that the ratio of atoms not in direct contact with the support to the total number of atoms reaches a maximum at a particle size of 2-2.5 nm. This corresponds very closely to the maximum seen in the activity for CO oxidation when these supported nanoparticles are tested, in both gaseous and aqueous environments.

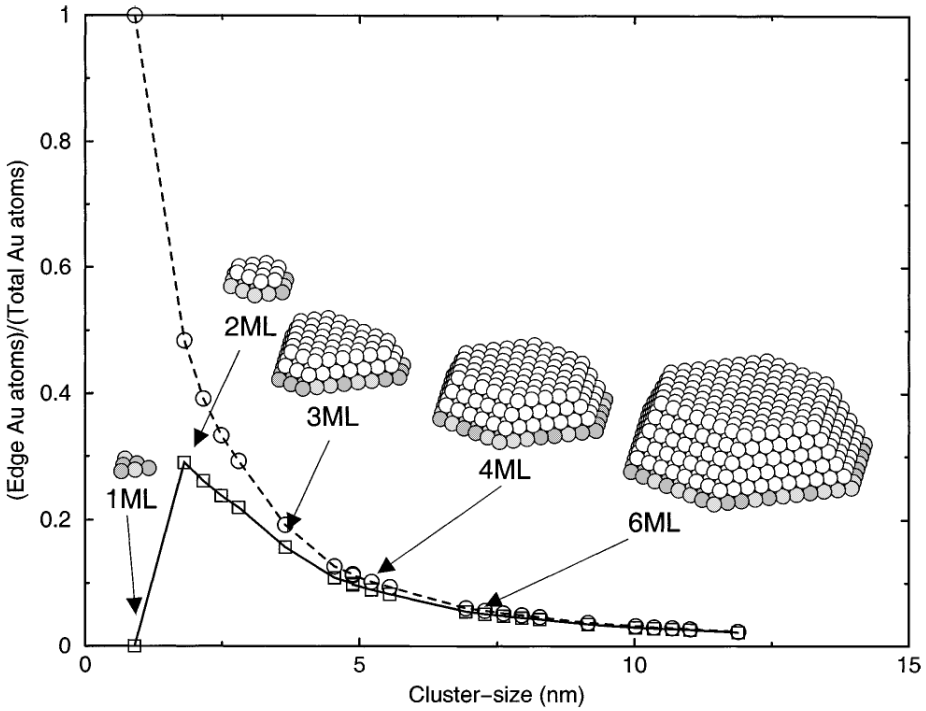

Figure 1.7 Calculated step densities for Au particles on titania. The circles correspond to the total number of step sites of the particles, whilst the squares are the step sites not in contact with the titania. Reproduced from Mavrikakis *et al.*[34]

Within this size range the particles also form such that they consist of two monolayers of gold, which, as discussed in further detail below, is also true for the particle systems tested in other works.

A further example of the effects that lower coordinated atoms have on the activity of gold comes in work by Bahn *et al.*[35] where they investigated the reactivity of extremely thin (in the order of single atoms) gold chains towards both oxygen and carbon monoxide. The relative reactivity of this and other gold systems can be seen below in Figure 1.8, where the interaction energy for both oxygen and carbon monoxide can be seen compared with the coordination number for atomic gold.

A number of different systems are used for this piece of data, notably, from highest to lowest, plain gold surface (9), stepped gold surfaces (7), Au_{10} clusters (4-5) and the gold chains mentioned above (2), with the bracketed numbers referring to the coordination number of the gold atoms present in these systems.

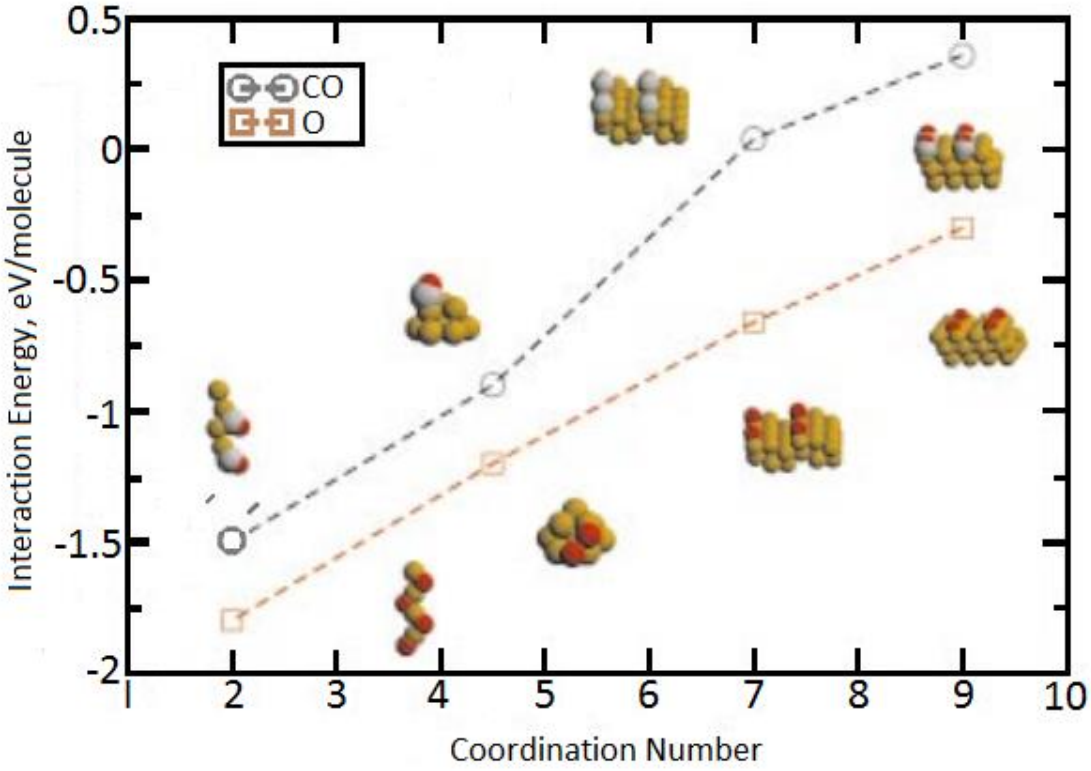

Figure 1.8 Interaction energy for oxygen and carbon monoxide vs atomic coordination number for a number of different gold systems. Examples of the systems that provide atoms with the coordination numbers are present, showing the relaxed state when either O_2 or CO is adsorbed onto the systems. Yellow atoms are gold, red oxygen and grey carbon. Graph taken Bahn *et al.*[35]

It can be seen that by decreasing the coordination number of the gold atoms, the stronger the bonds that form between the gold and the O_2/CO when adsorbed onto the surface. This corresponds with an increase in the reactivity of the gold towards these two materials: Bahn *et al*. described the atomic gold chains as the most reactive form of condensed gold possible, more so than the metal-oxide supported gold clusters we have been describing so far.

2. Titania induced electronic modification of gold

This corresponds to two different effects giving the activity increase: changes in the concentration of surface reactant species or the lowering of activation barriers. An excellent example of such electronic changes is that as the size of particles is decreased, the band gap of the gold begins to increase, as seen in Figure 1.9.

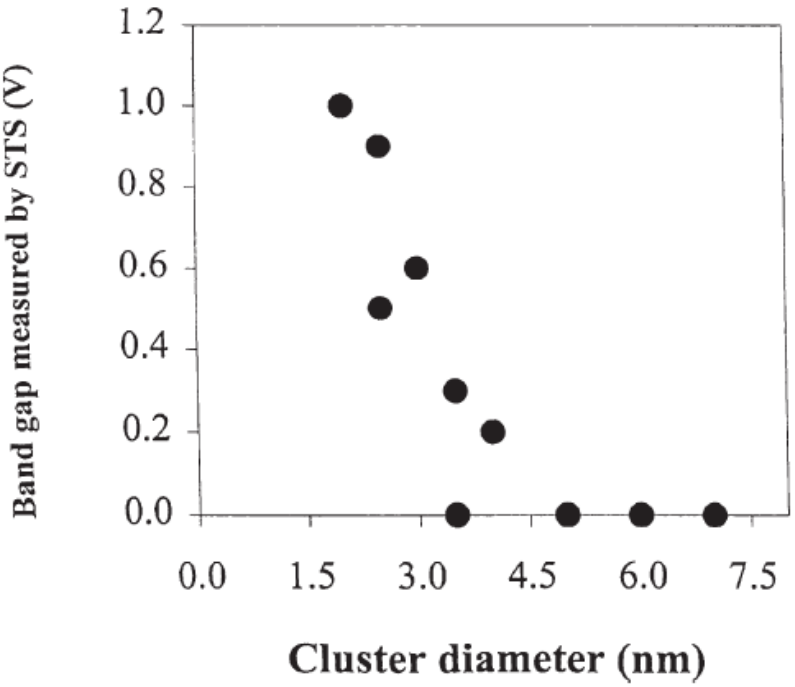

Figure 1.9 Scanning Tunnelling Spectroscopy (STS) produced Band Gap measurements for varying gold cluster on Au/TiO_2(001)/Mo(100). Distinct change can be seen in band gap as particle size is decreased. Figure taken from Valden *et al.*[36]

It was seen that the gold begins undergoes a transition from metal to non-metal at a particle sizes of ~3.0 nm. This roughly coincides with the maximum activity for these supported gold particles, as demonstrated in Figure 1.10, where the activity of the various particles is shown alongside the corresponding band gap.

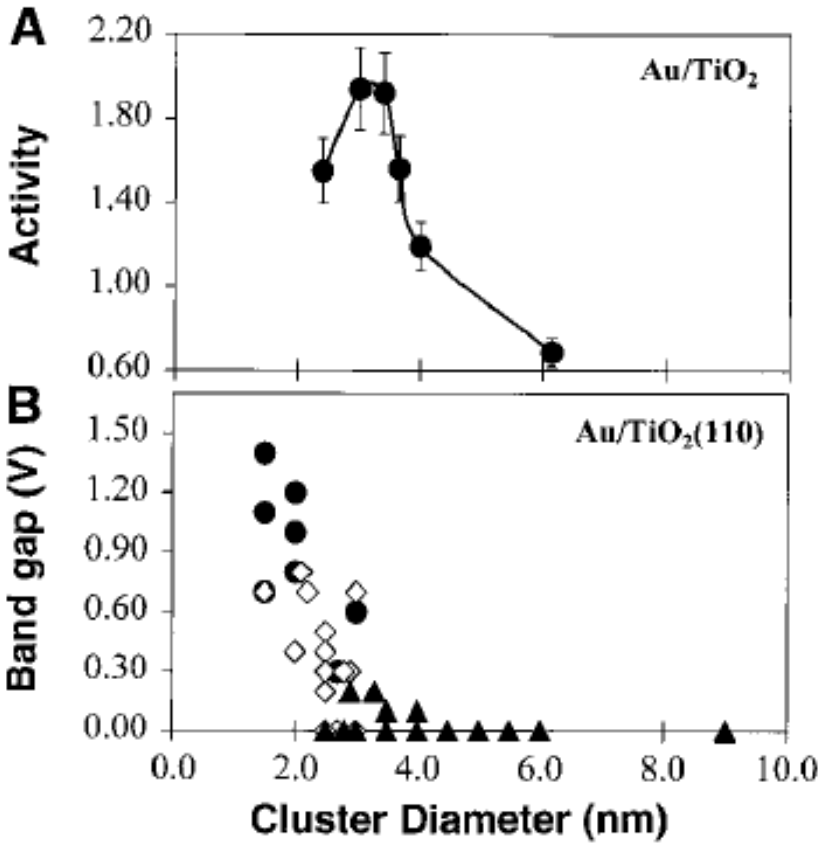

Figure 1.10 CO oxidation Activity and band gap data for varying diameter Au particles. The differing symbols in the band gap graph, B, correspond to variations in the composition of the particles: (●) two dimensional clusters, (◊) three dimensional clusters 2 layers thick and (▲) three dimensional clusters with three or more layers. Activity maximum is at ~0.3 nm diameter clusters with the ◊ clusters having the closest correlation with this maximum. Figure taken from Valden et al.[31]

The highest catalytic activity is seen for particles with a diameter of ~3 nm consisting of two monolayers of material; the band gap of the gold was measured to be 0.2-0.6 eV via Scanning Tunnelling Spectroscopy for particles of this size. This change in the band gap also corresponded with the change of gold from a metal to non-metal state, thus giving a possible explanation for the change in activity for CO oxidation. This also corresponds to the maximum seen in Figure 1.7, where particles with two monolayers of a size of ~3 nm gave the highest ratio of edge sites, adding an interesting correlation.

This bi-layer model was further upheld by a study of various levels of Au coverage on titania, with two monolayer thick gold giving the highest activity[37] (though it was

suggested that perimeter interactions of metal and metal oxide have no effect on the activity).

There are two possible explanations for this change in electronic activity: the first is that the interaction of gold with the support induces strain in the gold layer/particles which affects the activity of the surface Au atoms at smaller particle sizes[34]. This is shown in the binding energy of atomic oxygen; it was increased from -2.54 eV on an unstrained surface to -3.14 eV by adding a tensile strain of 10% to Au(111)[38], though this effect is less pronounced at step sites. The second explanation is that charge transfer may lead to $Au^{\delta+}$ forming, giving a higher activity, as electron transfer from the Au to the titania induces an interface dipole, whose electric field is screened more efficiently as the size of the gold nanoparticles is increased.[39]

3. Active sites at the Titania–Gold interface or Spill-over of reactants from Titania to gold particles[40]

These two techniques have a number of similarities to one another but some distinct differences are present, so further explanation is required. We will be specifically discussing the gas-phase system here; the processes for the gas-phase and electrochemical system are considered to be very similar to each other, however, so there is a large degree of overlap for the research of these two systems.

The process for both of these CO oxidation methods begins identically: the oxidant is removed from the electrolyte and adsorbs onto the surface of the support. At this point, the methods diverge, depending upon where specifically the oxidant adsorbs on the titania prior to oxidation occurring. In the first case, the oxidant adsorbs directly onto defects (most probably oxygen vacancies in the surface[41]) on the titania at the interface between the gold particles and the titania. From here, the carbon monoxide can shift into close proximity to the oxidant and react directly together. A representation of this process can be seen below in Figure 1.11.

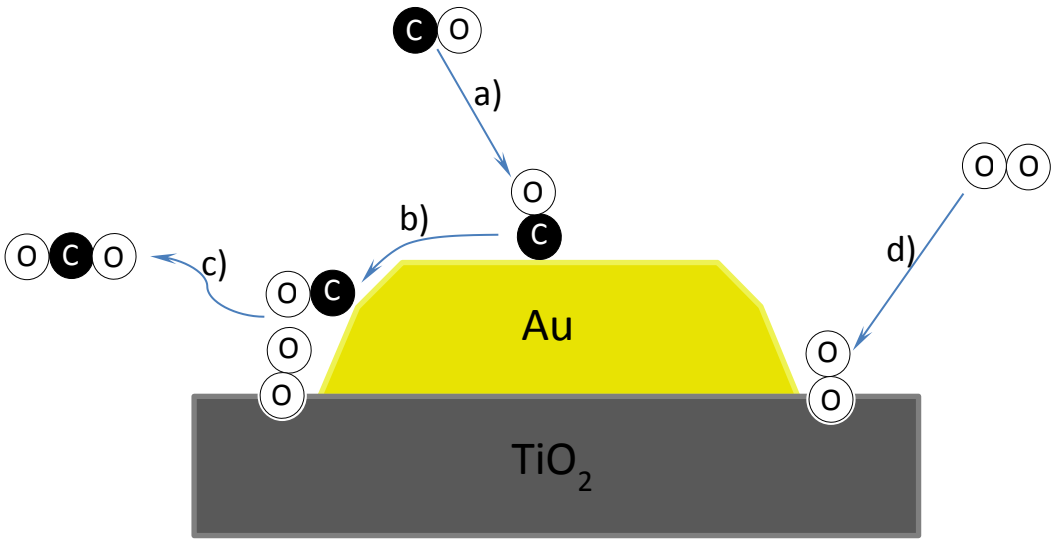

Figure 1.11 Schematic representation of the pathway for CO oxidation on Au/TiO_2 utilising the Au/TiO_2 interface. The process proceeds as follows: a) CO adsorbtion onto the Au, b) movement of CO to edge of gold, c) reaction of CO and O_2 to form CO_2 and d) Replenishment of the oxygen via dissociative adsorbtion at interface sites.[42]

The oxidant (oxygen here) adsorbs into oxygen vacancies present in the titania support at the gold perimeter (d) where the two are interfaced together. Carbon monoxide adsorbs onto the gold surface (a), where, due to a reasonable degree of manoeuvrability, the CO can move such that it comes into close proximity with the oxygen adsorbed at the interface (b). At this point the activated oxygen and CO react so as to produce carbon dioxide, which is then released from the gold (c) and the process repeats. It is this close proximity of the activated oxygen to the CO on the gold that gives the increased reactivity seen for the system.

This brings us to the second method, which is a modified version of the first; so named the spill-over effect (otherwise known as the Bi-functional Effect) after the action taken by the reactants (hydroxide or oxygen[43]). Spill-over is a process by which the active species (either adsorbed directly or formed on the surface) is transported from one surface onto another separate surface that does not adsorb or form the species naturally under the same conditions.[44]

In the system considered by us here, the oxidant is adsorbed onto the titania support and then migrates from the support directly onto the gold rather than attaching

themselves to interface sites between the gold and titania (though migration to the interface is also possible).

Once the oxidant has reached the gold, the reaction can proceed: CO molecules previously adsorbed onto the gold react with the spilled-over reactant and complete the sequence. This technique is very similar to the previously discussed method with the reactant deposited directly at the interface, with one particular caveat: the area that can be utilised by the intermediate oxidants is considerably larger for the spill-over mechanism. The reaction is not dependent on the immediate adsorption of molecules at the much smaller interface band for the reaction to occur, but instead can be supplied from an area of titania surrounding the gold particle.

An example of the mechanism for the gas-phase spill-over reaction as proposed by Grunwaldt and Baiker[43] is shown below.

$$1.\square_* + O_2 + e^- \rightarrow \square_* - O^-_{2ads} \qquad \textbf{Equation 3}$$

$$2.\square_* - O^-_{2ads} + 2\,Au \leftrightarrow 2Au - O_{ads} + e^- + \square_*$$

$$3. Au + CO \leftrightarrow Au - C \equiv O$$

$$4. Au - O_{ads} + Au - C \equiv O \rightarrow 2Au + CO_2$$

Mechanism for the low temperature oxidation of CO on a Au/TiO_2 system. 1. Irreversible adsorption of Oxygen onto vacancy sites ($\square*$) in the Titania, 2. Spill-over of adsorbed oxygen to gold surface, 3. Reversible adsorption of CO onto gold, 4. Reaction of CO with adsorbed oxygen on gold. Equations reproduced from Grunwaldt and Baiker.[43]

With the support aiding in the formation of activated oxygen prior to moving onto the gold, as oxygen does not easily adsorb directly onto gold, the rate of the CO oxidation increases to give a more efficient system and thus an increase in the CO oxidation activity.

1.4.2 Effect of moisture in Gas Phase systems

Of interest to the proposed Interface and spill-over methods for CO oxidation is the beneficial effect caused by the addition of water to the reaction process in the gas-phase system.[45] As seen in Figure 1.12, the addition of even a small quantity of moisture to the reactant gas can have a drastic effect on the reaction rate.

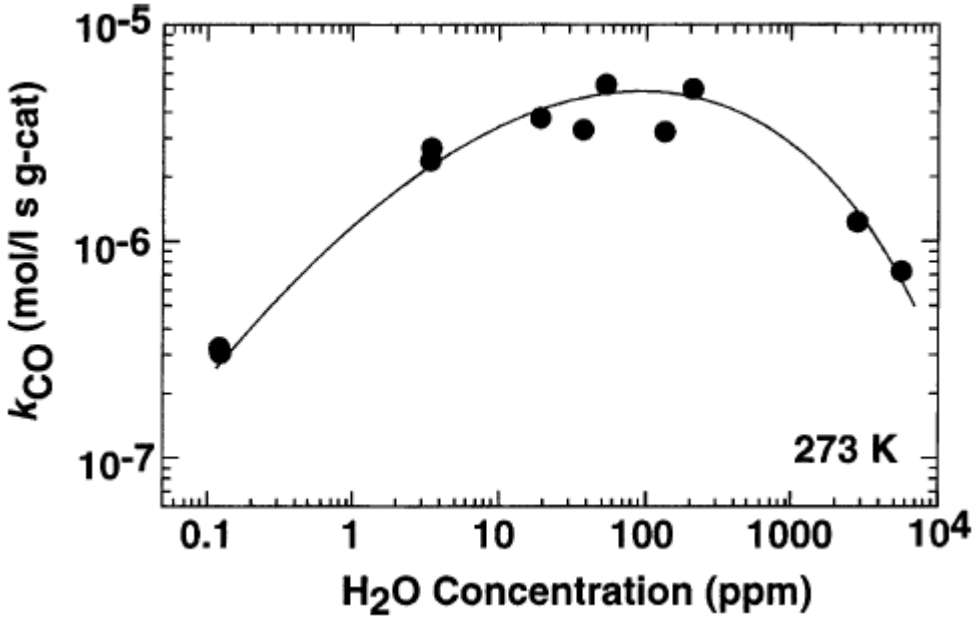

Figure 1.12 Au/TiO_2 CO Oxidation rate at 273 K dependence on moisture concentration in 1 Vol% CO in air. Reproduced from Date *et al.*[46]

The introduction of water increases the activity of the system towards CO oxidation by at least a magnitude, giving a maximum at ~200 ppm of moisture. However, higher levels of water (~6000 ppm) begin to reduce the effectiveness of the catalyst, which eventually reaches lower rates than in the system lacking hydration. This reduction in activity with increasing water concentration was considered to be because such a thick layer of adsorbed water being present blocked the active sites for the deposition of the other reactants.

The reason for this increase in activity is that once adsorbed onto the support surface, the water molecules can aid in the dissociation of oxygen pre-adsorbed at the Au-TiO_x interface oxygen vacancies, as well on the support prior to spill-over. This then allows for further reaction with the CO and easier completion of the oxidation process.[47]

A better understanding of this process can be obtained by viewing the reaction pathways as proposed by Date *et al*.[48] with the improved reactivity from the introduction of water explained thusly.

$$1.\ O_2(s) + H_2O(I) \rightarrow O^*(I) + 2OH(I) \qquad \textbf{Equation 4}$$

$$2.\ 2OH(I) \rightarrow O^*(I) + H_2O(s)$$

Formation of activated oxygen, as represented by *, via the reaction of oxygen and water for use in the oxidation of CO on titania supported gold particles. (s) refers to the molecule being bound to the titania surface and (I) denotes binding to the interface between the gold and the titania.[48]

Equation 4 denotes the central portion of the CO oxidation process, whereby the oxygen is activated for the oxidation of CO on the gold. The interesting factor is line 2, where this activated oxygen can be produced by the reaction of two hydroxyl groups bound to the interface without oxygen being present.

This allows for consideration as to the process by which the relevant active species is formed for the electrochemical environment. Of particular note is that titania may be hydroxylated prior to, or during, the procedure, depending upon the system pH. There is no evidence that the titania aids in the activation of water to produce more hydroxyls at low potential; however, it is possible that these original hydroxyl groups may be available to the catalyst by spill-over, thus removing the need for high over-potentials to activate water on the gold.

With this consideration of the effect of hydration on the system, our next section shall consider the electrochemical environment, which is naturally fully hydrated, and the activity seen for the electro-catalysis of CO oxidation with the Au/TiO_2 system.

1.5 Electrocatalysis of Titania supported Gold nanoparticles

1.5.1 Acidic Medium

The changes induced in activity with the titania supported gold nanoparticles[49] are not solely seen for the gas phase oxidation of CO. Similar increases in the CO oxidation activity have also been observed in the electrochemical system, though differences are present between the two.

The link between particle size and resulting activity in an acidic environment can be seen below in Figure 1.13 for the electro-catalytic oxidation of CO over titania supported gold nanoparticles; a maximum in activity is observed at diameters of ~3 nm, similar to the gaseous system.[31]

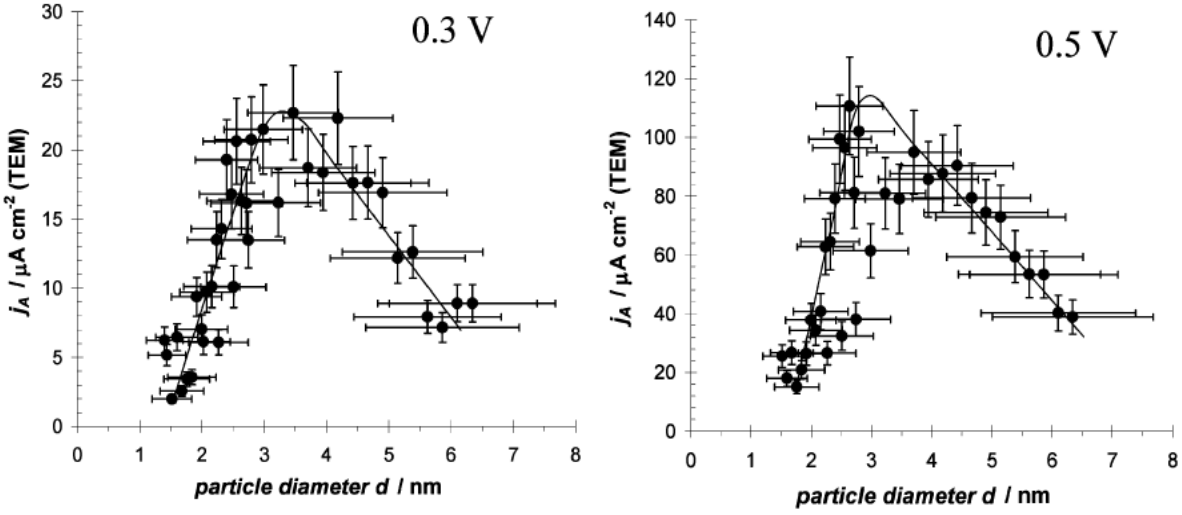

Figure 1.13 The effect on the specific activities (for the oxidation of CO in acidic media) by variation of the size of Au particles on TiO_x at two separate potential steps: 0.3 V and 0.5 V vs. RHE, 0.5 M $HClO_4$. Figure reproduced from Hayden *et al*.[32]

A sharper decline in activity is seen for particles below a diameter of 3 nm when compared to the gaseous system; with particles larger than 3 nm a more gradual decline is observed, which is more characteristic of the gas phase system. This sharp decline in activity with particles below ~3 nm has been observed to be independent of the support; this is clear from observing the CO oxidation activity of equivalent gold particles supported on carbon. The activity of these carbon supported gold nanoparticles is significantly different to that seen with the titania support, as in Figure 1.14 where the current density at 0.8 V is compared at varying particle sizes.

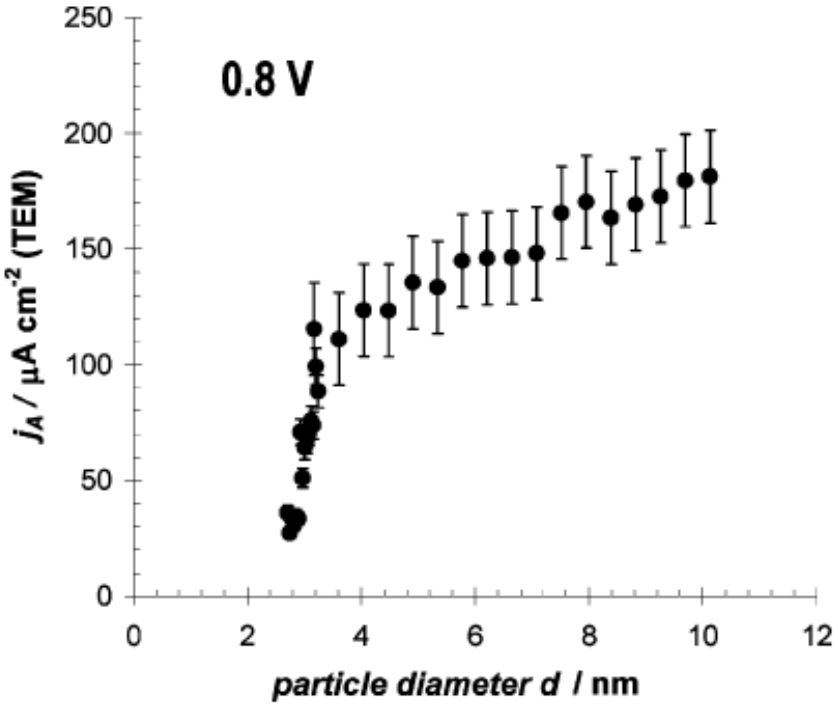

Figure 1.14 CO oxidation activity for gold nanoparticles deposited on carbon of varying sizes. Taken at 0.8 V vs SHE, 0.5 M $HClO_4$. Reproduced from Hayden *et al.*[32]

What is notable when compared to the titania supported system is that no obvious peak in activity can be seen; the activity steadily increases as the particles are increased in size from ~3nm. However, below this 3 nm point, there is a sudden drop in activity similar to Figure 1.13 and consistent with the particle sizes tested; due to this decline being present on both supports, it was suggested that an intrinsic particle size based deactivation of the gold is at play. Importantly, this also indicates that there is a separate, support based contribution towards the activity of the gold particles; it is this in the titania system that gives improving reactivity as particles size is decreased until particles of 3 nm are reached, where the intrinsic size effect overcomes this improved reactivity from the support.

It should be noted that a similar pattern has also been observed for the electro-reduction of oxygen on gold particles with carbon and titania supports.[50] A comparable peak in activity is seen at ~ 3 nm on titania, whilst the carbon support gives increasing activity with increased particle size as above. Both supports show a very similar drop in activity with particles below ~ 3 nm, once again supporting an intrinsic particle size dependence for the activity independent of the support.

Also relevant to this discussion are the data displayed in Figure 1.15; the perimeter length of the gold particles utilised in Figures 1.13 and 1.14 were calculated as a function of particle size. This was done to allow for the consideration of the activation of water at interface sites between the titania and the gold nanoparticles to explain the increased activity.

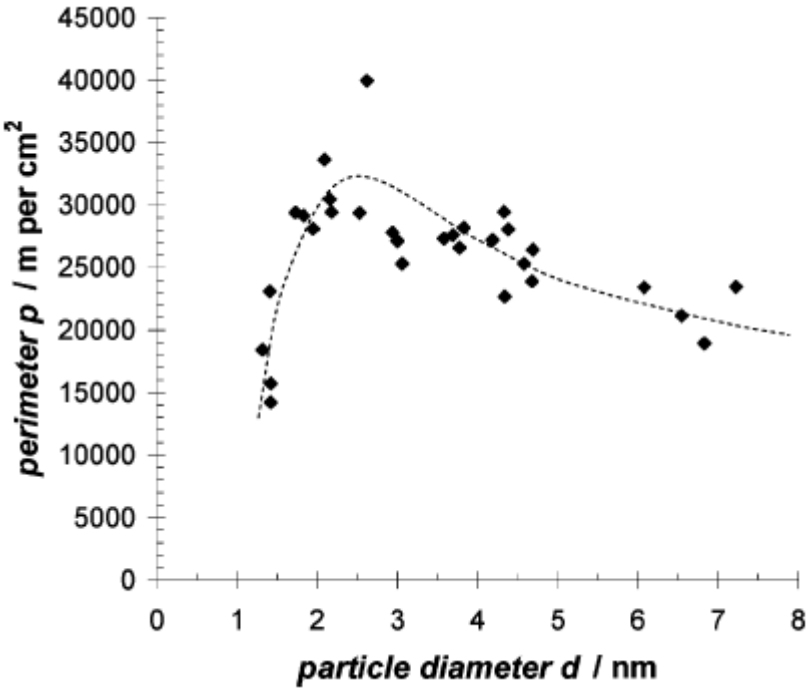

Figure 1.15 Size dependence of titania supported gold particle perimeters calculated via TEM. Reproduced from Hayden *et al.*[32]

The maximum perimeter is seen at particles of 2.5-3 nm diameter, correlating with the activity maximum observed in Figure 1.13. As such, it can be considered that a possible perimeter dependence for the observed particle size dependent activity increase is present, which provides support towards either an interface or spill-over based mechanism being responsible for the observed increase in activity. Some differences are present, however: the perimeter decrease at particles less than 2.5-3nm is less steep than the corresponding activity drop; this was attributed to the observed intrinsic particle size effect, which is independent of support.

1.5.2 Alkaline Medium

An interesting point for the electro-catalytic oxidation of CO on gold is the effect the environment has on the process, notably changes in the pH of the system. CO oxidation occurs at relatively high over-potentials,[51] giving its original consideration as a less than ideal catalyst. However, this differs when the pH of the system is modified; the catalytic activity drastically increases for CO oxidation on gold when performed in an alkaline environment, superior even to a similar platinum electrode.[52]

This shift can be seen clearly in Figure 1.16, where the hanging meniscus RDE of 3 separate Au crystal faces with varying CO concentrations is shown for both acidic and alkaline electrolytes.

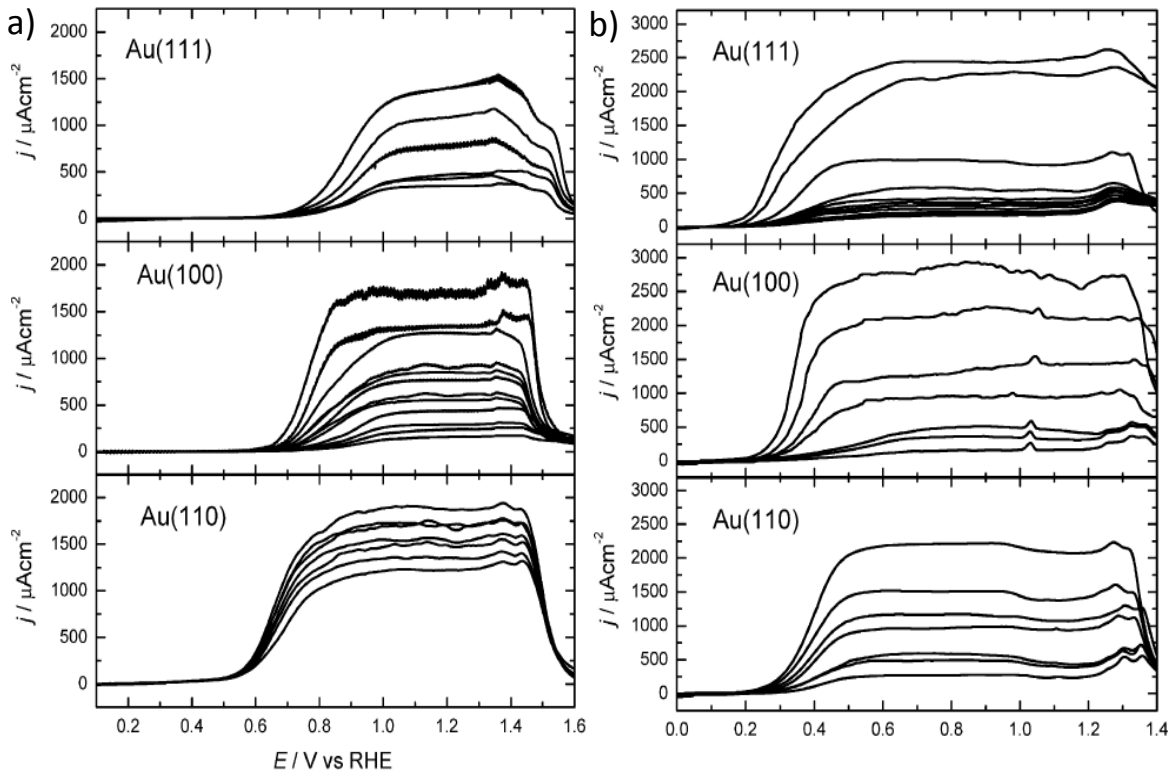

Figure 1.16 Comparison of CO oxidation over (111), (100) and (110) Au crystals faces. Performed utilising a Hanging Meniscus Rotating Disc Electrode setup with varying concentrations of CO. a) 0.1 M $HClO_4$, b) 0.1 M NaOH. Scan rate = 50 mVs^{-1}, Rotation Rate = 1100 rpm. Graphs reproduced from Rodriguez *et al.*[53]

It can be seen that there is a clear enhancement for the CO oxidation for the alkaline environment when compared to experiments carried out in acid. Rodriguez *et al.*[53] proposed the following mechanism for the oxidation of CO in an alkaline environment.

$$1.\ CO + Au \leftrightarrow CO_{ads} \qquad \textbf{Equation 5}$$

$$2.\ CO_{ads} + OH^- + Au_{nn} \leftrightarrow CO_{ads} + OH^-_{ads,nn}$$

$$3.\ CO_{ads} + OH^-_{ads,nn} \rightarrow COOH_{ads} + Au + e^-$$

$$4.\ COOH_{ads} \leftrightarrow COO^-_{ads} + H^+$$

$$5.\ COO^-_{ads} \rightarrow CO_2 + Au + e^-$$

Mechanism for alkali based CO oxidation as proposed by Rodriguez *et al.*[53] Ads = adsorbed on surface, nn = nearest neighbour binding sites

In the above sequence, the rate determining step is number 3, where the adsorbed CO and OH^- combine. An important consideration for this sequence is the designation of the site that the OH^- binds to as the "nearest neighbour" Au binding site. This comes from an earlier work by Rodriguez *et al*.[54] where they proposed that carbon monoxide promotes its own oxidation by enhancing the adsorption of its oxidant at neighbouring sites (the nn above).

What is of interest to our discussion here is the second equation, the step preceding the rate determining step (RDS), the combination of adsorbed CO and OH^-, specifically, how this step differs in an acidic environment:

$$CO_{ads} + H_2O + Au_{nn} \leftrightarrow CO_{ads} + OH^-_{ads,nn} + H^+ \qquad \textbf{Equation 6}$$

Replacement stage for Equation 5 step 2 for the oxidation of CO on gold in an acidic environment.

For both environments the oxidant is OH^-, but it must be produced in acidic media compared to the alkali environment where OH^- is more readily available. With CO and OH^- enhancing each other's binding, the enhanced CO oxidation in alkali compared to acid can be explained.

However, what is particular interest to us here is the relationship between the enhanced activities seen for gold in an alkali environment, even bulk Au, and that observed for gold supported as nanoparticles on titania; the improvements seen for the CO oxidation activity in both of these systems are very similar to one another. This links in with the proposed spill-over mechanism for the titania supported gold, as the titania aids in the formation of hydroxyl groups that then transfer to the gold (as they do not form easily on the gold itself) and react with the CO. As such, the spill-over mechanism can be considered of even higher interest for investigation.

With the relationship between particle size and activity in the electro-catalytic system tallying so closely with that seen in activity for metal oxide supported gold nanoparticles for the gas phase oxidation of CO (Figure 1.10), it can be considered that a consistent explanation may be behind the increased activity seen in both systems, with the three major methods described previously being of particular interest for both.

With this connection between the electrochemical and gas-phase oxidation of CO being catalysed in such a similar fashion for the titania supported gold nanoparticles, further investigation is required into the exact mechanism behind this change. One particular method that is gaining in popularity for examination of these systems is so-called “inverse” catalysis which will be of particular focus to us here.

1.6 Inverse Catalysis

A large number of the metal/metal oxide interactions that affect the catalysis of metal/metal oxide catalysts are considered to be due to the interface of the metal and metal oxides phases. The importance of the metal/metal oxide interface has led to interest in the use of so called inverse catalyst systems as they allow for a greater investigation of the metal/metal oxide role in the catalytic process.[55,56]

The concept of an inverse catalyst is rather simple, with the basic set-up being almost identical to those described above; however, whereas those consisted of a metal oxide film covered with metal nanoparticles, this system comprises a metal film decorated with metal oxide nanoparticles, thus “inverting” the catalyst. Figure 1.17 gives a comparison of these two systems.

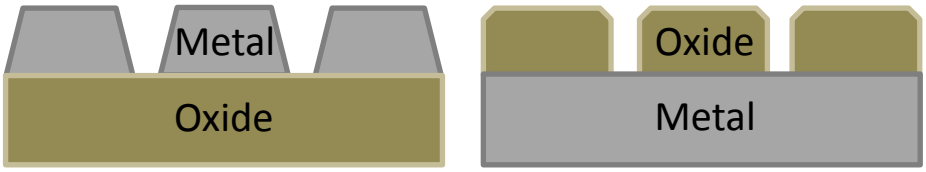

Conventional Catalyst **Inverse Catalyst**

Figure 1.17 Representation of both the conventional and inverse catalyst systems for supported nanoparticles.

The utilisation of inverse catalysts is not a recent development, especially in the case for oxide/metal systems.[57] An inverse system allows for a number of different interactions between the catalyst and the reactants that are not available to the non-inverse set-up. In the inverse system, the reactants can more freely interact with the defects on the metal oxide (often defects on the metal oxide act as guides for particle deposition in the non-inverse system and are thus less available), the surface of the metal and the interface between the two.

A number of reactions have been seen to be affected by the use of inverse catalysts such as these, the most notable being the water-gas shift reaction, which is relevant to us here with our interest in the oxidation of CO. In particular, it has been seen that metal oxides (such as TiO_x and CeO_x) on metal surfaces can be more reactive than the corresponding non-inverse system.[58,59] An example of this increased reactivity for the Cu/CeO_2 system is shown in Figure 1.18, with a comparison with the plain Cu also present.

It was proposed that in this system, water dissociated onto the oxygen vacancies present on the metal oxide surface, with carbon monoxide being activated by the gold atoms at the interface of the metal/metal oxide.

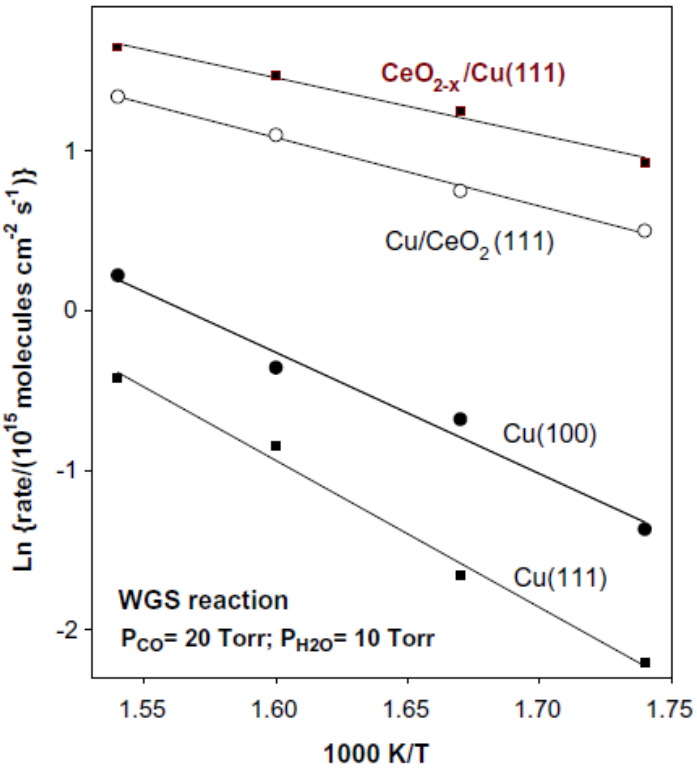

Figure 1.18 Arrhenius plot for the water gas shift reaction on various catalysts. Reproduced from Rodriguez and Hrbek[55]

Another system of interest was Yan *et al*.'s[60] investigation into the oxidation of carbon monoxide on Fe_2O_3/Au(111): the addition of iron oxide transforms the inert Au(111) crystal into an active catalyst for the CO oxidation. Yan *et al.* found that the rate of CO oxidation was dependent on the total coverage of iron oxide on the gold surface.

The activity of the system increases as the Fe_2O_3 coverage increases, with a maximum reached at ~0.4-0.6 monolayers; further deposition resulted in the activity decreasing before disappearing completely with Fe_2O_3 fully covering the Au(111). This led them to believe that it was the iron oxide/gold perimeter that was the active region of the catalyst, with the rate limiting step being the CO oxidation by chemisorbed molecular oxygen.

This pattern in activity with deposition could also be considered to be congruent with the spill-over mechanism: the Fe_2O_3 particles would only be able to affect a certain area of the gold, thus initially increasing the level of Fe_2O_3 would give increases in activity as the Spill-over reaches effects a greater degree of the gold. However, after reaching 0.6 monolayers, the area affected by spill-over from the Fe_2O_3 may begin to overlap, giving

the effective decrease in activity seen as further coverage with Fe_2O_3 does not increase the area affected by spill-over, but more of the gold surface is covered, leading to the decrease in activity seen, culminating in no activity when fully covered.

These examples agreed with work performed by others: Fujitani *et al.*[61] found that the turnover frequency and activation energy for the oxidation of CO at low temperatures on both TiO_2/Au(111) and Au/TiO_2(110) systems are very similar to each other, leading further credence to the interface/spill-over being the active area.

As such, in order to distinguish the origins of this improved electro-catalytic activity induced by a titania support for gold nanoparticles,[32,62] it was decided that the inverse system would allow for a suitable investigation, particularly into the possible role of a spill-over mechanism in the reaction. Utilising the inverse system allows for such a suitable investigation as it effectively allows us to discount a large number of the possible theories for the increased activity:

Firstly, in the Inverse system, no significant electronic changes will be present in the gold compared to the gold nanoparticles, or at least if so they will be significantly different. This comes from the gold being in its bulk state, with the energy states being far from the point at which they begin to separate out to give the non-metallic behaviour as described earlier for the gold nanoparticles.

The second method, the presence of a greatly increased presence of gold edge/corner atoms, can be discounted once more due to the presence of bulk gold instead of the particles: no gold edge/corner atoms will be present except for those caused by any ridges that were present preceding deposition, thus giving a severely reduced level of atoms of these types.

Thirdly, and finally, the likelihood that the sites at the interface between the gold and the titania are the same as in the standard system is not as high; though this possibility is still present, it can be considered to be reduced.

This should leave spill-over of the reactant from the titania to the gold as the main mechanism for the increased activity, and we should hopefully be able to see this mechanism in action. Thus, by testing this inverse system electro-catalytically for the oxidation of CO with varying degrees of titania coverage, we should be able to determine

the effect titania has on activity, and, if so, the degree to which the spill-over/interface sites are responsible for the increased activity seen. This is illustrated in Figure 1.19, where the difference expected between the normal and inverted systems for the spill over method, specifically for the movement of hydroxide ions from the TiO_2 to the metal catalyst, is displayed.

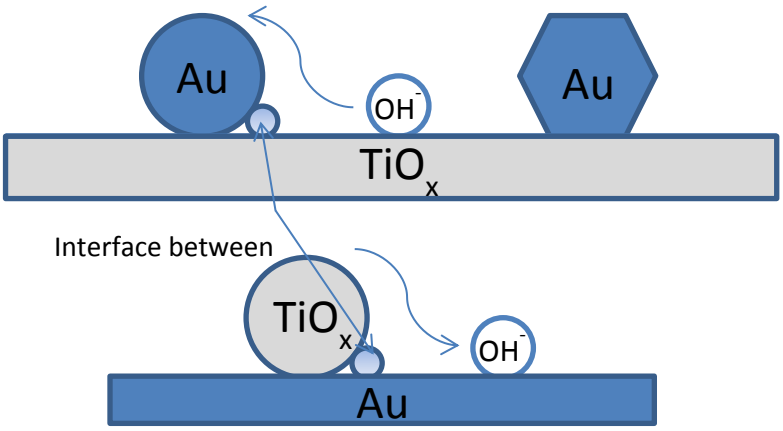

Figure 1.19 Schematic representation of the Au and TiO_x system for both standard and inverse catalysts, with the spill-over of hydroxide ions between the titania and gold being shown.

1.7 Growth methods for titania nanoparticles

With the electro-catalytic behaviour of the Inverse system being considered for further investigation in this project, a method for the synthesis of suitable titania particles on a gold substrate is required. To allow for the most significant comparison to be made between previous investigations and this project, the deposited titania was required to be of similar sizes and shapes to the nanoparticles used in those works, hopefully resulting in a range of particle sizes. As such, previous methods utilised to deposit titania nanoparticles onto a gold surface were investigated and are described below.

For this project, deposition methods that produced consistent particles with a good degree of reliability were required. A number of methods were considered for the controlled deposition of titania nanoparticles onto a surface in Ultra High Vacuum (UHV), with two standing out as most suitable.

The first method that we will discuss is known as reactive – layer assisted deposition (RLAD).[63] In this methodology, a multilayer of reactant (such as NO_2) is grown on the substrate surface at very low temperatures (~90 K). Once done, the second reactant with the required material for the final product (Ti for our purposes) is physical – vapour deposited (PVD) onto the initial layer. These layers are allowed to interact with each other to form the desired material (TiO_x) and the temperature is then increased to remove any unreacted molecules/ volatile reaction products from the surface. The heating step also produces the nanoparticles, with them forming as the evaporation occurs.

The RLAD method requires a very specific environmental set-up, notably a suitable system for cooling of the substrates coupled with simultaneous PVD onto the gold surface. As such a set-up was not available to us; a simpler method for the deposition of titania nanoparticles was thus required. The second, considerably simpler method that has been used by numerous people consists of depositing titanium directly onto a gold surface and oxidising the resulting particles to titania once it is on the surface. As this method does not require the substrate to be held at low temperatures, with no introduction of specific gases, this process much simpler than the RLAD method, and, more importantly, feasible with the experimental set-up available.

1.7.1 Substrate preparation

With this much less complicated method for the synthesis of titania on a gold surface, the synthesis of the Inverse system could be performed. However, with this simplicity come issues with maintaining control of the deposition process and ensuring the particles produced are consistent across all samples. The first step thus becomes choosing the correct form of gold to use as the substrate: the Au(111) crystal face is most commonly utilised in this capacity as, when sufficiently heated, the crystal surface reconstructs to form what is known as the “Herringbone” reconstruction, an example of which can be seen in Figure 1.20.

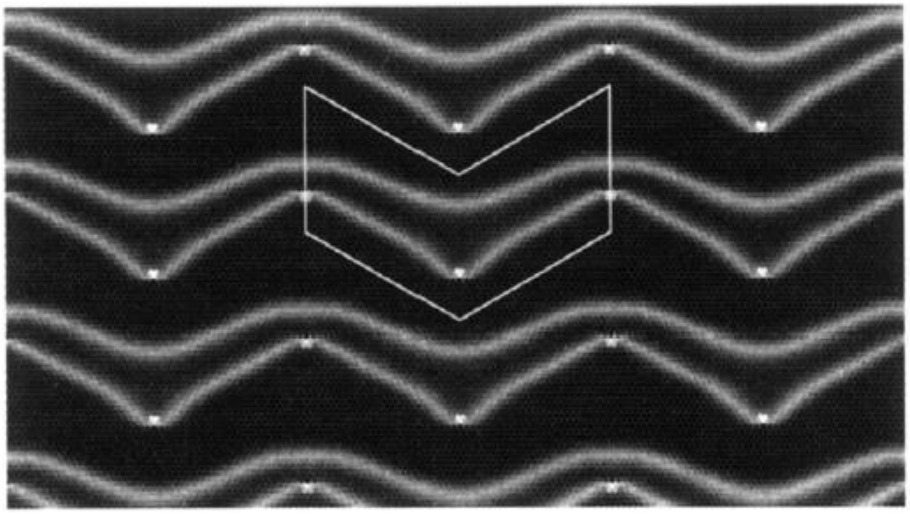

Figure 1.20 Reproduction of the herringbone reconstruction of the Au(111) surface after heating. Image reproduced from S. Narasimhan and D. Vanderbilt.[64]

This reconstruction comes about from the uniform compression of surface atoms along the (110) direction, resulting in a unit cell with lattice vectors of 22a*√3a.[65] This shift of the surface atoms results in repeating pairs of ridges forming on the gold surface; the specific corrugated angling that these ridges take as they progress across the surface gives the distinct structure visible above, coined the Herringbone reconstruction due to its supposed resemblance to the pattern of fish bones.

Figure 1.21 illustrates a cut-through representation of one of these line pairs, demonstrating the ridging that occurs to give the visible surface formations.

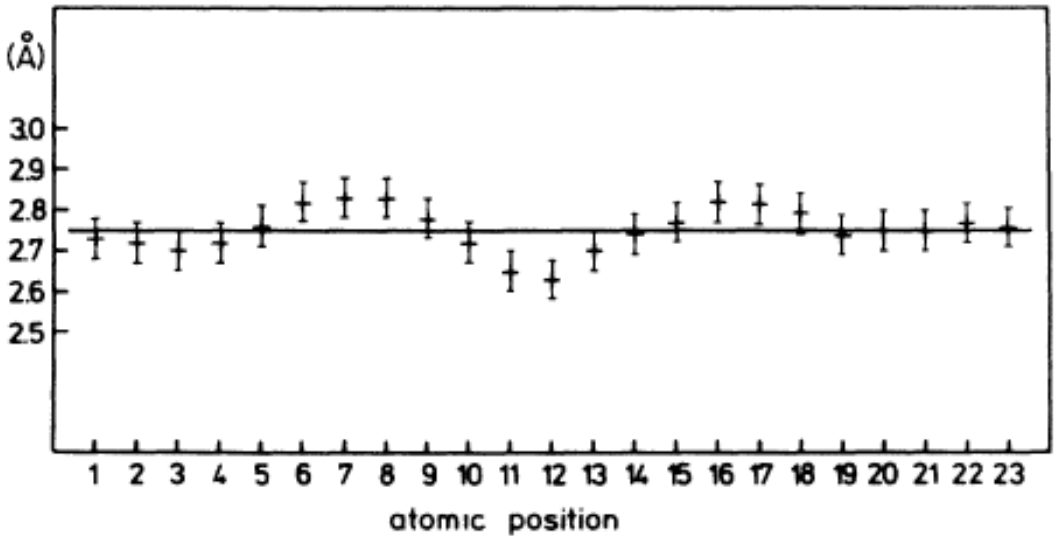

Figure 1.21 Atomic Representation of side view of gold(111) surface after heating, showing restructuring of surface during the Herringbone reconstruction. Image taken from Barth *et al.*[66]

This particular reconstruction is preferred for the deposition of metals onto gold as it has been noted (for a significant variety of metals[67, 68,69]) that nanoparticles deposited on the reconstructed Au(111) surface with PVD preferentially form at the elbows of the herringbone reconstruction. A large degree of the control of the particle distribution comes from this preferred deposition of the metals, and is thus of vital importance to us here.

A very clear representation of this preference can be seen for Ti in the work by Carrozzo *et al.*[70] The initial particle growth nucleates on the elbows at low Ti levels, though even at these levels the elbow sites are filled; some particles are seen forming on sites other than the elbows, though only in small quantities. Further deposition leads to increased particle sizes rather than further individual particle formation. This difference can be seen more clearly in Figure 1.22, where Ti deposition has filled all of the elbow spaces with a deposition of 0.05 ML, compared to the elbows filling all spaces only at ~0.14 ML, with a small amount of coalescence beginning.

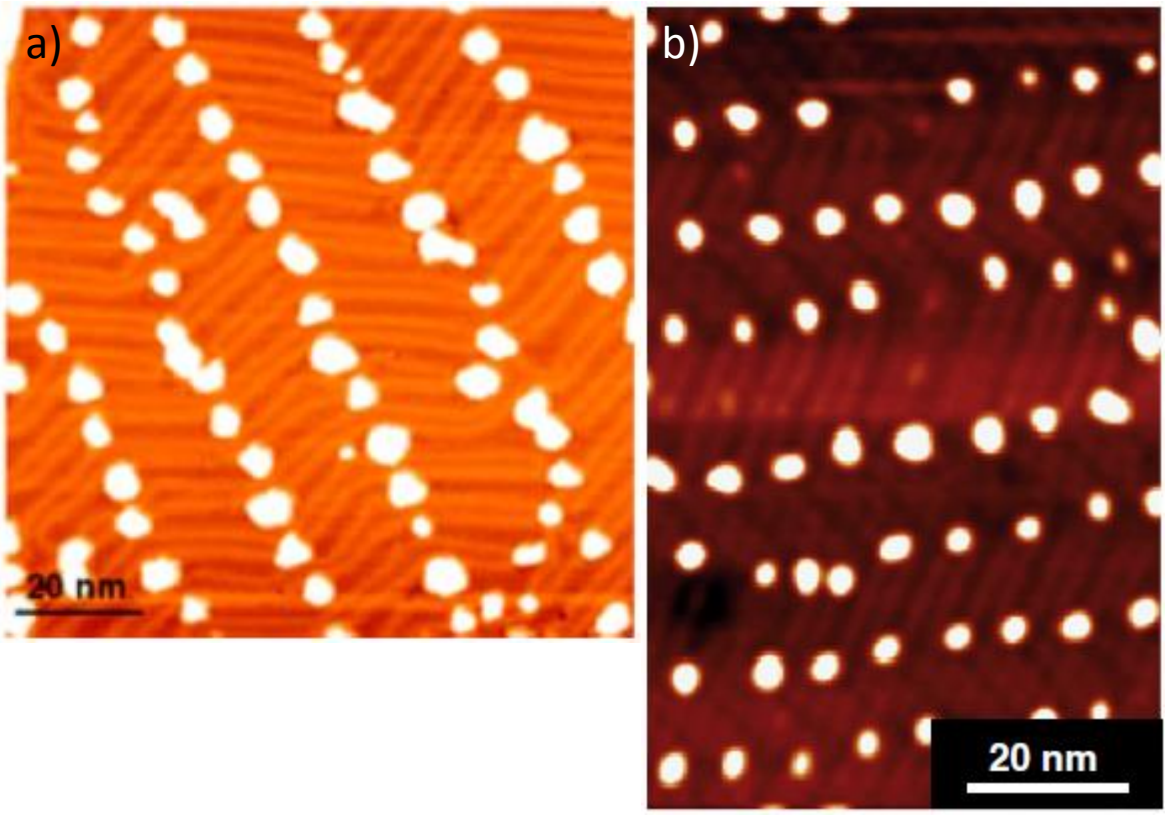

Figure 1.22 STM images of metal particle growth at elbows of herringbone reconstruction on Au(111). a) Pd growth with 0.14 ML deposition, reproduced from Casari *et al.*[61], b) Ti growth with 0.05 ML deposition, reproduced from Carozzo *et al.* [70]

This preferred adsorption and growth at the elbows comes about due to a two-step process occurring during the nanoparticle formation. As the initial Ti is deposited, the Au atoms at the elbows place exchange with the deposited metal: this specifically occurs at the elbow sites as the distortion of the electronic/atomic structure of the gold at the elbow apex makes them the preferential sites for this process compared to other areas of the surface. Once this exchange has occurred, this then gives a nucleus for the depositing atoms to aggregate on, leading to the preferred adsorption of the metal at the elbow sites[71] and thus a measure of control over the deposition procedure.

1.7.2 Variations in PVD methodology

Once the titanium has been deposited, the oxidation to titania can be considered. There are a number of variations in the processes that utilise this particular synthesis method (where the initial PVD of titanium onto the surface is followed by oxidisation to titania) considered for this project. The standard method for the synthesis (as used by Biener *et al.*[72]) deposits the titanium nanoparticles onto the gold via PVD with the above reconstructed surface whilst the substrate is held at 300 K.

The titanium is then oxidised by the addition of oxygen to the system, whilst the system is annealed; varying heating treatments are utilised, both during and after the oxidation process, leading to differing titania stoichiometry in the final particles. The initial monolayer coverage of Ti modifies both the size and density of the Ti nanoclusters formed. This method produced particles with a size range of 5-20 nm, which was not suitable to us here for our synthesis needs, as the investigation of the inverse system required a higher level of particle consistency across the samples, allowing for better investigation into the effect of the titania particles on the surface.

As such, further investigation was performed and a method that improves on this initial technique was found: one put forward by Potapenko and Osgood.[73] In this paper, the synthesis procedure was identical to that used by Biener *et. al* with one modification: the addition of a supplementary step in the synthesis between the deposition of the Ti and the subsequent oxidation.

In this additional step, the sample is annealed (to a value of ~900 K) before the oxidation step, which leads to the gold and titanium forming an alloy. This alloy has a particularly interesting feature: due to the interatomic distances of Ti and Au, the alloy they form together has a structure and atomic density very close to that of pure gold. As such, due to the ease with which gold alloys with titanium[74], it was thought that the titanium would fully dissolve into the bulk of the gold and thus would be lost for further use in the synthesis process.

It was for this reason that the temperature of the sample was kept at room temperature during the titanium deposition in previous syntheses so as to prevent a too significant loss of titanium into the gold. Potapenko and Osgood found, however, that this was not the case: Auger electron spectroscopy (Figure 1.23) showed that, even after being annealed to 900 K, some of the titanium remains near the surface of the gold and is, as such, still available for use in the titania synthesis.

Once the Ti-Au alloy had been formed, the system is exposed to oxygen at high temperatures, as with the Biener *et. al* technique, leading to the growth of titania crystallites on the gold surface. These crystallites were shown to form with a rutile structure: distinctive structural layers were observed in these particles of 0.23 nm, which is very close to the 0.299 nm of the rutile interlayer distance.

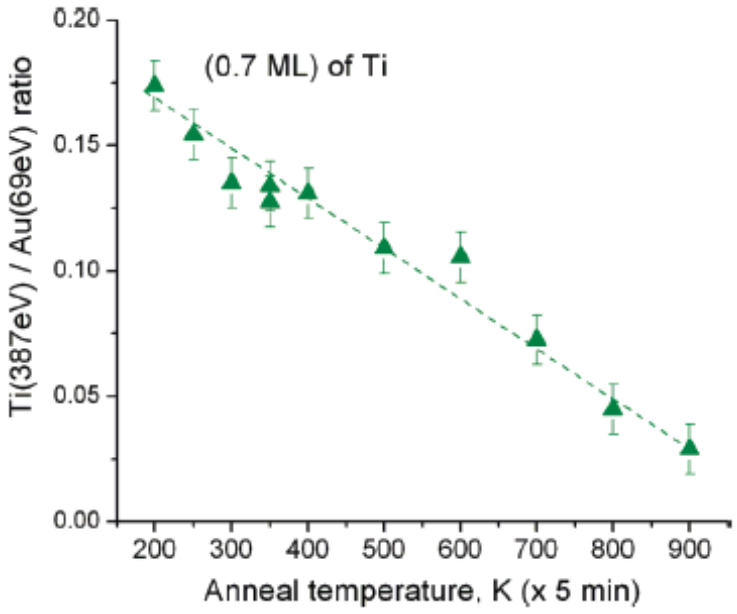

Figure 1.23 Auger electron spectroscopy ratio of Ti 387 eV and Au 69 eV signals. A clear decrease in the amount of Ti at the surface is seen as the annealing temperature is increased but even at 900 K Ti is still present near the surface. Figure reproduced from D.V. Potapenko and R.M.Osgood[73]

This pre-annealing of the surface leads to better structural homogeneity and a narrower size distribution of the TiO_x clusters on the gold. This higher effective control over the particles comes about during the oxidation step. Initially, as oxygen is introduced, titanium atoms near the surface of the crystal are oxidised first: once this process has begun, titanium atoms from further into the bulk of the gold-titanium alloy are to then react, this means that the crystallite size is much more controlled during the oxidation step. Both of these methods are simpler to perform than other suggested methods, as they do not require very low temperatures.

As such, the use of this alloying method is preferred due to the larger amount of control over the size and distribution of the nanoparticles formed on the metal surface. Thus, it was decided that this would be the technique used for the sample syntheses in this project, so as to enable a more distinctive control over the particles to allow for a better comparison with previous work done, most notably by the Hayden group.

1.8 Project Overview

The Inverse catalyst system of titania nanoparticles supported on a gold surface will be used to investigate the improved reactivity observed by the non-inverse system towards the electro-catalytic oxidation of CO. By varying the size and distribution of these deposited particles, we hope that a distinctive change in the activity of the system towards CO oxidation will be witnessed and allow us to determine the cause behind this change, or at the very least discount the expected Spill-over method for increased activity.

Utilising the Ti-Au surface alloy deposition method as described by Potapenko *et al.*[73] the titania should form into distinctive and consistent shapes, as well as give control over the placement of these particles over the surface. The density and size of the particles will be monitored via imaging using a STM set-up attached to the deposition chamber, which will also allow for determination of the state of the Au(111) crystal prior to the deposition.

These systems will then be tested utilising the BCEC for their electro-catalytic activity for CO oxidation and the effect of the particles will be observed and displayed here.

2 Model Electro-catalysis

Gold has long been considered to be the noblest of all metals, due to its apparent lack of activity[24] and thus considered to not be of use as an electro-catalyst. High over-potentials are required to drive electro-catalytic reactions on gold, such as the reduction of water to hydrogen, or oxygen evolution. In the case of CO electro-oxidation however, both the pH and the support can significantly reduce the over-potential.

This chapter will describe the processes seen for gold during electro-catalysis, as well as descriptions for titania supported gold particles and the corresponding inverse system.

2.1 Electrochemistry of Gold

2.1.1 Polycrystalline Gold

For this project, we shall be considering the cyclic voltammetries of gold in an acidic medium, specifcally perchloric acid. An example of a CV taken in such an environment with varying potential limits is shown in Figure 2.1.

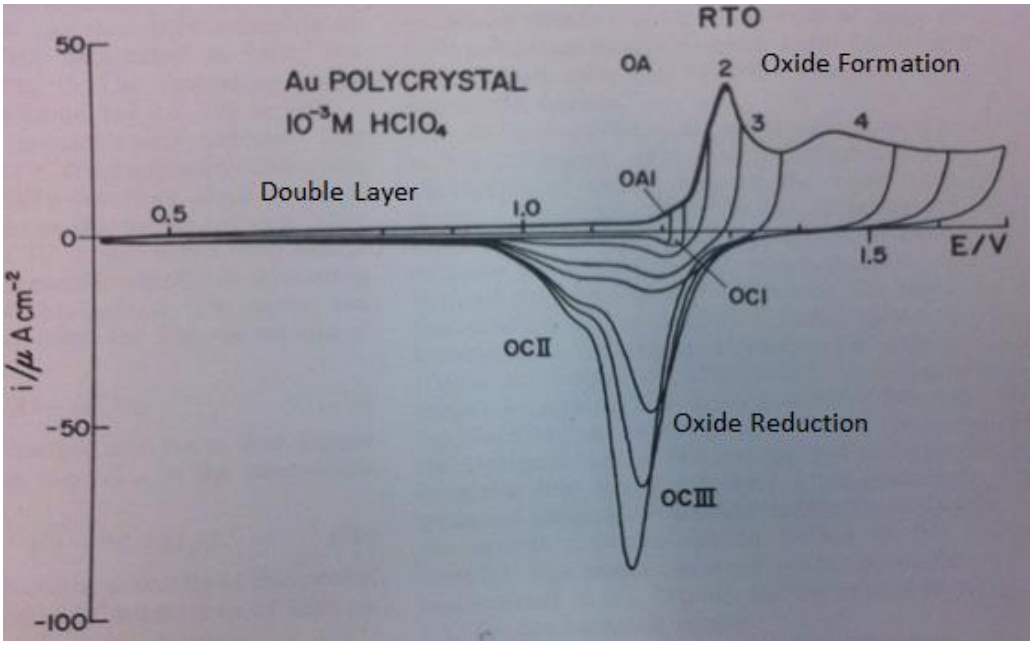

Figure 2.1 Standard CV of polycrystalline gold. Varying potential limits, 20 mV s^{-1}, 0.01 M $HClO_4$.Reproduced from Angerstein-Kozlowska *et al*.[75]

The most notable features are the peaks associated with oxygen effects on the surface. During the positive sweep, a current increase is seen at ~1.35 V vs RHE; resulting from the initiation of oxide adsorption and the subsequent monolayer formation. The overall formation of this oxide in aqueous electrolytes is generally accepted to follow the process seen in Equation 7.[76]

$$a)\ Au + H_2O \rightarrow AuOH + H^+ + e^- \qquad \textbf{Equation 7}$$

$$b)\ AuOH \rightarrow AuO + H^+ + e^-$$

Gold oxide formation at positive potentials. a) Initial oxide formation, b) Further oxidation of surface oxide

Figure 2.1 shows a number of the forward sweep oxide region positions labelled from OA1-4: these correlate to varying stages in oxide formation at the gold surface. OA1 corresponds to deposition of water onto the surface, filling spaces between any previously adsorbed electrolyte anions (ClO_4^- in this case). This peak is very small, only visible with a fast sweep rate or, as here, very low $HClO_4$ concentration; gold readily adsorbs anions from the surrounding electrolyte, giving minimal free space for water to adsorb onto and this results in the minimal current seen.

OA2 is the second half of this process, resulting from the deposition of water onto the gold surface but displacing the originally adsorbed anions in the process; this gives the considerably larger peak seen when compared to OA1. OA3 corresponds to the completion of the OH monolayer formation.

As shown in Equation 7b, the adsorbed OH progresses to eventually form gold oxide. This process is believed to occur via place exchange of the initially adsorbed species (OH) with gold atoms at the surface; this occurs during OA2 and 3. Following this, a second electron is transferred to give the AuO form. Figure 2.2 gives a model for the entire process by which oxidation of a metal in an aqueous environment occurs.

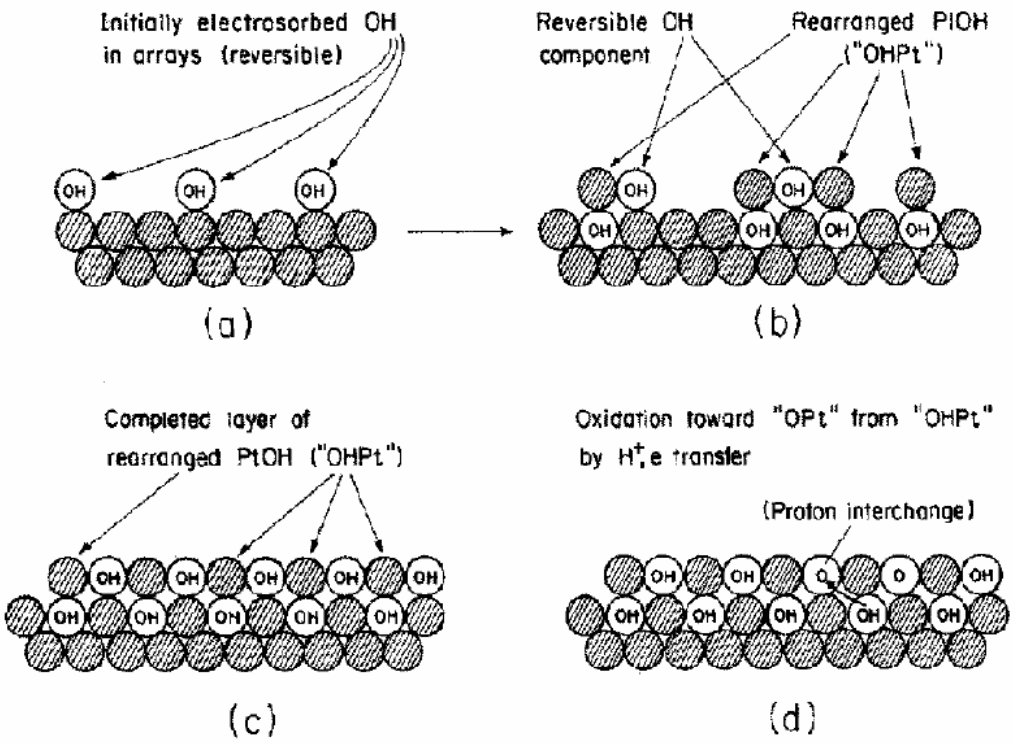

Figure 2.2 Process model for metal oxide formation. Shows progression of surface transformation from initially deposited 2-d adsorption to a pseudo 3 dimensional state via place exchange and final full oxide formation. Reproduced from Conway *et al.*[77]

Platinum is specifically referenced in Figure 2.2, but this mechanism is also fully applicable to the gold system for oxide formation at posiyive potentials. The major difference seen between the platinum and gold for this process comes from variation in adsorption of anions from the electrolyte: gold is considerably more susceptible to this and thus oxide formation begins at slightly less positive potentials on platinum than gold, with the equivalent of peak OA1 not present.

It is considered that this swapping of metal and metal oxide positions during oxide formation occurs because by doing so, stress/lateral repulsion in the surface layer prior to the full oxide formation is relieved. An example of this strain removal can be seen in Figure 2.3 with the charged species manoeuvring to reducing the repulsion between them.

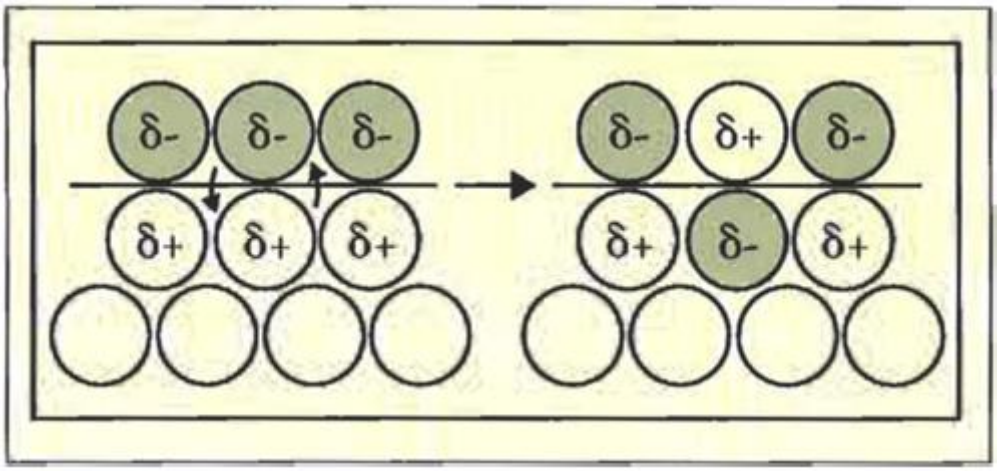

Figure 2.3 Schematic representation of stress reduction in metal oxide by place exchange. Shaded circles represent adsorbed oxygen species, with unshaded surface gold atoms. Reproduced from Burke and Nugent.[78]

Other oxide forms can also possibly form at positive potentials, such as Au_2O_3 or $AuOH_3$; however, these forms require significantly increased potentials (well above 1.5 V vs RHE) or prolonged exposures to oxidative potentials. As the potential will be limited to ~1.6-1.7 V vs RHE during this project, these oxide forms are not a concern for us here.

The next part comes with the peak seen on the reverse scan corresponding to the reduction of oxide formed during the positive scan. Three peaks are labelled for oxide reduction in Figure 2.1; OCI, II and III, corresponding to the various forms of the oxide described above.

OCI is the only one of these peaks that is the reversible reduction of material: corresponding to OA1. This peak is lost when more positive potentials are utilised and other reduction peaks become more apparent. OCIII appears for the removal of reconstructed material formed from the place switching of surface atoms and subsequent second electron transfer. The increasing size of this peak with higher potentials relates to this: as more of the oxide monolayer forms and place switching occurs, higher currents are required for the subsequent reduction. The final reduction peak, OCII, corresponds to the removal of OH sublattices on the anion free surfaces.

2.1.2 Au(111)

For the synthesis of inverse catalyst systems, utilising the (111) crystal face for the gold substrate has proved to be suitable for providing control over the final position of deposited titania nanoparticles. As such, we must consider the differences seen in the electrochemistry of this crystal plane in comparison to the polycrystalline form. Examples of CVs for such a clean Au(111) crystal can be seen below in Figure 2.4.

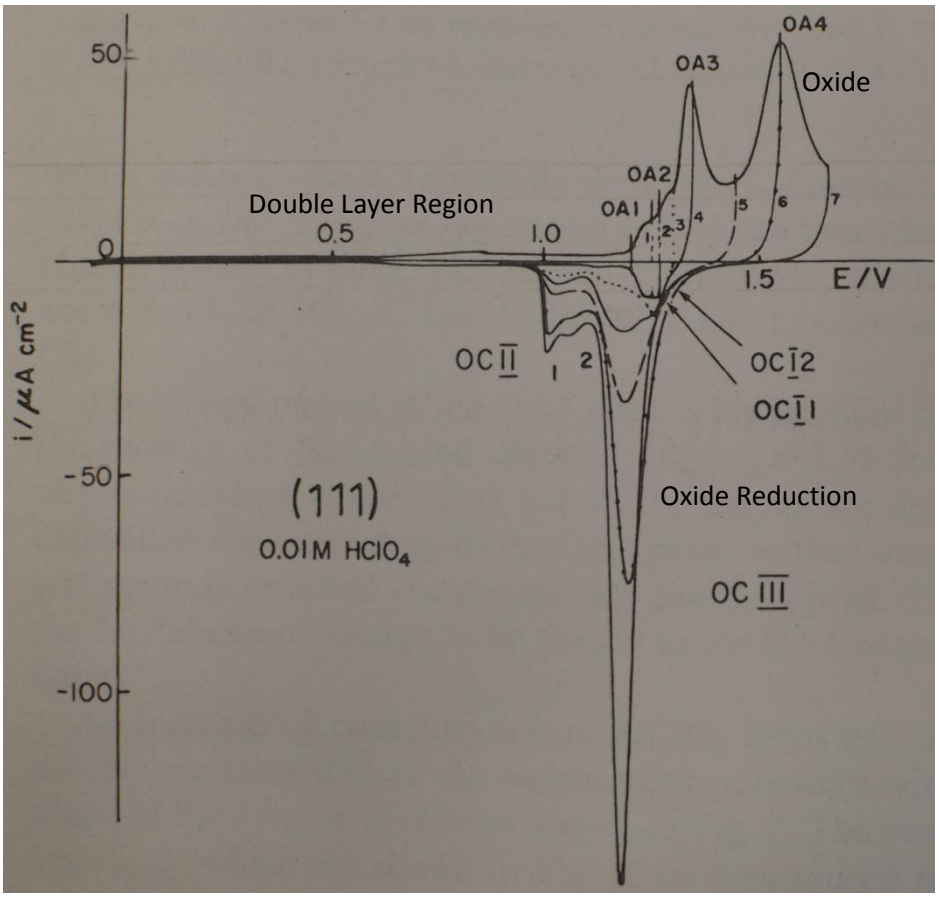

Figure 2.4 Standard CV of Au(111) single crystal. Varying potential limits, 20 mV s^{-1}, 0.01 M $HClO_4$ vs SHE. Reproduced from Angerstein-Kozlowska *et al*.[79]

As to be expected, the CV is very reminiscent of that seen for polycrystalline Au, though with some distinctive differences. OA1 and OA2 correspond to the reversible deposition of OH onto the surface, once again forming on open areas between already adsorbed electrolyte anions. OCI and II are the matching negative sweep peaks for the reduction of said oxide. This leaves OA3 and 4: the majority of place swapping of the oxide occurs at OA3 at ~1.34 V, with the secondary electron transfer being seen in OA4.

The reduction peak OCIII is almost identical to that seen for the polycrystalline system: not unexpected, as the final oxide formed is similar between the two systems.

OCII is considerably more distinct in the (111) system: as they correspond to the reduction of surface hydroxide on an anion free surface. This is most likely due to the differences in binding efficiency on the (111) face compared to the polycrystalline substrate: anions from the electrolyte bind more efficiently due to the close packing of this face having a trigonal symmetry, which more easily matches the symmetry of the binding ClO_4^-.[75]

2.1.3 Carbon Monoxide Oxidation on Gold

The oxidation of carbon monoxide on gold single crystals has been suggested[80] to proceed through a Langmuir-Hinshelwood mechanism, as shown below.

$$Au + CO \leftrightarrow Au - CO \qquad \textbf{Equation 8}$$

$$Au + H_2O \leftrightarrow Au - OH + e^- + H^+$$

$$Au - CO + Au - OH \rightarrow Au(CO_2H)$$

$$Au(CO_2H) \rightarrow CO_2 + e^- + H^+$$

Langmuir-Hinshelwood mechanism for the oxidation of carbon monoxide on gold.

The formation of the adsorbed OH species is considered to be the rate determining step for this reaction, as is the case for platinum[81], with the reaction of the adsorbed CO and OH being a considerably quicker process, though Edens *et al.*[80] also considered the decomposition of the final hydroxycarbonyl to be the rate determining step. This proposed mechanism is supported by the observation that the potential for the CO oxidation is shifted considerably lower in an alkaline environment, where the presence of hydroxide ions in the solution allows for easier formation of the adsorbed hydroxide on the gold's surface, without the need to dissociate water first.[82] An example CV of the oxidation of CO on an Au film in 0.1 M $HClO_4$ is shown below in Figure 2.5.

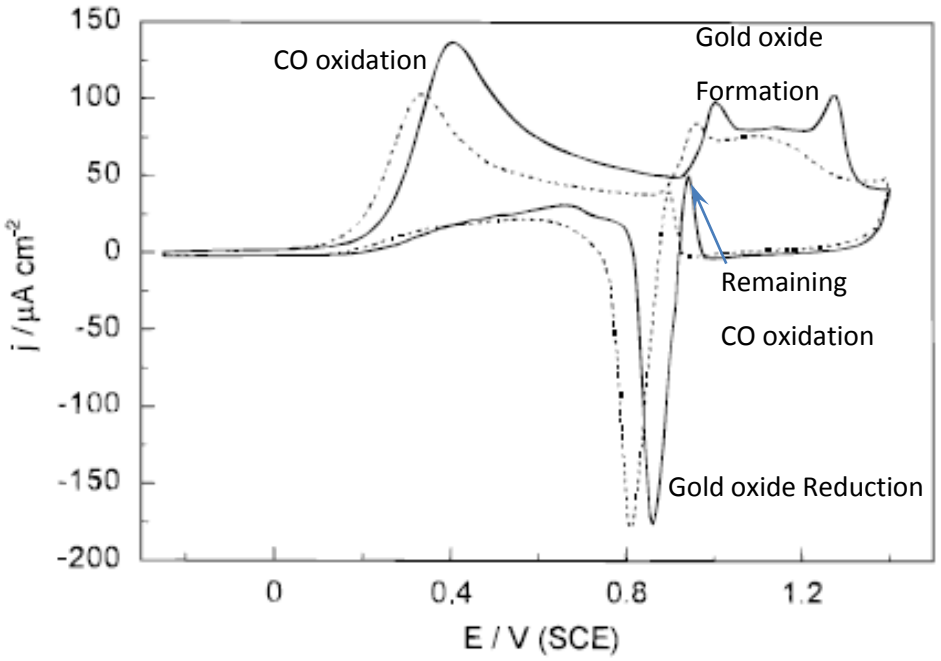

Figure 2.5 CV of CO oxidation on an Au film in CO saturated 0.1 M $HClO_4$, 50 mV s^{-1}. Dashed line represents surface prior to heat treatment, with the solid line for post heating. Reproduced from Sun *et al.*[83]

Familiar features can be seen in this CV, notably the gold oxide formation (~0.9-1.4 V vs SCE) and reduction (~0.95 V vs SCE) regions, The additional peaks are attributed to the presence of CO during the scans. During the positive potential sweep, the CO oxidation peak begins at ~0.34 V vs SCE. This is attributed to CO adsorbed whilst the potential was held at 0.0 V before the scan began.

In the negative sweep, between 1.4 and 1.0 V, the current drops to around zero, indicating that the no further solution CO can be oxidized. This comes from the surface Au oxide formed during the positive sweep inhibiting the oxidation of CO.[47] As the gold oxide reduction region is entered, there is a sharp positive peak at ~ 1.0 V vs SCE; this corresponds to remaining CO being oxidised as gold oxide is removed, indicating only a very small area of gold is required for CO oxidation to occur. This is followed by a large reduction current peak at ~0.9 V vs SCE for the full removal of gold oxide from the surface.

2.2 Supported Gold Catalysis

2.2.1 Titania Supported Gold Carbon Monoxide Oxidation

As mentioned in Chapter 1, the utilisation of a metal oxide support for gold particle systems gives a significant increase in the activity of the system towards carbon monoxide oxidation. The activity of these gold particles on a titania support has been investigated in great detail by the Hayden group,[32,62,14] with a particular emphasis on variation of the size of the particles having been of particular interest. An example of the activity of the titania supported system, alongside the corresponding carbon supported samples, is displayed below in Figure 2.6.

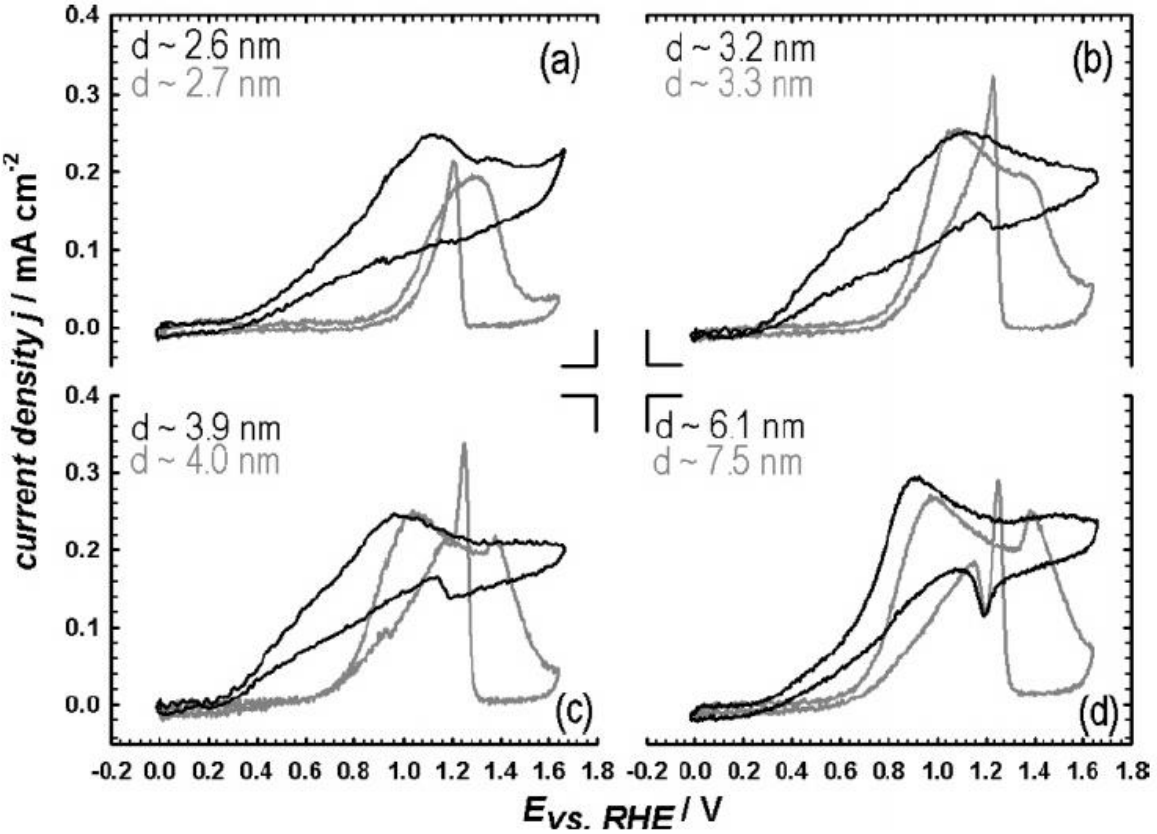

Figure 2.6 A comparison of the cyclic voltammetries of supported gold particles of varying sizes, as indicated, in CO saturated 0.5 M $HClO_4$ with a scan rate of 50 mV s^{-1}. The grey scans correspond to a carbon support whilst the black scans indicate a titania support. Data taken from Hayden *et al.*[32]

The difference in support has a distinct effect on the CO oxidation: titania support gives a decided negative shift in the onset of the CO oxidation, thus indicating a much improved reactivity on this support compared to the carbon, where the activity was seen

to be much closer to that of the bulk gold. As was described in greater detail in Chapter 1, the highest activity when supported on titania was seen with particles with a size of ~3 nm, with activity dropping sharply with lower size.

The features visible in the CVs for the titania supported gold is heavily dependent on the particle sizes utilised. At smaller particle sizes, the gold oxide formation is not visible, becoming more apparent as the particle sizes increase, most notably with the reduction peak reappearing on the larger particles.

2.2.2 Inverse Titania and Gold Catalyst System

The effect of utilising an inverse system has been thoroughly investigated for a gaseous environment, with the results of such described in Chapter 1. However, the electro-catalytic activity of such inverse systems has been considerably less extensively investigated.

The most prominent of such an investigation for gold supported titania is a paper by Rodriguez *et al*.[84] where differing levels of gold supported titania nanoparticles were electrochemically investigated. The synthesis of these samples was performed via drop-casting of a titania nanoparticulate colloidal suspension (created by the cathodic corrosion method of Ti wire in NaOH) in an Ar atmosphere onto the relevant support.

In this work, the activity of these gold supported titania nanoparticles was investigated alongside the non-inverse system. An example CV of such a TiO_2 modified gold surface in an acidic environment can be seen below in Figure 2.7.

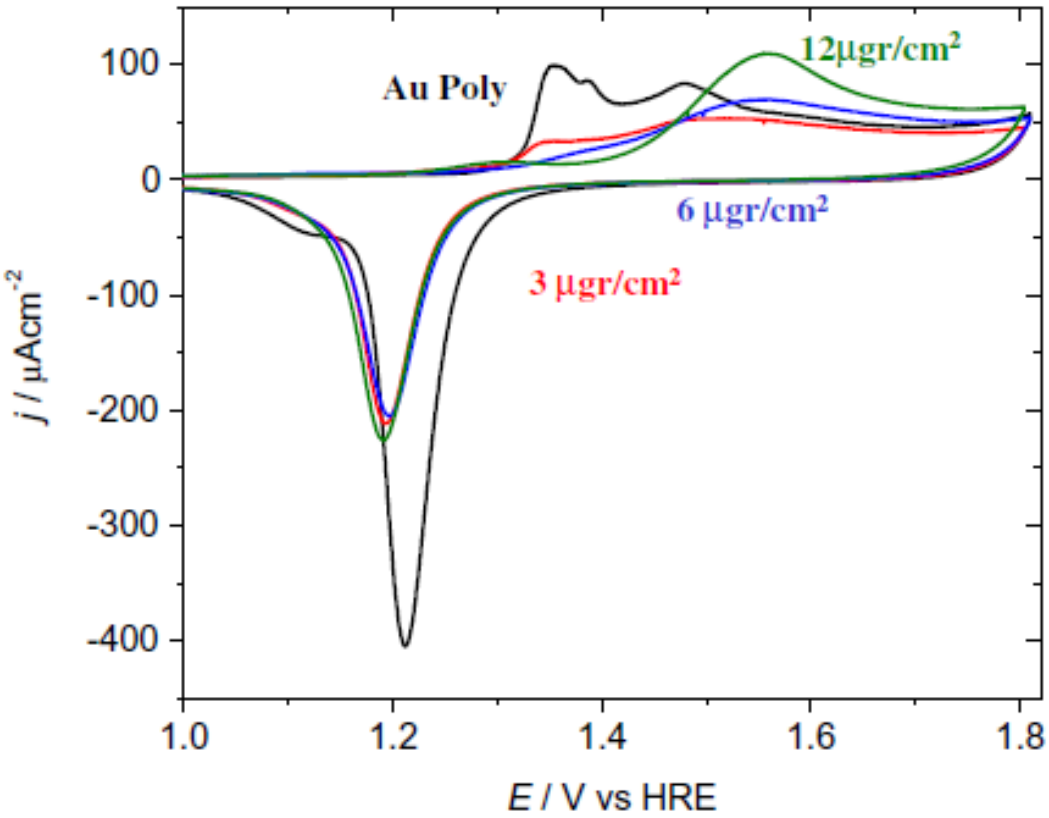

Figure 2.7 CV scans of polycrystalline Au modified with varying TiO_2 concentration. Scan Rate 50 mV s^{-1}, 0.1 M $HClO_4$. Reproduced from Rodriguez *et al.*[84]

The view has been limited to 1-1.8 V vs RHE, however notable changes can be seen with the addition of titania to the gold surface; the oxide peaks appear at more positive potentials. The oxide formation peaks appear to be shifting to higher potentials, with a peak at ~1.55 V vs RHE becoming more distinct as the titania concentration is increased. The oxide reduction peak is also shifted in a negative direction ~0.3 V.

The oxidation of CO in this system was also investigated by Rodriguez *et al.*, producing the CV in Figure 2.8. Only the forward scan is shown for ease of observation.

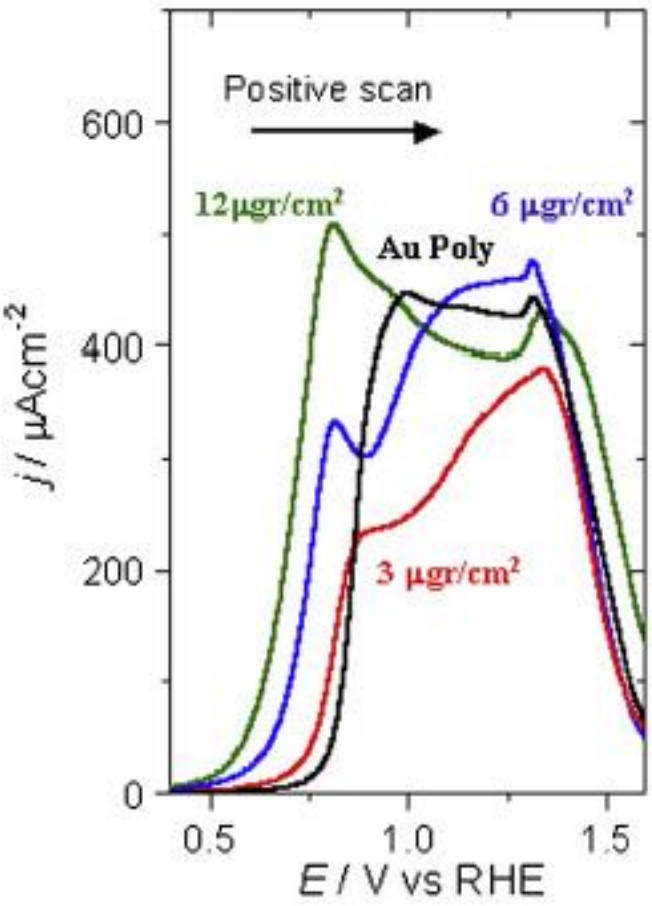

Figure 2.8 Forward Voltammetry scan of polycrystalline gold modified with varying TiO_2 concentrations. Scan Rate 20 mV s^{-1}, CO saturated 0.1 M $HClO_4$. Taken from Rodriguez *et al.*[84]

As can be clearly seen, increasing the titania concentration has a noticeable effect on the CO oxidation: the onset is shifting negative as the quantity of titania increases, indicating a decrease in over-potential for the oxidation. Unfortunately, the titania in the samples investigated above was in the form of 200-600 nm rods with a diameter of 5-10 nm.[85] As we will be investigating the deposition of individual particles comparable to hemispheres with a diameter of ~10 nm, a direct contrast will not be possible for our investigation.

However, this paper is the most direct comparison for the TiO_x/Au Inverse system found, and thus the conclusions reached are still worth considering. Rodriguez *et al.* concluded that there was insignificant evidence to support that quantisation of energy levels or the size/structure of particles (whether gold/titania) was responsible for the increased reactivity seen in metal oxide supported gold particles.

Rather, it was thought that an electronic effect was responsible, evidenced by the effect on activity seen being similar between both the standard and inverse systems. The presence of $Au^{\delta-}$ species was decided as the most notable factor, brought about by the movement of oxygen vacancies in the titania induced by interaction with the gold particles, thus changing the valence bands of the gold by shifting the Fermi level more negative.

Rodriguez *et al.* did not, however, rule out other electronic effects such as the interface between the particle, support and electrolyte, as well as surface dipoles and pH effects being dominant factors in addition to those described above.

3 Experimental

The following chapter describes the general experimental procedures and instrumentation utilised in work for this thesis, alongside background for these techniques and instruments.

3.1 Physical Vapour Deposition (PVD) systems

Physical Vapour Deposition (PVD) consists of a selection of techniques that are utilised for the purpose of depositing a variety of materials onto differing substrates. Thin films or nanoparticles can be deposited with these techniques, though the suitability for specific variations varies between techniques.

The basic process behind any PVD synthesis is the vapourisation of materials, where, whether as atoms or molecules, the materials travel towards the substrate surface, at which they condense together and form a film (or particles) across the surface. There are a number of different variations of the PVD technique, distinguished mostly by the method of deposition method used.

The utilisation of Ultra High Vacuum (UHV) conditions for our syntheses comes about due to PVD being highly affected by intervening atmosphere between the evaporation source and the substrate. Any degree of atmosphere allows for collisions between evaporated material and molecules present in that atmosphere prior to reaching the substrate, in addition to these residual molecules depositing on the surface themselves, thus interfering with the desired material formation. By performing PVD in as high a vacuum as possible (with pressures of 10^{-8}-10^{-10} mbar considered standard for UHV), the contribution from any atmosphere is negated and pure material of the desired composition can be deposited, alongside any additional modification steps.

Two separate UHV systems were utilised by us here for the synthesis and investigation of Titania-Gold Inverse Catalyst samples: the High Throughput system and the Scanning Tunnelling Microscopy system.

3.1.1 High-Throughput PVD Ultra-High Vacuum System

For the synthesis of high-throughput titania nanoparticle samples, a UHV PVD system produced by DCA Instruments was used. This system allows for the simultaneous co-evaporation of multiple elements onto a substrate, with variation of the elemental configuration being individually controllable[86].

A schematic representation of this system can be seen below in Figure 3.1, consisting of two growth chambers (A/B), where PVD of materials takes place, a low pressure chemical vapour deposition chamber and a surface characterisation chamber, currently fitted with an X-ray Photoelectron Spectroscopy system.

Growth chamber A was utilised for the high-throughput sample syntheses in this project: the vacuum is maintained initially by a combination rotary/turbo pump (Pfeiffer) to bring the pressure to 10^{-4}-10^{-5} mbar, followed by a cryopump (Helix Tech. Corp.) allowing for the achievement of the required UHV conditions, with a base pressure of 1-3 *10^{-8} mbar as standard. Samples were transferred to the chamber using the transfer line/arm: the line contains a selection of trolleys that move along the line, with the transfer arms being used to manoeuvre the samples from the line trolleys to the chamber. The load lock allows for the loading of sample substrates into the system without disrupting the internal vacuum, as it can be individually vented to atmosphere and then pumped to UHV.

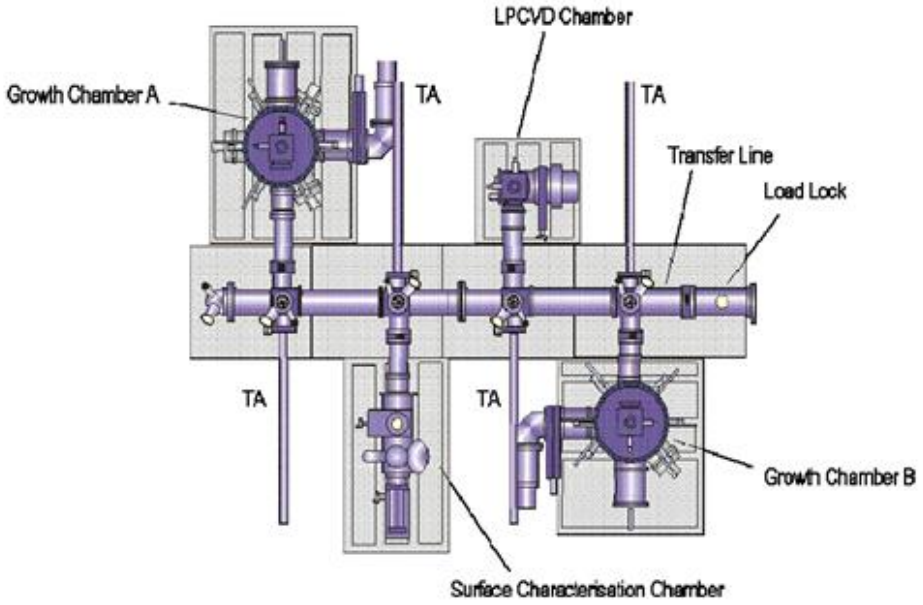

Figure 3.1 Schematic picture of the PVD system used to synthesise the Ti particle samples. TA = Transfer Arm, LPCVD = Low Pressure Chemical Vapour Deposition. Taken from Williams thesis.[87]

The growth chamber consists of six possible off-axis deposition sources (Figure 3.2): three Knudsen (K) cells (DCA HTKS) and three electron beam guns (e-guns, Temescal). During this project, one of the K-Cell positions (K-cell 2) was taken up by an oxygen plasma source, though this was not utilised for our depositions, as molecular oxygen was sufficient.

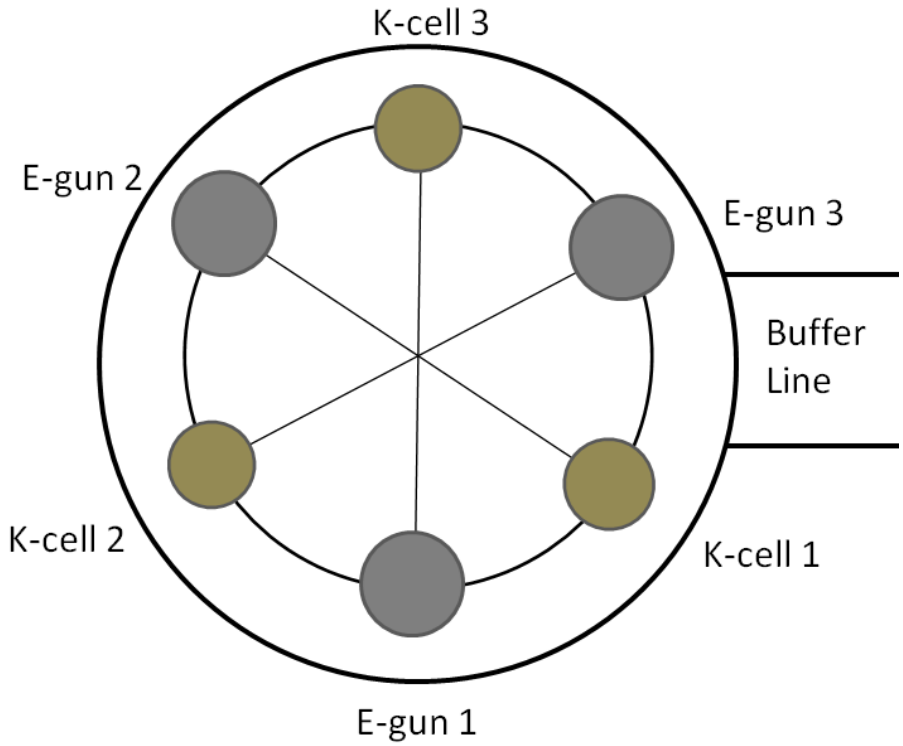

Figure 3.2 Schematic representation of Growth Chamber A source positions: K-cell = Knudsen cells, E-gun = Electron beam gun

A series of shutters and wedges allow for control of the material deposition, most notably allowing for the deposition of a gradient of material across a substrate surface, though this feature was not utilised in this project.[86] For the initial titanium deposition prior to further oxidation, one of the e-guns was utilised to heat the titanium, with a quartz crystal microbalance present to allow for measurement of the deposition rate.

As described in further detail in Chapter 5, titanium (99.995% granules, Testbourne) was deposited using an e-gun, where an electron beam is used to heat and thus evaporate the material, at a temperature of ~1800 °C, with a consistent rate of 0.2 Å s^{-1} being used for all samples synthesised. Gold (99.999%, Goodfellows) was deposited via K-cell, at temperatures of ~1400 °C and Oxidation was performed with molecular oxygen (BOC Special Gases, N6 Grade).

3.1.2 Scanning Tunnelling Microscopy System

For the preparation and initial characterisation of inverse catalyst systems on a single plane metal crystal (111), a UHV STM system with attached preparation chamber was used (supplied by *Omicron* NanoTechnology GmbH).

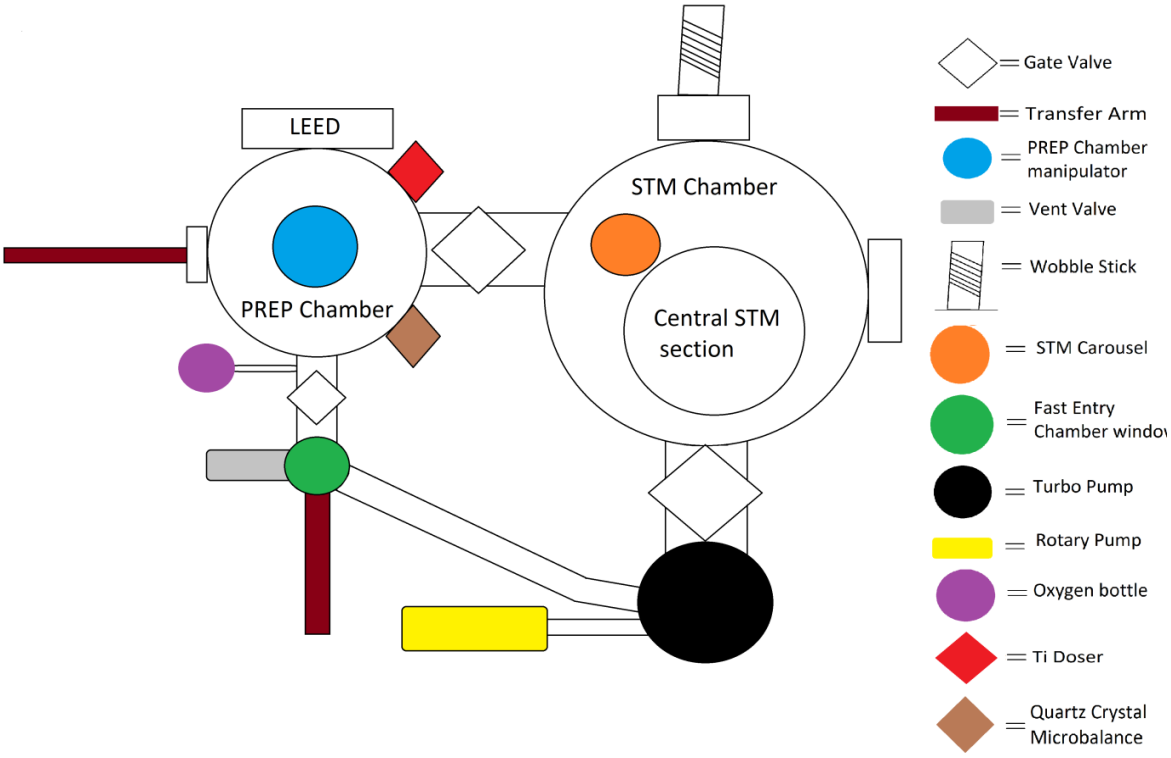

Figure 3.3 Schematic representation of the STM systems, consisting of the STM chamber, the preparation chamber and the Fast Entry Chamber (FEC).

As seen in Figure 3.3, the system consists of two separate main chambers; the Preparation chamber, where equipment for cleaning and PVD of samples are contained, and the STM chamber, consisting solely of STM equipment for the imaging of the sample surfaces.

The chambers are connected by a transfer arm that allows for the transfer of sample/tip plates throughout the system. The base pressure of the system was stable, with an average base pressure of around ~5 x 10^{-9} mbar present throughout the project. This pressure in the chambers was maintained using Ion-pumps (Varian), initially backed by a turbo-molecular/turbo pump system (Pfeiffer).

The preparation chamber contains Low Electron Energy Diffraction (LEED) optics, a Quadrupole Mass Spectrometer (QMS), Ti doser, quartz crystal micro-balance (tectra

GmbH), sputter gun and sample heater. The STM is a low temperature scanning tunnelling microscope, which allows for imaging of various samples at both room temperature and below, approaching 23 K, though for this project only room temperature scans were taken.

The transfer of samples/tips between the Fast Entry Chamber (FEC) and the various sections of the system is performed using a selection of carrier plates, as can be seen in Figure 3.4.

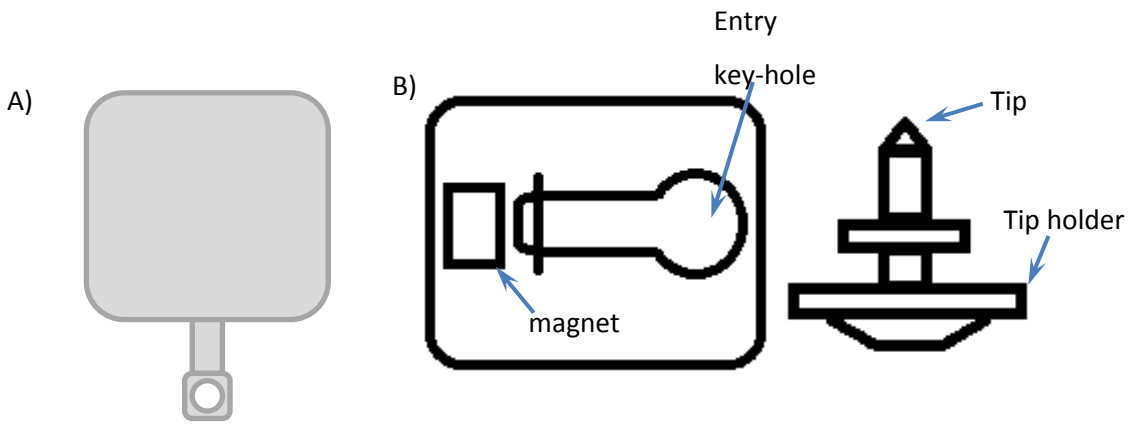

Figure 3.4 Example of tip and sample transfer plates. A) sample plate, B) tip carrier plate alongside a tip holder.

For our purposes, the Au(111) crystal was attached to a sample plate via a Ta foil cradle, welded at four separate locations to ensure the crystal position remained steady during movement, deposition and scanning. The tip holders fit into the key-hole of the carrier plate and are held in place by a magnet at the end.

The Ti doser consists of a 0.38 mm diameter high purity (99.99%) Ti wire wrapped around 0.7 mm diameter tungsten wire filament, which is then surrounded by a steel shield. A representation of this doser is shown in Figure 3.5, alongside images of the device. By passing a current through the connecting rods, the filament is resistively heated, which in turn causes in the titanium to melt onto the filament and begin expelling material. The shield allows for directed dosing of the titanium, to prevent damaging of any delicate systems, with the quartz-crystal microbalance used for control over the deposition rate.

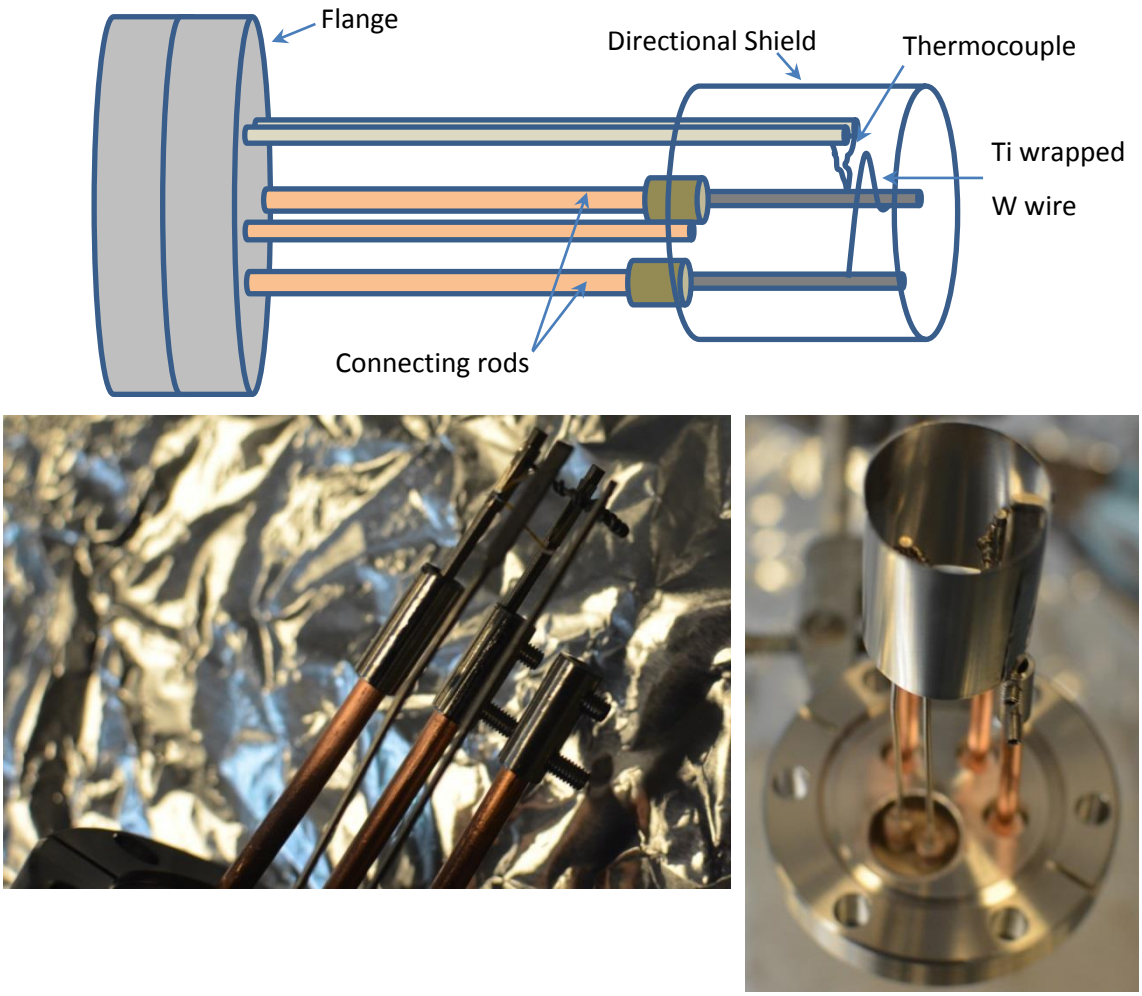

Figure 3.5 Titanium doser schematic alongside images of the doser both with and without the protective shield.

3.2 Sample substrates

3.2.1 HT-PVD System

Initially, titania particle samples were synthesised on 11*11 mm gold supported on glass substrates (Arrandee metal GmbH + Co. KG), held in place via a tungsten mask to allow for proper heating during the formation of the titania. All initial tests to determine the conditions required to give proper variation in titania particles were performed on these substrates and are described in detail in the Chapter 5, in addition to being used for initial electrochemical testing.

These substrates were prepared for the vacuum system by first rinsing in acetone (Aldrich, 99.995%), with residual fluid removed by Kimwipe^{TM}. Once dry, this step was repeated using ethanol (Aldrich, 99.999%). After each section of rinsing/drying, the substrate was heat treated: the substrate was held in the central flame cone of a blowtorch, providing temperatures of roughly 1700 K. Heating was only performed for instances of 10 seconds before the substrate was removed from the flame, as extensive exposure resulted in a loss of structural integrity, warping the substrate. This heating step was performed to remove any remaining residual material from the surface, as well as allowing the surface to form (111) terraces prior to being placed in the vacuum system.

These substrates were used for the initial depositions, and were instrumental in the determination of the particle size and distribution. However, these particular substrates proved to be very difficult to adapt to the electrochemical cells available during this project; as such, an alternative was required. The later testing was performed using 10*10 gold electrode arrays supported on silicon nitride wafers. These allow for the deposition of 100 individual materials on 100 individually addressable electrodes, and as such allow for a much greater range of samples to be tested in equivalent conditions. A diagram of such an array is shown in Figure 3.6.

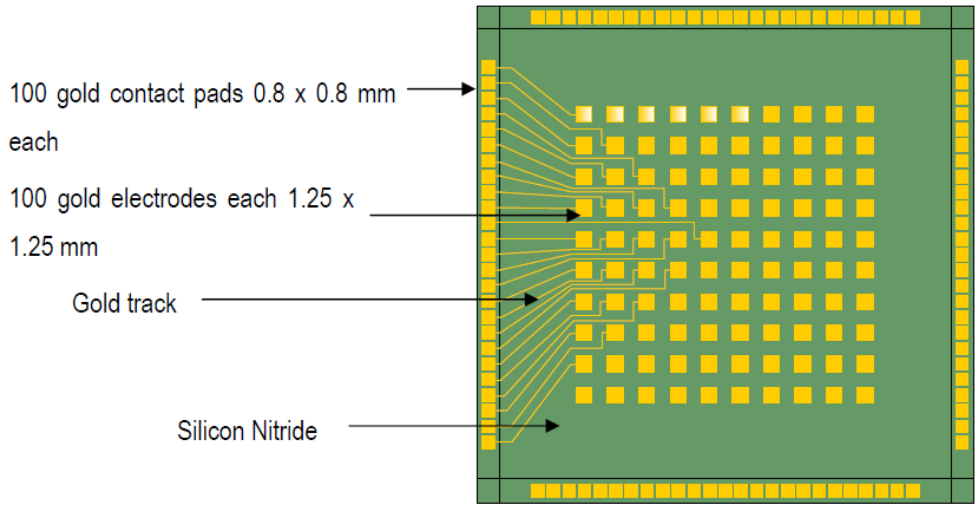

Figure 3.6 Electrochemical array consisting of a silicon nitride wafer supporting 10*10 gold electrodes which are individually addressable. Diagram reproduced from Williams' thesis[87]

Prior to Ti deposition, the arrays were cleaned by rinsing with ethanol (Aldrich, 99.999%) followed by pure water (Elga, 18.2 MΩ cm). To ensure deposition occurred solely on these electrodes, a suitable mask constructed of tungsten (so as to allow for high levels of heating during the titania formation) was used.

To provide the required variation in titania formation, Ti deposition was controlled using the main shutter of GCA so as to allow for deposition on selected electrodes on the arrays, giving consistent variation of deposition across our samples. After deposition, the samples were heated to 723 K (as this was the maximum temperature before the possibility of damage to the arrays becomes too significant), followed by an oxygen atmosphere of ~$1.5*10^{-5}$ mbar being introduced. After being held in this atmosphere, samples were cooled and the oxygen removed.

As stated, initial depositions were attempted on the described gold 10*10 arrays: however, before any substantial progress was made in analysing the particles formed on these arrays, their use became no longer viable due to supply concerns. These arrays were thus replaced with ones where the gold electrodes/tracks instead consisted of Indium Tin Oxide (ITO), necessitating the deposition of gold onto the electrodes prior to titanium deposition.

3.2.2 STM System

For samples synthesised in the STM system, a single disc crystal of Au (111) (11 mm diameter, 5 mm thick, 99.999% Goodfellows) was utilised for all samples produced during this project. As mentioned previously, the manoeuvring of samples within the STM system was performed using a carrier plate: as such, the crystal was mounted upon one such plate, held in place by a cradle formed from Ta foil. This cradle was welded onto the plate at four separate locations, so as to ensure a proper hold on the crystal, and thus kept at a consistent position parallel to the ground.

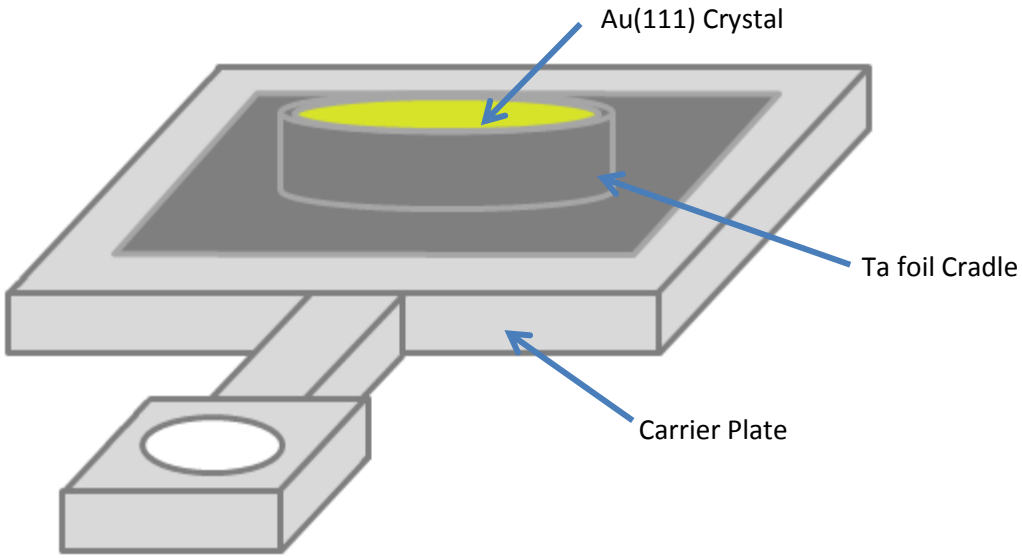

Figure 3.7 Representation of the Au(111) crystal mounted on a carrier plate with a Ta foil cradle. Set-up used for all sample depositions

Due to the semi-permanent method by which the crystal was mounted, removal of each individual synthesised sample from this particular set up for electrochemical testing was not feasible. This was also particularly untenable due to the requirement for the crystal to be replaced on this sample plate upon electrochemical testing being completed to allow for further STM of the surface and for re-use in further sample preparation. As such, the testing of samples required a unique set-up to allow for the proper investigation of their electrochemical behaviour without the need to remove the crystal from the Ta cradle for each individual particle composition.

3.3 Electrochemical analysis of Titania particle samples

As described in Section 3.2, two separate chamber systems were used for the deposition of titania on differing gold substrates. Despite three separate substrates being used during sample depositions, only two separate cell set-ups were utilised for the electrochemical testing of the samples synthesised throughout this project. These are the HT-PVD electrochemical cell, for the testing of the 10*10 gold/ITO arrays, and the Bead Crystal Electrochemical Cell (BCEC), used for the Au(111) crystal samples, and initial testing of the gold/glass substrate samples.

3.3.1 HT- PVD Electrochemical Cell

Electrochemical analysis of the PVD titania particle samples deposited on 10*10 electrode arrays was carried out at room temperature using a three-compartment glass cell with a water jacket as described by Hayden *et al.*[32], with a schematic of such shown in Figure 3.8. For these experiments, the electrolyte used was 0.1 M $HClO_4$, prepared by diluting a commercial $HClO_4$ solution (GFS, 70%) with distilled water.

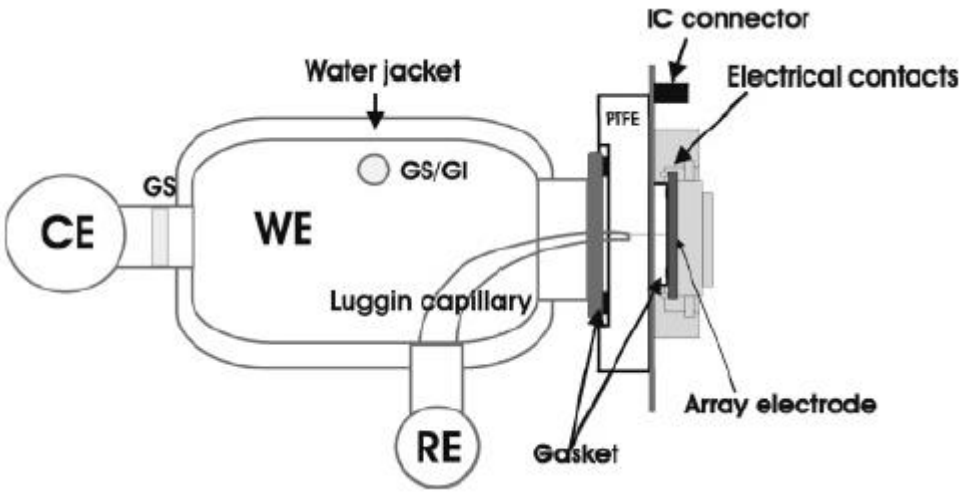

Figure 3.8 Electrochemical array cell. CE = Counter Electrode, WE = Working Electrode, RE = Reference electrode, GS = Glass Sinter and GS/GI = Glass Inlet with Glass Sinter. Reproduced from Hayden et al.[32]

The arrays were clamped into the cell, allowing for all 100 of the electrical contacts to be firmly held in the system. A Viton® seal was placed around the face of the

array to form a water-tight seal to prevent any undesired contact between the electrical contacts and the electrolyte. The glass cell was attached to the system and filled with the electrolyte. The GS/GI was used to bubble gases (notably nitrogen and carbon monoxide) through the electrolyte. Nitrogen gas was used to purge the electrolyte prior to any experiments being performed, with carbon monoxide required for proper testing of the synthesised sample. Pt gauze was used as the counter electrode, with a Saturated Calomel Electrode (SCE), calibrated against the Standard Hydrogen Electrode (SHE), used as the reference electrode.

For the collection of the Cyclic Voltammetries (CVs) for these samples, the current was monitored in relation to the changing potential using a potentiostat, two 64 channel current followers and data acquisition cards. The data collected were visualised using the Paradise software package, created by Ilika plc[13] for use in the analysis of experimental data. The potential ranges used for these samples were 0 V – 1.2 V vs SCE, with a scan speed of 50 mV s^{-1}.

3.3.1 Bead Crystal Electrochemical Cell (BCEC)

As mentioned above, the BCEC was utilised for the testing of both the Au(111) and gold/glass substrates where titanium had been deposited, then subsequently oxidised to titania.

The description given here of the BCEC focusses on the Au(111) samples, as these provided the majority of samples used for testing with this set-up. As previously described, a notable feature of the Au(111) crystal is that it was held onto a transfer plates using a welded Ta cradle: it was therefore unfeasible to remove the Au crystal from the sample plate for electrochemical testing and then replace it for further imaging in the STM system.

As such, a separate method was required to allow for simple and easily replicable electrochemical testing of the samples. This meant that the utilisation of the transfer plate would be required during testing, and thus a set-up that allowed for a proper electrical connection between the potentiostat and the sample was called for.

The electrochemical set-up decided upon for these tests was initially utilised for the testing of bead crystals and consists of three sections; the first is a specialist glassware bulb/syringe within which the electrolyte is first placed and gases (either nitrogen or carbon monoxide depending on the specific experiments being performed) can be bubbled through the electrolyte. The second is the actual electrochemical cell, as represented in Figure 3.9, with the third being a gas jacket, allowing for the application of specific atmospheres to the electrochemical experiments.

The electrochemical cell itself is very simple: at its core, it is a single capillary tube topped with a small bulb and a further small section of capillary pipe opening at the top. Figure 3.9 shows a representation of the main cell: the bulb contains an integrated Pt wire, Pt foil and Pd wire, with connections through the wall of the cell allowing for electrical access outside of the glassware.

The Pd is used as the reference electrode for all experiments (Pd/H_2, +0.05 V vs SHE), but required charging prior to use as the reference. This was performed by connecting the Pt foil as the counter electrode, Pt wire as the reference electrode and Pd as the working electrode and sweeping between -0.9 and -0.85 V at 50 mV s^{-1}. This process charges the Pd with hydrogen, thus allowing for its use as a reference: this also allows for its use in subsequent experiments as the reference electrode, though considerations with regard to the discharge of the hydrogen, and thus loss of function as the reference electrode, with the passage of time, need to be taken.

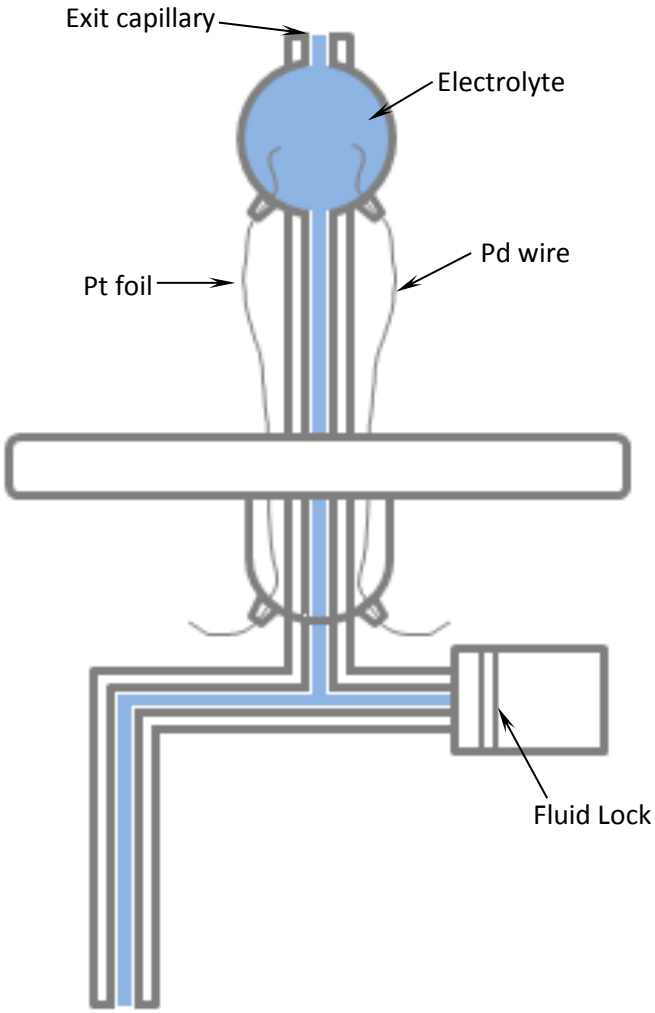

Figure 3.9 Representation of the BCEC. Fluid lock is used to allow for ingress of the electrolyte into the cell, as well as containing it once filled and preventing leaking of the electrolyte.

As shown in Figure 3.7, the sample carrier plate has a tag off to one side that is meant for use for manipulation of the samples whilst inside the STM system. This was determined to be the most likely point that could be used for the testing of the samples, and thus the cell-set up was modified to allow for testing of the samples: a series of brass connector rods upon which the sample plate could be attached. These allow for the sample to be suspended inside the gas shroud and still grant a section of the rod so an electrical connection can be made, thus ensuring functionality as the working electrode. Figure 3.10 shows the full set up of the cell with the Au(111) crystal present.

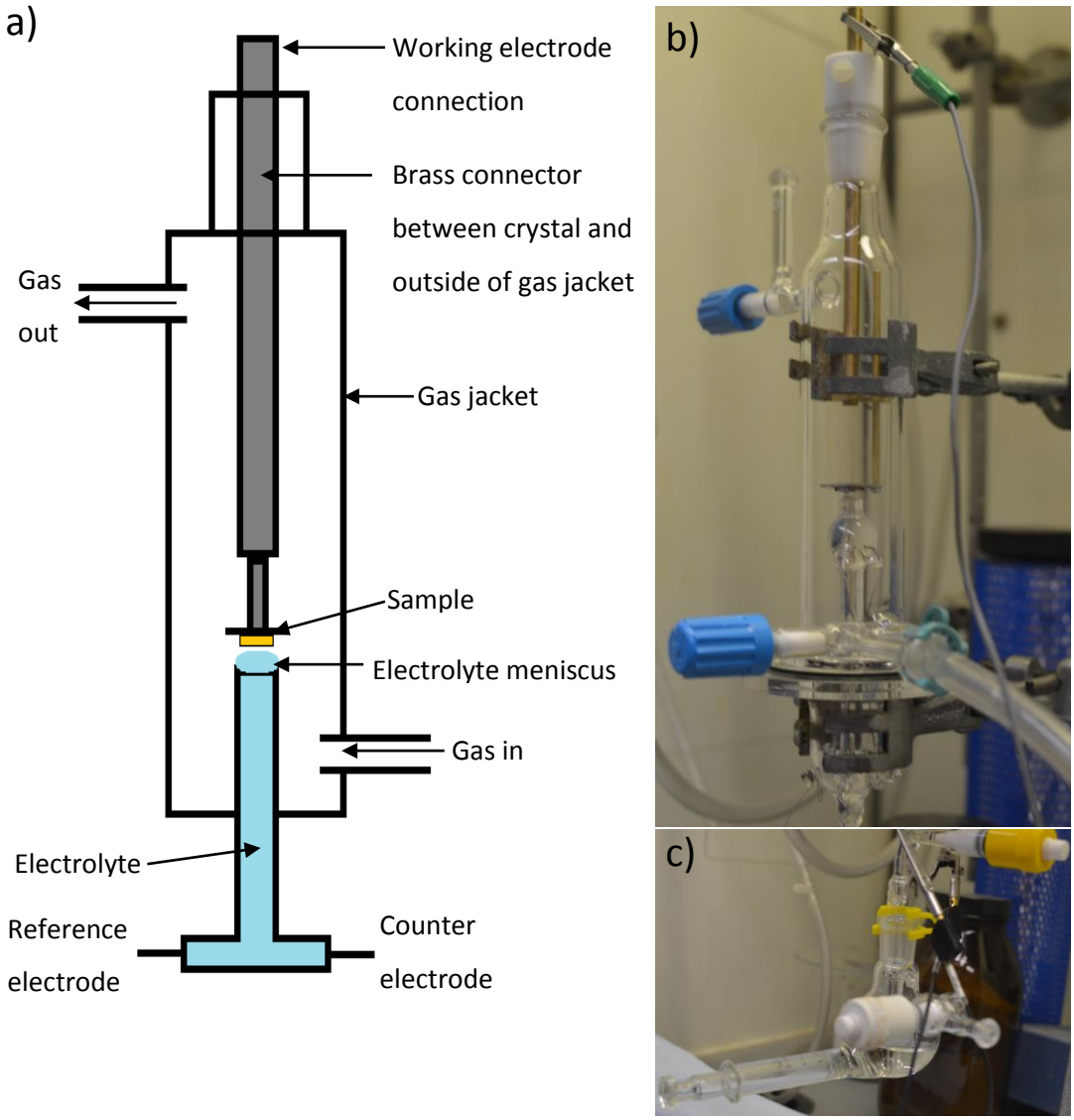

Figure 3.10 a) Schematic of the BCEC set up, b) BCEC set up for experiments with mounted Au(111) crystal visible on brass support, c) Lower bulb/syringe for electrolyte addition to cell

A notable feature of this electrochemical cell is the method by which contact is made between samples and the electrolyte: when filled with electrolyte by the syringe-bulb glassware, once the cell bulb has been filled, any further electrolyte added is forced into the exit capillary at the top of the cell.

Once electrolyte reaches the end of the exit capillary, a meniscus forms at the tip of the capillary tube, with the extent that it extends from the cell determined by the level of electrolyte. It is this meniscus which is then used to provide contact between the electrolyte and the samples: the sample is brought down until contact is made with the

electrolyte meniscus, thus adhering the electrolyte to the sample surface. The sample is then marginally raised, slightly extending the electrolyte bridge but maintaining contact between the electrolyte and the sample. A representation of this is shown below in Figure 3.11.

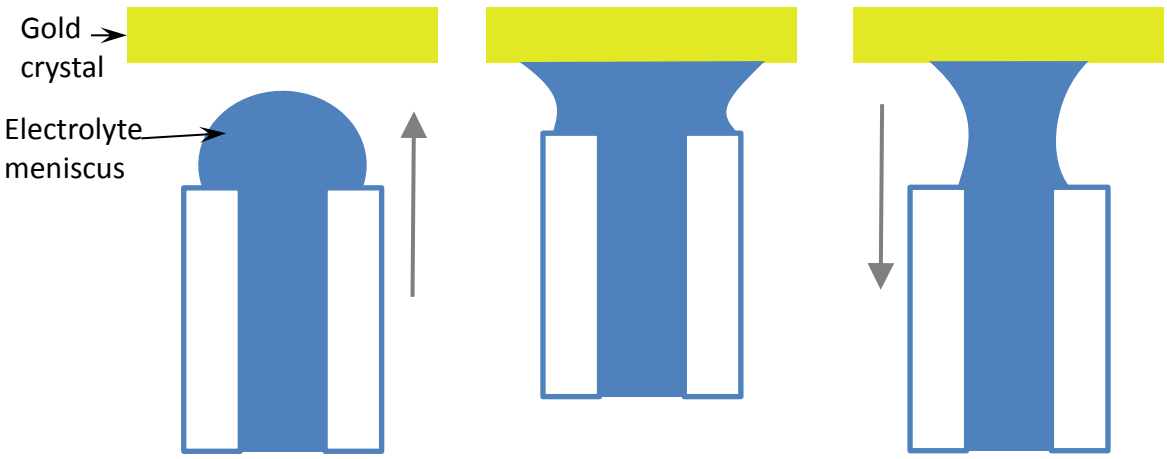

Figure 3.11 Forming meniscus contact with gold crystal in the Bead Crystal electrochemical set-up.

This meniscus contact between the electrolyte and the crystal allows for a proper electrical connection between the reference/counter electrodes and the crystal, thus allowing for electrochemical testing to be performed on the titania covered Au crystal without the need to remove the crystal from its mount.

An important point to note for this meniscus contact is that during the initial contact of electrolyte to the surface, no electrolyte can be allowed to engage with the edge of the gold crystal, as the surface tension of the electrolyte will cause any such contact to funnel the electrolyte down the side of, as well as underneath, the crystal, thus giving an inaccurate measure of the deposited material, as well as contaminating the results with the mount electrochemistry.

Once a proper connection has been made between the meniscus and the sample, the samples can then be used as the working electrode in the cell, with the Pt foil acting as the counter electrode and Pd/H_2 as the reference.

As initially mentioned, the BCEC was utilised for the testing of the gold/glass samples produced in the HT-PVD system in addition to the Au(111) crystal samples. To

allow for the testing of the gold/glass samples, the substrates were adhered to folded stainless steel connectors, which are shaped such that they can be connected to a clear transfer plate, and thus can be connected to the cell as described above. A silver epoxy connection between the gold section of the substrates and the steel connector is added so an electronic connection can be made, and thus the electrochemical testing can be performed.

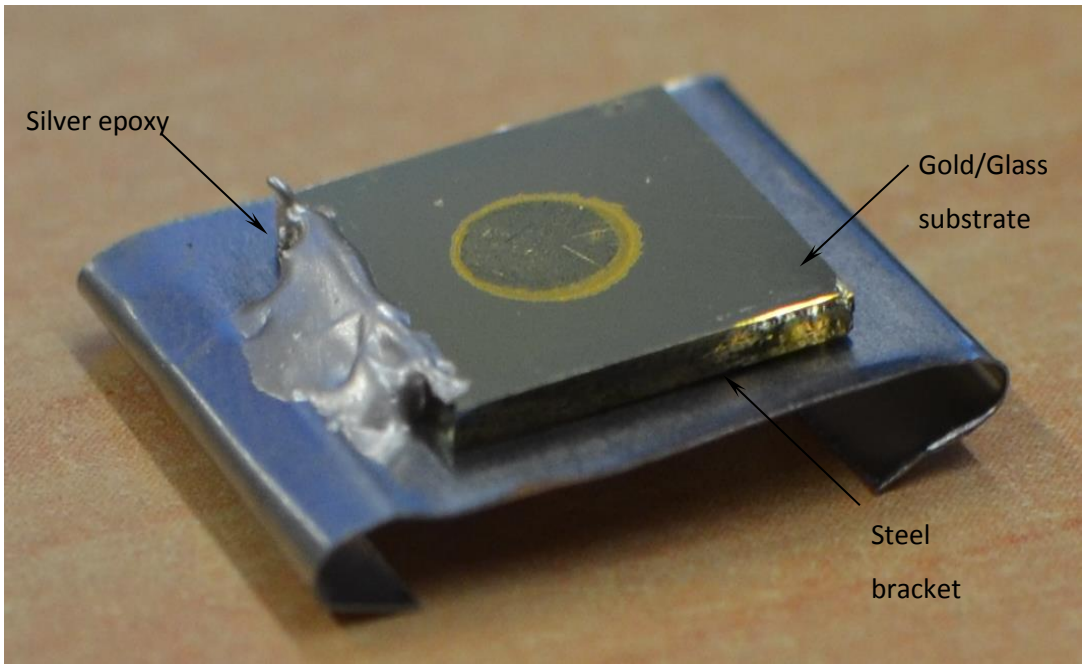

Figure 3.12 gold/glass substrate mounted on steel bracket for attachment to a sample transfer plate. Silver Epoxy allows for electrical connection from gold surface to the plate. Circular mark on surface was caused by contact with electrolyte.

3.4 Scanning Probe Microscopy

Scanning Probe Microscopy (SPM) refers to a large number of techniques used to investigate the properties of a sample, either at or near the sample surface. In general, these systems consist of a very sharp probe, where the tip tapers to a size ranging from tens of nanometres down to single digits, being brought either near or to the surface, where interactions between the tip and surface allow for determination of the surface conditions. For the majority of these techniques, the tips used are moved relative to the surface, with the particular interaction utilised being dependent on the individual techniques.

The tips used in SPM are, as mentioned, very sharp: depending on the particular technique, possibly even down to single atom status. The reason for this required level of sharpness is that, due to the method by which images are taken, the sharper the tip used to collect the data, the higher the resolution in the final images produced. This does, however, mean that to give any useful degree of data size, this relative movement across the surface needs to be performed over a reasonable area.

There are two major methods by which this movement across the surface can be performed: either the tip mount can be moved with the sample held in place, or the sample itself is scanned with the tip being held in place. The particular method used is dependent on the specific piece of equipment in use, though, generally, either technique can be used for most SPM methods.

The most common usage for SPM systems, and the use for which they were put to in this project, is to provide topographical imaging of planar sample surfaces. Due to the particulars of SPM, this generally allows for very finely detailed images of the surface, as well as providing the relative heights of features on the surface as the sample is scanned. An illustration of the action of such a probe as it is scanned across a surface is shown in Figure 3.13.

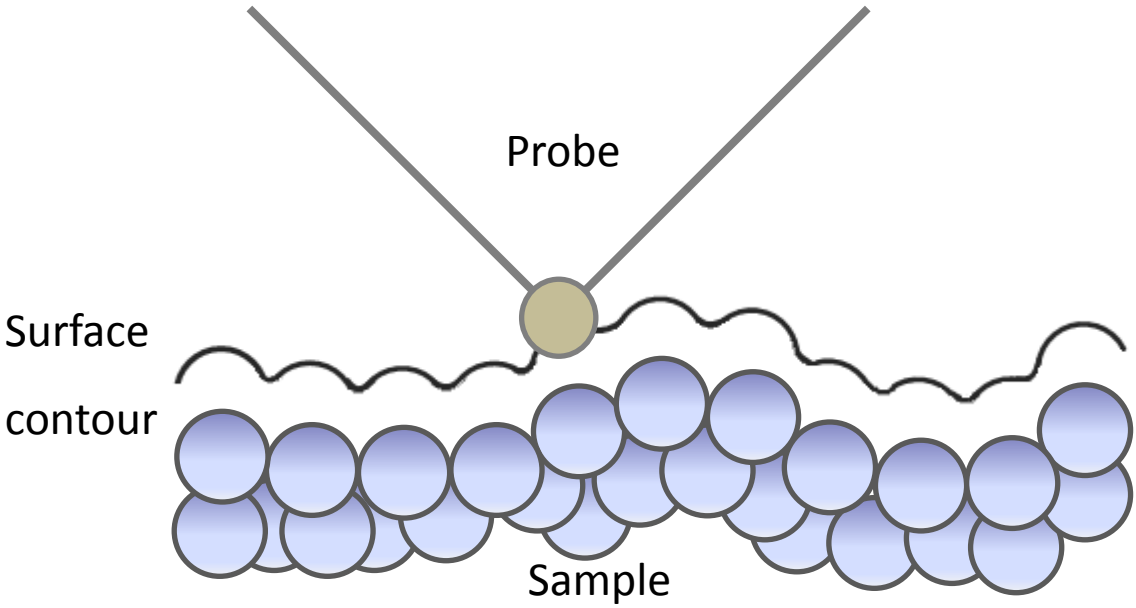

Figure 3.13 Representation of the imaging of a sample surface using Scanning Probe Microscopy. The tip follows the contour of the surface, giving an idea of the structure of the surface.[88]

As the tip moves across the sample, it follows the contour of the surface. The specifics for what determines the distance between the surface and the probe tip is dependent on the individual technique being used, as well as whether the probe or surface are being moved relative to the other. As the tip/sample moves relative to the other, the interaction between them is measured; this is then used to build a representation of the surface being scanned.

During this project, two SPM techniques in particular were used: Atomic Force Microscopy and Scanning Tunnelling Microscopy. Both were used for the imaging of titania particles on a gold surface, synthesised via separate methods. These techniques are discussed in more detail below.

3.4.1 Scanning Tunnelling Microscopy (STM)

Initially invented by G. Binnig and H. Rohrer in the early 1980's[89], STM is a technique that allows for the investigation/manipulation of conductive solid state materials, allowing for imaging of the surface down to atomic resolution. An example schematic of a STM set-up is shown in Figure 3.14.

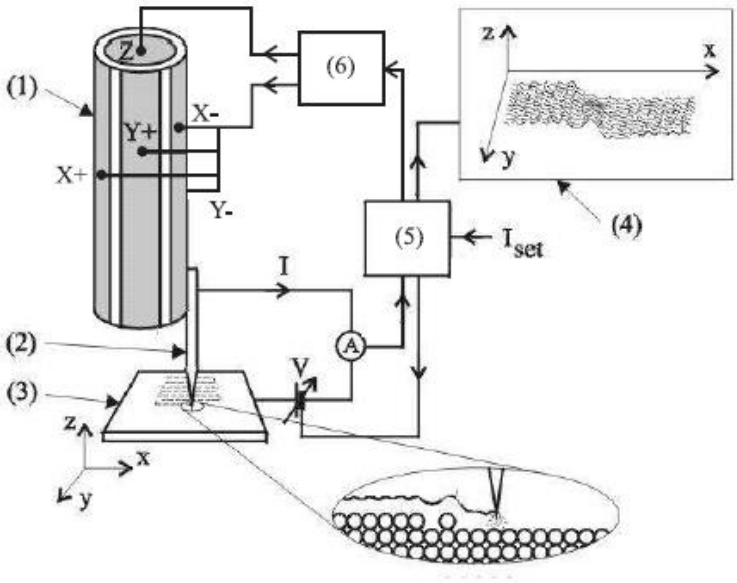

Figure 3.14 Working scheme of a STM: 1) piezoelectric tube, 2) STM-tip, 3) sample, 4) image, 5) control unit and 6) piezoelectric power supply.[90]

The operation of a STM is based on the tunnelling of electrons between a tip and the sample, forming an electronic circuit (thus necessitating the sample to be conductive). Electron tunnelling is an application of general quantum tunnelling where an elementary particle passes (tunnels) through a barrier. This is modelled via the one-dimensional solution to Schrödinger's equation as shown in Equation 9

$$-\frac{\hbar^2}{2m}\frac{\partial^2\varphi_n(z)}{\partial z_2} + U(z)\varphi_n(z) = E\varphi_n(z) \qquad \textbf{Equation 9}$$

1 dimensional solution to Schrödinger's equation. ħ is the reduced Planck's constant, m is the mass of an electron, U(z) is the potential and z is the position of the electron.[91]

The tip (made as close to atomically sharp as possible) is brought into close proximity to the sample surface such that an overlap occurs between the tip and the sample wave functions. If a bias voltage is applied to the sample, electrons can tunnel

across the gap between the tip and the sample (in either direction depending on the polarity), thus forming an electrical circuit. The rate of flow of these electrons is known as the tunnelling current; the distance between the tip and the surface is exponentially dependent on this current, as shown in Equation 10.

$$I \propto e^{-2\chi s} \qquad \textbf{Equation 10}$$

$$\chi = \frac{2m\phi}{\hbar}$$

Relationship between current and distance between surface and tip. $\boldsymbol{\phi}$ is the effective local potential barrier height; s is the distance between the surface and the tip.[92]

Due to this relationship between distance and current and its incredibly sensitivity to any modification (a change in distance of 0.1 nm reduces the tunnelling current by a factor of 10) the surface can thus be imaged.

There are two scanning modes that can be used with STM: constant current and constant height. In constant current, the current is kept constant whilst the tip is moved across the surface. As the tip is moved across the surface, the topography of the surface varies: due to a feedback loop between the tip and the surface, the system adjusts the height of the tip as it scans to maintain the same tunnelling current. By measuring this adjustment of the tip position, a topographical map of the surface can be made, sensitive enough to detect individual atoms.

The other method used is constant height mode, where the height is instead kept constant and scanned across the surface, with the changes in the tunnelling current as the distance between the surface and the tip varies being used to produce the surface image. This method is much faster than utilising the constant current mode, but runs the risk of crashing tips into the sample if the surface is not relatively flat. As such, the constant current method is the most often used method, as well as the one used by us here.

3.4.2 Atomic Force Microscopy (AFM)

For samples produced in the HT-PVD system, imaging and characterisation of deposited particles was performed using an N9483-90001 Agilent 5600LS Atomic Force Microscopy system.

AFM as a technique was first proposed in 1986 by Binnig *et al.*[88] as a way to allow for the imaging of small features on surfaces, whilst circumventing the main limitation of Scanning Tunnelling Microscopy; the requirement for the sample being imaging to be conductive. As AFM utilises a different interaction between the tip and the sample, it allows for the production of images of a surface down to the atomic scale without requiring the ability to form an electrical circuit.[93]

Figure 3.15 shows a basic representation of the AFM system: the basic set up consists of a sharp (<10 nm) silicon tip (WindsorScientific NANOSENSORS PPP-NCHR) mounted at the end of a cantilever. As first introduced by Meyer and Amer[94] to replace electrical methods, a laser deflection detection method is utilised by the AFM system, whereby a laser is shone onto the back of the end of this cantilever such that it reflects onto a position sensitive photodiode detector. As the tip is brought into contact with the surface of the sample it interacts with the surface, causing the cantilever to bend: as the cantilever flexes, the position of the reflected laser beam on the photodiode moves. This interaction and subsequent change in the beam position results in a signal being generated known as Deflection, with the unit of Volts. Using this value, a picture of the surface topography can be formed as the tip is moved across the sample, theoretically providing a resolution down to the atomic level.

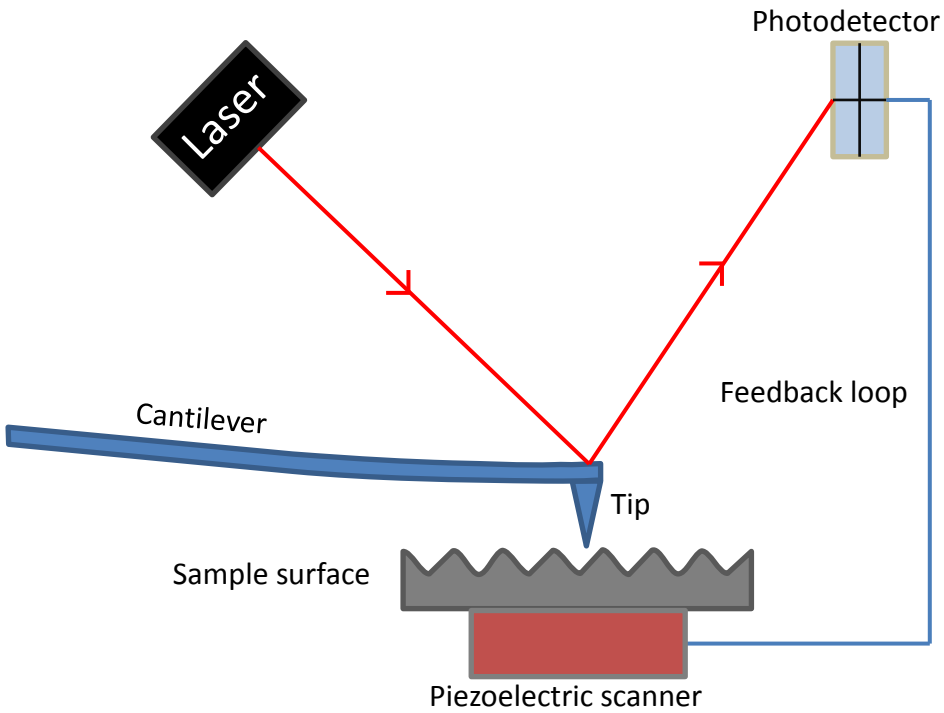

Figure 3.15 A simplified representation of AFM set-up. A sharp tip is mounted on the end of a cantilever which interacts with the sample surface. This interaction is monitored using a position sensitive photodiode with a laser deflected from the back of the cantilever.

The method by which the force interactions between the tip and the surface can be thought of follow what is known as the Lennard-Jones Potential Model (LJPM) of the interaction between two atoms/molecules, as can be seen in Figure 3.16.

Initially, there is no interaction between the tip and the surface, due to the large distances involved. As they start to close, there is a weak attraction between the atoms of the tip and surface. This is known as the “Non-Contact” zone, where there is interaction between the tip and the surface but no physical contact between them. As the tip and surface are brought closer, they enter into the “Intermittent Contact” zone where repulsive van de Waals interactions begin to dominate. At a distance of a few Ångstroms the interactions between the tip and surface balance out and thus the overall force falls to zero. As the tip is further brought closer, the force becomes repulsive again, as the tip enters the “Contact” zone.

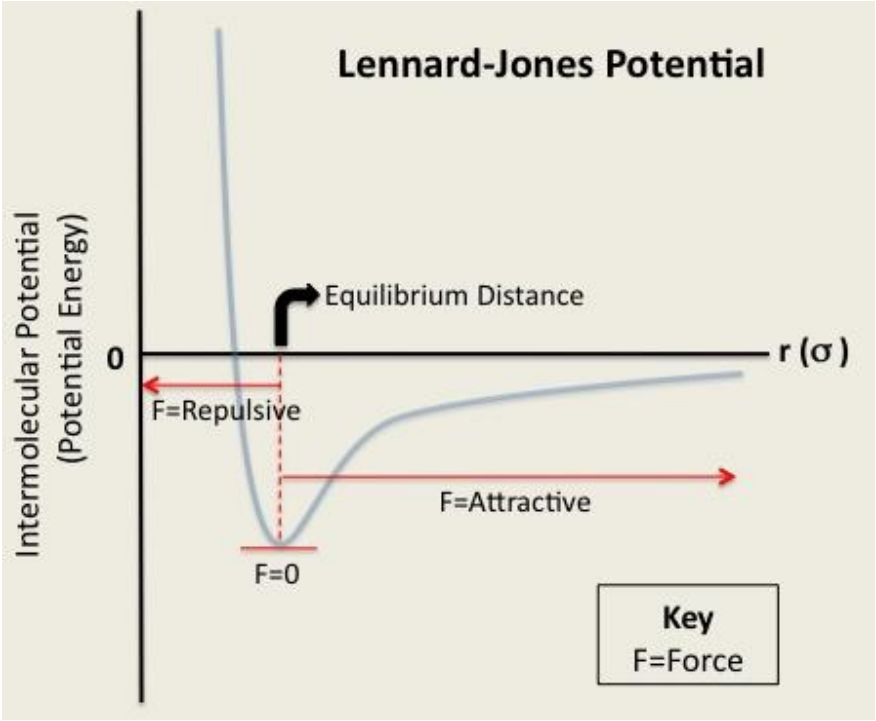

Figure 3.16 Lennard-Jones potential graph representing the interaction of two atoms/molecules. Image taken from webpage by Rabia Naeem.[95]

In AFM there are three main modes for the collection of topographical data on surfaces with AFM: Contact, Intermittent-Contact and Non-Contact. The names of these modes are indicative of the method by which images are obtained.[96]

Contact mode brings the tip very close to the surface such that the tip remains in the repulsive zone of the LJPM and the tip is effectively "dragged" across the surface to provide the images. Non-Contact mode is the opposite of this, where the tip is oscillated at its resonant frequency and the interaction between the surface and the tip via attractive forces allows for the imaging. Intermittent-Contact mode (otherwise known as "Tapping" mode) is the newest of these methods, where, like Non-Contact mode, the tip is oscillated at/near its resonant frequency, but the tip is close enough to the surface such that the oscillations bring the tip between the attractive and repulsive force sections, thus forming intermittent contact between the tip and the surface, effectively making the tip "tap" the surface.

The system used by us here was the Agilent 5600LS and images were taken utilising what is known as Acoustic AC mode (AC as an alternative name for Intermittent-Contact mode) where the Acoustic appellation denotes the method by which the tip is vibrated.

The reason for this is that, despite contact mode providing for very accurate topographical images, doing so exerts a significant amount of force on the sample: enough that less substantial features, such as the titania nanoparticles desired by us here, can be damaged as the tip is moved across the surface. As such, tapping mode was used so as to produce the most accurate images with the least chance that the sample would be damaged during scans prior to electrochemical testing.

3.5 Low Energy Electron Diffraction (LEED)

For the synthesis of the inverse samples on the Au(111) crystal, determining the cleanliness and crystallinity/ordering of the surface was of vital importance prior to the deposition of titanium on the surface. The reconstructions of the Au(111) crystal can also be determined using this method, which was similarly attempted.

LEED as a technique was first demonstrated in 1927 by Davisson and Germer[97], proving in the process the wave nature of electrons. The basic premise is that low energy electrons (20 – 200 eV) are fired at a sample using an electron gun. Due to this low energy, the wavelength of the electrons is sufficiently low that the atoms of the bombarded material act as diffraction gratings for the electrons: these electrons strike the sample and are then scattered by the surface. Only the elastically back-scattered electrons are of interest as they can interfere constructively and thus produce a diffraction pattern. This pattern can then be used to determine the state of the surface under scrutiny. As seen in Figure 3.17, the detector consists of a fluorescent screen with various grids in between the sample and the screen. These grids are set at various potentials to filter the incoming electrons, so as to remove any inelastically scattered electrons from reaching the screen.

The diffraction pattern shown on the fluorescent screen is a representation of the surface, specifically the reciprocal lattice, as such giving an indication of the structure of the surface and any changes in that surface.

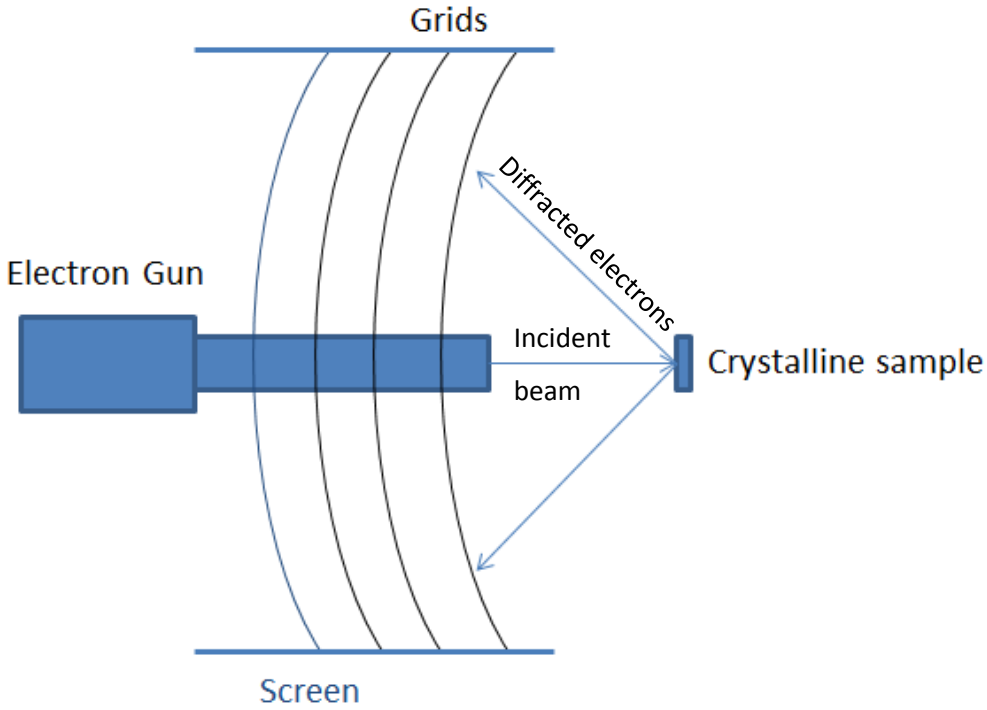

Figure 3.17 LEED schematic for experimental set up on STM system. The electron beam is diffracted back towards the screen, where they form a distinctive LEED pattern. The grids filter the inelastic electrons from the back-scatter.

3.6 STM Tip preparation

The most difficult stage in the imaging of a material using an STM is the preparation of the tips for use in the system, being described as being closer to an art than a science.[98] The manufacture of suitable tips is difficult because of the need for the tips to be as close to atomically sharp as possible to allow for a single "contact point" between the tip and the sample surface. Another consideration is that STM tips should have as small an aspect ratio as possible (reducing the effective length of the tip end) so as to reduce the mechanical vibration of the tips during scanning as much as possible.

A large number of methods have been used for the preparation of tips suitable for STM[98] with the two most common materials used being Pt-Ir and W. The simplest method for producing tips is a mechanical method whereby a Pt-Ir wire is cut at an angle with a wire cutter whilst pulling the wire in the opposite direction. This leads to a ragged surface with numerous projections from the surface that allow for tunnelling to occur. This

method produced tips with a tendency towards irregular shapes with a large curvature of their macroscopic radius[92] and thus is less than ideal.

Electrochemically etching W wire provides production of a more desirable tip shape, in addition to a higher level of consistency in the tips produced. The basic principle is that a wire (most commonly tungsten) is submerged in an electrolyte with a counter electrode already present and a voltage (AC or DC) is applied between the two. This leads to a reaction that dissolves the wire where the electrolyte is in contact, thus allowing for the production of sharp tips.

In this project, the electrochemical etching method was utilised to produce the tips used for STM imaging, though the exact details have been modified over time. The initial method, based on a paper by Bryant *et al.*[99], consisted of the set-up shown in Figure 3.18.

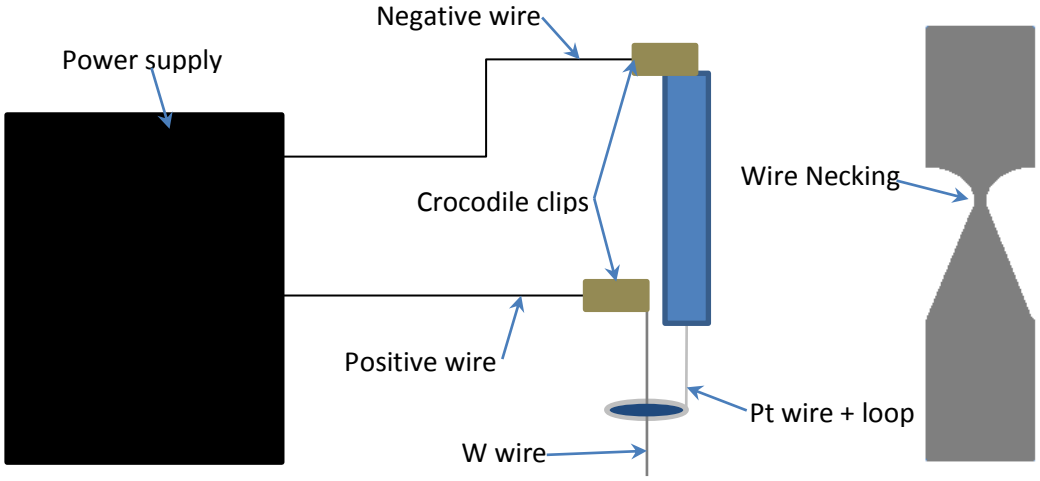

Figure 3.18 Initial STM tip preparation set up. Necking of W wire seen during the etching is shown.

A platinum ring with attached power supply (negative) is suspended: the positive connection was then attached to the W wire used to hold it in place during the process. The wire (0.3 mm W) was placed such that it passed through the loop of the Pt wire with about 4-5 mm extending from the underneath the ring. The ring and wire were held to be as close to parallel to each other as possible.

The system was submerged in 4 M KOH (Fisher Scientific) solution such that the Pt ring was completely covered. Once removed from the solution, a meniscus of the

electrolyte remains behind in the ring, leaving the W wire passing through this meniscus, thus providing completion of the circuit, with the connection part-way up the W wire.

A DC voltage of ~ 7 V was applied, resulting in bubbling to occur at the meniscus as the reaction between the electrolyte and the W wire takes place, causing the removal of wire where the electrolyte is in contact. As time passes, the wire begins to form a neck, until eventually, the weight of the bottom section of the wire is sufficient to cause the tip to detach from the wire, with the voltage stopped as soon as this drop off was noted. Both the bottom and top sections of the wire produce a tip, so comparisons were made between them, though the drop off sections were difficult to procure in an undamaged way. The tips produced were viewed using a *10 magnification eye lens for initial tip capability. These initial tips were then viewed in greater detail using the JEOL JSM5910 SEM system so as to give a proper indication of how suitable they might be for the STM. Examples of some of the tips formed using this method are shown in Figure 3.19.

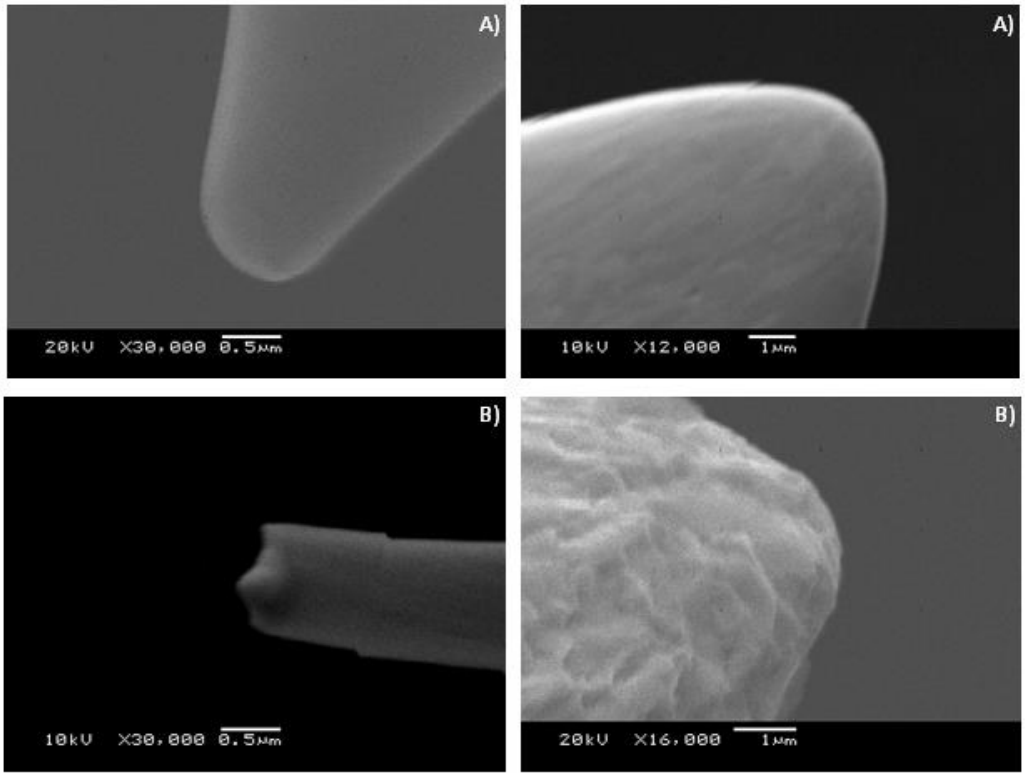

Figure 3.19 SEM images of various tips synthesised with the first attempted etching method. Those marked as A) are those created from the upper section of the wire, while B) are from the drop off. The magnification is shown on the images.

As can be easily seen, the tips formed using this method are not ideal, though the drop off tips were seen to be considerably more suitable than the upper sections (most likely due to the cut-off of the voltage being too slow to prevent blunting of the tip).

To fix this issue, some changes were made to the process for tip formation. The first set of these came from a paper by Tahmasebipour *et al.*[100] which explored the effect of a number of parameters on tip sharpness. The set up used by them differed slightly to that used by us here, but the process was similar enough to allow for utilisation of the techniques.

They proposed a significant number of differing conditions that produce the most reliable tips. The first of these relates to the power supply, with AC and DC producing significantly different tip shapes: AC gives a conical shape with low sharpness, whilst DC gives hyperbolic, much sharper tips, and thus DC is the preferred type. The use of an electronic control system to terminate the voltage supply once the process is complete is also ideal[101], as this limits the amount of blunting the tip undergoes before the process finishes, though this was not feasible for us here.

The second set of parameters proposed relate to the experimental set up: electrolyte concentration, wire immersion length, cathode diameter and the process voltage. They concluded that the best conditions for these were, respectively, 2 M KOH, up to 4 mm, 55 mm and up to 3.5 V. As such, these conditions (barring the cathode diameter, which was fixed here) were utilised in the second procedure for tip formation. Other methods mentioned in *"Nanotechnology Cookbook: Practical, Reliable and Jargon Free Experimental Procedures"* were also useful in fine tuning the procedure.[102]

The most successful method utilised an identical set-up to previously, but with some modifications: the electrolyte concentration was changed to 2 M KOH, the maximum length of wire extending through the loop was 4 mm and the system was suspended no more than 1 cm above a petri dish filled with shaving foam in order to catch the drop-off tip once it disengaged in such a way to prevent its being damaged.

One of the most drastic revisions, however, was the utilisation of a two-step preparation, rather than single step as used previously. This was introduced due to the way in which the necking procedure progresses in the single step process; the lower section of the wire that hangs under the meniscus and drops-off gives sharper tips, as it

does not suffer from continued etching like the upper sections left in the meniscus do. Thus, the drop-off tip is the more desirable of the two, which is why the foam catch was included into the procedure. The issue that comes about from this is that if the etching is done in a single step, the tip formed by the drop off possesses a very long neck, which induces problems with vibrations when used in the STM. To prevent this from occurring, the two step process was implemented; the wire is etched initially as per normal until the etching process is mostly complete (monitored using the *10 magnification eye piece). The etching is then stopped and the wire is flipped, so the originally upper section becomes the drop-off, and thus has a considerably shorter neck than it would otherwise have, but still has the required sharpness given by being the drop-off tip.

The final addition was the introduction of an AM413MT5 Dino-Lite Pro digital microscope that allowed for considerably higher magnification of the tips during the etching process, as well as the ability to record images as they were being taken. This allowed for a much quicker appraisal of the quality of the tips without the need for SEM (and thus a severely reduced chance of damage to the tips). Some examples of the tips made with this new process are shown below in Figure 3.20, with images from the digital microscope and SEM for comparison.

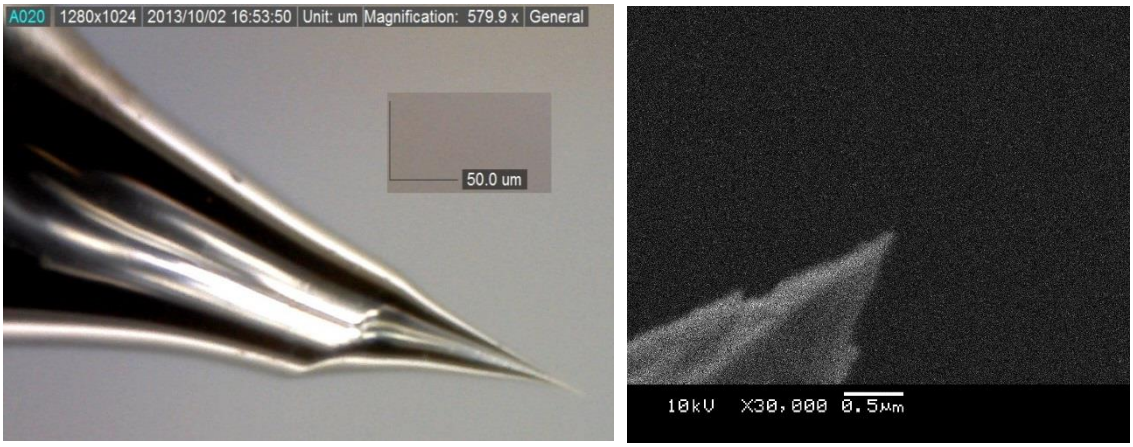

Figure 3.20 Tips synthesised with modified etching method. Left hand image comes from Dino-Lite digital microscope, whilst the right is from the SEM (Beam energy 10 kV, spot size 40)

As can be seen, these tips are considerably sharper than seen with those produced with the previous single-step method, and have considerably less necking (though still more than would be ideal). This technique was used to produce the majority of tips used

in the STM as the tips produced had a much higher consistency in their effectiveness compared to those produced with the single step method.

3.7 X-Ray Photo-Electron Spectroscopy (XPS)

X-ray photoelectron spectroscopy[103] is a technique that has been used for many years for the studying of the elemental composition/chemical states of surfaces. Initially referred to as "Electron Spectroscopy for Chemical Analysis" by its creator Kai Siegbahn[104], due to a number of other techniques coming into being that aim to obtain the same information with a similar methodology, the name eventually became XPS so as to distinguish it from others.[105] Figure 1.21 shows a representation of the XPS system showing the path of the x-ray beam and resulting photoelectrons.

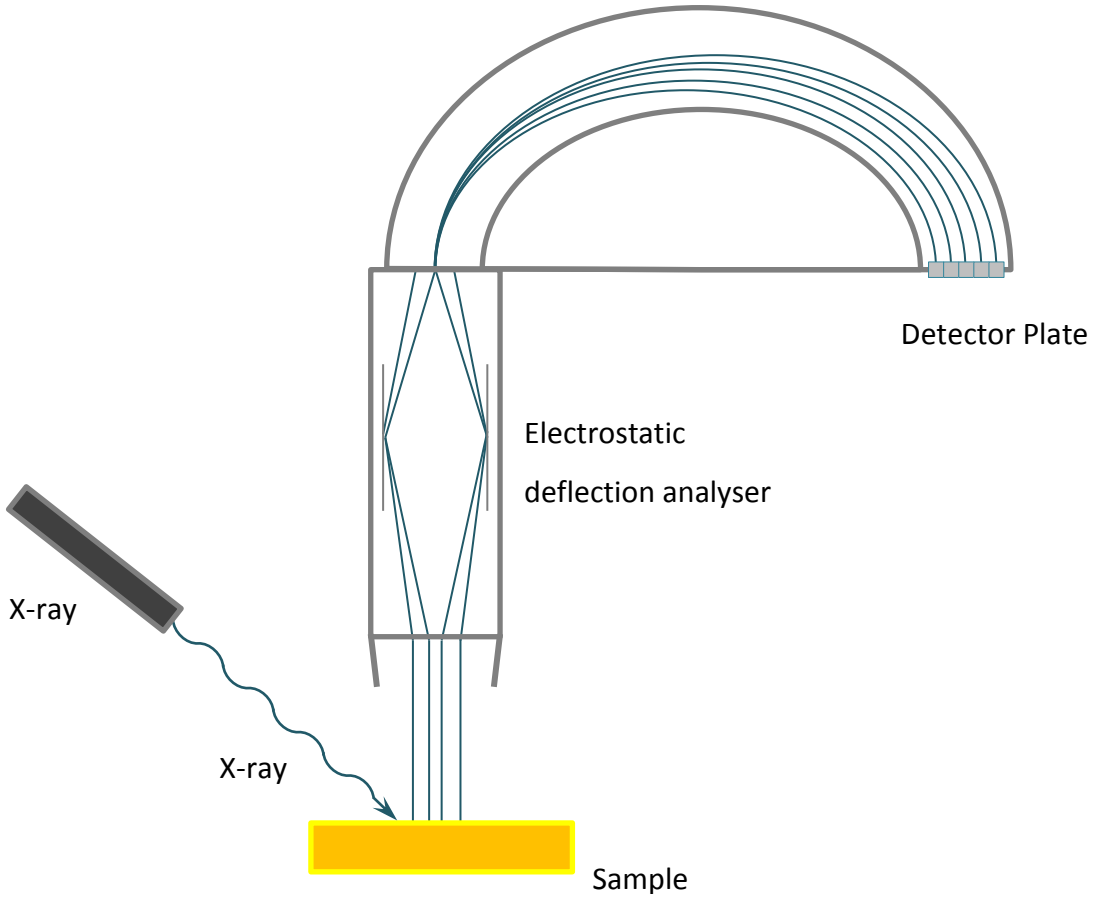

Figure 3.21 Schematic representation of the action of an XPS system. X-ray beam strikes the sample, and photo-electrons are released from the surface. The Electrostatic deflection analyser screens for the desired electrons and the detector plate detects the remaining electrons for proper analysis.

As may be determined from the title, the integral principle behind this technique is the photoelectric effect, initially seen by Heinrich Hertz where he noted that electrodes illuminated by ultraviolet light were more easily able to create electrical sparks[106], which was further refined into the photoelectric effect as put forward by Albert Einstein (for which he was awarded the Nobel Prize in Physics in 1921).

In brief, the photoelectron effect posits that when photons of suitable energies strike a material, they can excite electrons from the occupied electronic states and this results in their escaping the material with a very specific kinetic energy. This is described by an equation based on the work by Ernest Rutherford, as given in Equation 11.[107]

$$E_B = hv - E_k - \phi$$ **Equation 11**

Einstein equation for the photoelectron equation. E_B = electron binding energy, hv = energy of the incoming photon, E_k = emitted electron kinetic energy and $\boldsymbol{\phi}$ = work function of the spectrometer.

If the incoming photon energy, subsequently emitted electron kinetic energy and work function of the material are known values, the binding energy of the material electrons can be determined. A visual representation of this process can be seen in Figure 3.22.

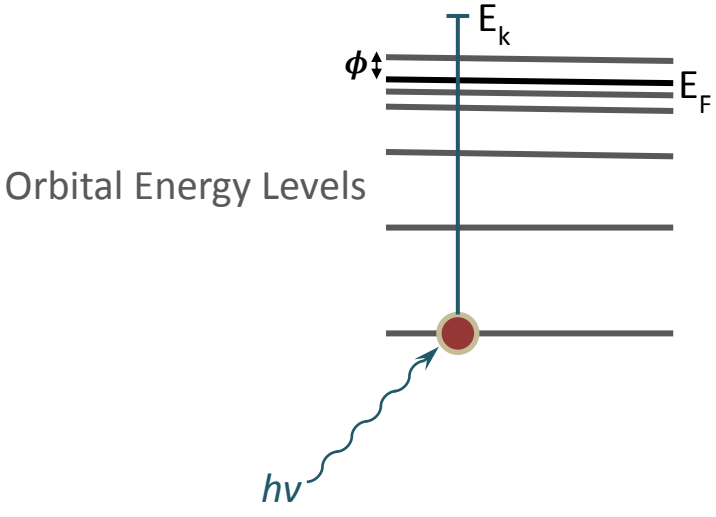

Figure 3.22 Schematic representation of the photoelectric effect. hv = energy of the incoming photon, E_k = emitted electron kinetic energy, $\boldsymbol{\phi}$ = work function of the material and E_F = Fermi level

In the XPS system used the incoming photon energy is known, as the particular x-ray sources produce photons of particular energies: for our measurements an Mg-K_a filament was used, with an energy of 1253.6 eV. By utilising an electrostatic deflection analyser, which screens electrons of specific energies by applying an electrostatic field, the kinetic energy of the released electrons can be calculated. As the work function is known, the binding energy of the electrons can be calculated. As the binding energies of these electrons are unique to individual elements, the detected binding energies can be used to determine the elemental composition of the materials being tested.

An important point to note is that the equation seen in Equation 11 is only an approximation, specifically following what is known as the Koopmans' theorem[108] where the binding energy of the released electron is equal to the difference between the initial and final electron states of the material. This is, however, only true if there is no change in the electronic state of the environment caused by the photoemission process. This is not the case: once the photoemission takes place, the remaining electrons respond to the creation of a core hole by rearranging themselves, mostly by relaxing to lower energy states, so as to minimize the energy present in the ionized atoms.

Due to these shifts in the remaining electrons, the energy of the photo-emitted electron is not exactly equal to the expected binding energy, and thus appears shifted relative to the expected values. However, because these shifts have been identified, it has allowed for the use of the measured energies to determine proper chemical shifts within the material. As such, XPS can be used to identify differences in the chemical states of the scanned materials, whether oxidised or reduced, thus allowing for a greater amount of available information for the state of the material.

Finally, it is important to note that XPS as a technique is only surface sensitive. Despite the significant penetration of solids by x-rays, electrons are considerably less able to do so. This is because as the excited electrons travel through solid matter, they lose their imparted energy over a very small distance and as such only those electrons released from material near the surface are able to escape and thus reach the detector.

4 Au(111)-Titania Inverse Electro-catalyst

The model Inverse electro-catalyst designed and synthesised here will be the inverse analogue of the titania supported gold electro-catalysts: rather than the gold nano-particles supported on titania, the inverse catalyst will be nano-particles of titania supported on gold. Assessment of the catalytic activity of this inverse electro-catalyst will allow insight into the mechanisms responsible for the substrate induced promotion of gold activity when supported on titania (Chapter 1). In particular, in order to assess the role of spill-over from titania to gold, as well as the interaction at Ti-Au interface sites, it is imperative to disperse a high density of titania nano-particles on a gold surface in the inverse catalyst in order to promote effective spill-over/interaction.

4.1 Au(111) Crystal Preparation

4.1.1 Herringbone Reconstruction

The Potapenko/Osgood Ti-Au alloy method[73] was used to produce titania supported particles on an Au(111) reconstructed surface. The Au(111) surface was first cleaned to produce the well-known herringbone surface reconstruction by repeated cleaning and annealing cycles.

The heating was performed using the sample stage in the preparation chamber of the STM system. The sample was heated by electron bombardment: a tungsten spiral filament in close proximity to the sample was heated to produce the emitted electrons and held at 600 V so that electrons were accelerated to the back of the Au(111) crystal mount which was kept at earth potential. The sample was annealed to ~850 K for about 60 minutes between Ar^+ sputtering cycles (8 kV) of 10 minutes duration.

Once a number of these cycles had been performed, the surface structure was assessed by LEED: an example of one the LEED images is shown in Figure 4.1

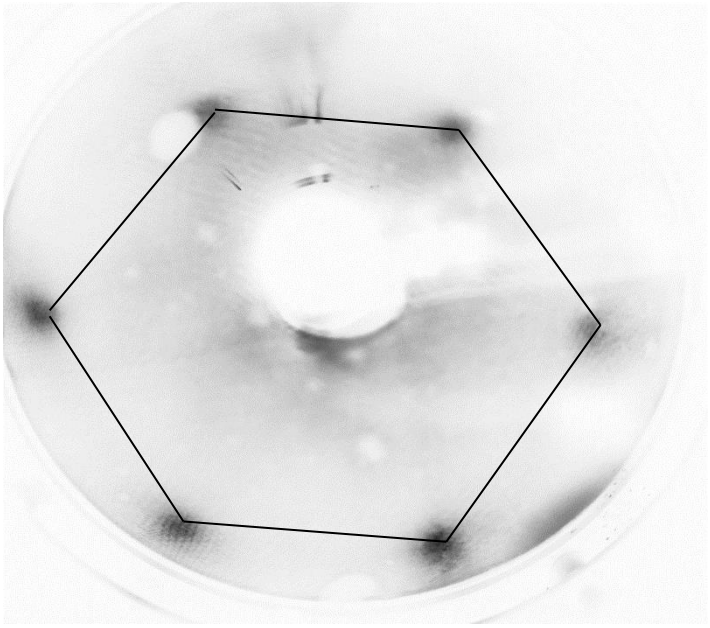

Figure 4.1 LEED Image of the Au(111) crystal after preparation by sputtering and annealing. Image greyscaled and colour inverted for clearer image of beams. Darker areas correspond to spots from the crystal, with the hexagon indicating the first order spots (1*1) pattern. Recorded at a beam energy of 62.3 eV.

A clear (1*1) pattern can be seen from the Au(111) crystal, indicating a well ordered (111) surface. Unfortunately, the desired LEED images indicating herringbone reconstruction were never observed. As shown in Figure 4.2, the reconstruction should result in satellites surrounding the first order (1*1) diffraction spots.

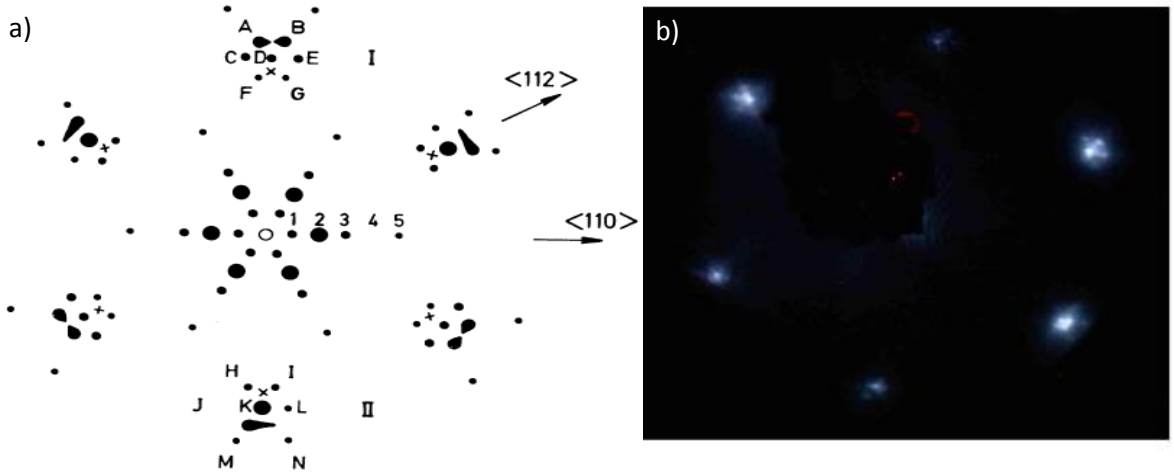

Figure 4.2 (a) Schematic representation of the diffraction pattern for Au(111) herringbone reconstruction. The crosses represent the diffraction spots for an unreconstructed surface. Reproduced from Harten *et al*.[109] (b) LEED image of Au(111) reconstruction recorded at an energy of 60 eV Reproduced from Biener .[110]

Despite LEED not showing the desired pattern for the reconstruction despite repeated cleaning cycles, the surface of the cleaned crystal exhibiting sharp (1*1) spots on the Au(111) surface was imaged using the STM as an alternative: the distinctive herringbone reconstruction was clearly visible on the Au(111) surface.

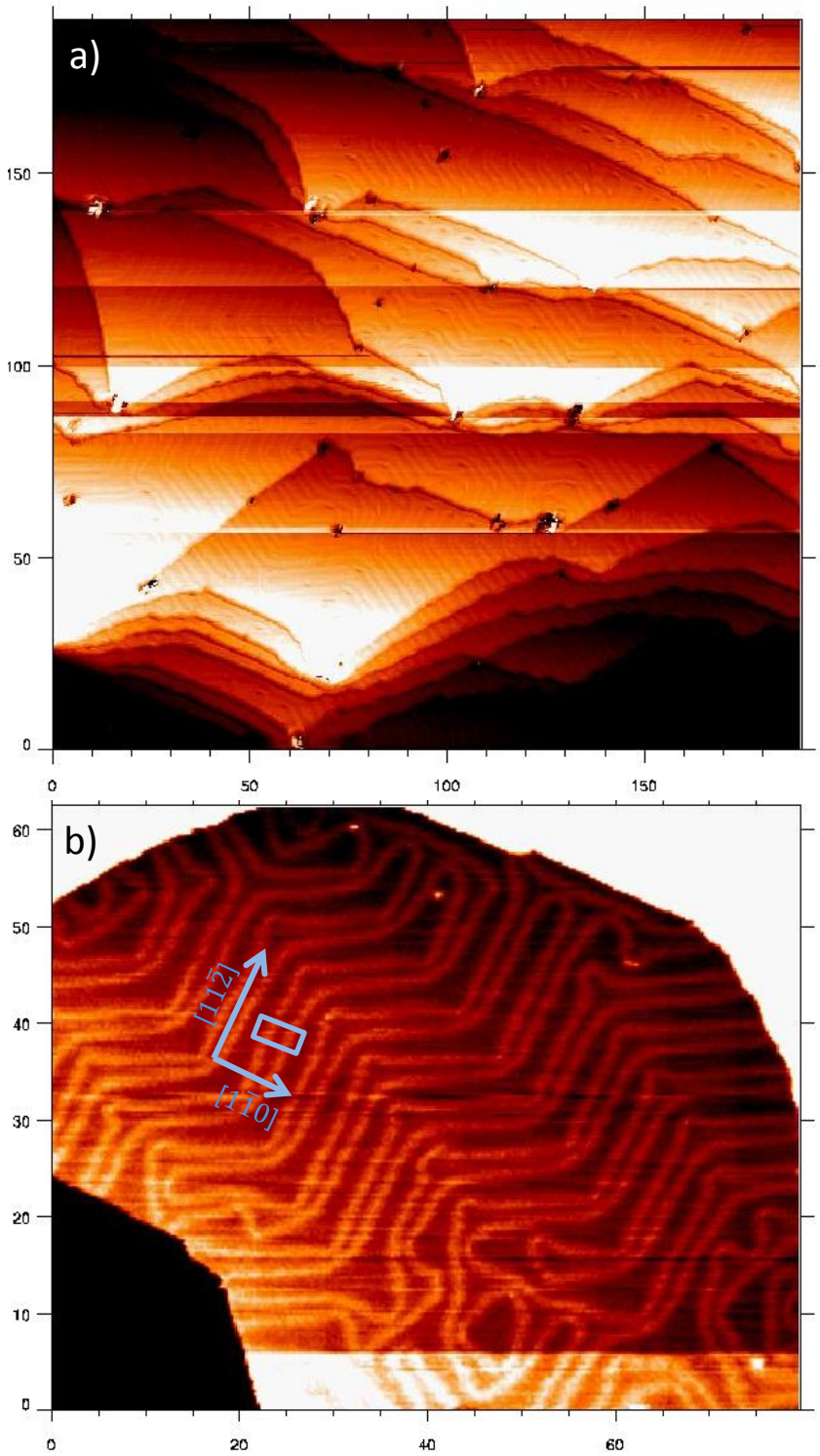

Figure 4.3 STM images clean of Au(111) surface with herringbone reconstruction visible. a) 190*190nm, b) Zoom of (a) 80*62 nm with unit cell and vertices. Constant Current Mode: Tip Voltage (V_g) = 0.8 V, Tunnelling Current = 0.5 nA, Gain = 1.0 %

The unit cell of the Au(111) 22*√3 reconstruction, as shown in Figure 4.3 (b), should have dimensions of 63 Å (‹$1\bar{1}0$› direction) x 4.7 Å (‹$11\bar{2}$› direction).[66] As atomic resolution was not achieved in these images, ascertaining the full unit cell using the above images was not possible. However, determining the ‹110› direction component of the unit cell was viable: a value of ~60±5 Å was determined. This is consistent with the literature values above, and thus the scaling of the STM system was determined to be correct.

Image (b) in Figure 4.3 shows an example of the extent of steps and plateaus present on the surface, also indicating the extent of the herringbone reconstruction on a continuous section of the surface. These plateaux are indicative of the general size of the more distinct plateaux seen on the Au(111) crystal throughout this project, with widths of ~ 60-80 nm being common, though often extending longer along step edges. Image (a) shows that the larger plateaux (where the reconstruction is more clearly visible) are occasionally interrupted by smaller steps, with a typical width of 2-8 nm. The herringbone reconstruction does not appear to be interrupted by these smaller plateaus, continuing across them from terrace to terrace.

This structuring of the surface, with occasional small steps separating more common larger plateaux, was seen across the majority of images for the cleaned Au, regardless of the extent of cleaning performed, as well as images taken of the titania modified surfaces. In an attempt to increase the size of these plateaus, as well as reducing the number of the intermediate steps, the crystal was polished, though this did not appear to have a notable effect on the structure of the surface.

Despite the lower size of the plateaux compared to those seen in the literature[66], where widths of 100-150 nm are more commonly seen, the herringbone reconstruction was clearly visible on the crystal surface when imaged via STM. It was this smaller average size of the plateaux across the surface that was determined to be the cause for the lack of the expected satellites appearing in LEED images of the surface despite the reconstruction being present.

As a more exact measure of the state of the crystal surface was given by utilising STM compared to LEED, it was utilised for the determination of the surface cleanliness/reconstruction of the Au(111) crystal prior to all titanium depositions.

4.2 Titania Nanoparticle Synthesis

4.2.1 Determination of Ti Coverage Limit

Once the Au(111) crystal surface reconstruction had been established by LEED and STM, titania nanoparticle synthesis on the clean surface could begin. Titanium deposition was performed using the directional doser mounted on the preparation chamber, with the crystal mounted in the same fashion as during the cleaning cycles.

The exact effect the deposition conditions had on the final titania particle size/distribution was mostly unknown initially. Some later work performed by Potapenko *et al.*[111] utilising this method noted a possible relationship between particle size and the annealing temperature used during oxidation. This possibility was not investigated further in the literature and as it was not prominently mentioned in the paper, was thus missed at the time of reading and was subsequently not investigated in this work.

The major factor for investigation was the effect of the initial titanium concentration prior to alloying on the final titania nanoparticles formed. As such, determining the upper limit of Ti concentration that produced distinguishable titania nanoparticles was necessary before film formation began. Higher Ti deposition levels than those used by Potapenko and Osgood were initially investigated so as to determine where this barrier between nanoparticle and film formation lay.

An initial deposition of ~1.2 nm effective thickness (ET) titanium (as determined via quartz crystal microbalance) gives titania film formation. Figure 4.4 shows STM images taken of such a sample once oxidation had been completed.

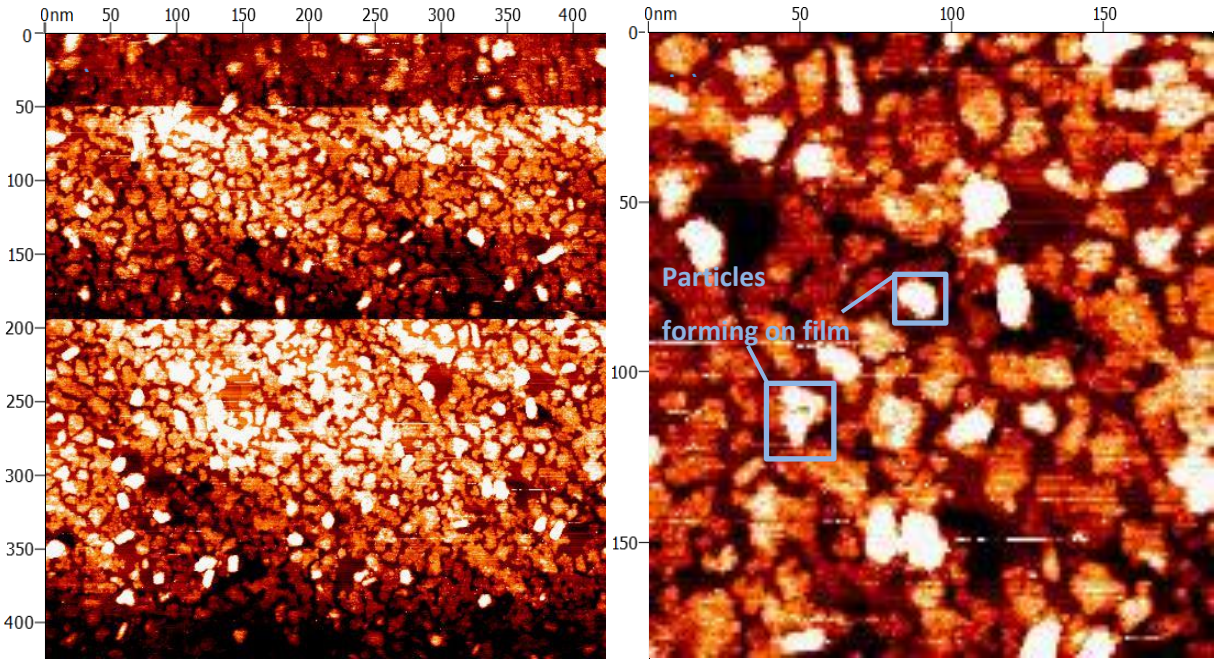

Figure 4.4 STM image of TiO_x/Au(111) with 1.2 nm ET intitial Ti deposition. a) 422*422 nm, b) 139*139nm (magnification of a). Constant Current Mode: Tip Voltage = 0.8 V, Tunnelling Current = 0.5 nA, Gain = 2.0 %

It can be clearly seen that the surface has been considerably modified from the clean gold crystal: a film of titania has formed on the crystal surface, consisting of individual particles agglomerating together, though total coverage of the complete surface has not yet been reached. An oddity of this process, however, is the second effective layer of particles that appears to be forming on top of the first agglomerating layer. That these are indeed secondary particles rather than fluctuations in the first layer particles is supported by the fact that that the relative height of the second layer particles to the first layer is ~1.5 nm, which coincides with that of the lower layer.

The reason for these additional particles forming prior to completion of the initial film, or the lack of continuous film growth giving “particles”, must be associated with the mechanics of growth: a similar distribution was seen by Carrozzo *et al*.[70] for the deposition of Ti on Au(111), which was modelled using the “diffusive growth model” as proposed by Cohen *et al*.[112] The reason that the TiO_2 nanoparticles synthesised here produce this second layer formation is unknown, as any differentiation between upper and lower layers from the initial Ti should be removed by the alloying step. Such a large coverage also makes determining the state of the crystal underneath difficult: some raised areas are somewhat visible, though nothing significant enough to give a proper

indication of the underlying crystal state. These additional particles do allow us to determine the particle growth progression, despite the initial film formation: rough triangular/elongated shapes can be made out in these top particles, which have been seen previously with this particular synthesis method, alongside more rounded versions of the same. These particles average ~ 10-12 nm, slightly larger than was initially hoped, but still viable for use here.

4.2.2 Titania Nanoparticle Distribution on Au(111)

With the deposition limit having been determined, the synthesis of distinct particles directly on the surface could be considered. It was found that by reducing the initial Ti deposition, the corresponding volume of titania formed on the crystal surface was also decreased, as would be expected. An example of a typical sample made with lower Ti concentration can be seen below in Figure 4.5.

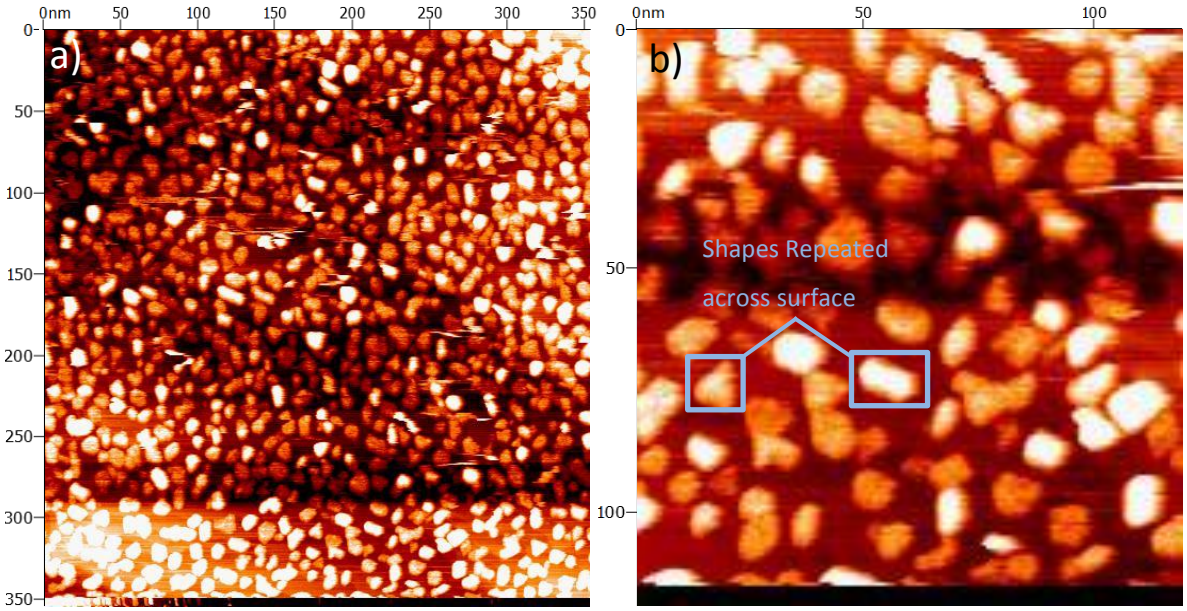

Figure 4.5 Example of titania particles formed on Au(111) (initial Ti 0.7-0.8 nm ET) a) 353*353 nm, b) 118*118 nm magnification of a). Constant Current Mode: Tip Voltage = 0.8 V, Tunnelling Current = 0.5 nA, Gain = 5.0 %. Distinctive particles visible, with hexagonal and triangular shapes repeated across surface

The reduced initial Ti concentration (~0.75 nm ET) has led to a definite difference in the final sample produced. The titania has formed into distinctive particles when compared to Figure 4.4, where agglomeration resulted in particles in the second layer.

With the ability to distinguish particles with greater fidelity having been gained, the configuration of these particles can thus be properly determined. Similar to Figure 4.4, the most common shapes seen on the samples synthesised are either triangular or distorted hexagonal in nature, as indicated in Figure 4.5 (b); other shapes are present, though generally these shapes were predominant. These were the shapes seen by Potapenko *et al.*[73], thus providing evidence that the synthesis method was performing as expected; as such, we can consider the titania to most likely be in a similar form to their work, in this case rutile.

Once individual particles had been shown to develop with lower titanium levels, further investigation of the initial Ti deposition and final particle concentration/size relationship could begin. It was expected that by varying this factor, the formed particles size would shift; with the concentration of Ti in the Au-Ti alloy varying, the changes in available Ti would lead to changes in the sizes of the subsequent particles. This was found to not be the case: it became evident that varying the Ti deposition resulted in variations in particle distribution and concentration across the surface, but the size of the particles remained moderately consistent across samples regardless of the initial Ti deposition level.

An example of this variation is illustrated below in Figure 4.6, where a comparison between the surfaces of three separate samples with differing initial Ti concentrations is visible: a linear relationship between initial Ti deposition and the final titania coverage was initially expected but this was determined to not be the case. Sample (a) is the same as that in Figure 4.5, with a ~0.75 nm Ti deposition giving a final surface coverage of ~59.8%. This is in contrast with (b), where a deposition of ~0.5 nm Ti was used, yet the concentration of particles on the surface was 63.1%. Sample (c) was more in line with the expected pattern, as ~0.35 nm Ti resulted in a coverage of 47.1%, though this was still higher than might have been expected considering the significant decrease in Ti.

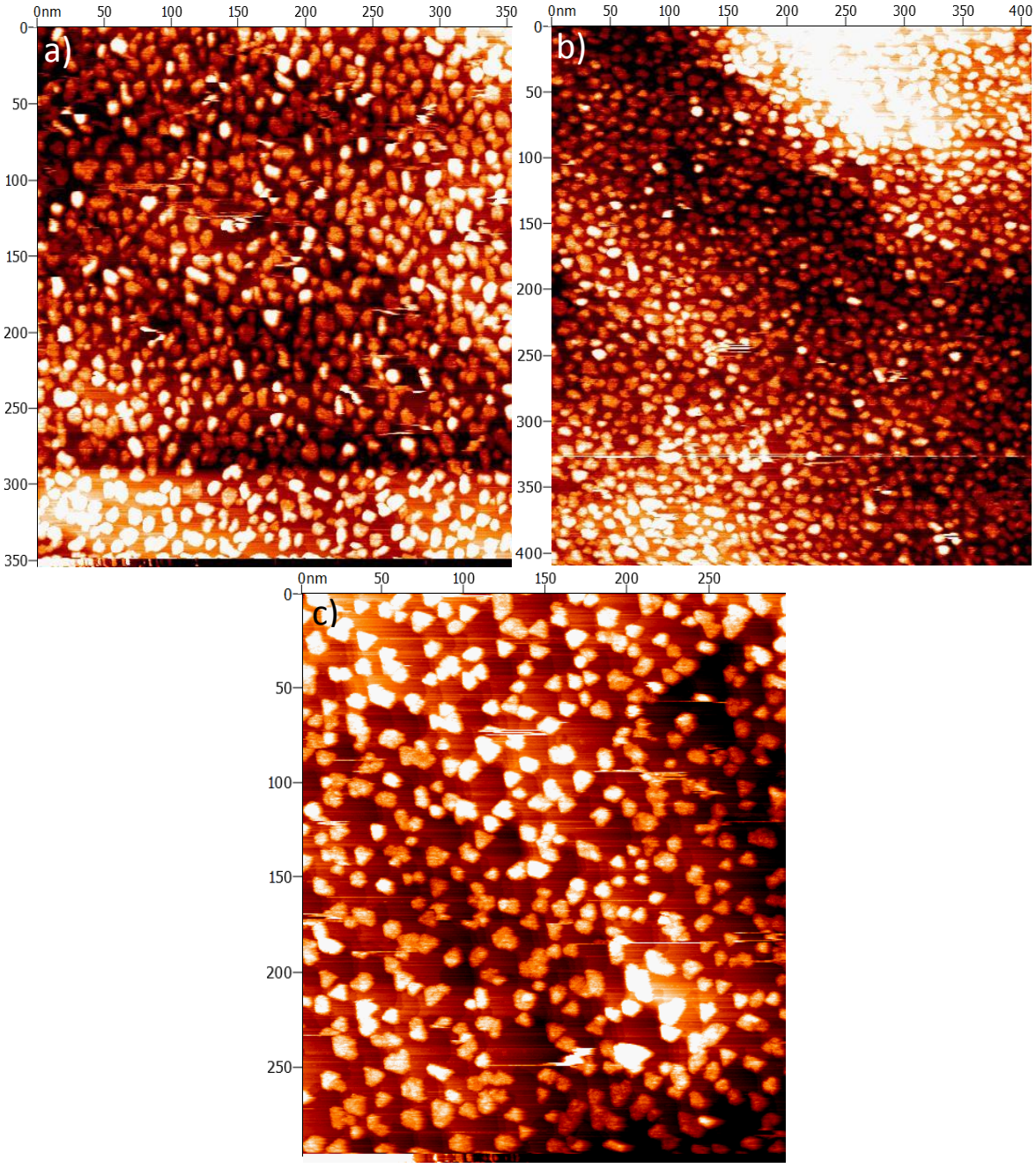

Figure 4.6 Comparison of TiO_x/Au(111) samples with differing initial Ti concentrations. Constant Current Mode: a) ~0.75 nm ET Ti: 353*353 nm V_g = 0.8 V, Tunnelling Current = 0.5 nA, Gain = 5.0 %, b) ~0.5 nm ET Ti 408*408 nm, V_g = 0.8 V, Tunnelling Current = 0.5 nA, Gain = 5.0 %c) ~0.35 nm ET Ti: 297*297 nm V_g = 0.8 V, Tunnelling Current = 0.5 nA, Gain = 2.0 %. Particle variation varies with initial Ti concentration.

In contrast to previous images, the gold surface can be made out to a considerably greater degree. This is most easily seen in sample (c): no significant changes have occurred with the plateaux/steps, though the herringbone reconstruction is no longer clearly visible beneath the particles. Potapenko and Osgood[73] did not indicate if the

herringbone returned after oxidation, though a very distorted herringbone was seen for STM images of the alloyed surface immediately prior to oxidation (which has not been repeated here). The herringbone was observed to remain in the synthesis utilised by Biener *et al.*[72], though this can most likely be attributed to lack of an alloying step between Ti deposition and oxidation.

The disconnect observed between the deposited Ti and expected final titania density on sample b) was not consistent with the expected linear correlation: a similar level of disconnect was present throughout this project but its cause was not immediately apparent. The reason was determined to come from the fact that the same Au(111) crystal was used for all samples; the crystal was cleaned as above after each set of electrochemical testing and reused once fully clear of any residual particles. The effect of this recycling of the crystal for subsequent samples was not initially considered; however, this lack of correlation between Ti deposition and final particle concentration led to such consideration being required.

It was initially thought that any residual Ti remaining alloyed in the crystal post oxidation would either move fully into the gold bulk during cleaning, thus not affecting subsequent syntheses, or migrate to the surface and be removed during sputtering. However, with the observed lack of Ti/TiO_x correlation between samples, it was considered that more Ti might remain available for titania formation between samples than initially thought. Either, Ti did not migrate as extensively as expected or the crystal was becoming saturated with Au-Ti alloy, resulting in higher Ti availability during synthesis with subsequent samples.

To determine if this residual Ti was indeed the cause of the fluctuating titania levels, a simple experiment was performed: after the standard cleaning/reconstruction was performed on the crystal post electrochemical experimentation, no further titanium was deposited on the surface. Instead, the crystal was immediately exposed to the alloying and oxidation steps of the synthesis. The ensuing sample was imaged in the STM chamber, the results of which can be seen below in Figure 4.7.

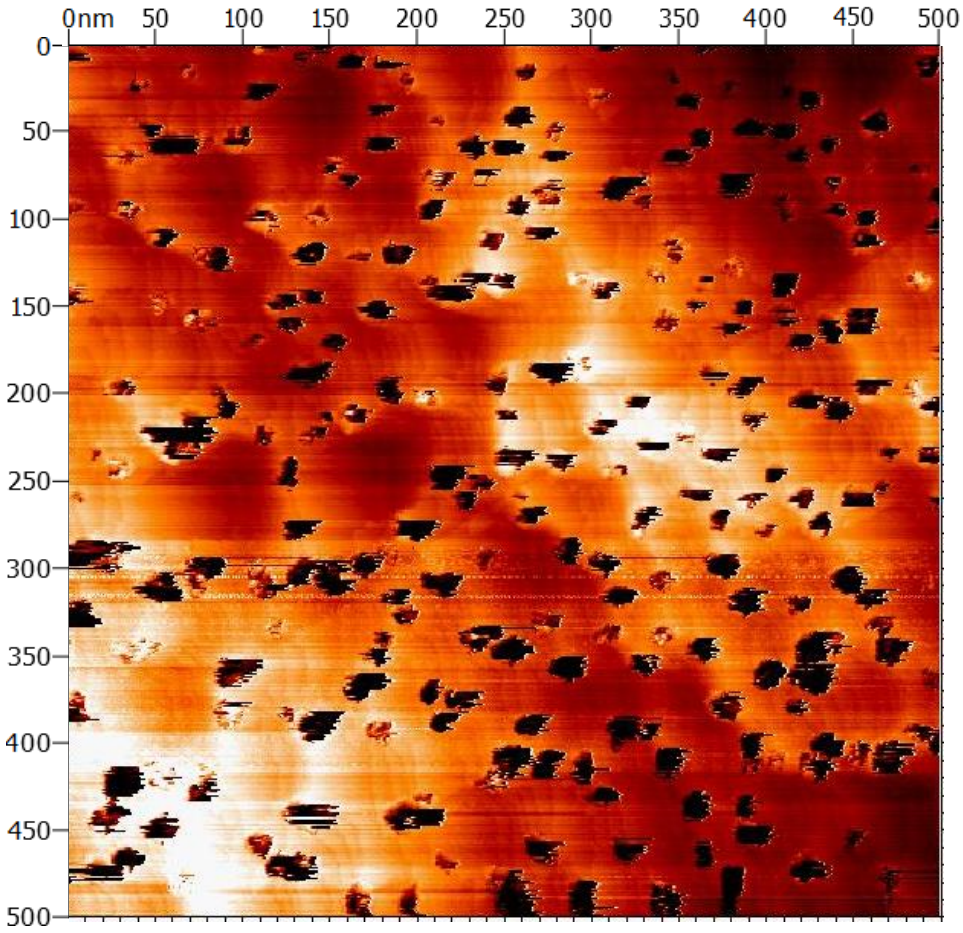

Figure 4.7 Initial image for Sample exposed to Oxidation step whilst lacking initial Ti deposition. Darkened areas correlate to depressions in the surface of the sample 500*500 nm. Constant Current Mode: V_g = 0.8 V, Tunnelling Current = 0.5 nA, Gain = 3.0 %.

Despite the lack of deposited Ti, depressions are observed across the surface once the synthesis process had been completed, alongside the image being considerably noisier than other images. This differs from previous samples where, despite utilising identical imaging conditions, particles were immediately visible once the synthesis was complete. However, these pits do appear to adhere somewhat to the general particle shapes seen in our other samples, so they may be related to titania formation. Of particular note is the large concentration of steps present between the larger plateaux: the surface was cleaned as extensively as previous samples, with other images of the surface showing larger areas lacking such steps. These images are the cleanest of those taken, however, and thus will be used to showcase the surface.

To achieve better resolution, as well as to determine if these were in fact particles or pitting of the surface, the scan conditions were modified. It was established that increasing the tip voltage from 0.8 to 2.0 V resulted in the pits resolving into particles that were considerably closer to the expected size/shapes, with the triangular shape being particular prevalent. From this it can be considered that residual titanium was indeed retained in the gold between experiments.

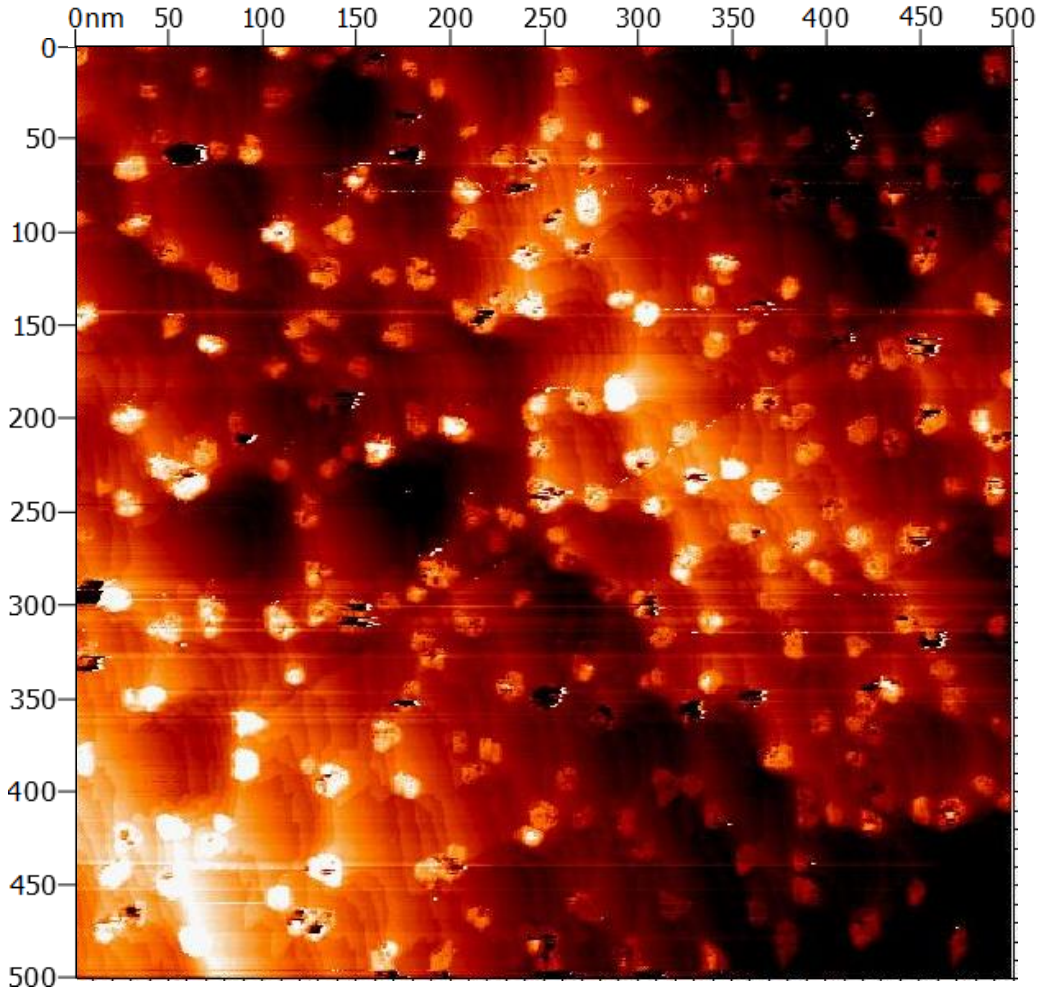

Figure 4.8 Modified scanning conditions of Figure 4.7. a) 500*500 nm. Constant Current Mode: V_g =2.0 V, Tunnelling Current = 0.5 nA, Gain = 2.0 %

The density of particles on this sample is considerably lower than previously: this is to be expected due to lower levels of available titanium during oxidation. With these supposed particles visible, it can be concluded that residual Ti was retained in the crystal from previous syntheses: however, as the particle density was considerably lower than previous samples, full saturation had not been reached. This provides an explanation for the observed variation in titania density compared with initial Ti deposition: the varying

concentration of Ti remaining in the gold crystal modified the particles formed in subsequent syntheses.

This sample also gives an indication of the particle formation process as seen in Figure 4.9; comparing this sample to one with a higher coverage shows that the particles begin forming along step edges. Due to the larger than average number of steps present, the particles appear to straddle a number of steps rather than being limited to edge sites: however, earlier images show that a there is a definite preference for edges regardless of the step quantity: the image in Figure 4.8 was used as it provided the cleanest image.

A similar effect was observed by Biener *et al.*[72]: during their initial deposition, no Ti particles formed along step edges. However, as the alloying step was not part of their synthesis, the oxidation was performed immediately following deposition. Protrusions along edges only appeared once the oxidation step had been performed; this was attributed to the small quantity of Ti alloyed during deposition being drawn out of the Au during the oxidation process similar to the synthesis utilised by us here, thus the preference seen here for forming along edges is not unexpected. When higher levels of Ti are available during the oxidation, particles begin forming on the more central sections of the terraces.

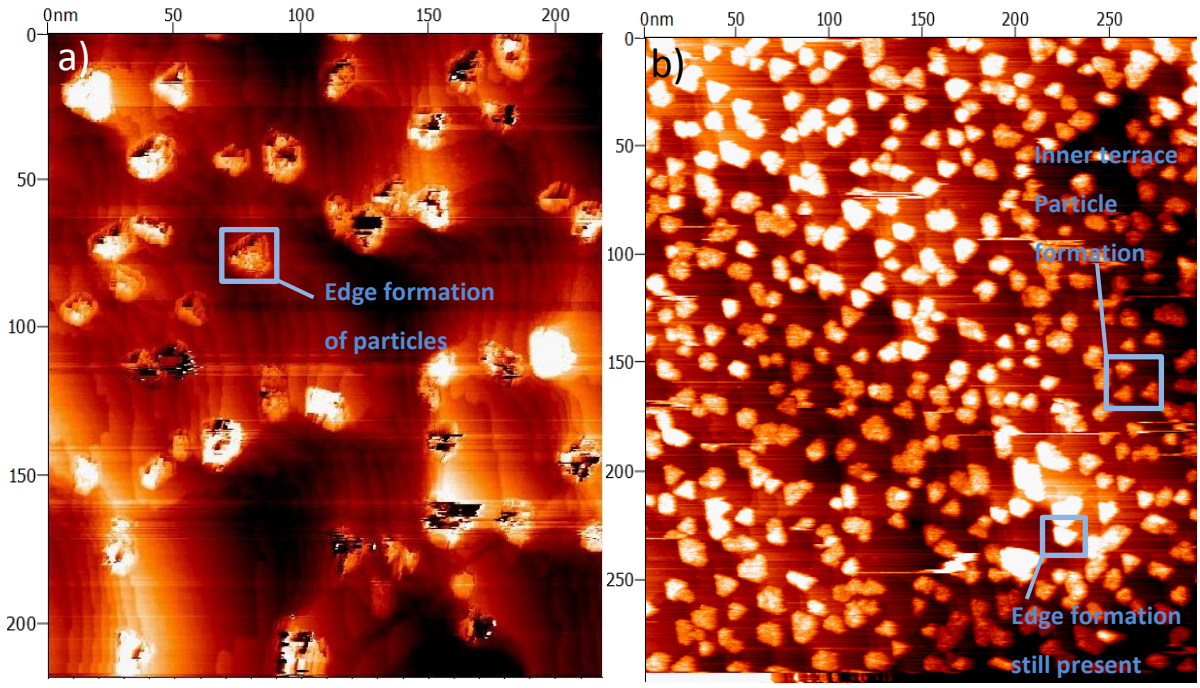

Figure 4.9 Example of particle formation progression: formation begins at the edge of plateaux, with particles appearing towards central sections of plains as the available Ti increases. Constant Current Mode: a) 218*218 nm zoom of Figure 4.8 V_g =2.0 V, Tunnelling Current= 0.5 nA, Gain = 2.0 %, b) 297*297 nm V_g = 0.8 V, Tunnelling Current = 0.5 nA, Gain = 2.0 %.

4.3 Particle Analysis

Despite the relationship between deposited Ti thickness and the titania particles formed being complicated by residual Ti in the crystal, enough distinct samples were synthesised displaying significant variation in particle density for investigation into the system. As mentioned, it was first thought that particle size would vary with initial Ti deposition: despite this, and with increasing Ti alloy saturation in the crystal, the particles formed during these syntheses were of comparable sizes/shapes. Table 4.1 shows the variation in particle size alongside percentage coverage of the crystal by titania.

Table 4.1 Titania particle size and coverage comparison. Coverage represents area percentage of gold covered by titania.

Deposited Ti Effective Thickness/ nm	TiO_X coverage of Au(111)/ %	Average Particle Size/ nm
0.5	63.1±3.16	10.92±2.89
0.75	59.8±2.99	11.34±2.23
0.8	55.1±2.76	12.26±2.21
0.35	47.9±2.40	11.58±2.75
0	18.5±0.91	12.85±3.21

The particles vary slightly in size across samples, but an average of ~11.5±2.5 nm is observed for all samples manufactured during this project. Because of this, a comparison with the CO oxidation cannot be made with size variation in mind as was initially planned (noting that it is possible to vary the size of deposited particles; variation in the deposition temperature rather than initial deposition level gives size change in the particles[111]). Another method for comparison is, however, available: utilising the effective density of particles as a measure of the possible spill-over effect and the action of interface sites. By analysing the variation in particle separation, as calculated from the average inter-particle distance on the surface, a measure of titania density can be made; an example of this procedure can be seen in Figure 4.10.

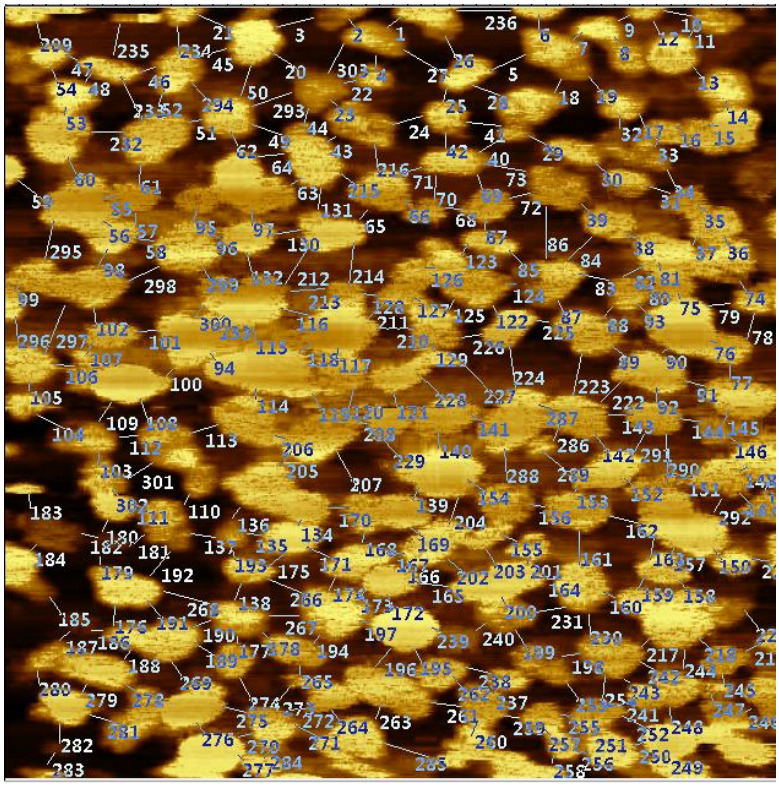

Figure 4.10 Particle Separation calculation on 55.1% coverage sample. Lines correspond to individual distance calculations. 139*139 nm, Constant Current Mode: V_g = 0.8 V, Tunnelling Current = 0.5 nA, Gain = 2.0 %

This methodology allowed for an approximation of the average separation between particles for each of the samples: the values of which are shown in Table 4.2.

Table 4.2 Titania surface coverage and particle separation.

Deposited Ti Effective Thickness/ nm	TiO_X coverage of Au(111)/ %	Mean Particle separation/ nm
0.5	63.1±3.16	3.48±0.98
0.75	59.8±2.99	4.72±1.57
0.8	55.1±2.76	5.04±1.62
0.35	47.9±2.40	7.43±2.22
0	18.5±0.91	19.05±4.21

As one would expect, there is a correlation between the effective coverage of the surface with titania particles and the mean particle separation; this can be seen in Figure 4.11.

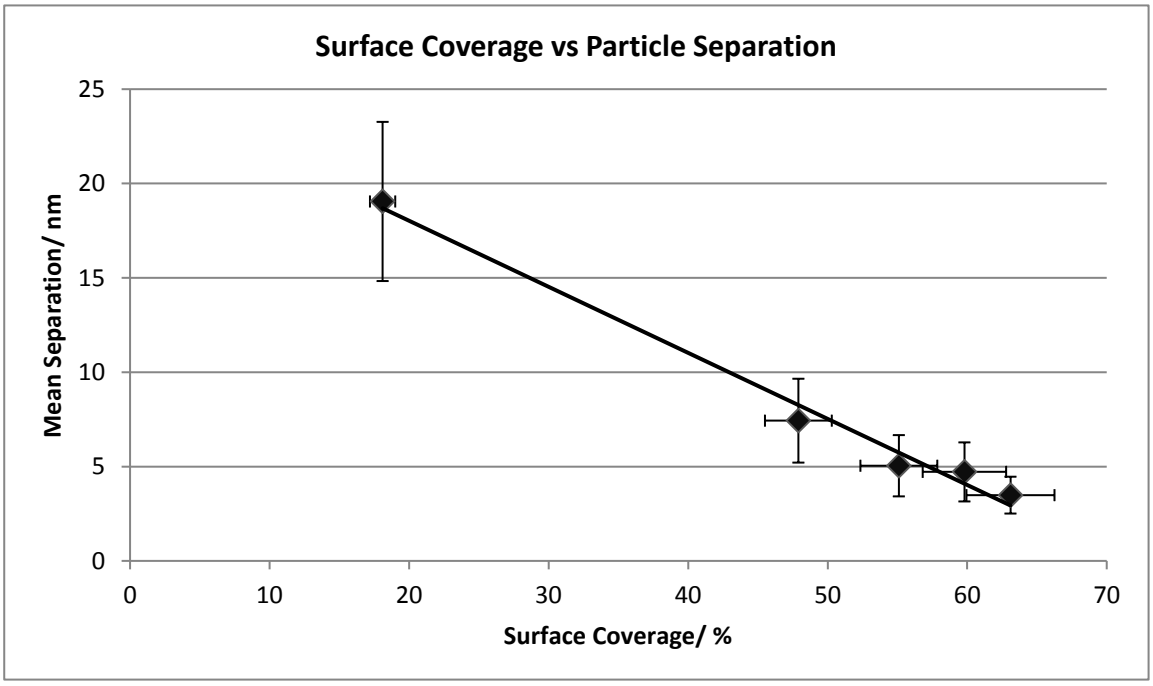

Figure 4.11 Graphical comparison of the change in particle separation with total surface coverage.

A reasonably linear relationship is visible between particle separation and the total surface coverage; such a pattern is not unexpected considering the consistency of particle size across samples. With this trend having been determined, the relationship between particle separation/surface coverage and the relevant CO oxidation electrochemistry can be investigated.

4.4 Electrochemistry

4.4.1 Clean Au(111) Cyclic Voltammetry

Prior to studying the electrochemistry of the Au(111) supported titania particles, the electrochemical behaviour of the clean/reconstructed Au(111) required determination. As well as providing a baseline for comparison with future samples, this also allowed a proper test of the electrochemical cell set-up, as well as proving that transfer of the crystal from UHV to the electrochemical cell was reproducible and clean. An example of the CVs seen for the clean Au(111) surface can be seen below in Figure 4.12.

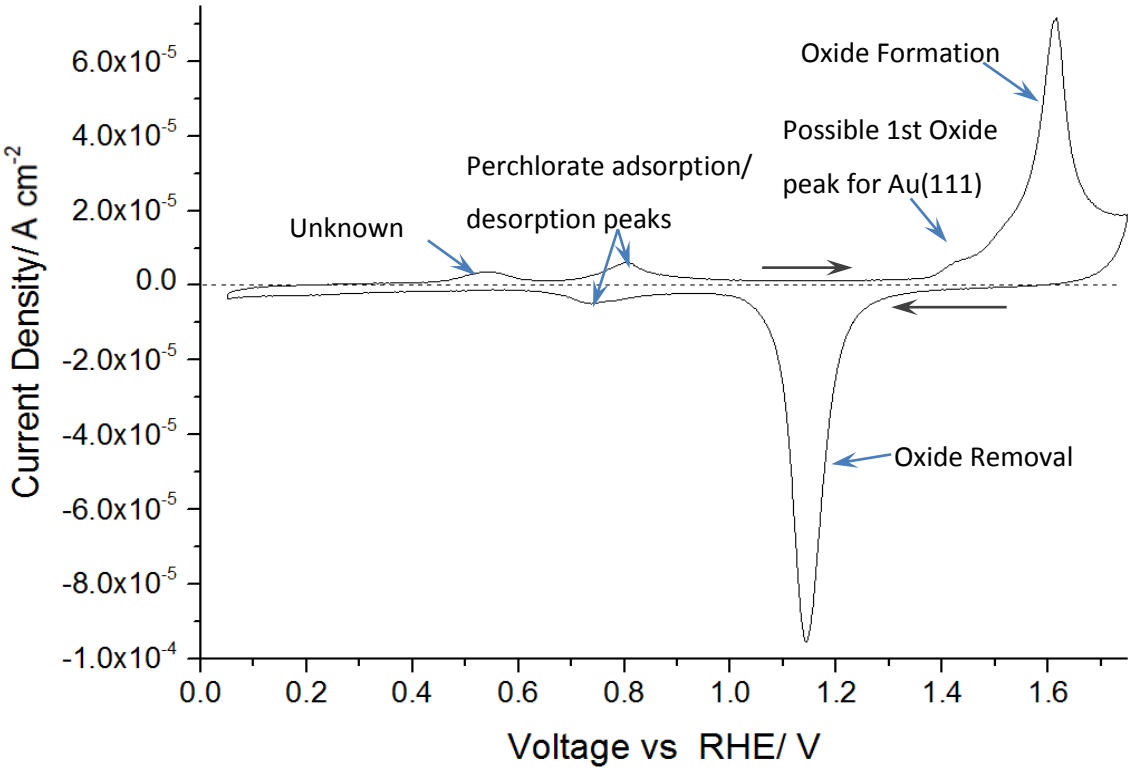

Figure 4.12 Clean Au(111) CV, 0.05-1.75 V vs RHE. Scan speed = 50 mV s^1 0.5 M $HClO_4$

The CV is reminiscent of those seen in the literature[78], however, when compared to the Au(111) CV in $HClO_4$ some differences do appear. Hamelin[113] found that in the oxide region, two peaks should appear at ~ 1.34 and 1.6 V vs RHE for the (111) plane. These peaks correspond to the passage of electrons during the replacement of surface adsorbed anions for OH. The first oxide peak is much smaller than expected, with the second being considerably more prominent, which remains consistent for all scans taken on the crystal utilised in this project: these CVs are more reminiscent of the CVs seen for Au(111) in sulphuric acid[114], though the reason for this is unknown. The perchlorate

adsorption/desorption peaks seen were consistent with those in the literature: as the CVs observed remained consistent across the project, these were deemed suitable for comparison with the Ti modified surfaces. In addition, an extraneous peak is present at ~0.55 V: this peak is removed in later CVs so is assumed to be due to a slight contamination of the electrolyte used for this set of scans and is thus of no concern.

Once the general CV for Au(111) in 0.1 M $HClO_4$ had been established, the CO oxidation on the clean crystal was investigated. CO gas was bubbled through the electrolyte for ~15 minutes prior to measurement, with a CO atmosphere maintained during the scans. The corresponding CV can be seen in Figure 4.13.

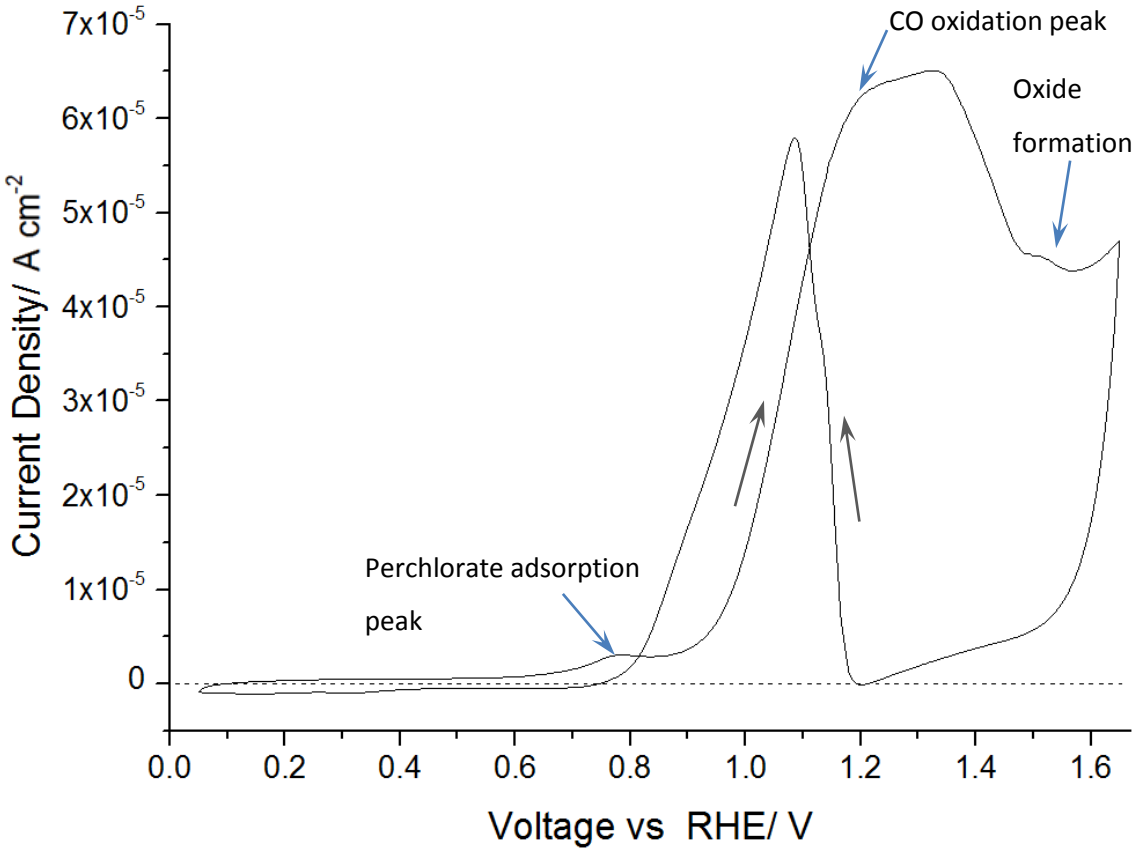

Figure 4.13 CV of clean Au(111) in CO dissolved electrolyte with CO atmosphere. Scan speed = 50 mV s^1, 0.1 M $HClO_4$

The CO oxidation onset occurs at ~0.9 V, though the exact position is somewhat masked by the perchlorate adsorption peak. The shape of this CO peak is reminiscent of that seen on Au(111) crystals in the literature[115], though with the onset/plateau positively shifted ~0.2 V, with the peak dropping away at similar potentials prior to oxide formation. It is important to note that the CO oxidation is mass transport limited; a lower sweep rate

may bring the CV closer in line with literature values, though the onset was consistent with the literature[116,117] so the reason for this difference is not clear.

A second CO oxidation peak is seen at ~1.1 V on the negative sweep, which is also in line with the literature. The oxygen reduction peak seen at a similar potential in the CO free electrolyte does not appear, as the CO atmosphere allows for any removed CO to be swiftly replaced and the reduction is thus masked by the CO oxidation. The more negative potential of the return oxidation peak comes about due to the effect that oxygen has on the CO oxidation. As labelled above, the formation of gold oxide begins at a potential of ~1.55 V. The oxygen adlayer that forms acts as a passivation layer, inactivating the gold towards CO oxidation: as such, no further oxidation of CO can occur until this layer is removed (as observed in Figure 4.12), thus giving the negatively shifted potential of the negative sweep CO oxidation peak.

4.4.2 Current Density Calculation

An issue seen in the electrochemical tests utilising this specific cell sell-up is that a consistent crystal/electrolyte contact area cannot be obtained between samples: as electrolyte contact with the edge of the Au(111) crystal cannot be allowed the full crystal area could not be used. Due to this difficulty in accurately measuring actual contact area, determining the geometric current density for our samples was not viable. Calculating the specific current density utilising the gold oxide formation peaks was considered as an alternative: however, due to the maximum potential being limited to 1.15 V for the majority of experiments, the gold oxide region is not entered for most of our CVs and thus utilising the oxide peaks to calculate the specific current density was not feasible.

As the specific current density is required for a proper comparison of our samples, it was important that a value be determined using the data collected. As the oxide peak was not viable, a substitute was required: such an alternative was found in work by Angerstein-Kozlowska *et al.*[75] involving the peaks seen at ~0.9 V vs RHE, as seen in Figures 4.12 and 4.13 on Au(111) in an $HClO_4$ electrolyte.

These peaks come about from the adsorption of ClO_4^- ions on the gold surface during scanning; Angerstein-Kozlowska *et al.* determined that the charge required for this

adsorption is 6-10 µC cm^{-2}. By using this value in conjunction with the peak areas, the specific area for the gold, and thus the specific current density, for the samples can be calculated. The positive scan ClO_4^- peak was utilised in these calculations as this was the peak utilised by Angerstein-Kozlowska *et al.*

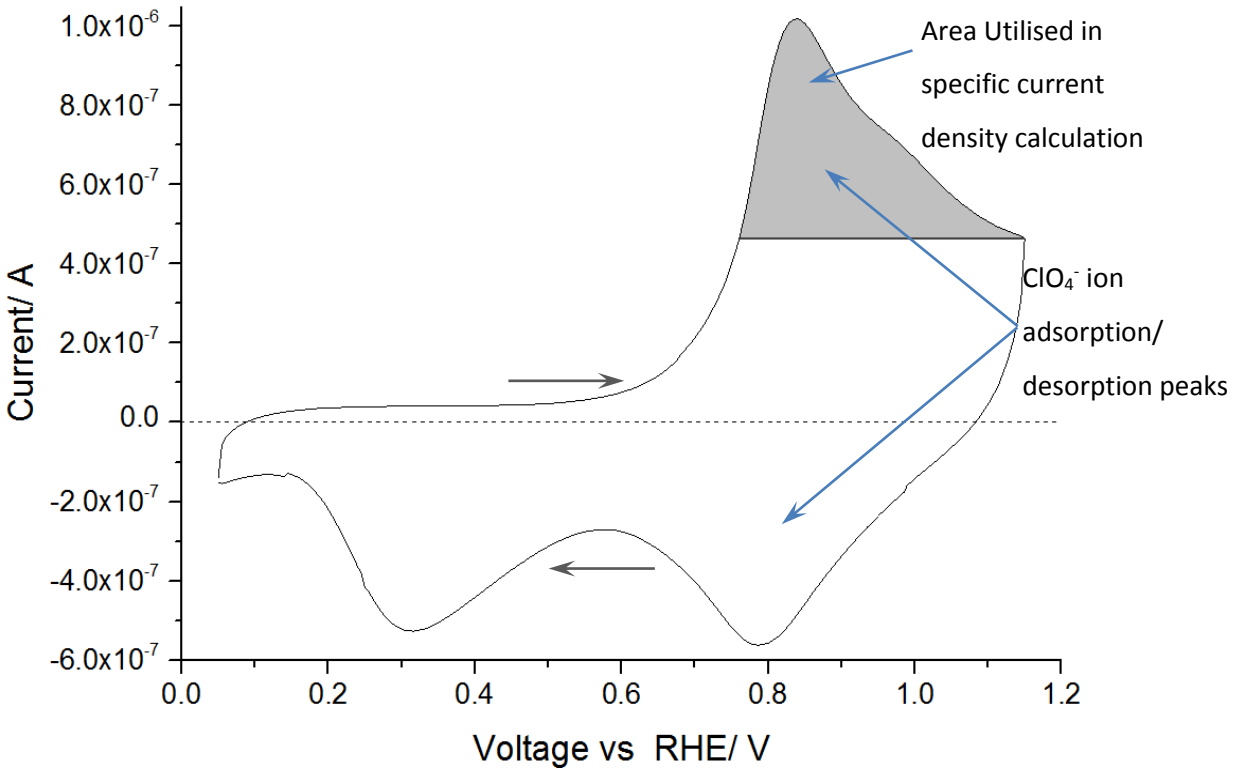

Figure 4.14 CV of clean Au(111) showing ClO_4^- ion peaks alongside an example of the area utilised in surface area calculations. Scan speed = 50 mV s^1, 0.1 M $HClO_4$

To determine whether utilising the perchlorate peak in this manner was accurate, a new scan with the potential limit extended to 1.8 V was performed. With this new limit, the contact area calculated via the reverse scan oxide reduction peak (~390 µC cm^{-2})[79] and compared to the corresponding calculation with the perchlorate peaks. The areas calculated were found to have a roughly 90-95 % level of consistency between them: it was thus decided that utilising the ClO_4^- peaks would be suitable for the contact area calculation in our experiments.

4.4.3 Au(111) Reconstruction during Cycling

For the majority of samples, the maximum potential was limited to 1.15 V vs RHE. There are two reasons for this: the first was an attempt to prevent the removal of particles during electrochemical scanning, which is expounded upon in greater detail during the particle modified surface electrochemical data analysis. The second more relevant reason is potential induced reconstructions of the Au(111) surface during electrochemical scanning.

For Au(111), when the herringbone reconstructed surface (√3*22) is cycled to ~0.85 V vs RHE the surface returns to the standard (1*1) structure[118]. This reconstruction can be seen in the CV by a negative shift in the perchlorate peaks of ~90 mV. This shift was observed in our clean Au scans, indicating removal of the herringbone reconstruction. As the herringbone reconstruction is lifted regardless of CO adsorption onto the surface,[116] this was an unavoidable occurrence for our investigation and as such did not warrant major investigation.

However, what is of more interest is the effect seen when scanning to more positive potentials with CO present. Figure 4.15 shows the first and second consecutive scans for the clean Au(111) with CO saturated electrolyte and a CO atmosphere: the scans are identical up to ~0.75 V, after which differences appear. During the first scan, CO oxidation begins at ~0.9 V, with the negative sweep peak appearing at 1.1 V. During the second scan, the onset of the forward CO oxidation has negatively shifted to ~0.7 V (masked somewhat by the perchlorate adsorption peak), with the negative sweep peak undergoing little modification between the two scans.

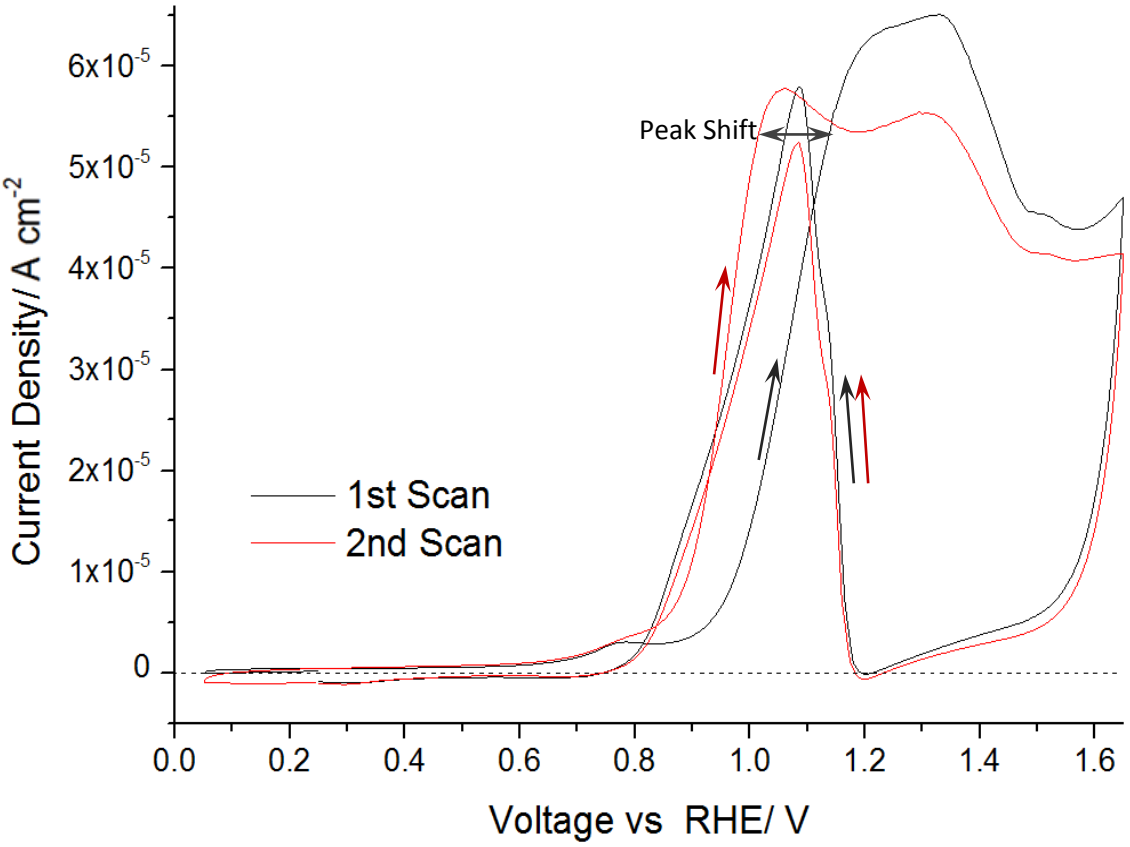

Figure 4.15 Consecutive CV scans of clean Au(111) with CO dissolved in electrolyte and CO atmosphere. Shift in CO oxidation peak onset can be seen. 0.05-1.65 V, scan speed = 50 mV s^1, 0.1 M $HClO_4$.

As this shift was observed on clean Au(111), it was decided that the potential limit required reducing so as to prevent any significant shifts in the CV data, causing changes in the observed CO oxidation data. It was initially thought that this shift might come from a slow poisoning of the surface ensuing from an intermediate of the oxidation process itself,[119] but this was later found to not be the case: Hamelin[120] showed that if a Au(111) surface is subjected to multiple scans which included oxidation and reduction, there is a negative shift in the capacity-potential curve for subsequent scans with the potential limited to more negative values when compared to the same surface where initial cycles had not included the formation of an oxide monolayer. This indicates a persistent change in the (111) surface if positive enough potentials are applied such that the oxide region is entered; this is supported by work from Shue *et al.*[115] where in situ STM imaging of the Au(111) crystal during cyclic voltammetry, where further modification to the (111) surface was seen with more positive potentials, though a full investigation into the surface for potentials above ~1.0 V was not performed.

Another possibility is what is known as "CO-annealing", a process seen for Pt(111) where nanoparticles are cycled up to 1.2-4 V in CO saturated electrolyte as a pre-treatment for the removal of surface irregularities. Arenz *et al*.[121] observed this for platinum nanoparticles, though it should be noted that removal of these irregularities decreased the activity, which is the opposite to what we are seeing here. A similar change was observed for polycrystalline gold by Chen *et al*.[122] where cycling from -0.2 V to 1.4 V in a CO saturated electrolyte smoothed the nanoparticles, increasing the number of terrace like sites, whilst removing step like sites. This fits with the STM imaging of our surface, which is relatively step heavy, thus such an effect might be considered to be causing a rather significant change with the gold surface.

As this possible modification of the surface was considered an issue with regards to removal of our particles, more negative potential limits were set so as to remove any such changes in the crystal morphology. For the first sample synthesised with distinct titania particles (59.8% coverage) the maximum potential limit was reduced to 1.45 V. However, as shown in Figure 4.16, it can be seen that this shift still occurs despite the more negative potential limit, but is more gradual than that seen with the 1.65 V limit.

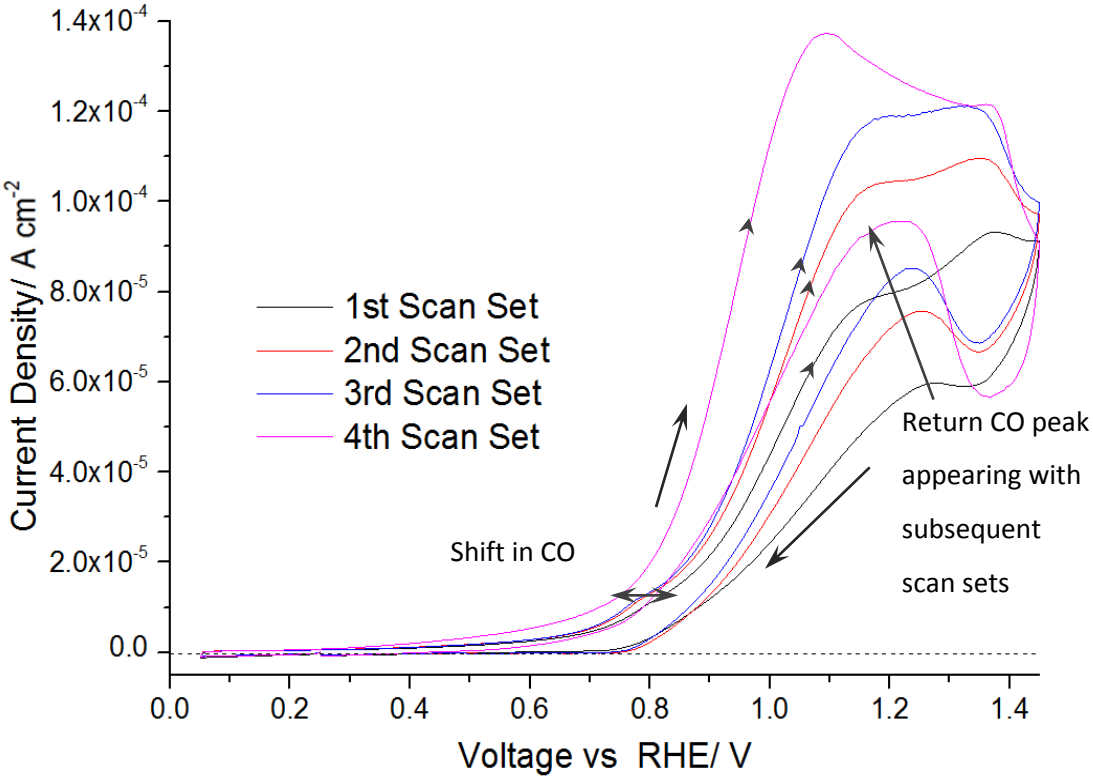

Figure 4.16 CO Oxidation peaks for 59.8% coverage sample. Scans shown are the initial scan for 4 consecutive sets of scans taken in quick succession. 0.05-1.45 V, scan speed = 50 mV s^1 0.1 M $HClO_4$, CO dissolved in electrolyte with CO atmosphere present.

As this shift progresses, more of both CO oxidation peaks become visible, with the forward CO peak beginning to show features seen at a 1.65 V limit, especially once the full CO shift has occurred. What is more notable is the peak that appears at ~1.1 V during the negative sweep: as the CO shift occurs, this peak becomes more apparent and defined.

The maximum potential limit was then increased to 1.65 V on the same sample: the initial forward CO peak had shifted positively towards its original position, though not fully to the initial values, but closer to the shift seen for the third set of scans in Figure 4.16. This indicates that without continuous scanning, the surface modification reverts somewhat. However, once the first 1.65 V scan was recorded, the forward CO peak shifted to the same value seen for the final set of scans measured with the 1.45 V limit, as well as the scans taken on the clean Au(111).

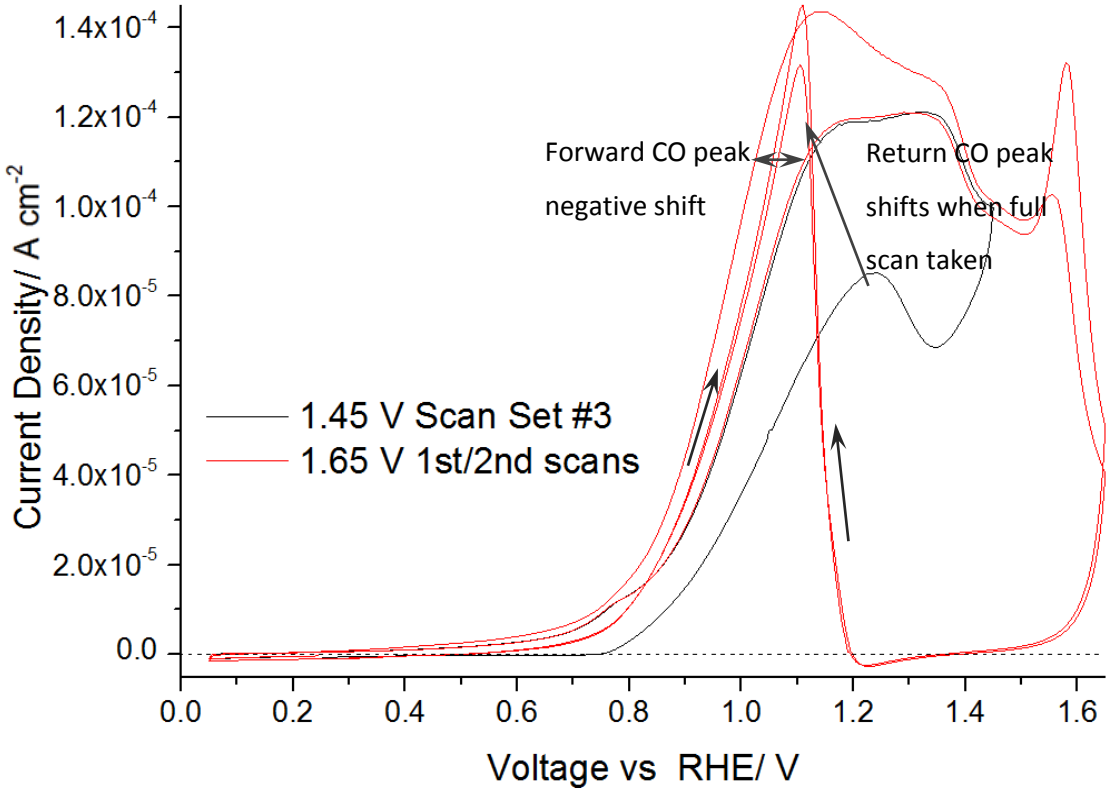

Figure 4.17 CO Oxidation data for 59.8% coverage sample. Comparison of 3rd set of 1.45 V limited scans with 1st and 2nd scans with 1.65 V limit. Scan speed = 50 mV s^{1}, 0.1 M $HClO_4$, CO dissolved in electrolyte with CO atmosphere present.

It appears that the reconstruction giving this shift in the forward CO oxidation peak begins to accumulate only once a certain maximum potential limit is reached. This

larger immediate shift in the CO oxidation when a 1.65 V limit is utilised remains for subsequent scans in CO, even with the potential maximum limited to 1.15 V once more.

What is important to note here is when the potential is limited to 1.15 V from the outset: the beginning of the CO oxidation peak is seen but the resulting negative shift in the onset is not, regardless of the number of scans performed within this limit. As soon as the maximum potential is increased, however, this shift in the CO oxidation is seen once more.

As mentioned, this shift most likely comes about from the reformation/ roughening of the Au(111) surface, possibly towards more polycrystalline forms. Limiting the initial maximum potential acts as a seemingly hard limit for this particular reformation. It is possible that by holding the crystal at these positive potentials we could effectively "activate" the surface for future scans (as described by J-P Suchsland[123] for gold nanoparticle supported on titania); however, this would require holding a rather positive potential for a significant period of time, thus giving serious risk to the particle system being damaged. As such, it was decided that all future samples would have their maximum potential limited to 1.15 V to prevent this possibility, as well as allowing for comparison of activity for CO oxidation between the titania modified gold samples and the clean gold to be performed with a minimal degree of modification between sample scans, giving a more complete indication of the effect of the titania particles on activity.

4.4.4 Titania modified Au(111) electrochemistry

The CVs seen for the oxidation of CO on clean Au(111) show very distinctive features, the most notable being the peak that begins at ~0.9 V on the forward scan. This feature was used as the focal point for all experiments. Unfortunately, due to issues with the electrochemical cell reference electrode (that were subsequently resolved) the high coverage sample seen in Figure 4.4 did not receive proper electrochemical testing and as such there is no useful data for comparison with subsequent samples.

Prior to investigation into the CO oxidation, the CVs for the electrolyte without CO must be considered: Figure 4.18 shows the first forward scans for all samples, with both the specific and geometric current densities considered.

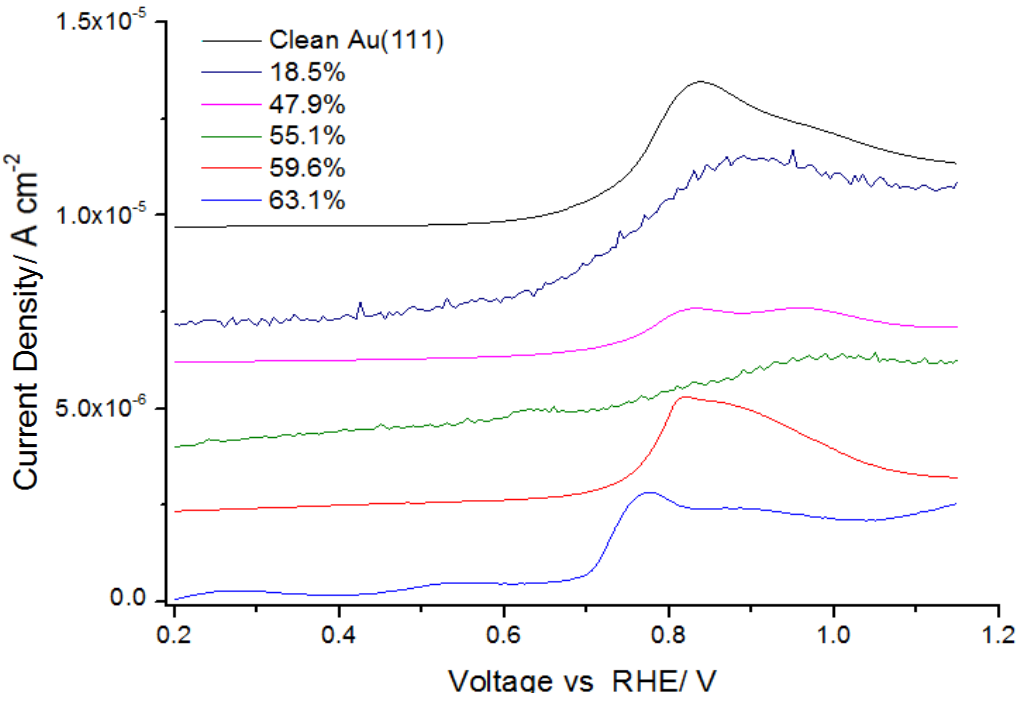

Figure 4.18 1st forward scans for titania modified Au(111) samples. Percentage refers to coverage of surface by Titania. 0-1.15 V, scan speed = 50 mV s^1, electrolyte = 0.1 M $HClO_4$

The expected perchlorate adsorption peak appears; some slight variation is present across the samples, with no particular pattern discernible. A secondary peak appears in the 47.9 % coverage sample, reappearing as a slight shoulder in the 59.6 %, 63.1 % and clean Au samples. The identity of this peak is unknown, though possibly some form of contamination present from the electrolyte: as these secondary peaks did not interfere with the subsequent CO oxidation scans their presence was not deemed of concern. As the effect of titania on the perchlorate adsorption peaks appears minimal, we will not concern ourselves further.

A point that must be considered when observing the areas calculated via the perchlorate adsorption peaks, is whether the calculated values match with the expected areas for contact between the electrolyte and the crystal surface. Unfortunately, these contact areas were never directly measured for the majority of our samples, as it was felt that with the large degree of uncertainty in determining contact area from visual means, as well the changes in contact area over time as evaporation of the electrolyte occurred, that the calculations with the perchlorate ions was the most reliable method available to us. However, a very rough estimate can be made for the contact area from inspection of the residue left on other samples that utilised the same electrochemical cell and were not

reused for other purposes. This gives a contact of sizes centring ~0.4-0.6 cm across, with a rather larger margin for error due to age of the residue rings, as well as the slight inaccuracy in the measurements.

As such, we must compare these values to those calculated via the perchlorate adsorption peak to determine how reliable our calculations are likely to be. Table 4.3 shows the values calculated for the electrolyte contact areas, alongside the corresponding areas when the titania coverage is taken into account.

Table 4.3 Electrolyte contact area calculations with coverage modified values

Titania Coverage/ %	Perchlorate Calculated Contact Area/ cm^2	Coverage modified Contact Area/ cm^2
63.1±3.16	0.115	0.311
59.8±2.99	0.122	0.302
55.1±2.76	0.199	0.443
47.9±2.40	0.175	0.336
18.5±0.91	0.125	0.153
0	0.262	0.262

In general, the calculated contact areas are within the expected values, which should range from ~0.1 to 0.3 cm^2, with only the 55.1% coverage sample falling significantly outside of these limits. This is quite possibly accurate, as the contact areas did fluctuate greatly between samples, which the measured residues may not have shown completely. However, this consistency does allow for a reasonable degree of confidence in the calculated contact areas, even if it is not the most ideal method.

As mentioned, there were two motivations behind reducing the maximum potential limit from 1.65 V to 1.15 V during our cyclic voltammetry experiments. The first was the permanent shift in the onset for CO oxidation seen when the Au(111) was taken up to 1.65 V. The second reason was the concern that particles were being stripped from the surface during electrochemical scanning.

The first sample where definable titania particles were observed (59.6% coverage) reached a maximum potential limit of 1.75 V during electrochemical experiments. Once these experiments had been performed, it was returned to the STM system for post-electrochemical imaging. Imaging of the sample surface proved to be difficult, with the images either very indistinct or so noisy as to not be useful: Figure 4.19 shows an example of one of the more viable images.

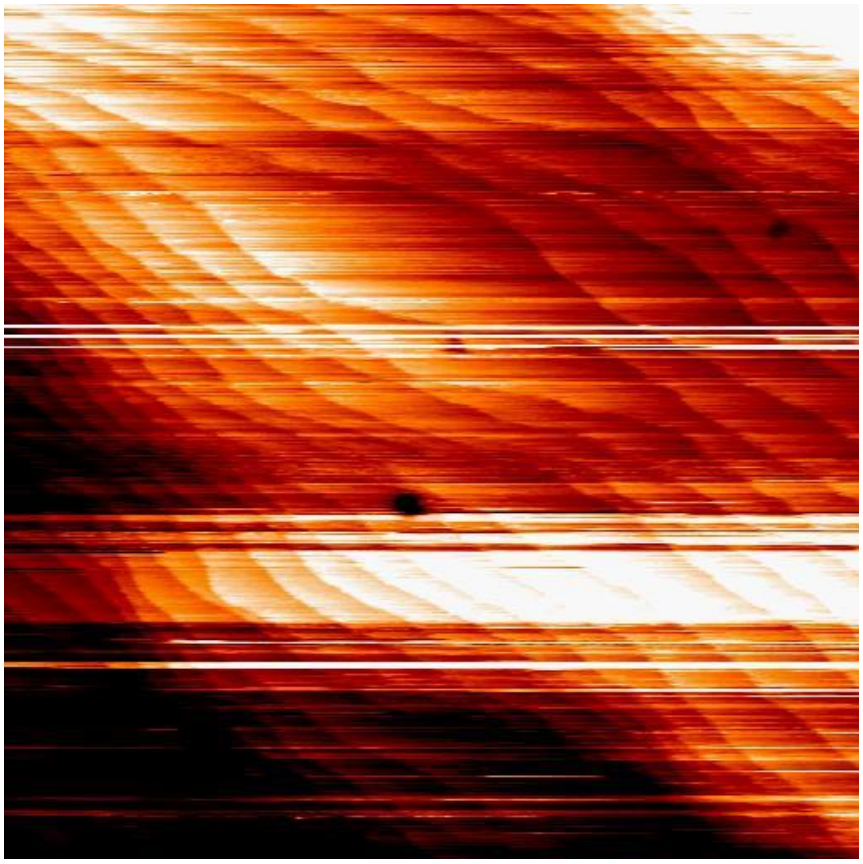

Figure 4.19 post electrochemical testing of 59.6% coverage sample. Maximum potential applied to this surface: 1.75 V vs RHE. 320*320 nm, Gap Voltage = 0.8 V, Feedback set = 0.5 nA, Loop Gain = 5.0 %

Despite the noise of this image, it can be seen that the surface appears to have been cleared of any titania particles, though a great number of steps are present, with a rough increase of 5-10 times the number of steps appearing post electrochemistry. This is possibly due to shifts in the surface during electrochemical scanning. Other than the removal of particles, there do not appear to be any additional effects on the surface, though the herringbone reconstruction was never viewed in post-scan images. Because of this apparent removal of the titania, coupled with the observed shifting of the CO

oxidation peak at more positive potentials, it was decided that future experiments should be limited to 1.15 V so as to prevent this removal from occurring.

When the subsequent sample (63.1% titania coverage) was electrochemically tested, it was found that this removal of the particles was still occurring despite the lowered maximum potential limit. Figure 4.20 shows a representative of the surface post electrochemical screening; the imaging was considerably higher quality than previously, with a much reduced quantity of noise seen.

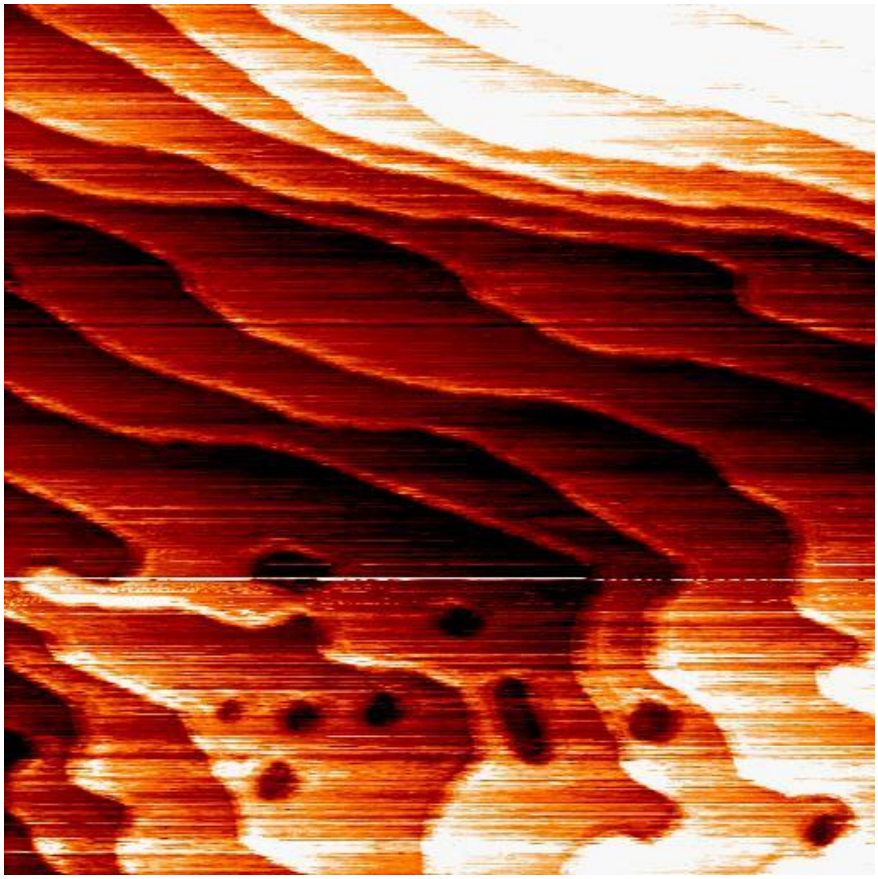

Figure 4.20 Image of 63.1% coverage sample post electrochemical screening. Maximum potential limit used: 1.15 V vs RHE. 194*194 nm, Gap Voltage = 0.8 V, Feedback set = 0.5 nA, Loop Gain = 5.0 %

The images once more show a reasonable step density, though less severe than the previous, with no titania particles visible on the surface. Figure 4.21 shows the initial three scans taken for the 63.1% sample with no CO present.

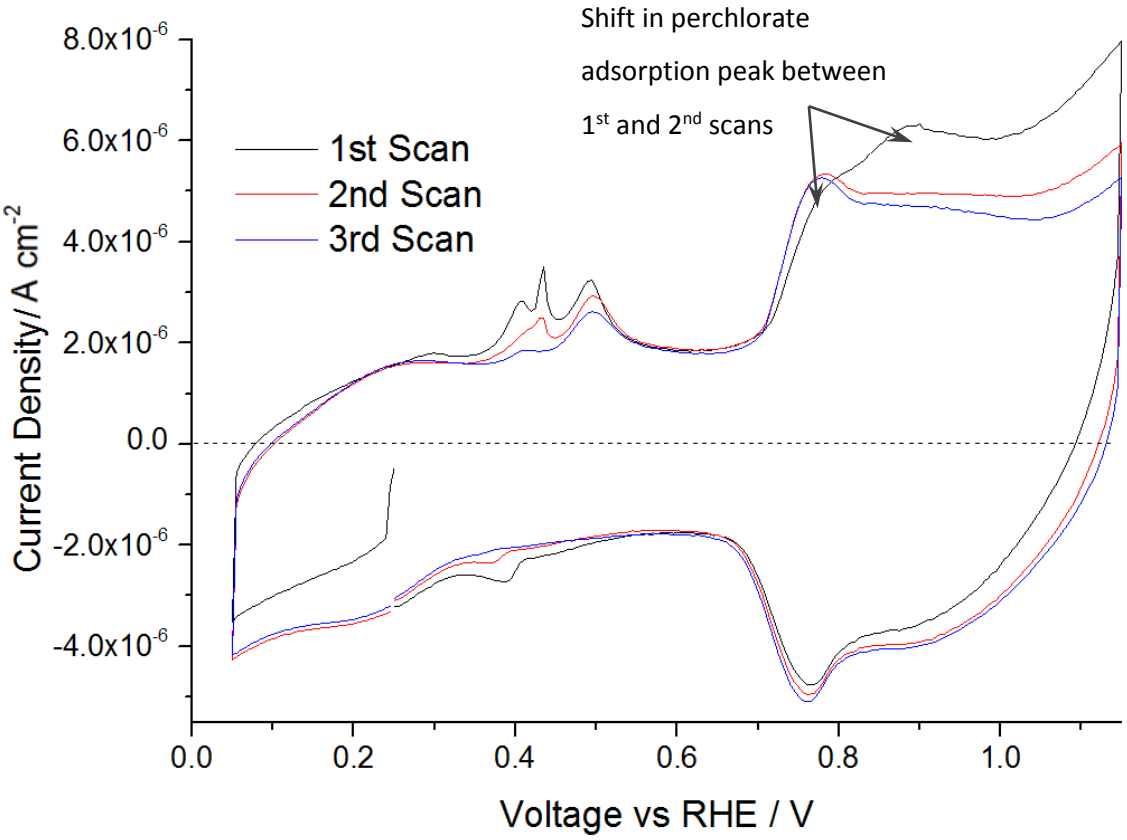

Figure 4.21 Initial electrochemical scans taken of 63.1 % coverage sample. Labels refer to scan order. Potential limits 0.05-1.15 V vs RHE, Scan speed = 50 mV s^{1}, electrolyte = 0.1 M $HClO_4$

There is a shift in the perchlorate adsorption peak, though a similar process occurs on the clean Au(111) from reordering of the surface, so is not of concern. The only possible area that could be construed as concerning are the peaks that appear at ~0.4-0.5 V, which are being removed as the scans progress, with subsequent scans recorded for the sample being completely free of these peaks. As these peaks are most likely caused by a small degree of contamination, either from the sample or the electrolyte, these peaks are most likely not the cause of particle removal.

All subsequent scans, whether with or without CO present, gave consistent CV scans across multiple cycles, and as such the reason for this apparent loss of particles was not determined, especially as the electrochemical data do not indicate any significant reduction in TiO_2 coverage during our experiments.

4.4.5 Titania modified Au(111) CO Electrochemistry

We will first consider the 1.15 V limited clean Au(111) CO oxidation, as shown below in Figure 4.22. By having limited the maximum potential, only the beginning of the CO oxidation peak is present, but as the oxide region is not entered, no interference occurs with the CO oxidation and a continuous series of peaks can be seen.

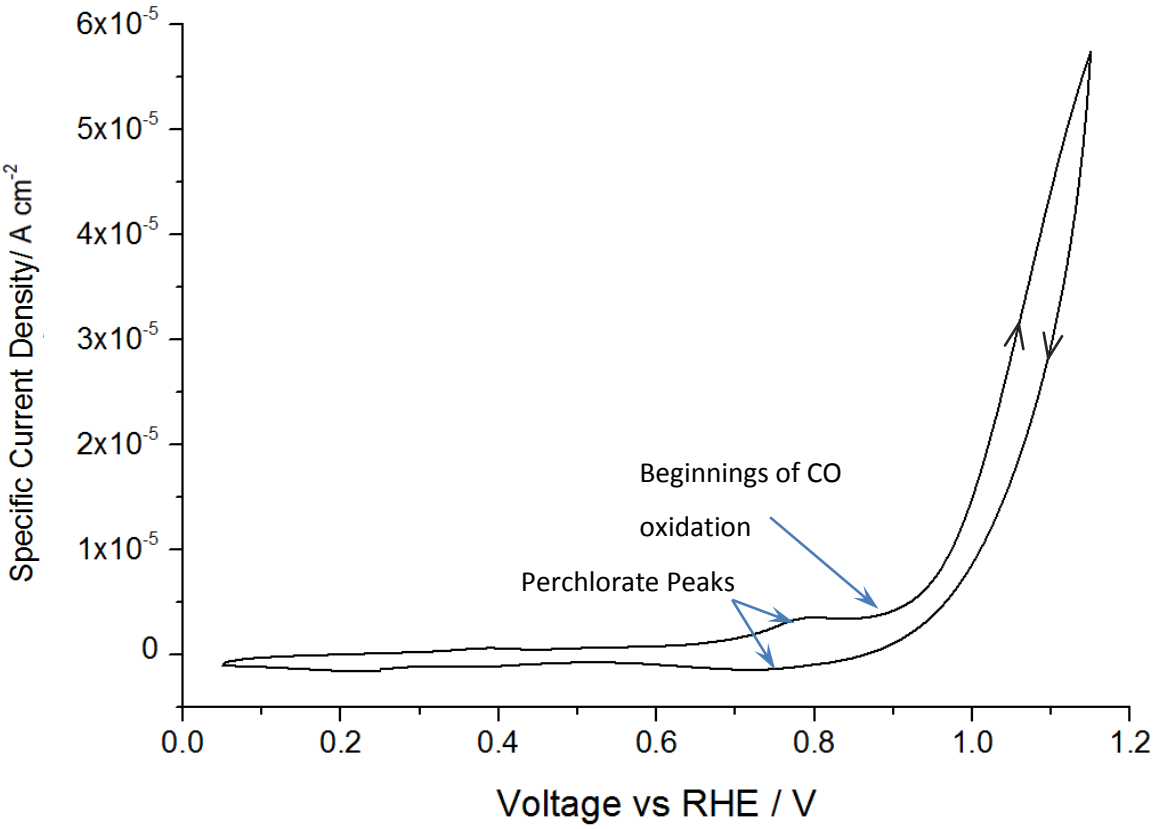

Figure 4.22 Clean Au(111) CV with CO dissolved in electrolyte and CO atmosphere. Potential limited to 1.15 V. Scan speed = 50 mV s^{-1} 0.1 M $HClO_4$

With the baseline having been determined, investigation of the titania modified crystal CO oxidation behaviour could proceed. Significant differences were immediately apparent in the electrochemical behaviour between the clean Au(111) crystal and the titania modified samples, most notably the CO oxidation onset shifting to more negative values. An example of this shift for a sample with 55.1% coverage sample can be seen in Figure 4.23.

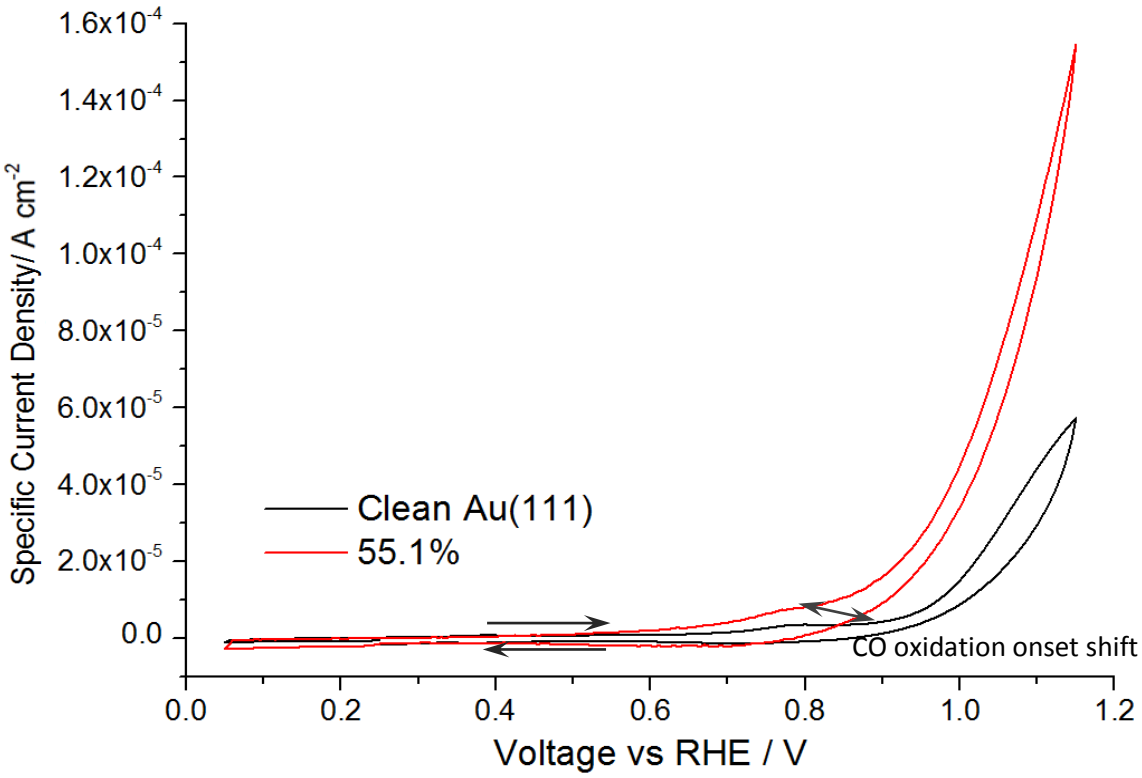

Figure 4.23 CV of clean Au(111) and 55.1% TiO_2 particle coverage with dissolved CO. CO oxidation onset shifted with titania addition to surface. Scan speed = 50 mV s^{-1} 0.1 M $HClO_4$

A clear shift of ~0.1 V is present in the onset of the CO oxidation between the clean Au and the 55.1% titania coverage sample, which is further modified by varying coverage level as seen below in Figure 4.24. Due to the number of samples synthesised in this project, for the purposes of ease of viewing all following CVs of titania modified Au(111) samples will only show the 1st forward scan, so scans can be more easily distinguished from one another.

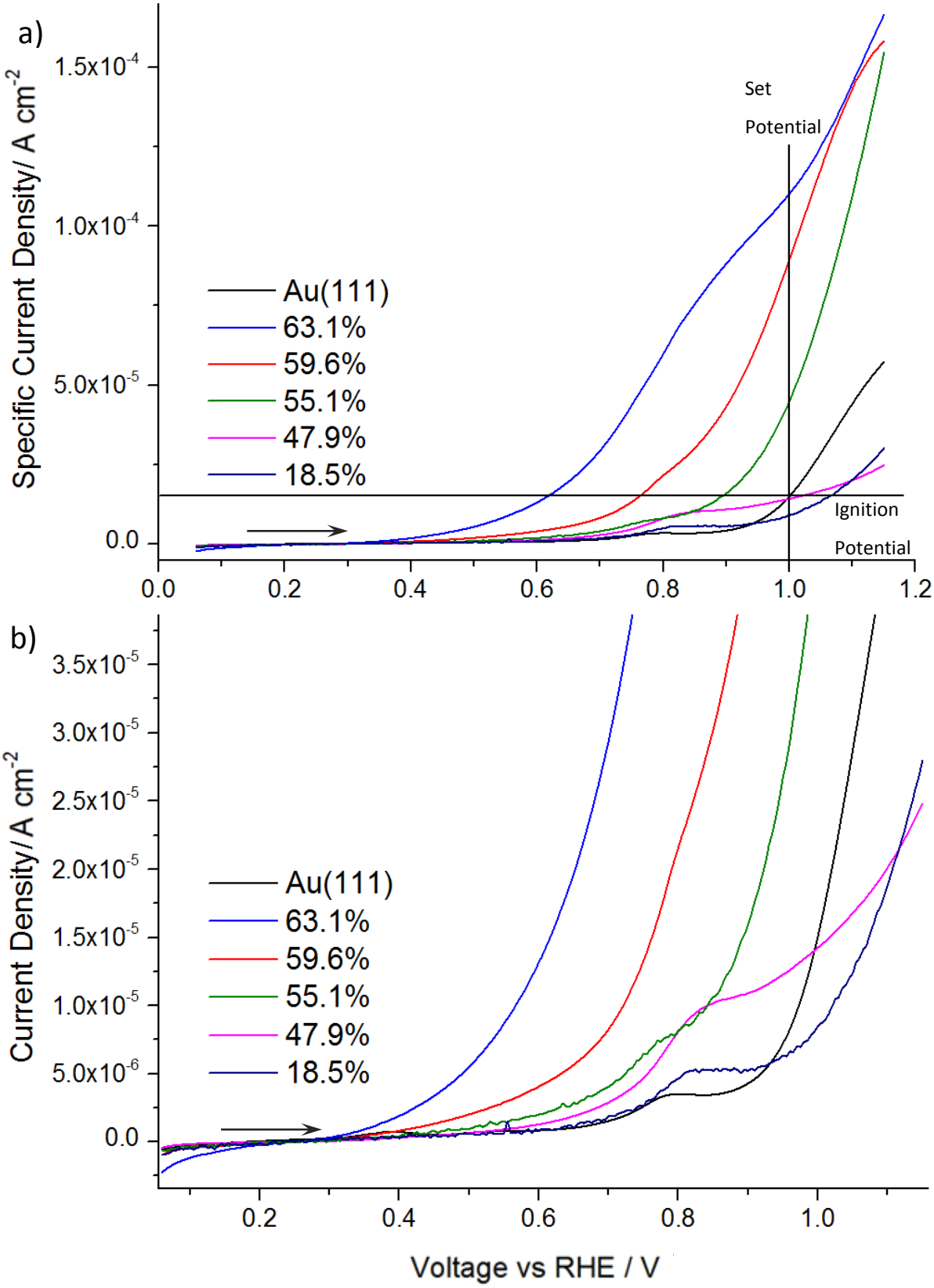

Figure 4.24 1st Forward scan of CO oxidation for all synthesised samples and clean Au(111) for specific current density with ignition potential and set potential indicated. a) Full scale scans, b) Magnification of a). Percentage refers to Titania surface coverage. 0-1.15 V, Scan speed = 50 mV s^{-1}, electrolyte = 0.1 M $HClO_4$

The addition of TiO_2 particles to the Au(111) surface has had a distinctive effect on the CO electro-oxidation: at 18% coverage, the oxidation is slightly inhibited by the titania, whilst the perchlorate adsorption peak remains unchanged. Increasing the titania coverage further to 48% gives a slight increase in oxidation activity, with a concomitant obscuring of the perchlorate adsorption. Once coverages above 50% are reached, the CO oxidation is increasingly promoted, as evidenced by the increasingly more negative potential at which the oxidation is observed (Figure 4.24), indicating lowering of the over-potential for CO electro-oxidation. This effect is demonstrated in Figures 4.25 and 4.26, where the ignition potential, defined here as the potential at which the CO oxidation current density reaches $1.5*10^{-5}$ A cm^{-2}, is shown as a function of surface coverage and the inter-particle distances, respectively. At this constant low current, the observed decrease in ignition potential is believed to be dominated by changes in the surface kinetics of the oxidation reaction.

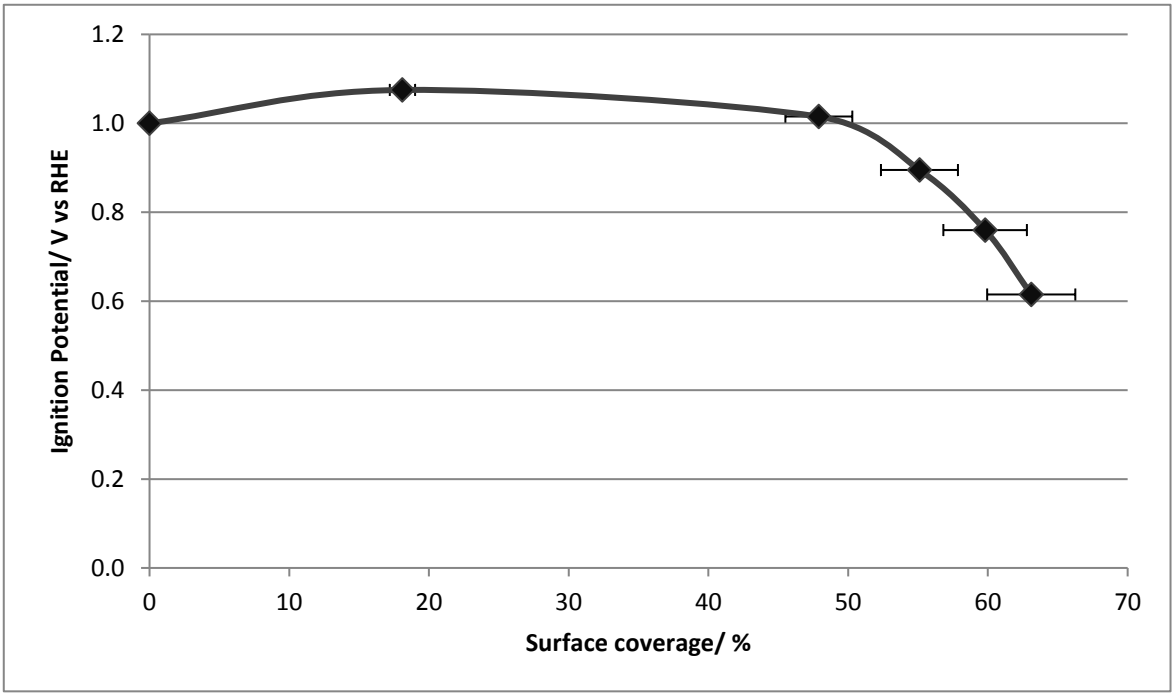

Figure 4.25 Ignition potential vs surface coverage. Voltage refers to value required to give $1.5*10^{-5}$ A cm^{-2} current density.

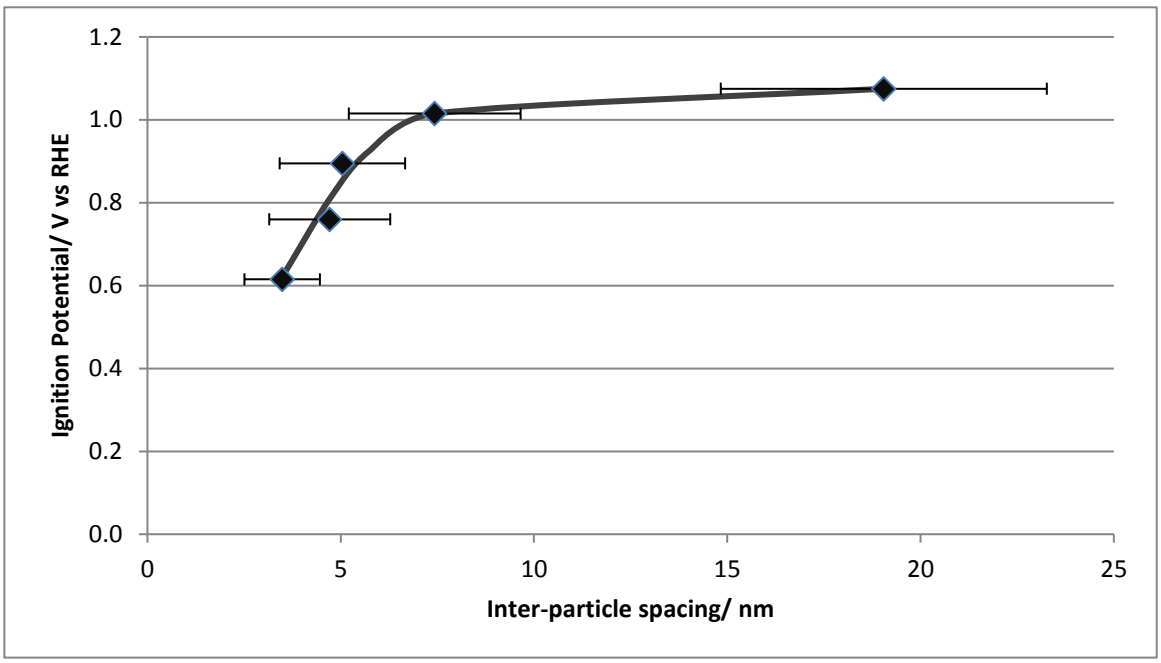

Figure 4.26 Ignition potential vs inter-particle distance. Voltage refers to value required to give for $1.5*10^{-5}$ A cm^{-2} current density.

The inhibition of CO oxidation relative to the clean Au(111) for 18% coverage is somewhat unexpected: this implies that at low coverages, the titania is interfering with the CO oxidation despite the benefits provided by the particles, as observed with the higher coverage samples. The first consideration we must make is for differences between the 18% coverage sample and the higher coverage samples: this brings us back to the STM images of these surfaces (Figure 4.9) where it was determined that for low coverage samples, a distinct preference was seen for particles to form along step edges, with only higher coverage samples showing any significant formation of particles on terraces, whilst retaining the step edge coverage. This would indicate a possible relationship between the Au(111) edge sites and the CO oxidation: this is supported by previous works where it has been shown that CO molecules on Au(111) have a preference for adsorption at step sites (usually in the form of Au(211)) over terraces, both in a vacuum[124,125] and when held at 0.1 V in 0.1 M $HClO_4$[115] (as for our samples).

This relationship is supported by Wang et al.[126] (2016), where it was shown that, in vacuum, on Au(111) CO bonds preferentially to herringbone elbow and step edge sites, with the movement of CO performed by mobile Au-CO complexes rather than diffusion; CO extracts Au atoms, followed by surface reconstruction transporting the complex. Despite being described for a vacuum system rather than the electrochemical setting

used for our experiments, confirmation provided by Shue *et al.*[115] for preferential binding at edge sites during electrochemical scanning allows us to consider that a similar procedure is present, or at the very least that this edge CO is more reactive than terrace bound atoms. From this, we can deduce the reason behind the observed decrease in activity for low coverage samples: as initial formation of TiO_2 occurs predominantly at edge step sites, this precludes the formation of the more active CO found at these locations, thus introducing an initial disruption to the activity for CO oxidation.

It would be thought that as no herringbone reconstruction was observed for our surfaces post titania formation (Biener *et al.*[72] observed herringbone remain for their samples, but this may be accounted for from the lack of an alloy step during their synthesis), even at 18.1% coverage where terraces were most distinguishable, that CO would be reasonably evenly distributed along the remaining terraces, thus providing available CO for the improved activity provided by the particles to act upon and thus would limit this deactivation provided by the blocking of edge sites. However, there are two considerations that need to be made: firstly, as the particles are concentrated along edge sites, whether interface sites or spill-over is responsible for the improved CO activity, part of this improvement would be disrupted by being present on edge sites between terraces, thus possibly limiting the improvement possible to CO oxidation.

The second, and more detrimental, is the consideration of the condition of the surface during electrochemical scanning: it is known that as a potential is applied to Au(111), the surface reforms numerous times during scanning[115], the most notable of which is the formation of the herringbone reconstruction when a potential of 0.1 V_{RHE} is applied. As our samples were subjected to electrochemical scanning in CO free electrolyte prior to the application of CO, and experiments concluded at this potential, we can assume that the herringbone reconstruction was present for our tests of the CO oxidation. As such, CO, with its preferential binding to the herringbone elbow sites, will be less evenly distributed across the terraces, adding additional limits to the beneficial effects from the presence of titania on the surface. We can thus conclude that the reduction in activity observed for the CO oxidation despite the presence of activating TiO_2 comes from the reduction in the most reactive form of CO present in the Au(111) system, found at gold edge sites, which is not compensated by the activation effects provided by the TiO_2, thus disrupting the oxidation of CO at low titania coverages.

As titania coverage increases, however, particles form in greater levels on terrace sites, and as such the improved reactivity provided by the titania becomes more prevalent, with either titania-gold interface sites or spill-over more able to interact with CO on the surface, though in the case for the spill-over method, whether OH or CO is being transported is unknown. The activity, however, only increases past that seen for the clean Au(111) at coverages higher than 50 %, which indicates that the improvement to activity is relatively minor compared to the loss in activity from disruption of the CO. However, above 50 % the activity begins to increase at an accelerated rate, with a significant negative shift in the observed Ignition potential. It would be expected that as the coverage increases further the Ignition potential will reach a plateau, with further addition of titania not significantly effecting the onset of CO oxidation.

A similar demonstration of this promotion of the CO oxidation by the TiO_2 particles at coverages greater than 50% can be obtained by plotting the current density in the cyclic voltammetry at a fixed potential, as shown by Figures 4.27 and 4.28. In these plots, the CO oxidation current has been extracted from the CV at 1.0 V_{RHE}: this potential was chosen to minimize the influence of the perchlorate ion adsorption peak whilst still allowing for comparison of the current densities on the TiO_2 modified surfaces with the clean Au(111) surface, with an increase in CO oxidation activity once more indicated with TiO_2 coverages above 50 %, with a similar deactivation present for lower coverages. There are limitations with utilising this approach for indicating relative activity, however; notably, as the current density increases, the increasing contribution of mass transport will lead to underestimation in changes in the surface kinetics.

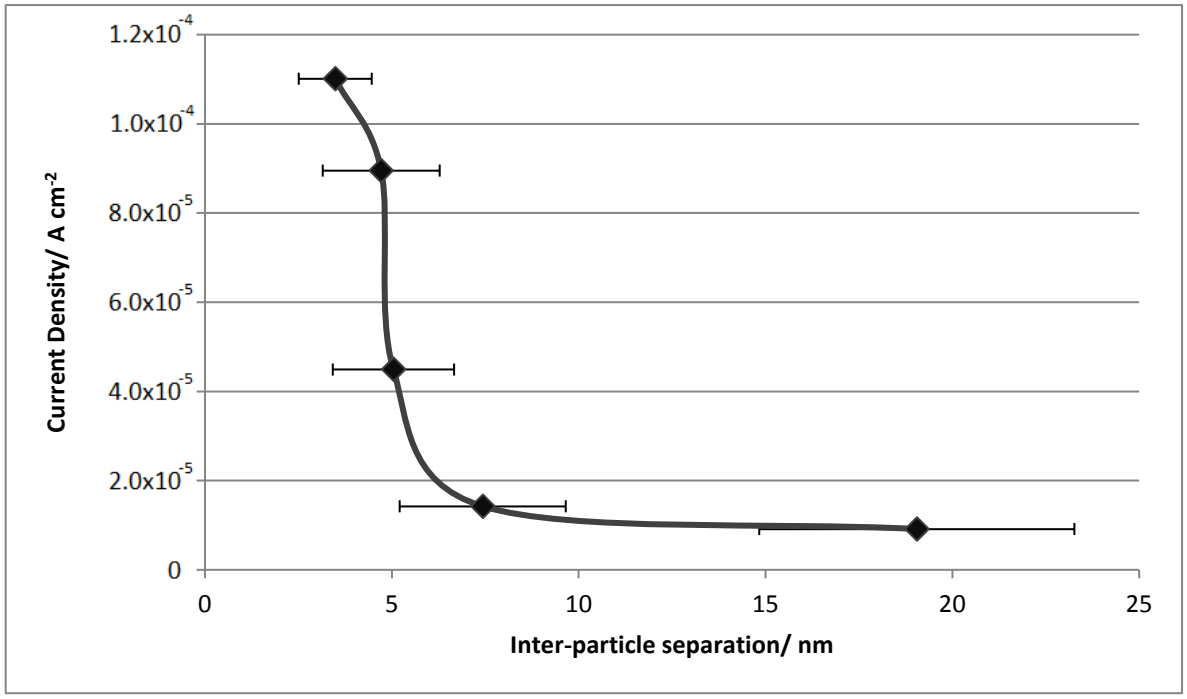

Figure 4.27 Inter-particle spacing vs current density.

Current density values taken at potential of 1.0 V_{RHE}.

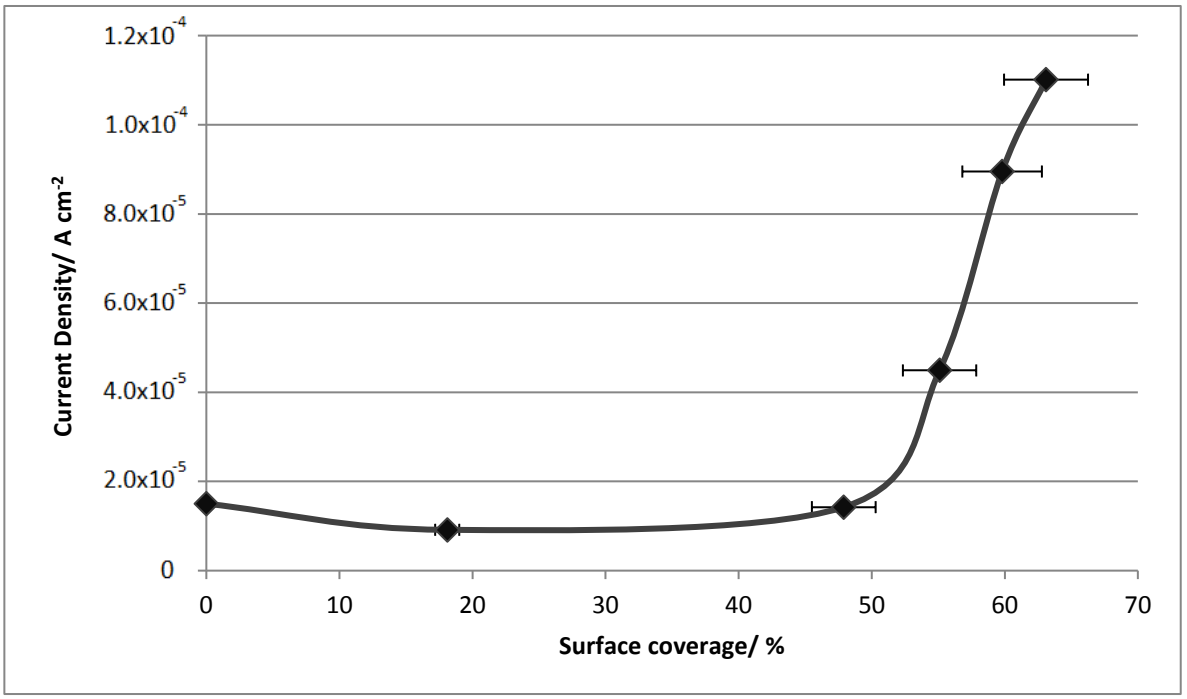

Figure 4.28 Surface coverage vs current density. Current density values taken at potential of 1.0 V_{RHE}.

The origin of this increased activity for the TiO_2 modified Au surfaces, a reaction which takes place at the gold, cannot be explained by an electronic effect. It is unlikely that TiO_2 particles will be able to modify the density of states of the bulk single crystal surface, or not nearly to the same extent as seen for gold nanoparticles in the non-inverse system, and as such cannot be considered by us here. This leaves two possible explanations for the observed increase in activity: local reactive sites at the periphery of the TiO_2 particles are more active towards the CO oxidation or, alternatively, the CO oxidation on the Au(111) surface is promoted by oxygen/hydroxide spill-over from the TiO_2.

Unfortunately, from the above data we are unable to determine which of these methods is more prominent: in an attempt to do so, we shall consider the cyclic voltammetry data where the total contact area is considered rather than solely the active gold. Using the titania coverages determined from STM imaging of the modified gold surfaces, the contact areas can be modified to give the effective “total” contact area for each set of experiments, the values of which are described in Table 4.3 as the coverage modified surface areas. It should be noted that despite referring to these values as the geometric areas, using these “total” contact areas cannot give the “geometric” current density as it is generally thought of: the initially calculated specific contact areas account for surface roughness, which remains in the subsequently calculated “total” contact areas, resulting in the geometric current densities used by us here should be considered a modified version of the classical geometric current density.

The cyclic voltammetry data using these geometric areas can be seen in Figure 4.29; despite the change to the geometric areas, CO oxidation activity has remained consistent with that seen for the specific current density values. The comparison of the ignition potentials for the specific and geometric area CV data is shown in Figures 4.30 and 4.31. It can be seen that the greatest difference lies at lower titania coverages, with the specific area data at this level of coverage indicating a greater decrease in activity. At higher coverages, the ignition potentials are much closer in value, with a slightly steeper decline seen for the specific data. This indicates that at higher coverages, the effect of titania on the CO oxidation onset does not differentiate significantly between the specific gold and the total contact area activity, suggesting that there is a limit for improving the onset that bridges the two.

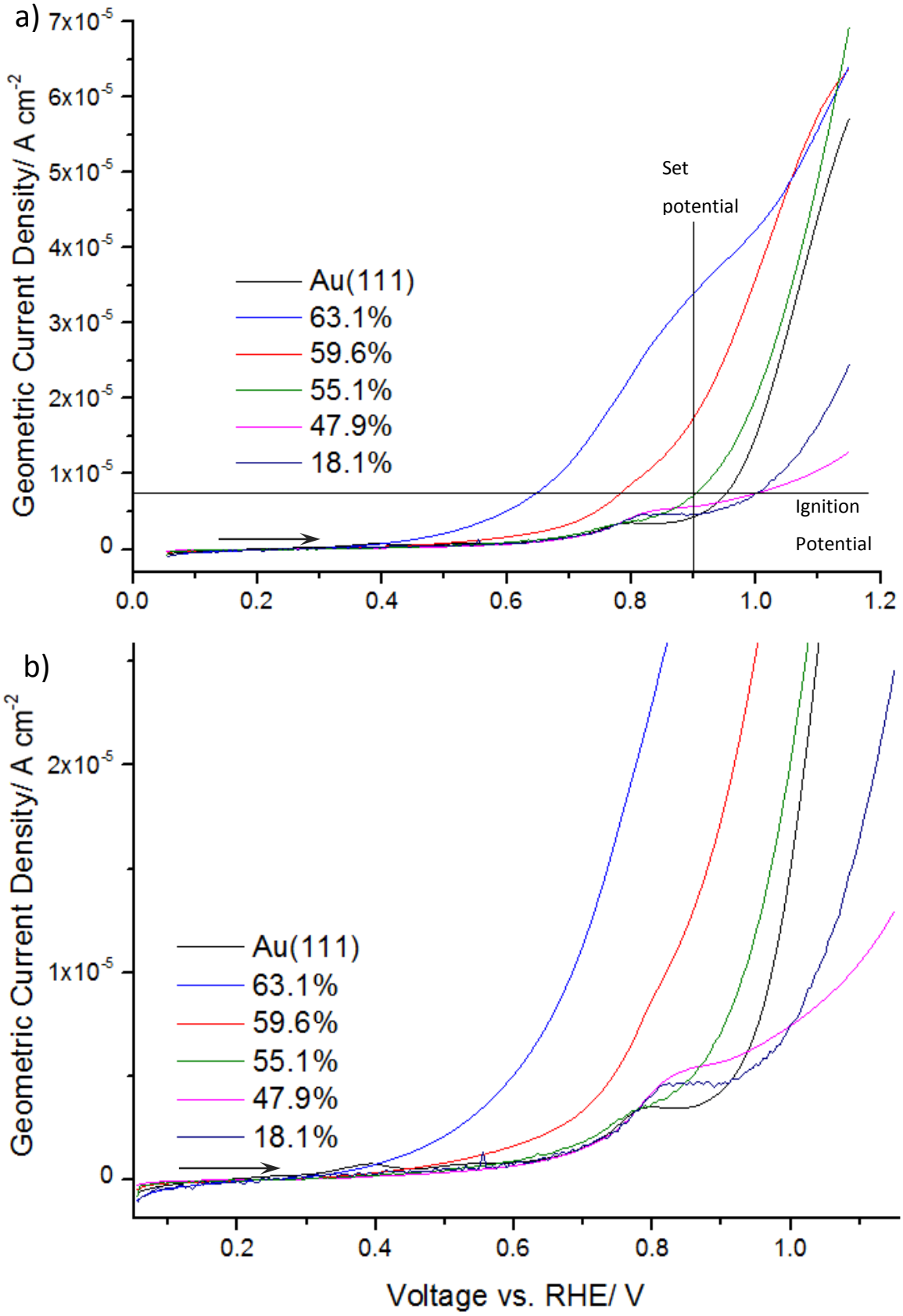

Figure 4.29 1st Forward scan of CO oxidation for all synthesised samples and clean Au(111) for geometric current density, with ignition potential and set potential indicated. a) Full scale scans, b) Magnification of a). Percentage refers to Titania surface coverage. 0-1.15 V, Scan speed = 50 mV s^{-1}, electrolyte = 0.1 M $HClO_4$

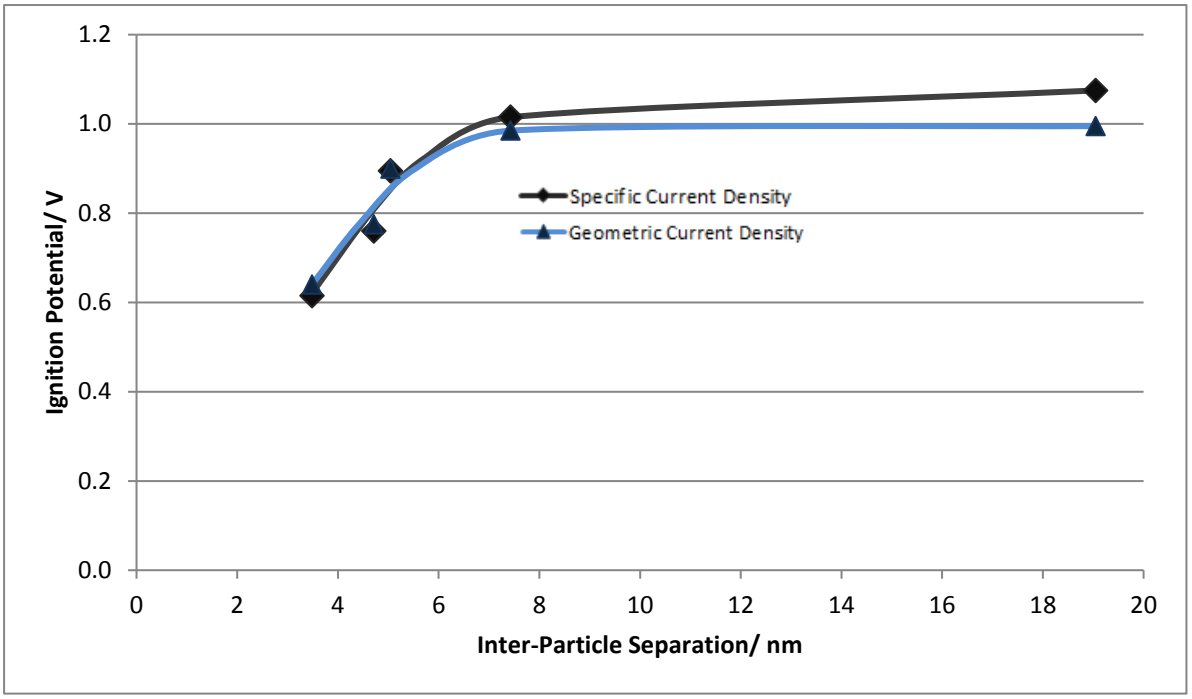

Figure 4.30 Ignition Potential vs Inter-particle separation: comparison of specific and geometric areas. Current density for ignition potential: specific = $1.5*10^{-5}$ A cm^{-2} and geometric = $7.5*10^{-6}$ A cm^{-2}.

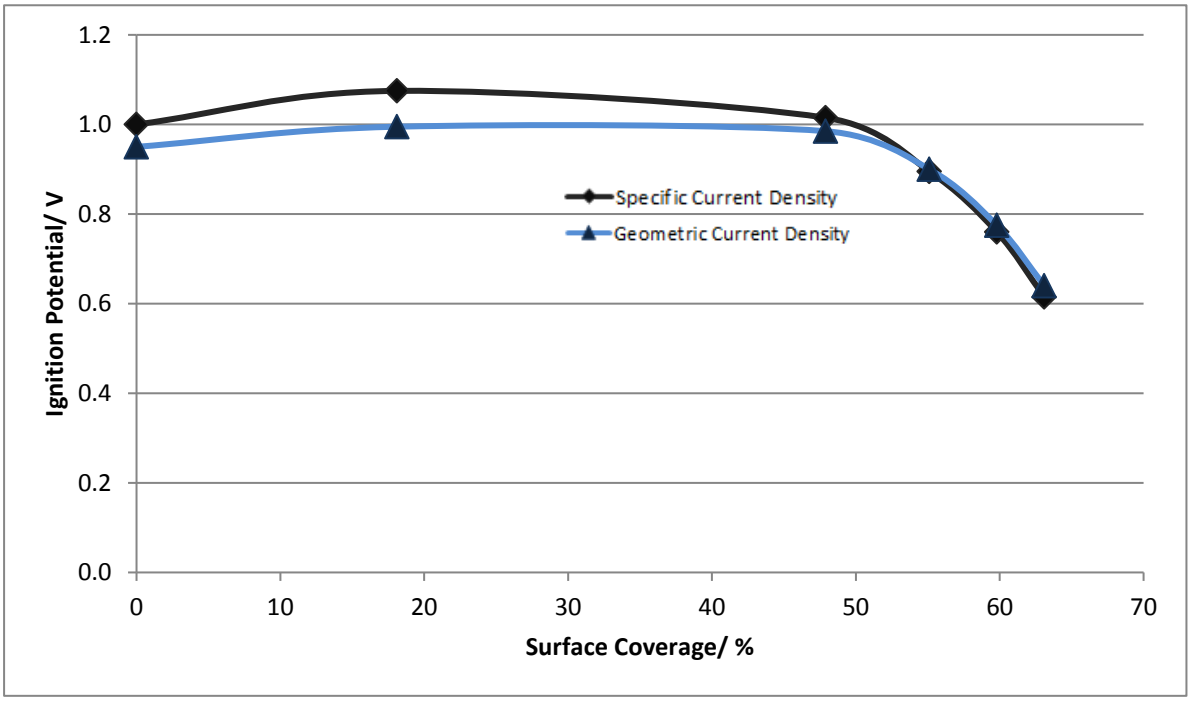

Figure 4.31 Ignition potential vs surface coverage: comparison of specific and geometric areas. Current density for ignition potential: specific = $1.5*10^{-5}$ A cm^{-2} and geometric = $7.5*10^{-6}$ A cm^{-2}.

This change at lower titania coverages between the specific and geometric area data provides some support to the consideration of the removal of active CO at gold edge sites being responsible for the initial lack of activity increase with the addition of titania to the gold surface. A significant separation is seen between the ignition potential values moving from clean Au to coverages below 50 %: as coverage exceeds this, the ignition potential for both the geometric and specific data begin to give almost identical values for both.

This provides an interesting comparison with the corresponding data when we consider the current density values seen at a set potential value. Figures 4.32 and 4.33 show the comparison of the specific and geometric current density given with a set potential of 1.0 V_{RHE}. The samples of low Titania coverage indicate a very slight change between the specific and geometric value, which is once again not unexpected, due to the minimal change in areas between the two. However, at higher coverages, it can be seen that for specific area the activity gradient is steeper than that of the geometric data. This difference is more distinct than that seen for the ignition potential, but is not unexpected: the improvement to the onset of the CO oxidation should exhibit a trend towards the same values regardless of whether active gold or total area is used, whilst at a set potential, the activity should continue to increase for the specific area, where only the area of active gold is being considered, contrasted with the geometric data where, despite the increased activity of the gold resulting from higher titania coverages, the relative current density values will decrease as the relative active gold to total area decreases more swiftly than the improved activity provided from deposited titania, though for both, the limitation brought about by the increasing contribution of mass transport leading to underestimation in changes in the surface kinetics remains.

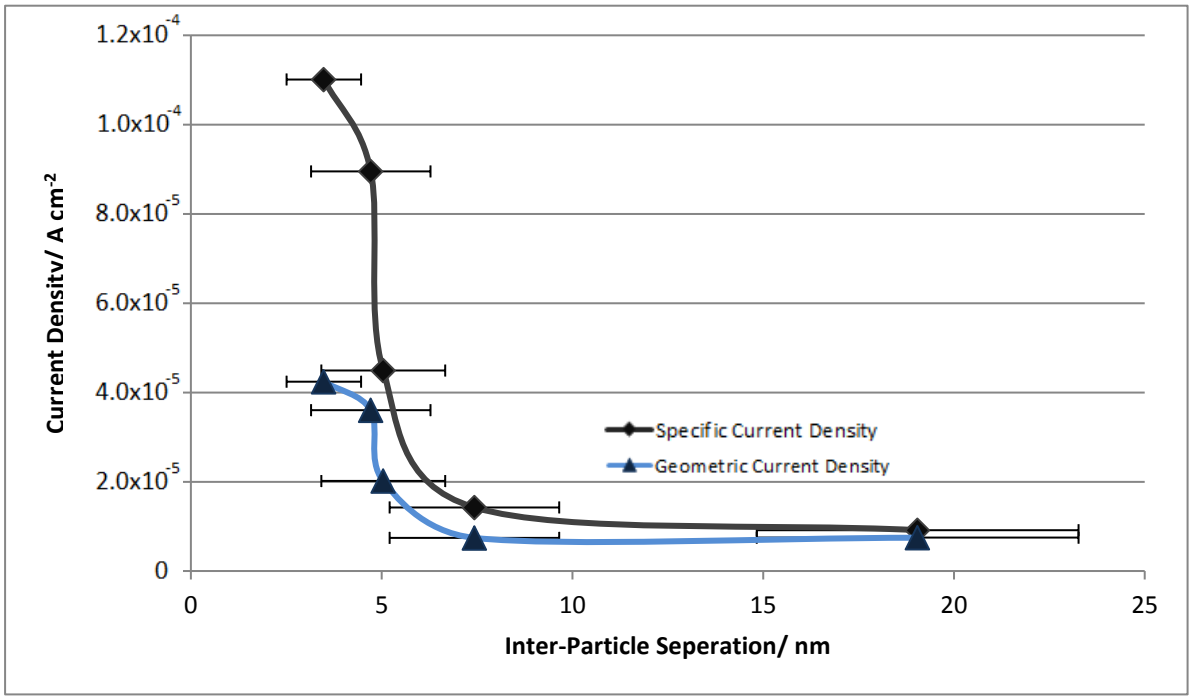

Figure 4.32 Inter-particle spacing vs. current density: comparison of specific and geometric current density values. Current density values taken at potential of 1.0 V_{RHE}.

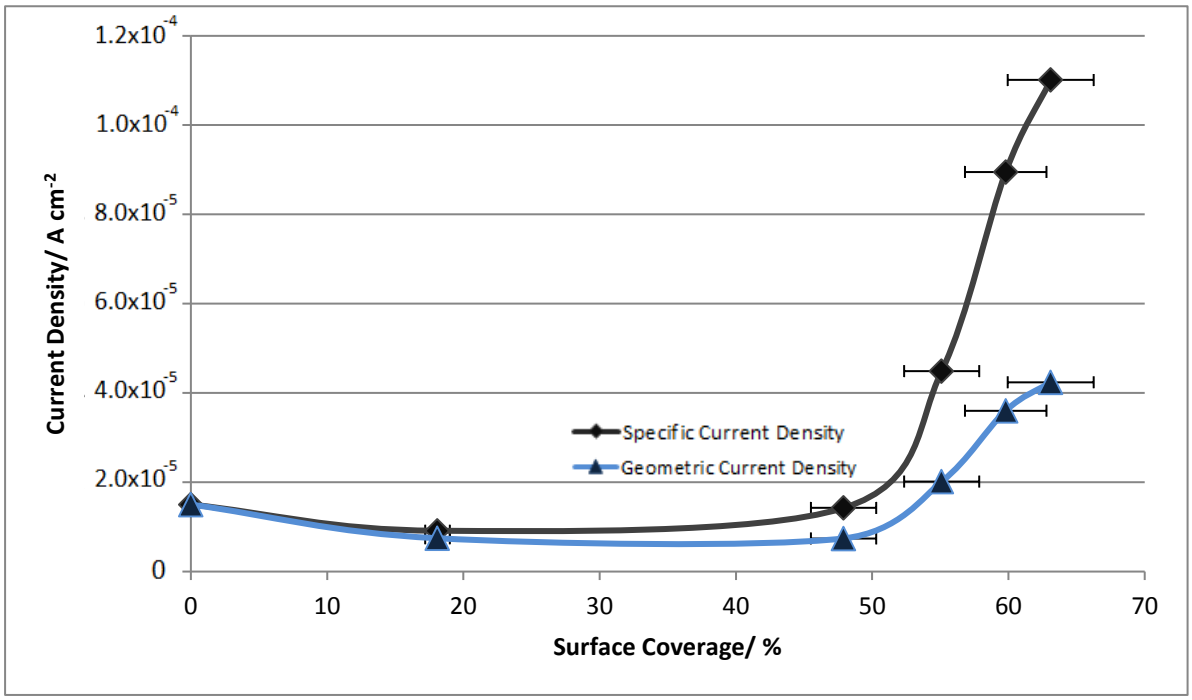

Figure 4.33 Surface coverage vs. current density: comparison of specific and geometric current density values. Current density values taken at potential of 1.0 V_{RHE}.

It should be noted that the gradient of the increasing activity begins to decrease at higher coverage levels in our data for current density at a set potential: an eventual loss in activity, resulting in an activity peak, is expected for both the specific and geometric data, though the exact position of this peak will be determined by differing factors between the two. For the geometric data, eventually the ratio of active gold to total area will decrease such that any increase to activity from deposited titania will be overshadowed by the low level of gold available for the reaction to occur on. The specific data do not have this issue, as the current density is observed relative to the quantity of active gold in the system, so will continue to increase as the level of active gold in the system increases: however, eventually there will come a saturation point (whether spill-over or interface sites are responsible for the increased activity) where further deposition of titania removes active gold from the system without activating any further gold, thus leading to a downturn in activity, though at higher coverages than that seen for the geometric data.

This eventual loss in activity for the individual systems is more clearly exemplified in Figure 4.34, where representations of the TiO_2 nanoparticles on a gold surface are shown, with the corresponding periphery sites and spill-over areas displayed. The effect of increasing particle density is also represented, with image b) indicating the concurrent increase in active area seen with both methods.

The spill-over effect supposes (in non-inverse catalyst systems) that the intermediate reactant (hydroxide ions here), can bind to the support (titania) more readily than gold and can subsequently shift (“Spill-over”) from the support to the gold to facilitate the oxidation of CO bound to the gold surface. In the non-inverse system all available gold is within the Spill-over area of the titania; thus distinguishing this specific effect from others is not feasible. A similar consideration can be made for the periphery site method, where the reactive area is limited to the interface between the titania and gold, compared with the larger effective active area for the Spill-over method.

By utilising the Inverse system, it can be thought that for both methods, the area surrounding each titania particle where the improvement in activity that is seen by us here is limited. For Spill-over, it is reasonable to assume that there is a maximum level of reactant that can be supplied by the comparatively limited titania particles (at least compared to bulk titania in the non-inverse system), resulting in each particle only able to

provide the R.D.S reactant to a specific region surrounding itself before effectively exhausting its supply. For periphery sites, the level of improved activity provided at the titania-gold interface should be equal when only the interface area is considered.

We must consider the effect of changes in titania density on the activity provided by both of these methods, as performed in the experiments described by us here. We shall first consider the Spill-over methodology. It is unknown if the spill-over area varies with particle size (though it is likely to have some effect): as the particles synthesised here were consistent in size, we can assume that the spill-over area for individual particles remains relatively constant for all samples. By referring to Figure 4.34, it can be seen that as the effective distance between titania particles decreases (representing increasing particle density), the areas affected by spill-over shift closer together and thus cover a larger extent of the surface.

As such, we can consider that as the density of particles on the surface increases, the effect of the spill-over/interface sites on CO oxidation should increase in potency as a larger percentage of the gold is affected by this spill-over area. This has been clearly shown with the CV data (Figure 4.24), indicating that as more of the surface is covered by the Spill-over area, the oxidation activity increases, despite the decreased area of available gold. Notably, as exemplified by Figures 4.27 and 4.28, despite the decreasing area of available gold as coverage increases, the current density also increases with increasing particle density. Considering both the spill-over and periphery methods, it would be expected that eventually a peak in activity would be displayed: the only difference between these two methodologies should be the exact position of this peak, with spill-over peaking at lower coverages than interactions at interface sites, as the activation of gold reaches the saturation point at lower titania levels with this method, due to the relatively larger affected area per particle.

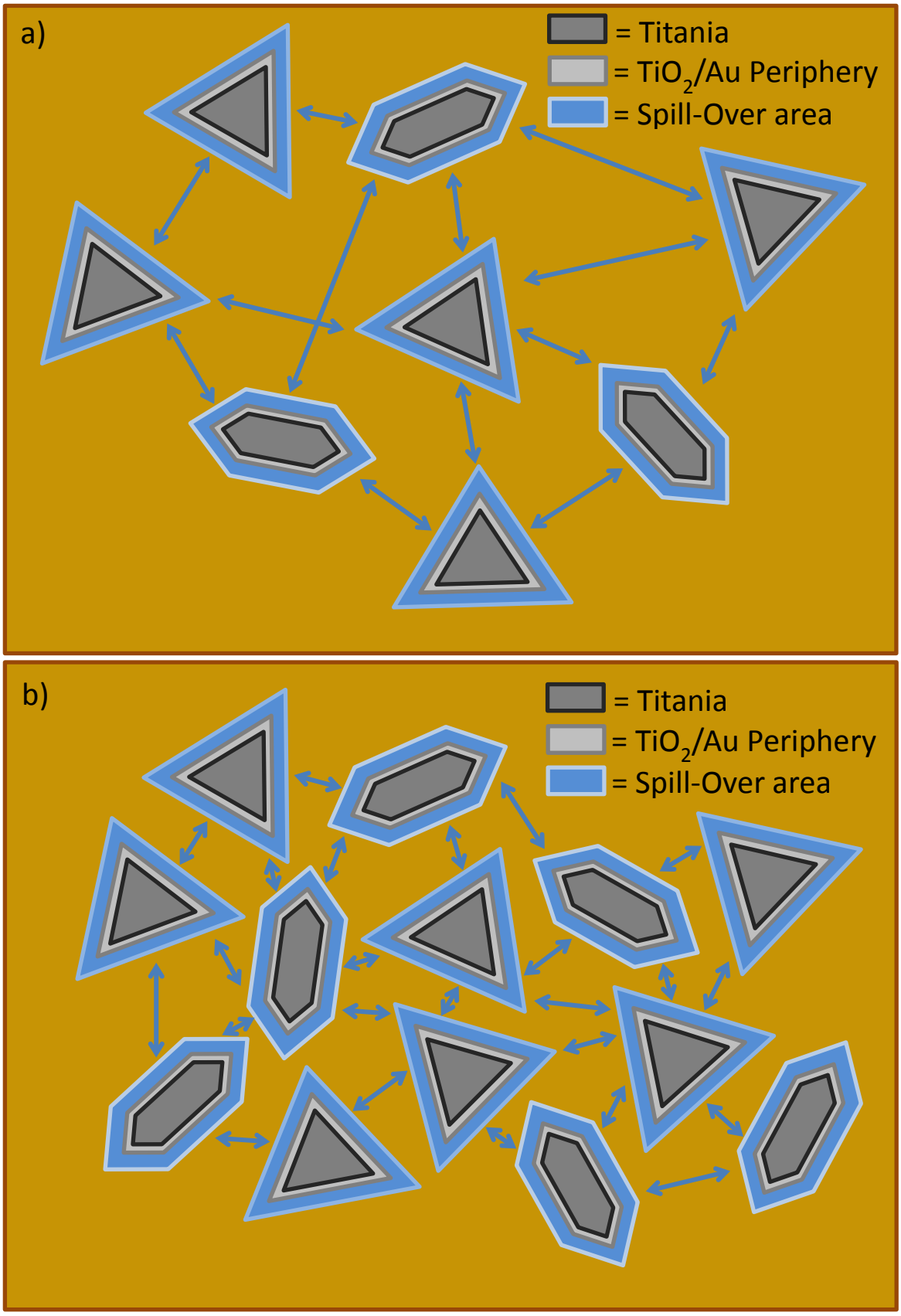

Figure 4.34 Titania particles on gold crystal surface. Representation of TiO_2/Au periphery sites and Spill-over. Effective particle density increase between a) and b).

With this consideration of the changes given with increasing titania particle density leading to our being unable to distinguish between spill-over and interface regions as responsible for the increased activity, we must consider other methods by which these two methods can be separated from each other. A major issue present in the data collected by us here is that mass transport becomes a serious limiting factor as current density increases in the system: the use of a system such as a rotating disc electrode (RDE) is required to mitigate this. This would allow for further investigation and determination of where the expected peak in activity appears, allowing for differentiation of the two methods.

Additionally, observing the effect of particle size on CO oxidation activity, as originally considered for this project would provide further insights. The methodologies can be distanced from one another when we consider the effect on each. Unfortunately, a number of unknown quantities are present when considering the effect of changing the titania particle sizes, adding some uncertainty. First we shall consider interface sites: as average particle size is decreased, the ratio of the particle perimeter length to total particle size will increase, providing an increase in the available interface sites per area of titania. We would thus expect to see that as particle size decreased, an overall increase in activity would occur, on the condition that the coverage of the surface remained constant. The data collected by us here indicate that a coverage of 50-60 % would be ideal, as increases to activity were only viewed for coverages above 50 %: as the activity was significantly improved with increasing coverage from this point, keeping the coverage values within those performed by us above would allow for a suitable comparison.

In the case of spill-over, it is unknown if the ratio of spill-over area to total titania will increase or decrease: however, changing particle size should provide further insight as the ratio of spill-over area to particle size will determine the observed effect on activity. If the ratio increases, the observed activity will also increase, if lowered, it will decrease, and if remains constant, then so will the observed activity, allowing for further insight into the activity provided by titania atop the gold substrate.

By combining these investigations with a continuation of the work performed by us here for higher titania coverages at set particle sizes, providing the extent to which these effects emanate from the particles, the determination of which of these two methods is responsible for the observed increase in activity should become possible.

4.5 Conclusions and further work

In this chapter we have described the deposition and imaging via STM of titania nanoparticles onto the surface of a Au(111) crystal. Utilising the deposition method as described by Potapenko *et al*.[73], the synthesis of particles with consistent triangular/elongated hexagon shapes was performed, with regular particle sizes of ~11.5±2.5 nm reached. The density of these particles across the surface was varied and the subsequent electrochemical oxidation of CO was investigated.

The electrochemical data for the oxidation of CO displayed a number of interesting phenomena: notably, the onset for the oxidation peak was significantly affected by the addition of titania onto the gold surface. By comparing this to the concurrent titania coverage prior to electrochemical testing, information can be gleaned about the method behind this increase in the activity. Notable information can be gleaned from comparison of the effective density of particles and the related inter-particle spacing for both current density at 1.0 V_{RHE} and the ignition potential. Initially, a decrease is seen in activity up to titania coverages of ~50 %, which has been attributed to a disruption of active CO at edge sites on the gold despite the augmentation provided to the CO oxidation activity provided by the titania. Once the coverage is increased past this point, a sharp increase in activity is observed, indicating a rising increase in activity with increasing particle density, as well as a significant decrease in the onset of the CO oxidation.

We can conclude that our suggestion of either spill-over of reactants or action at titania-gold interface sites is indeed likely to be responsible for the increased activity seen for the titania modified gold system, due to the increased activity remaining with the inverse system, as well as progressing as it does. However, the data collected do not allow for the definitive declaration of which of these two methods is responsible: further work is required to resolve this. Firstly, investigation into higher particle densities with an RDE set up is required for resolution of the expected activity peak position without mass transport limitations, allowing for a measure of active area provided by the particles. Second, whilst maintaining constant surface coverage where improved activity has been observed, modifying the size of the titania particles and observing the concurrent change in activity. Using such data, determining which of the proposed methods are responsible for the improved activity observed in the titania modified gold system should be possible.

5 HT-PVD Gold-Titania Inverse Electro-catalyst

5.1 Initial set-up

High throughput methods have been used extensively in the Southampton laboratory to investigate, understand and optimise fuel cell electro-catalysts. The evaporative HT-PVD method has enabled not only the effects of alloy composition to be investigated on ORR and HOR reactions, but the method is sufficiently controlled to allow the growth of metal and metal alloy particles. This has led to high throughput studies of particle size and support effects in electro-catalysts. Of the systems studied, the model system of CO electrooxidation by supported gold particles has featured extensively. Here the possibility of extending these types of high throughput synthetic and screening methods to the study of inverse catalysts has been explored.

Following the successful synthesis of Inverse catalyst systems on a Au(111) crystal, the production of such materials via a high-throughput method was considered, with the High-Throughput Physical Vapour Deposition (HT-PVD) chamber system used by the Hayden group[49,86] for synthesis. By utilising this system, a larger selection of samples with greater titania coverage distribution could be manufactured and as such a greater investigation into the effectiveness of the inverse catalyst system could be performed.

The synthesis method for production of Au(111) supported titania as described in Chapter 4 (Potapenko and Osgood[73]) was used to produce the gold modified surfaces with the HT-PVD system. Samples were initially synthesised on substrates consisting of an 11*11 mm gold film deposited on a borosilicate glass base, produced by Arrendee metal GmbH + Co. KG, for determination of the correct deposition conditions prior to deposition on 10*10 electrode arrays. Ti was deposited using an electron-beam source, subsequently heated and then oxidised with a molecular oxygen background pressure of ~$1.5*10^{-6}$ mbar.

Due to the different natures of the deposition chambers as well as the specific substrates utilised, some modifications to the synthesis process were required. Two significant differences in procedure were present between the samples synthesised in the STM system and those in the HT-PVD system. The first comes from variation in substrate surfaces: the gold/glass substrates were hoped to form Au(111) terraces upon pre-

synthesis annealing but because of a susceptibility to damage from sudden changes in temperature, 10*10 Array Echem Chips surfaces remained polycrystalline gold. The second is associated with the heating step for the alloying of Ti and the gold: due to limitations in the heating filament, as well as the 10*10 chips' temperature limitations, the temperature of alloying was lower and the rate of heating reduced.

Because of these changes, conditions determined using the STM system could not be directly utilised for calibration of the samples produced in the HT-PVD system; the slower heating procedure results in longer times spent alloying before the final annealing temperature is reached, as well as the lower overall temperature reached.

In addition to this sensitivity to sudden temperature changes, utilising the gold 10*10 arrays chips limited the maximum annealing temperature as it had been shown that the chips become increasingly susceptible to damage as they are heated, with a temperature of 723 K being the limit before the likelihood of damage becomes significant. As such, the maximum annealing temperature was limited to 723 K so as to minimise the possibility of the 10*10 arrays being damaged during the synthesis process.

5.2 Clean Gold Surface

For samples synthesised in the HT-PVD system, the imaging of the surface topography was performed via tapping mode AFM, as described in Chapter 3: contact mode, despite giving a closer indication of surface topography, was not used as the chance of damage to particles on our surfaces from interactions with the tip was a serious concern.

The gold/glass substrates were initially cleaned such as to remove any material from their surface, as well as to attempt to prepare the surface for particle formation. This cleaning procedure consisted of three steps: rinsing with acetone and isopropanol (with residual fluid removed via Kim-Tech wipe) and heat annealing via butane blowtorch (giving temperatures of roughly 1700 K). The surface of such a freshly prepared gold/glass substrate imaged via AFM can be seen in Figure 5.1.

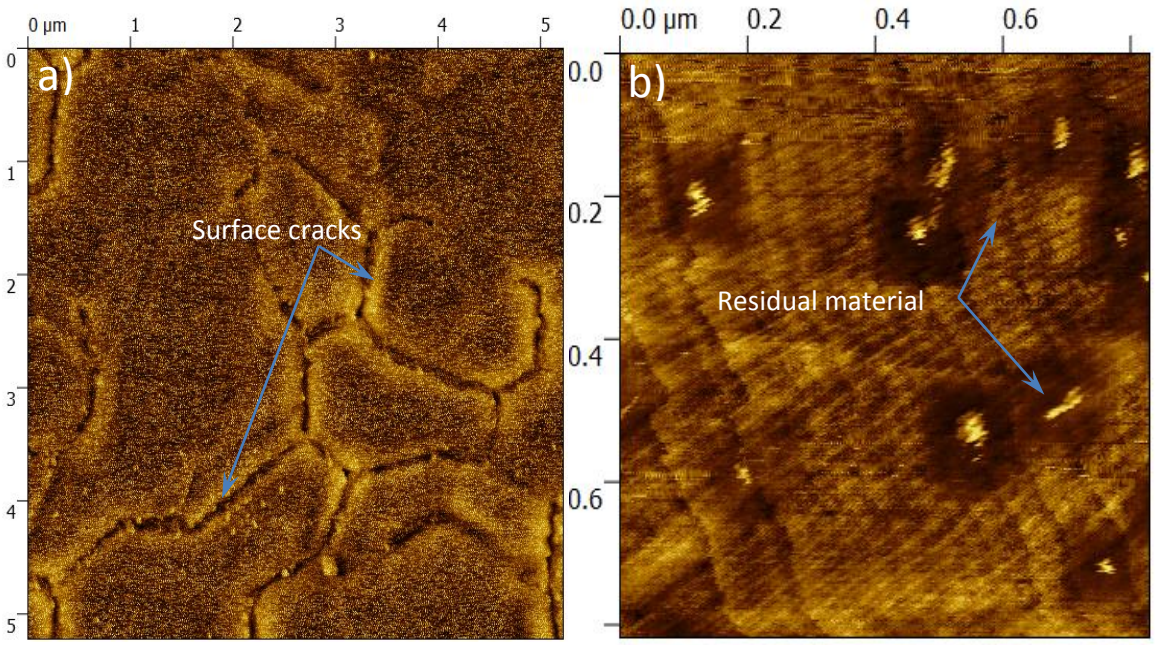

Figure 5.1 Images of clean gold/glass sample taken with AFM system. a) 5*5 µm, b) 822*822 nm. I = 10% P = 15%

It can be seen that despite the cleaning process, a slight amount of material remains on the substrate surface. Another notable feature that is visible at larger scan areas is what appear to be fissures in the gold film across the surface: these appear in all images taken of these substrates and are most probably brought about by thermal expansion of the surface during heat annealing. It was also hoped that by annealing the substrate, (111) terraces would form across the surface[127,128] and thus allow for a greater comparison with previous samples produced on a Au(111) crystal: this was unfortunately not observed for the clean Au/glass, but is visible in later images of the sample surfaces.

In spite of more thorough cleaning being performed on future substrates, in conjunction with more careful removal of the acetone/isopropanol washes, the residual material seen on these images remained a constant feature for all samples produced throughout this project, possibly being small areas of nucleated gold. In spite of this, synthesis and the subsequent imaging of the Ti modified samples was performed, as this remaining material on the surface was not considered sufficient to impede our measurements of the particle formation. The fissures forming on the surface were noted, but ultimately considered of no concern to future sample imaging, as the inter-fissure areas were sufficiently large for proper analysis of any synthesised particles.

Imaging of the clean 10*10 gold array surfaces was also attempted: the cleaning procedure for these chips was identical to that of the gold/glass substrates, with the heat annealing step removed due to the 10*10 array heat limitations discussed above.

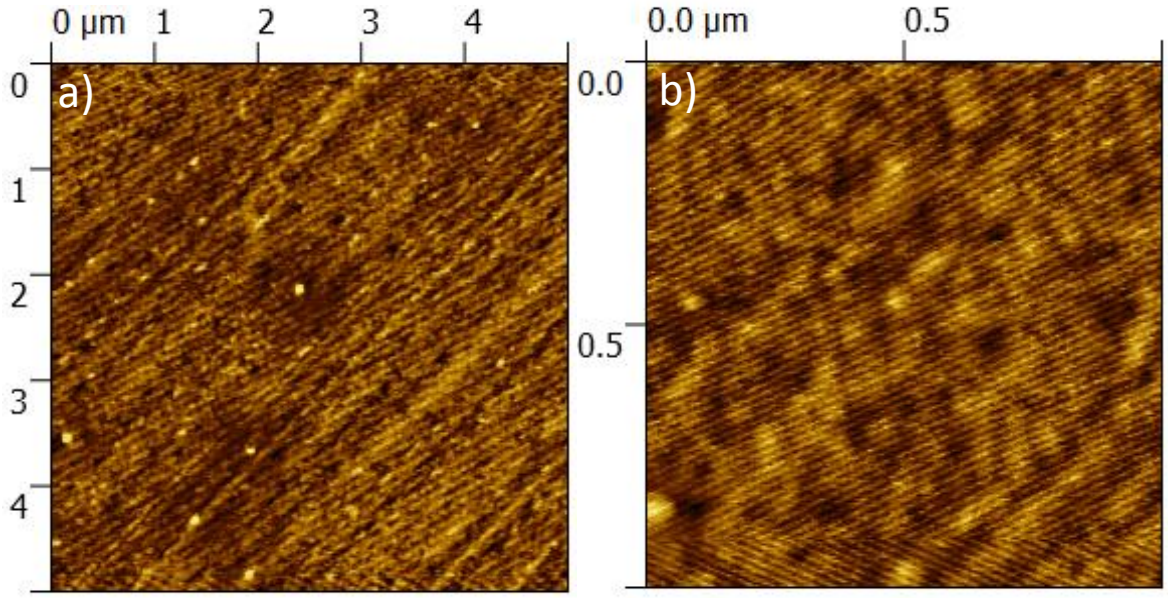

Figure 5.2 AFM images of single Au electrode from 10*10 array chip after cleaning procedure. a) 5*5 µm, b) 1*1 µm zoom of a). I = 5%, P = 1%

Figure 5.2 gives example AFM images of the pads of one such array post-cleaning. The surface can be made out, though the image quality is lower than would have been ideal: unfortunately, procuring images of the array surfaces proved difficult, with no significant improvement to the quality shown above. It was hoped that such images would prove to be sufficient for comparison with later samples, but the issues with imaging remained for samples synthesised on the 10*10 arrays, limiting our investigation of changes to the surface.

5.3 Inverse Titania-Gold catalyst preparation

5.3.1 Ti thickness Calculations

Using a 10*10 masked silicon substrate (resulting in 100 1.25*1.25 mm titanium squares), 5 distinct Ti thin films with differing thickness were deposited with 24 minute intervals, resulting in a maximum deposition time of 120 minutes. A rate of 0.2 Å/s was maintained for all Ti deposition in this project: this does not represent the exact rate for Ti deposition, being the measured value represented by the equipment and thus could not be used for thickness calculations, but does allow for consistent deposition between samples. The measurement of the thickness of deposited Ti was performed with tapping mode AFM, with Figure 5.3 showing the measured values: it can be seen that 0.2 Å/s gives a Ti deposition rate of 0.2047 nm per minute.

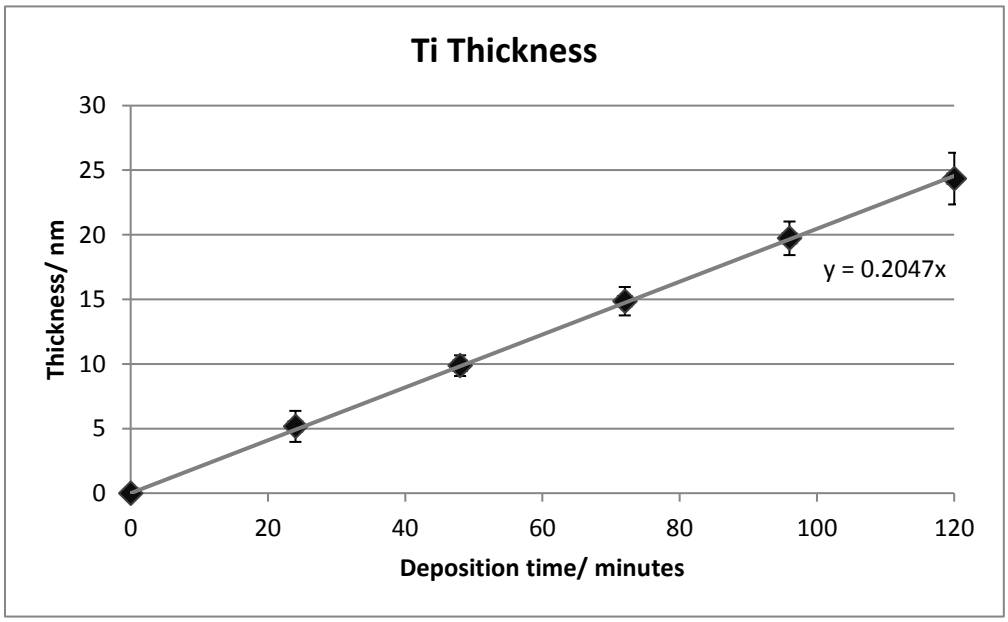

Figure 5.3 Initial Ti deposition calibration. Thicknesses measured using tapping mode AFM and are averaged for the 5 separate deposition times

5.3.2 Titania Synthesis

In keeping with the alloy synthesis method described by Potapenko and Osgood[73], once Ti had been deposited, samples were heated to 723 K at a rate of 25 K/min. Samples were held at this temperature for a period of 4 minutes, whereupon molecular oxygen was introduced, providing an atmosphere of ~$1.5*10^{-6}$ mbar. The temperature was held at 723 K during this a period and subsequently maintained for 10 minutes: the sample temperature was then reduced to room temperature at a rate of 25 K/min. The oxygen atmosphere remained until a temperature of ~500 K was reached, at which point it was removed. Once sufficiently cooled, samples were extracted from the vacuum system and imaged using AFM.

Initial depositions were performed so as to mimic those performed in Chapter 4; however this proved insufficient for the production of titania particles on the surface, indicating that higher Ti deposition levels were required. Figure 5.4 shows the progression of titania formation from clean Au to high titania coverages as initial Ti deposition is increased. Of note is image i), where distinctive triangular terracing can be made out on the surface: this originates from annealing of the substrate prior to synthesis, which results in (111) terraces forming on the surface[127,128]. These terraces are lacking in the majority of our images: the reason for this is unknown, as identical preparation conditions were used for all samples, and the effect was not visible for the clean gold/glass substrate, and thus we must consider them an uncommon feature of our surfaces.

A clear progression in final titania production is seen as initial Ti is increased: the 3 and 6 minute samples (c/d and e/f respectively) have initial Ti thicknesses of 0.6141 and 1.2282 nm, mimicking Ti deposition levels used for samples synthesised on the Au(111) crystal, with e/f having an initial Ti deposition level very close to that of the highest level deposited for those samples. Titania production, however, proved to be less prevalent than seen on the Au(111) crystal, with significant particle formation only occurring for deposition times above 6 minutes. Such a drastic increase is not necessarily unexpected, as samples synthesised on the Au(111) crystal showed significant changes in titania coverage with similar modifications to initial Ti thickness, though it was initially thought that the longer alloying step used for samples produced in the HT-PVD system would give a shallower gradient in particle formation.

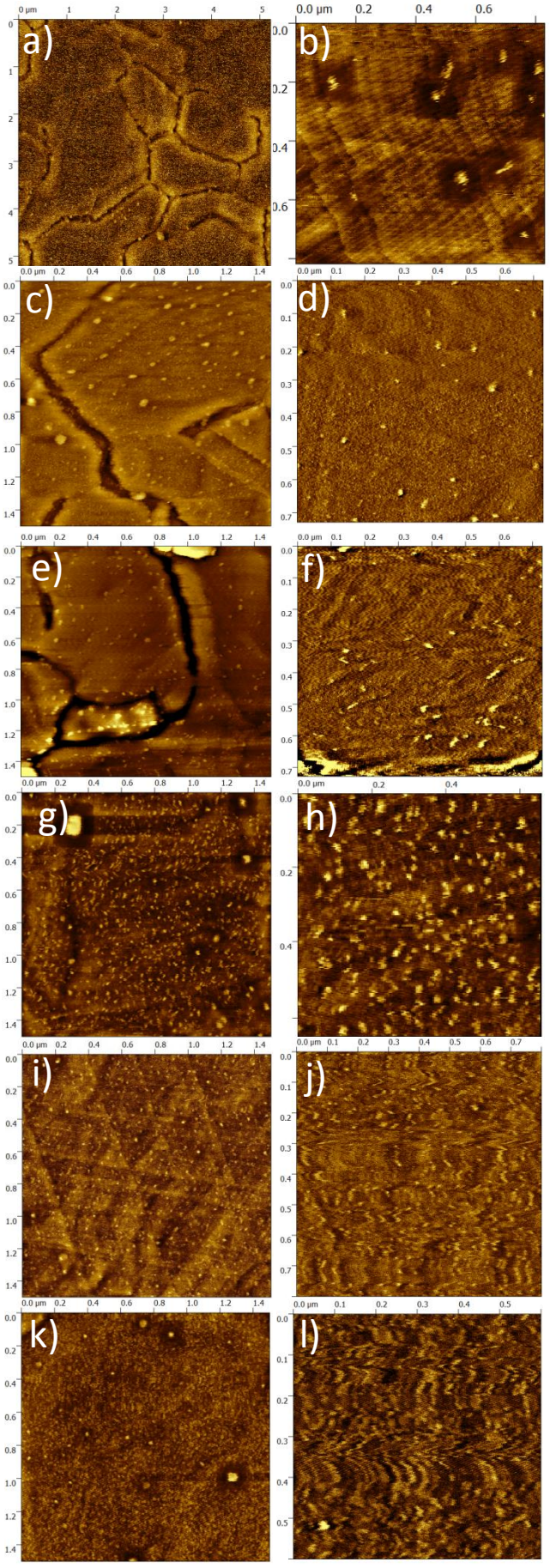

Figure 5.4 Progression of titania particle synthesis on gold/glass substrates. Imaged with tapping mode AFM at I=10 %, P=15 %. Initial Ti deposition times and corresponding thickness are displayed alongside corresponding images

High coverages are reached with an 8 minute Ti deposition; it should be noted that no obvious agglomeration of particles was witnessed, unlike chapter 4, despite further increases in initial Ti. This is most likely due to the relative difficulties in imaging the particles via AFM compared to STM; as previously noted, particles form on top of the titania layer produced via agglomeration before a complete film is produced, which may obscure the exact point at which agglomeration begins. However, a clear point of origin for particle formation was found, which allowed for further investigation into this system.

A general consistency was found in particle size across samples, as was observed previously for samples produced using this method; they are, however, larger than those synthesised on the Au(111) crystal, with an average size of ~20±3 nm compared to ~11.5±2.5 nm. This contradicts the effect observed by Potapenko *et al*.[111] where higher alloy temperatures gave larger particles, though an in depth study was not performed by them: it is most likely that the longer alloy times utilised by us here are the cause of this discrepancy, though further investigation would be required to determine if this were the case.

5.3.3 Effect of Alloy time on Particle formation

The required minimum Ti level for particle formation is higher for these samples than seen for those synthesised previously on the Au(111) crystal; ~0.6 nm compared to ~0.35 nm (possibly lower, though saturation of the crystal during experiments prevented proper investigation). This can most likely be linked to the increased length of time spent alloying, as it is more likely that deposited Ti is lost to the gold bulk during longer alloy steps, and subsequently not retrieved during the oxidation step.

Figure 5.5 offers a comparison of this phenomenon; the surface of two samples subjected to identical Ti deposition (7 minutes) is shown but with a) having been effectively exposed to the alloying step twice. Initially, alloying was performed as described above; however, the sample was immediately cooled and removed from the deposition chamber before the oxidation step so XPS measurements could be performed on the sample in its alloyed state. Because of this, when the sample was returned to the deposition chamber it had to undergo heating back to 723 K before oxidation could begin,

effectively performing a secondary pseudo-alloying step (though the 4 minute hold at temperature prior to oxidation was not repeated).

It can be seen that a) appears to have a larger level of titania at the surface, with a few particles being considerably more prominent than the rest. The reason for this larger level of particles is unknown: it would be expected that longer anneal times would give less titania as more titanium is lost in the gold bulk. It is possible that this particle layer is in fact significant roughening of the surface, though this is unlikely. Despite the modification of the surface being counter to that expected, modifying the alloy time was shown to have a significant effect on the particles formed when utilising this method, and as such XPS measurements of the alloyed state were removed from later experiments in order to reduce changes to the surface morphology between samples.

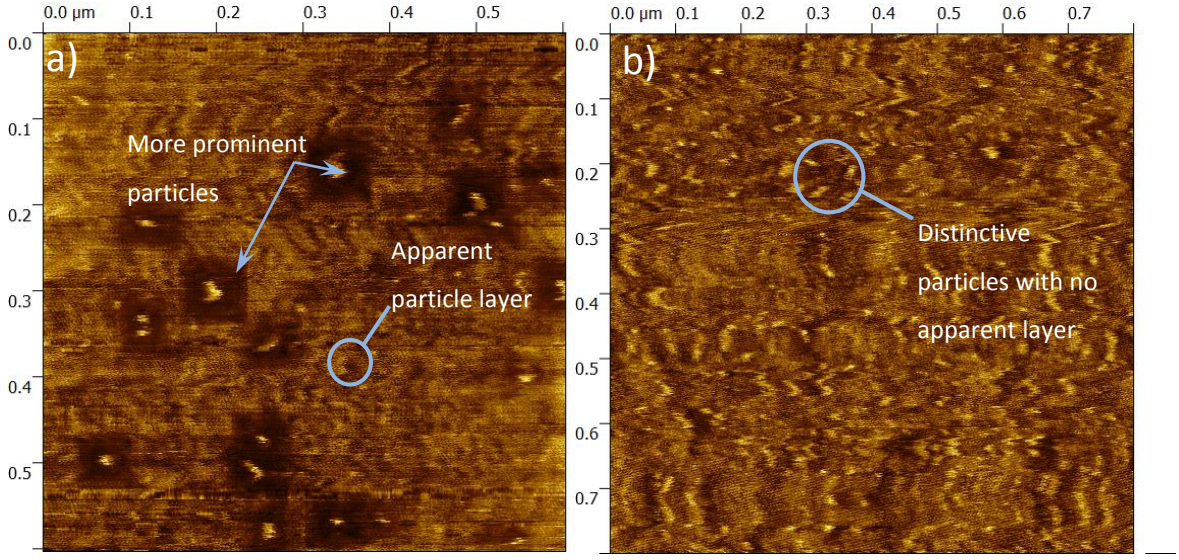

Figure 5.5 Comparison of the effect of alloy times on final titania levels. 7 minute Ti deposition, a) 603*603 nm with extra alloy step, b) 800*800 nm without extra alloy step. I=10%, P=15%

5.4 X-Ray Photoelectron Spectroscopy

A number of the samples synthesised on the gold/glass substrates underwent investigation with X-ray Photoelectron spectroscopy (XPS) to allow for the determination of the electronic states of Ti, O and Au before, after and, for some, during the synthesis process. This also allows for a comparison to be made with the work performed by Biener e*t al.*[72] where XPS was performed during synthesis of titania particles: despite the difference in specific synthetic methods, this is still a valuable comparison to make.

For all samples that underwent XPS, scans were recorded for the sample with initially deposited Ti and post oxidation: scans were only recorded for the clean Au for early samples due to time constraints, as well as initial samples providing sufficient data for our purposes. Scanning of the post alloy state prior to oxidation was only performed for early samples; due to the resultantly larger alloying times this necessitates, and the subsequent differences in final titania formation that resulted after oxidation (Figure 5.5), these scans were discontinued so as to allow for less inconsistency in the final titania. For all scans, the corresponding carbon 1s peak (~284.8 eV) was used as a reference.

5.4.1 Gold XPS

Prior to deposition, the 93-78 eV region was scanned so as to determine the position of the Au $4f_{7/2}$ and $4f_{5/2}$ peaks, the main peaks for Au. Figure 5.6 shows the XPS spectra collected for the clean Au: the characteristic peaks can be seen, with the $4f_{7/2}$ peak corresponding very closely to the expected binding energy of 84 eV (as indicated by the dashed line). The spacing of the two peaks is measured at ~3.68 eV, which is also the expected value. The peaks themselves are broader than may be expected for a pure sample, causing some overlap between them: this is most likely due to limitations brought about from the equipment but as this does not impact on our ability to interrogate the data, it does not concern us here.

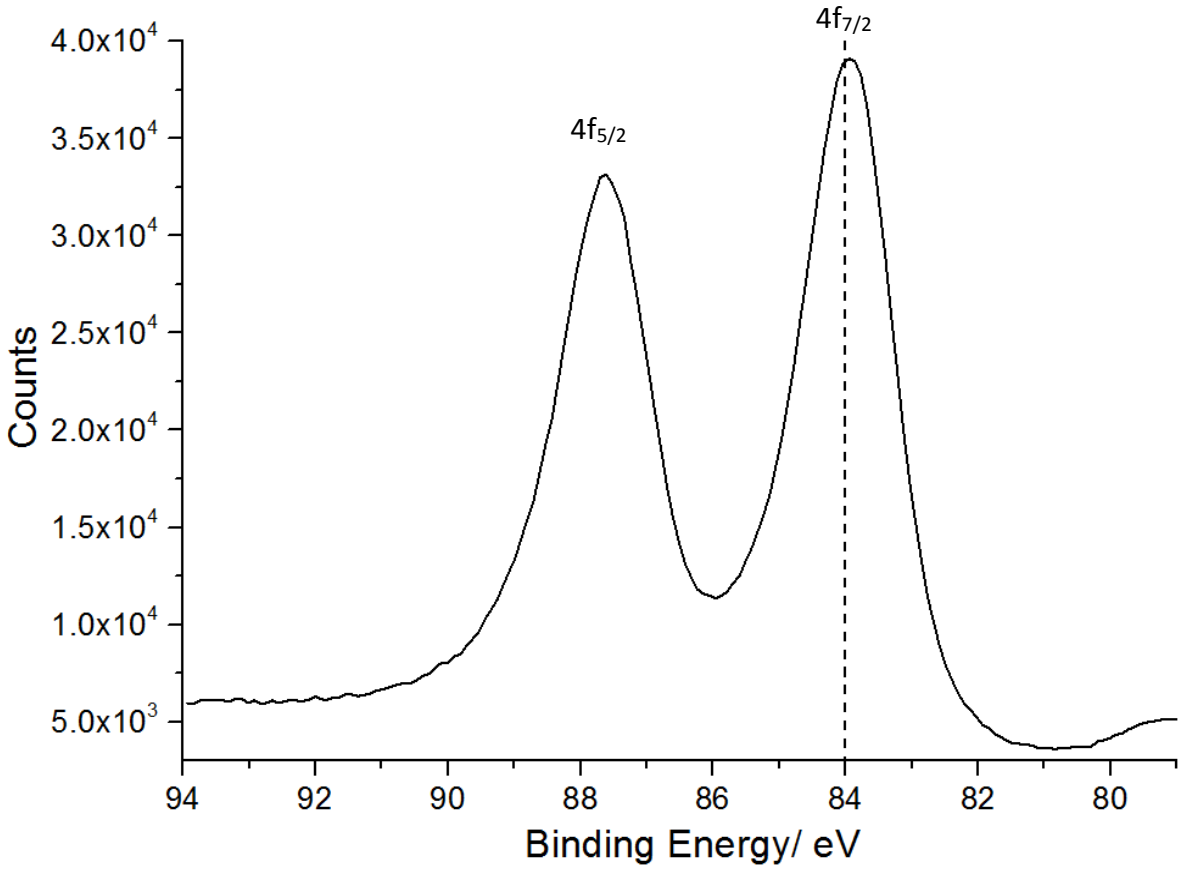

Figure 5.6 XPS data for 7 minute Ti deposition sample Au 4f peaks adjusted via C 1s peak. Mg filament utilised, 10.5 kV. Dashed line represents expected unmodified gold $4f_{7/2}$ peak position.[129]

With the standard Au peaks having been confirmed, we must consider the scans for the remaining synthesis steps. Figure 5.7 shows the Au $4f_{7/2}$ and $4f_{5/2}$ peaks for a sample with an initial Ti deposition of 7 minutes at 4 distinct stages of the synthesis: Clean Au prior to Ti deposition, after Ti deposition on the surface, after Ti-Au alloying and the final sample once the alloy had been oxidised, with all peaks having been shifted with reference to the corresponding C 1s peaks.

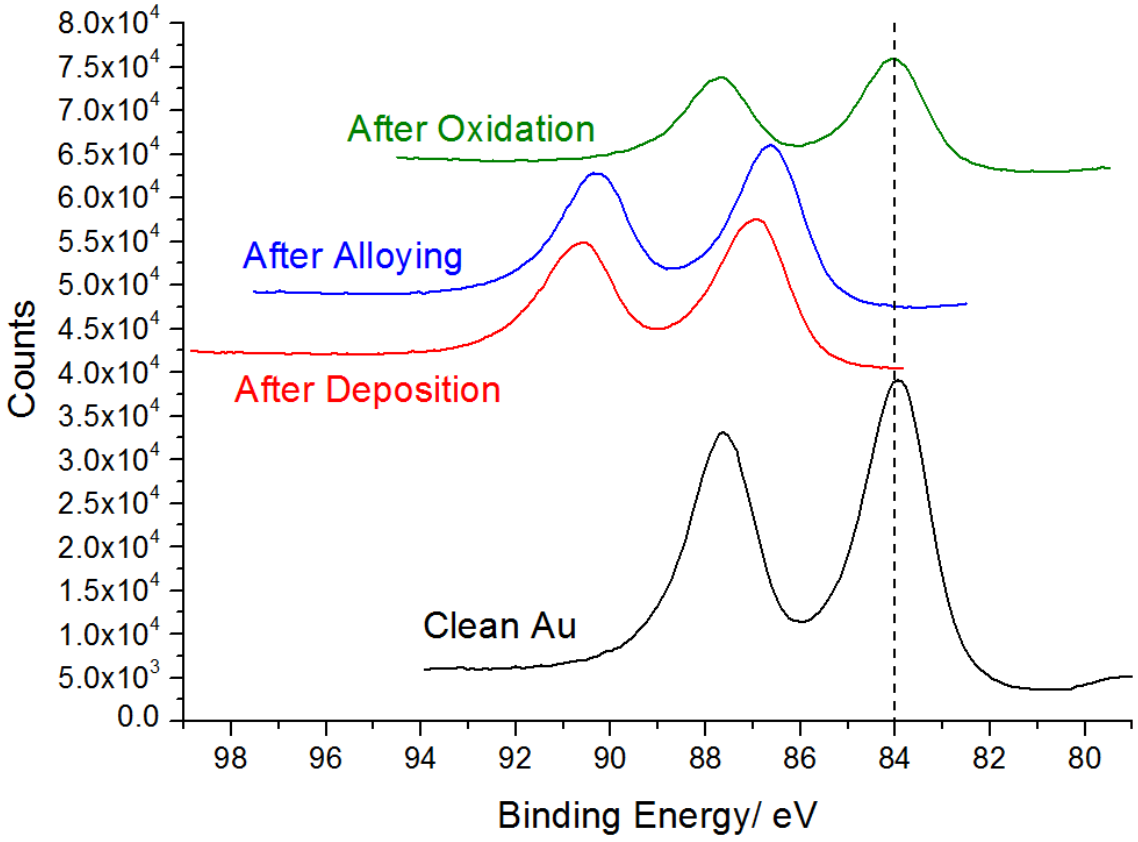

Figure 5.7 XPS data for 7 minute Ti deposition sample Au 4f peaks for clean Au, after deposition, after alloying and the final product after oxidation. All peaks adjusted via respective C 1s peaks and spaced for ease of viewing, Mg filament, 10.5 kV. Dashed line represents expected unmodified gold $4f_{7/2}$ peak position.[129]

It can be seen that the Au 4f peaks for clean Au and the final product line up sufficiently well with the anticipated 84 eV: this is to be expected for the clean gold, though less so for the final sample. The other stages require further consideration: Bzowski and Sham[130] in their paper "Electronic structure of Au-Ti intermetallics" investigated various stages of the alloying of Au and Ti. They found for XPS that alloying gold with titanium resulted in a positive shift of the Au 4f peaks, with Au_2Ti and $AuTi_3$ giving shifts of 0.49 and 0.76 eV, respectively.

A positive shift is indeed seen in the Au 4f peaks of our alloyed sample, though the shift is considerably larger, ~3 eV, compared to the values determined previously. However, it may be considered that the Ti-Au ratio might be much higher in our samples; given the relatively short alloying time Ti may have not had sufficient time to move into

the gold bulk. Bzowski and Sham did observe the higher Ti ratio sample gave a larger shift in the Au peak position, so a more extreme version of this may have occurred here.

It is interesting, however, that the Au peaks for the sample with Ti prior to alloying also exhibit a large positive shift, slightly greater than that of the alloyed sample. This would appear to indicate the possibility of Ti alloying as it is deposited, but this is proven false when the Ti XPS data is considered, as expanded on below. As such, it may be considered that the shift is not dependent upon the alloying of Ti to the Au to occur, but solely the presence of Ti affecting the electronic state of the gold.

The data for the final sample post oxidation shows an interesting change in that the Au peaks have shifted back to roughly the expected metallic Au positions. This would appear to indicate that the titania formed during oxidation is no longer providing as significant an effect on the gold's electronic state: possibly due to oxygen bound to Ti resulting in the positive charge of the Ti having a reduced effect on the gold.

5.4.2 Titanium XPS

In order to determine the specifics of this interaction between Au and deposited Ti, we must consider the Ti 2p peaks at the same stages of the synthesis. Figure 5.8 shows the XPS data for Ti immediately following deposition and prior to alloying.

The $2p_{3/2}$ and $2p_{1/2}$ peaks are clearly visible; a positive shift of ~3.1 eV from the expected metallic Ti peak positions can be seen. This shift is somewhat unexpected: a small degree of movement in the positive direction may have been anticipated, given the Ti 2p peaks have been observed to have a positive shift when alloyed with gold,[130] but not to the extent seen here: for the Au_2Ti and $AuTi_3$ formations shifts of 0.2 and 0.1 eV were observed, following the expected electronegativity trend.

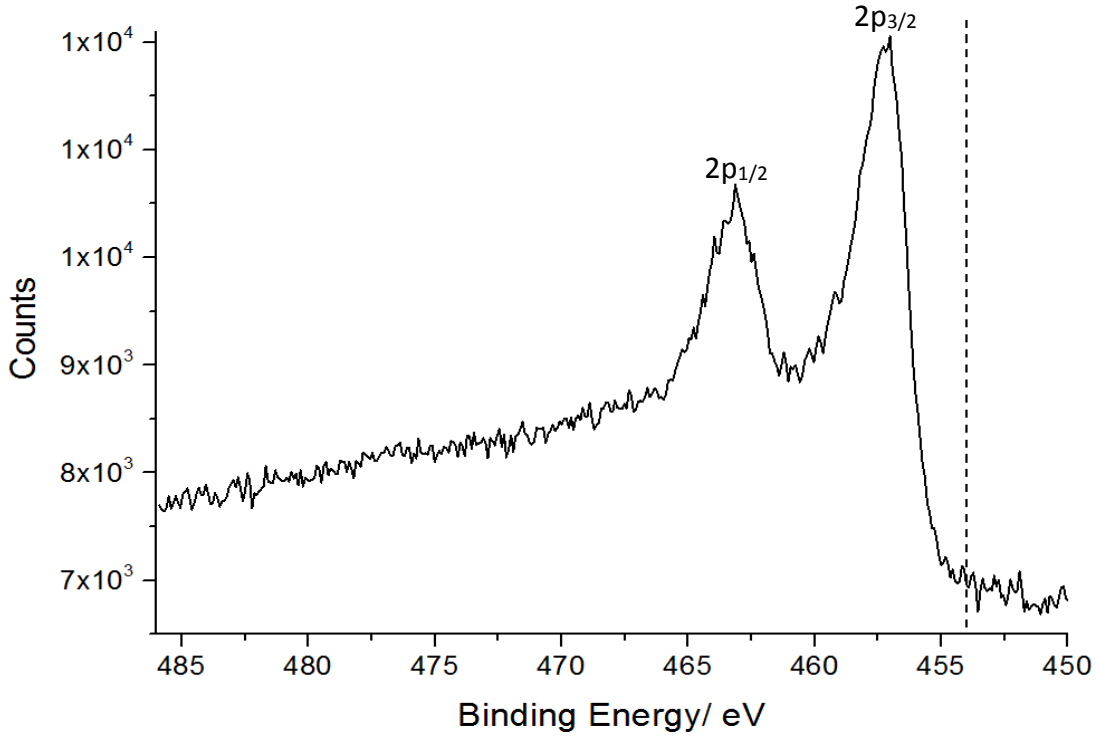

Figure 5.8 XPS data for 7 minute Ti deposition sample immediately following Ti deposition. Spectrum has been adjusted via C 1s peak. Mg filament utilised, 10.5 kV. Dashed line represents expected Ti $2p_{3/2}$ peak for metallic Ti.

However, this can be explained by noting that oxygen appears at this stage despite the supposedly pure Ti deposition, which would explain the shift seen: the presence of oxygen indicates that some form of titanium oxide has formed. Figure 5.9 shows the peaks assumed to compose the data seen in Figure 5.8.

There are two peaks sets that comprise the original data: the $2p_{3/2}$ peaks fall at 457 and 459.1 eV. For Ti these positions correspond to 3^+ and 4^+ titanium,[131] which is not necessarily unexpected when considering the oxygen presence, though it might have been thought that the level of oxygen available in the Ti source would not be sufficient to give such a supposedly complete oxidation of the deposited material.

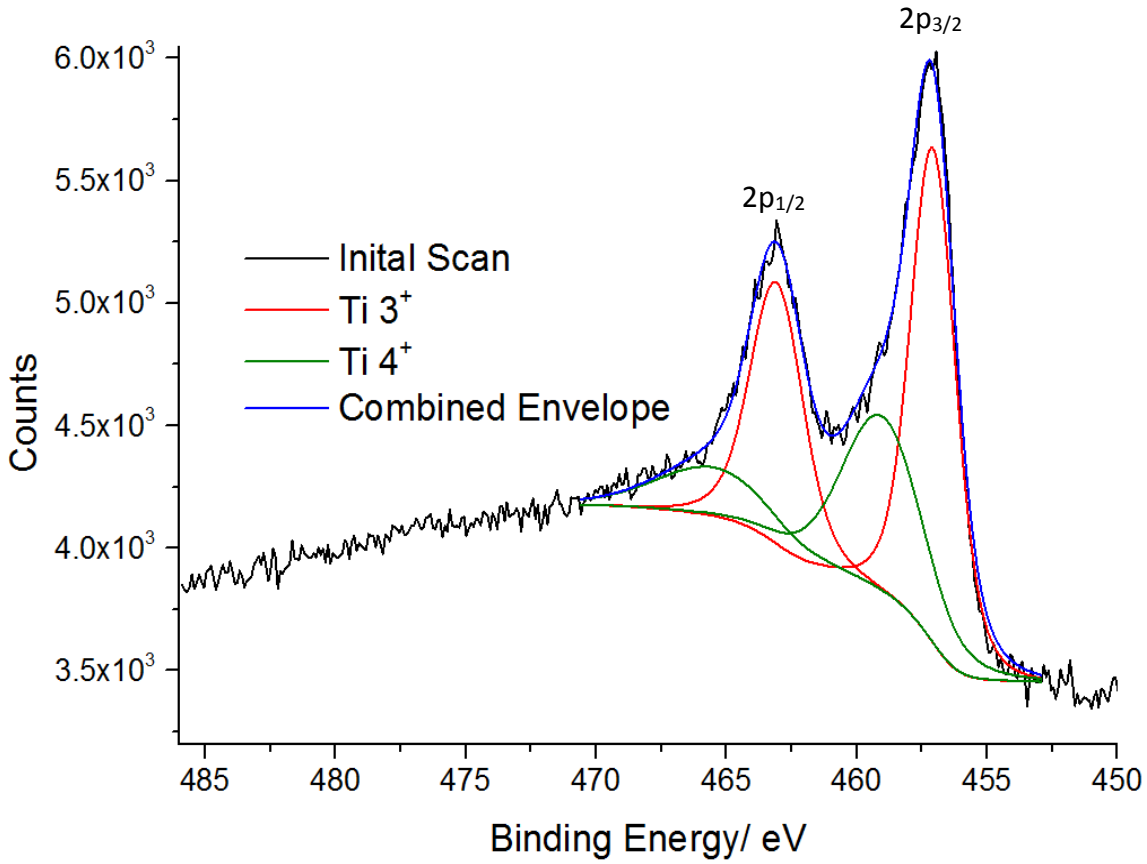

Figure 5.9 XPS data for 7 minute Ti deposition sample immediately following Ti deposition with XPS peaks separated. Spectrum has been adjusted via C 1s peak. Mg filament utilised, 10.5 kV. Ti 3^+ and 4^+ peaks visible.

When comparing those data with those from the literature we can see some significant differences for the surface with Ti deposited prior to oxidation. This is particularly well observed with the work performed by Biener *et al.*[72]: XPS was performed at various stages in their synthesis, similarly to the scans performed by us here. However, when considering the spectra observed for their initial Ti deposition, the 2p peaks are not visible, with the only indication being a very indistinct rise in the background that could be possibly attributed to peaks forming. A similar formation was seen during our synthesis after the alloying step; as seen in Figure 5.10, the Ti 2p peaks have become submerged together, but a distinctive increase can be seen indicating the presence of the Au-Ti alloy.

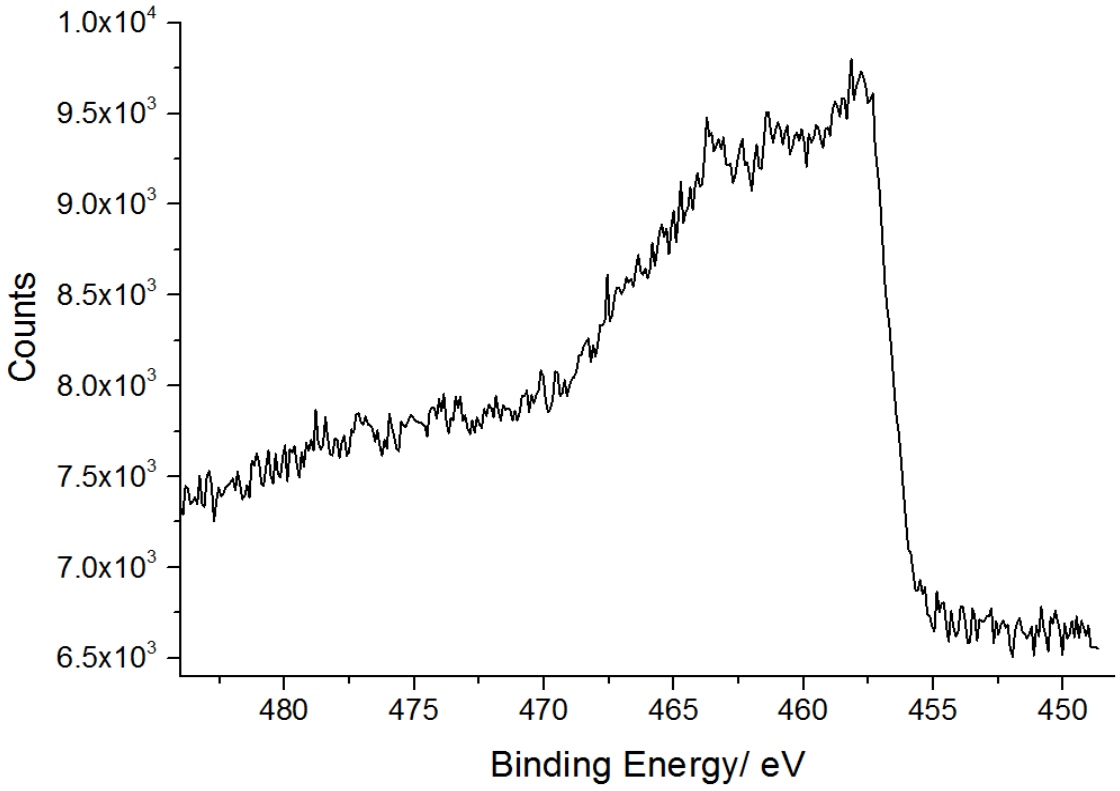

Figure 5.10 Ti 2p data XPS data for 7 minute Ti deposition sample for alloyed Ti-Au. Spectrum has been adjusted via C 1s peak. Mg filament utilised, 10.5 kV.

This suggests that the spectrum seen by Biener *et al.* may have been related to alloying at the surface: however, as no heating had been performed at this stage of their synthesis, another explanation is more probable. Oxygen was found by them to be present at all stages, even at initial Ti deposition, as is the case for our samples; however, the quantity of this oxygen was very low, and it is possible that the relative quantities of oxygen were higher in our samples during Ti deposition, giving a more complete oxidation of the Ti and thus resulting in the 2p peaks seen during initial deposition. A more exhaustive indication of the titania can be gathered from observing the 2p peaks once the full synthesis had been completed.

Figure 5.11 shows the Ti spectrum for the completed synthesis and it is much closer to that expected for TiO_2: the $2p_{3/2}$ peak sits at 258.6 eV, which is within the expected deviation for the Ti^{4+} form, indicating that the titania formed was indeed TiO_2. As no shoulders can be seen in these peaks, we can consider the Ti to be very close to being purely Ti^{4+}, as is expected for TiO_2[131,132,133] with little to no contamination from

other forms. The other features of this spectrum, notably the satellite peak seen at ~471 eV, are as expected for this form of titania.

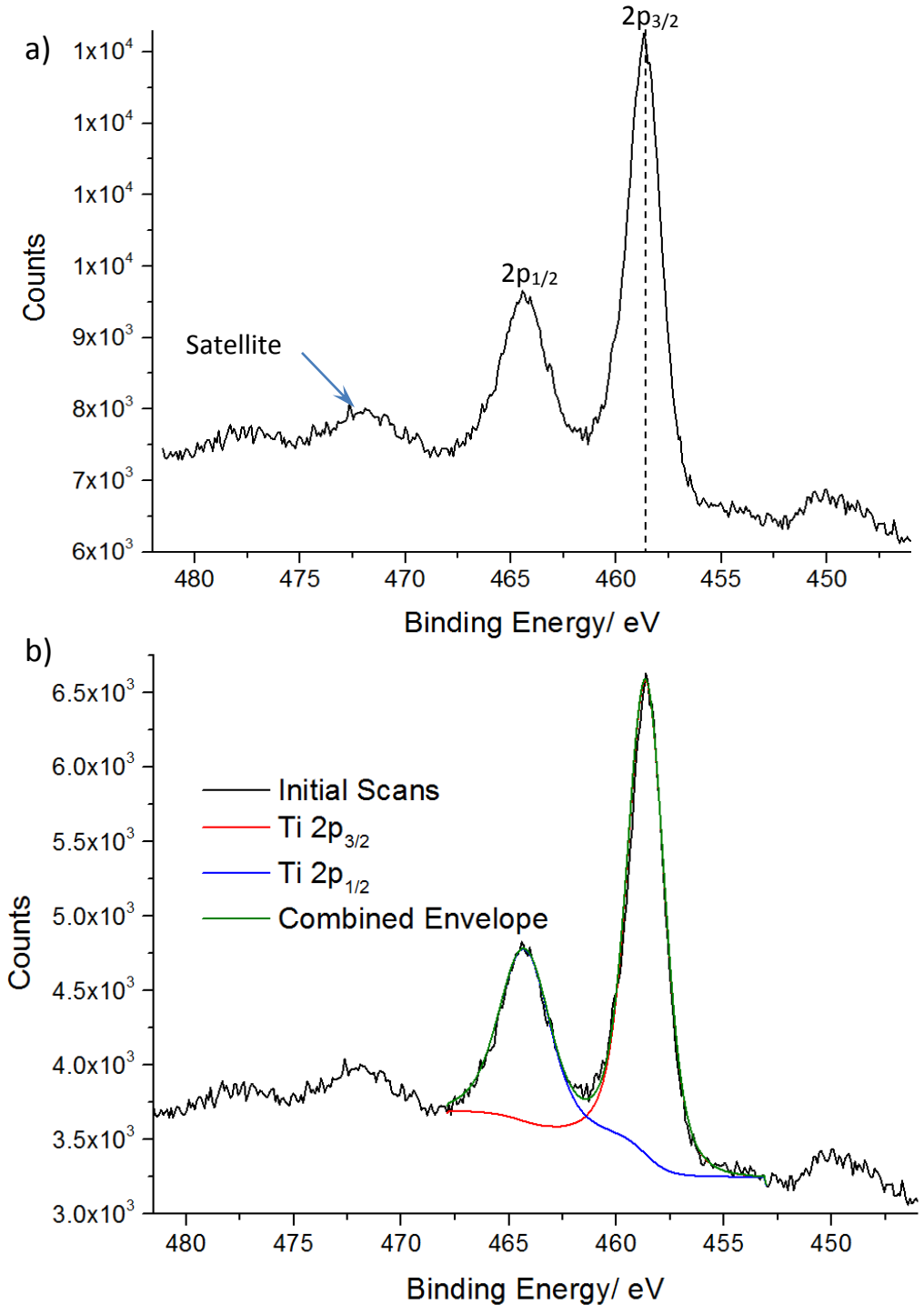

Figure 5.11 Ti 2p XPS data of final oxidised 7 minute Ti Deposition sample. a) overall scan, b) spectrum components. Spectrum has been adjusted via C 1s peak. Mg filament utilised, 10.5 kV. Dashed line represents expected Ti $2p_{3/2}$ peak for Ti^{4+}.

Figure 5.12 combines the XPS data from Figures 5.8, 5.10 and 5.11, collecting the Ti $2p_{3/2}$ and $2p_{1/2}$ peaks for all stages of the synthesis to give a clearer indication of the progression of the Ti 2p peaks as the synthesis is performed. The clean Au spectrum has been added for the sake of completeness.

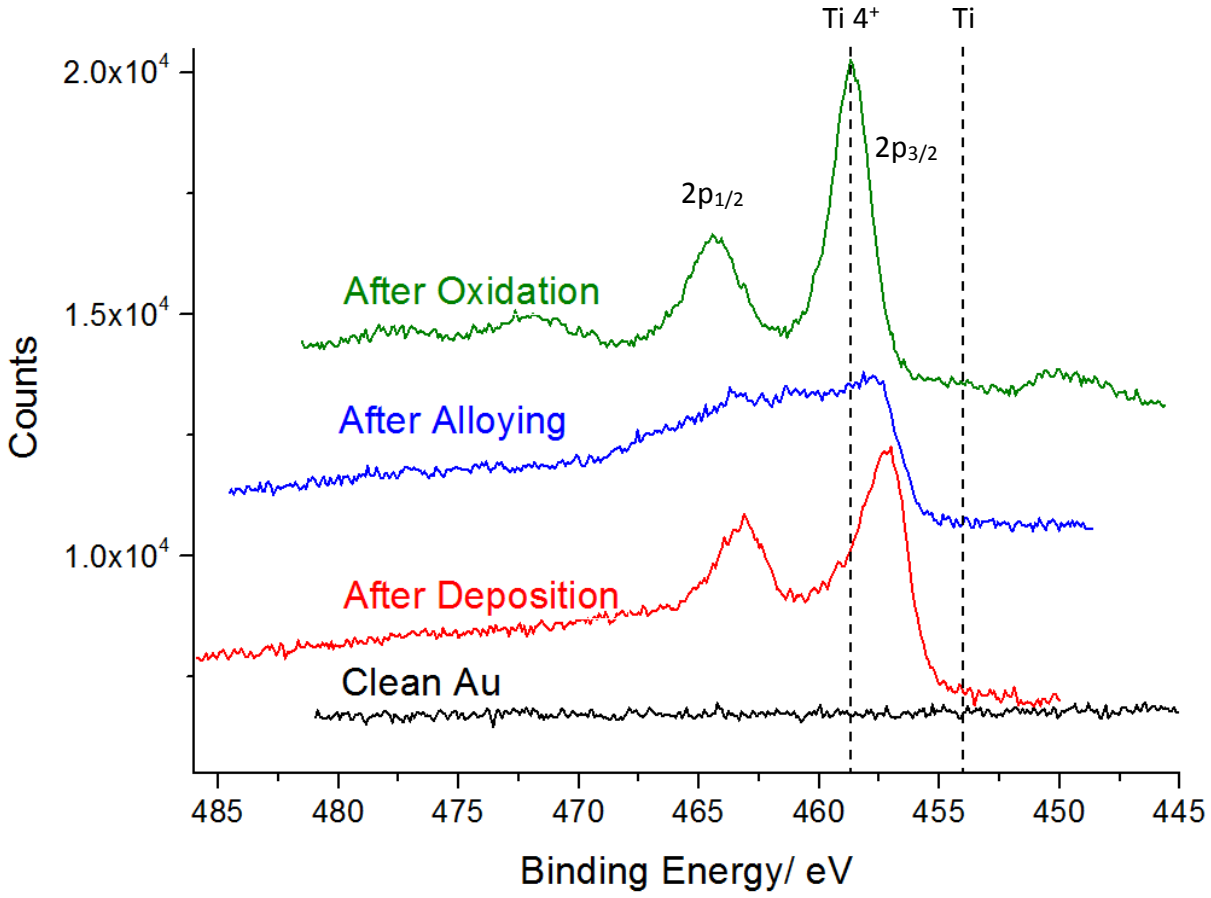

Figure 5.12 XPS data for 7 minute Ti deposition sample Ti 2p peaks for clean Au, after deposition, after alloying and the final product after oxidation. All peaks adjusted utilising the relevant C 1s peaks and spaced for ease of viewing, Mg filament, 10.5 kV. Dashed line represents expected unmodified Ti $2p_{3/2}$ peak positions for metallic Ti and Ti 4^+ as expected in TiO_2.[129]

Once again, the positions of these peaks give a clear indication towards the status of the surface and allow for an interesting comparison with the Au 4f peaks. The peaks for the sample immediately after Ti deposition have been positively shifted by ~2.2 eV compared to the expected value for pure Ti, though this can be explained by the presence of oxygen during deposition.

5.4.3 Oxygen XPS

The final area for consideration is that of the O 1s peak spectra, as has been briefly referred to in relation to some of the Ti data described above. These peaks can be seen below in Figure 5.13 for all stages of the synthesis.

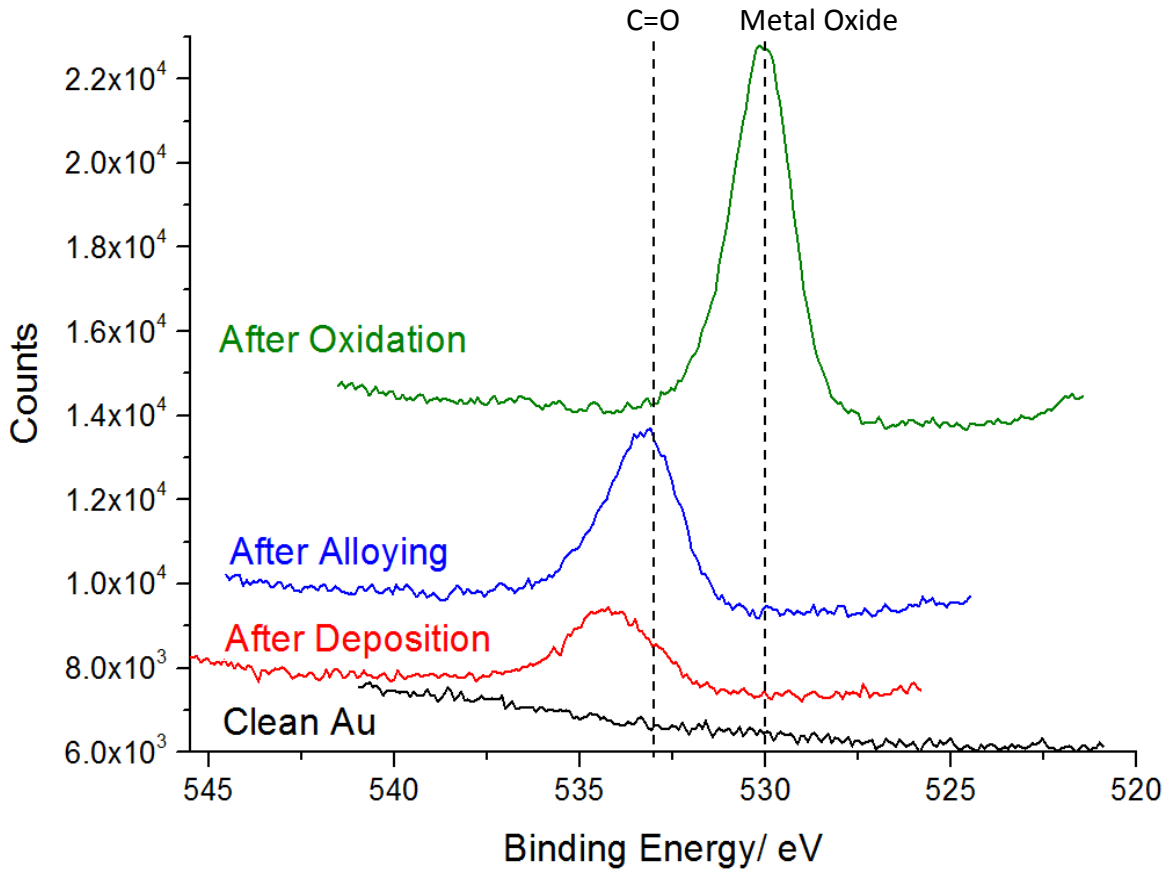

Figure 5.13 XPS data for 7 minute Ti deposition sample O 1s peak for clean Au, after deposition, after alloying and the final product after oxidation. All peaks adjusted utilising the relevant C 1s peaks and spaced for ease of viewing, Mg filament, 10.5 kV. Dashed lines represent expected metal oxide and rough C=O peak positions.

The clean Au scan indicates that the short heating procedure performed prior to synthesis (473 K for 30 minutes) removes any residual oxygen from the gold substrate. The oxygen peak is as expected for the sample post-oxidation, sitting at the expected value of ~530 eV for oxygen in a metal oxide system, as seen by Biener *et al.*[72] where a heating process of 600 K gave a major oxygen peak at ~530.3 eV.

However, what is more interesting is the appearance of the O 1s peak with deposition of Ti prior to alloying and oxidation of the sample. This is most likely due to oxygen present in the Ti prior to evaporation: notably what appears to be oxygen bonded to carbon, as indicated. This is not expected, but it is supported when the carbon 1s spectra are considered.

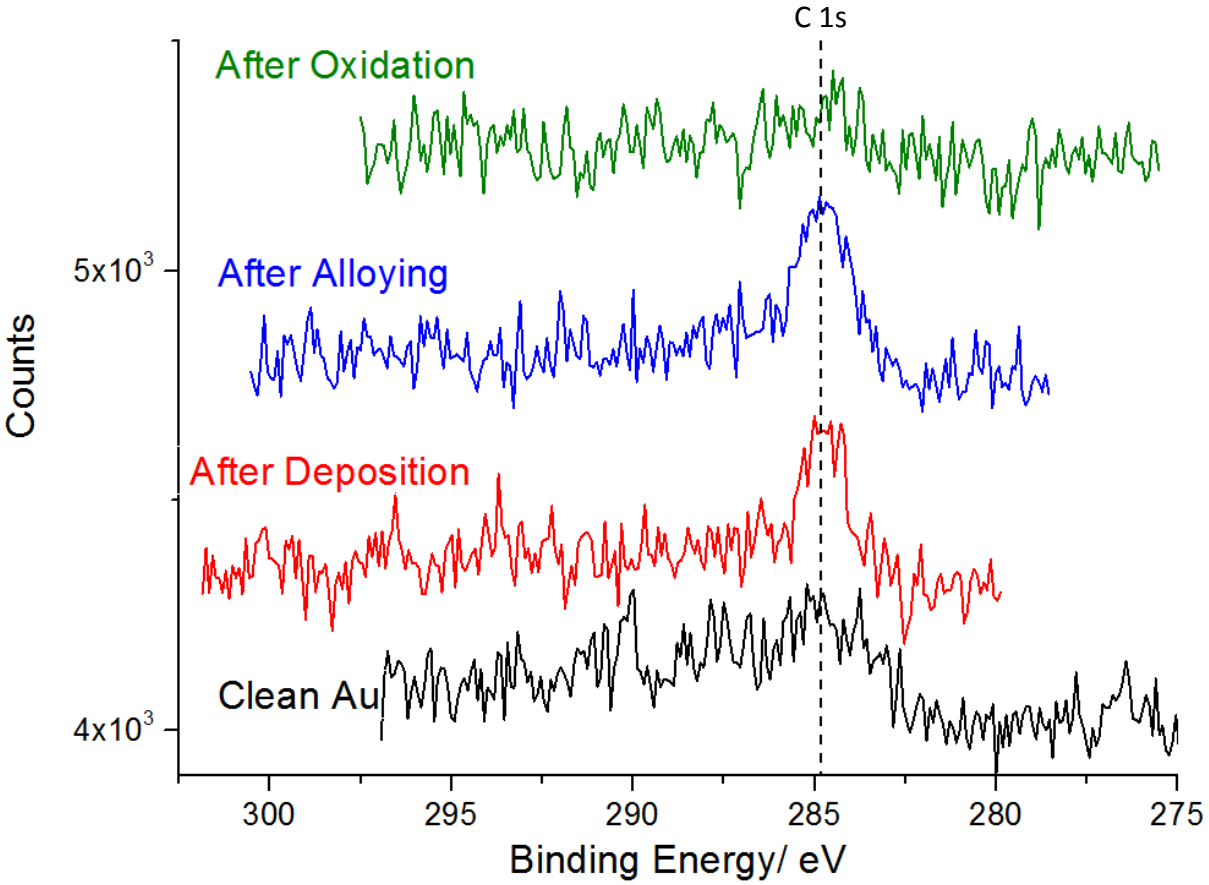

Figure 5.14 XPS data for 7 minute Ti deposition sample C 1s peak for clean Au, after deposition, after alloying and final product after oxidation. All peaks spaced for ease of viewing, Mg filament, 10.5 kV. Dashed line represents expected position for carbon, from which these peaks have been adjusted to fit to for reference to other scans.

As seen in Figure 5.14, carbon appears more clearly after deposition, but seemingly mostly vanishes after the final oxidation: the quantities present are miniscule compared to the other elements scanned, though this is to be expected. This adds an interesting conundrum for our use of the carbon as a reference for the middle two sections of the synthesis: if, as the oxygen spectra indicate, this carbon is in the form of C=O, the C 1s peak should reside at ~288.5 eV: however, if this were used as the reference value for the carbon, all spectra shown so far for the deposition and alloy steps would have a further

3.5 eV positive shift, which would then negate the supposed oxygen support for this by placing the peaks at 537.8 and 536.8 eV for the as deposited oxygen and after alloying, rather than values closer associated with the C=O bonds.

With this in mind, the most likely explanation is that the majority of carbon on the surface is C-C, giving the positions as determined in Figure 5.14: however, the oxygen that was deposited alongside the Ti is mostly bound to carbon, giving the positions seen in Figure 5.13 until the full oxidation has been performed. This can be supported by observing the composition of the oxygen peaks, noting the presence of multiple components, as seen in Figure 5.15,

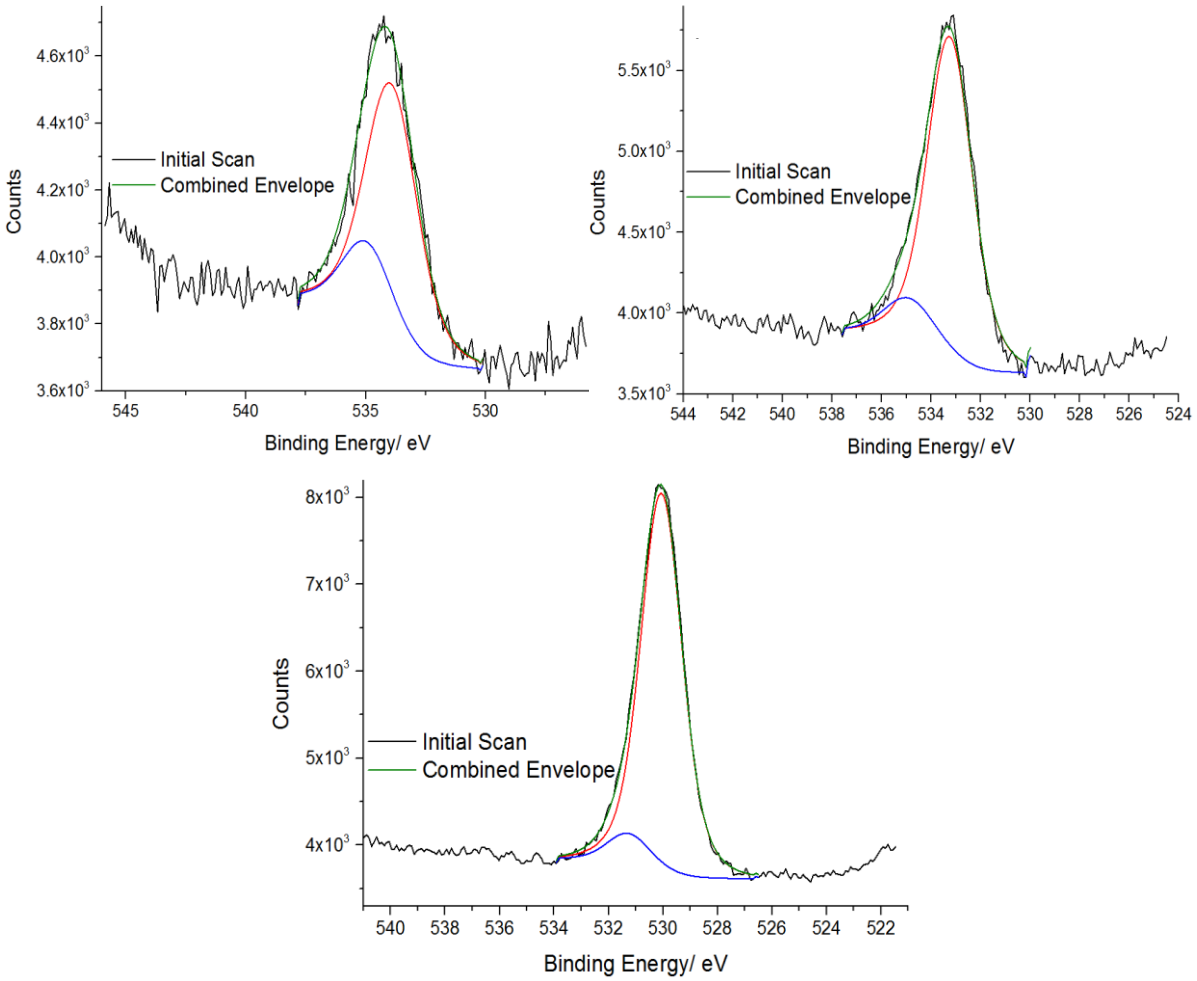

Figure 5.15 XPS O 1s spectra for 7 minute Ti Deposition sample. a) after Ti deposition, b) after alloying, c) after oxidation. Mg filament, 10.5 kV. Compositional peaks shown with combined full envelopes.

The oxygen 1s peaks appear to be composed of multiple forms: the specific peaks present depend upon the stage of the synthesis observed. The notable features are the smaller peaks (in blue above) present alongside the larger major peaks (in red). For the central stages of the synthesis the oxygen indicates the presence of oxycarbons on the surface, having been brought along with the deposited Ti. The presence of the two peaks in the 1s peaks prior to the oxidation are most probably present from C-O and C=O oxygen. This ties in with the secondary peak at ~531.7 eV for post oxidation: this is most likely to be due to a small presence of metal carbonate formed from the initial presence of carbon species coming through with the final titania. The majority of the oxygen present is that from TiO_2, as indicated by the larger peak at ~530.1 eV and thus we can say with a reasonable degree of confidence that the vast majority of the titania formed is TiO_2.

However, because of this, we know have to consider the unexpected Ti peak shifts during deposition and alloying, originally considered to be due to oxygen contamination resulting in titania formation: the O 1s peaks do not indicate the presence of any metal oxide oxygen, removing titania from consideration. We must conclude that these shifts in the Ti 2p peaks most likely originate from interactions between the titanium and the gold, the results of which were observed in the Au 4f spectra.

5.4.4 Quantification of XPS Spectra

The XPS data collected by us here has indicated that the final product of our system does appear to be TiO_2 with no indication of impurities in the titania. This is the major contributor of XPS to our investigation: however, another use for the XPS data is available to us here that allows for a more quantifiable determination of the final product.

As described by Seah[134], there are methods by which the coverage of an adsorbate onto a surface can be calculated utilising XPS. Two particular equations are available for the determination of coverage using these data, depending on whether the adsorbate has coverage below or above 1 monolayer. The equation for the calculation of the sub-monolayer coverage of A (φ_A) on a substrate B can be seen below in Equation 12.

$$\varphi_A = \frac{\lambda_A \cos\theta}{a_A} \times \frac{I_A/I_A^{\infty}}{I_B/I_B^{\infty}}$$ **Equation 12**

Calculation for sub-monolayer coverage of substrate B by adsorbate A.

With I_A/ I_B corresponding to the detected signal of A/B (corresponding to the XPS peak areas), I_A^{∞}/ I_B^{∞} to the signal from pure A/B (also known as the atomic sensitivity numbers), λ_A the inelastic mean free path of A in nanometers, θ is the angle of emission and a_A is the thickness of one monolayer of A in nm. For coverages above 1 monolayer, Equation 13 is utilised instead, with d_A being the thickness of the adsorbate layer in nanometres:

$$d_A = -\lambda_A \cos\theta \ln\left(\frac{I_A^{\infty} I_B}{I_A I_B^{\infty} + I_A^{\infty} I_B}\right)$$ **Equation 13**

Calculation for Coverage of substrate B by adsorbate A thicker than 1 ML.

By utilising these equations alongside the peak data from our XPS spectra, we can calculate the coverage of the gold substrate by adsorbate Ti in our samples and thus provides another method by which we can quantify titania formation on the surface alongside the AFM data.

Table 5.1 Ti coverages determined via XPS Ti 2p and Au 4f peaks. Calculated coverages for initial Ti deposition and final oxidised samples are displayed.

Sample	Deposition time/ min	Initial Ti Coverage/ nm	Ti Coverage after Oxidation/ nm
01	10 (longer alloying step)	1.41	1.67
02	7 (longer alloying step)	1.03	1.05
03	8	1.27	1.51
04	7	0.999	1.08
05	6.5	0.892	0.882

Table 5.1 shows the values determined from our XPS data for samples that have been previously shown via AFM such that they bracket the formation of titania particles and

the beginning of film formation. Samples #01 and 02 had extended alloy times, as indicated, to allow for the collection of XPS of the alloyed sample surface. The calculated values for Ti thickness appear to be behaving in the expected manner, with Ti thickness decreasing as deposition times decrease.

By comparing samples 02 and 04, we can see the effect of the longer alloying step on our samples: the titania thickness on 02 is only an increase of ~0.02 nm from the initial Ti, while 04 shows an increase of 0.09 nm. This indicates that by increasing the time spent alloying, the quantity of titania produced post oxidation relative to the initial Ti thickness is decreased. This is not surprising, as increasing the alloying time allows for more Ti to be lost in the gold bulk and thus not be available during the oxidation process.

These values also make for an interesting comparison with those measured via AFM for the thickness of deposited titania, as described in Figure 5.3. It was determined that ~0.2047 nm Ti is deposited per minute. The values calculated via XPS are ~0.4 nm less than would be expected using the AFM measurements: this is not necessarily unexpected, as the titanium used in the AFM thickness measurements was deposited on a silicon substrate, not gold as for our actual samples and some could have been lost into the substrate during deposition, thus giving the lower values calculated above.

5.5 Electrochemistry

Initially, electrochemical experiments were performed on gold/glass substrate samples, using the BCEC described in Chapter 3, with steel foil and silver epoxy forming electrical contact between the sample and the cell. It was hoped that these samples would provide groundwork prior to synthesising samples on the 10*10 arrays, so suitable conditions synthesising the desired particle densities could be determined.

It was expected that these would function similarly to the (111) crystal used in Chapter 4, especially as the gold/glass substrates form (111) terraces when exposed to heat annealing, (Figure 5.4 i); however this turned out to not be the case.

We shall first consider the CV for the clean glass/gold substrate prior to deposition: Figure 5.16 shows such a CV of the gold/glass substrate, with identical potential limits as used with the Au(111) crystal. No particular features can be seen, which is unexpected if the expected Au(111) faces were present, as the perchlorate ion adsorption/desorption peaks should appear at ~0.8 V.[75]

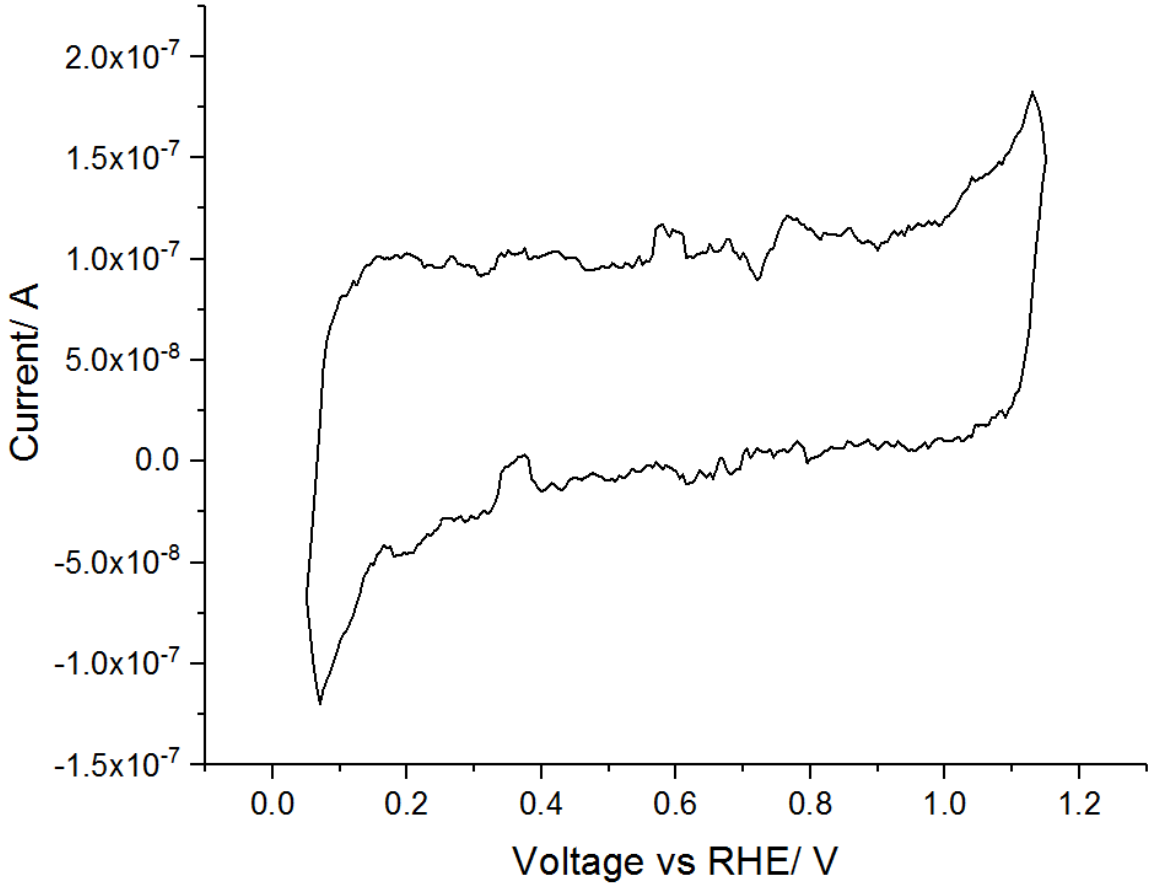

Figure 5.16 1st scan of clean glass/Au substrate. Scan has been smoothed so as to remove unnecessary noise from image. 0.05-1.15 V, Scan speed = 50 mV s^1, electrolyte = 0.1 M $HClO_4$

This indicates a distinct lack of activity from the substrate, which should not be the case: this continues when for the clean gold/glass with carbon monoxide introduced into the electrolyte as seen in Figure 5.17. Initially, introducing CO had no appreciable effect on the electrochemistry of the clean substrate. However, when the potential limit was subsequently increased to 1.55 V with CO present, the CV appears much closer to the expected gold CV, especially with the appearance of the perchlorate ion adsorption/desorption peaks, also indicating the presence of Au(111)[75]. The final scan is shown for the surface after this increase in potential, but with CO purged from the electrolyte, indicating the gold features remain: this indicates that some form of

contaminant was present on the surface prior to increasing the potential, whereupon it was removed and no longer affected the activity of the surface.

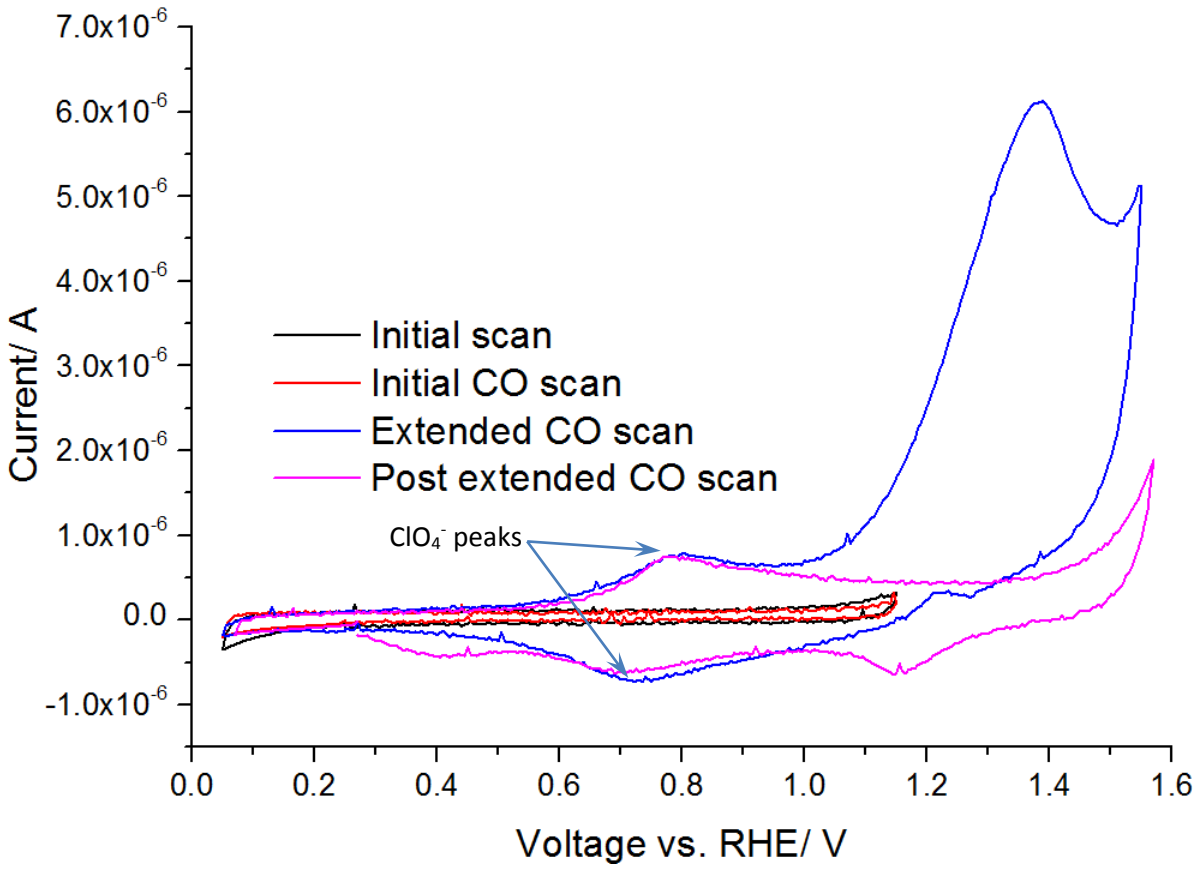

Figure 5.17 1st scan of clean glass/Au substrate at different stages of experimentation: initial scan in electrolyte limited to 1.15 V, same scan with CO introduced, the extended scan with CO present and scan taken in purged electrolyte after extended CO scans. Higher potential appears necessary to remove contamination of surface before features become present. Scan speed = 50 mV s^1, electrolyte = 0.1 M $HClO_4$

This indicated that the gold/glass substrates require a larger potential range to remove some form of contaminant from the surface: unfortunately, this was proven to not be the case with further testing of the titania modified substrates. The same lack of features is seen with the initial scan from 0-1.1 V, with a similar lack of change being observed with CO addition: however, unlike the previous sample, this situation was repeated when the potential limit was once again extended to 1.55 V (Figure 5.18), indicating that some other factor is responsible.

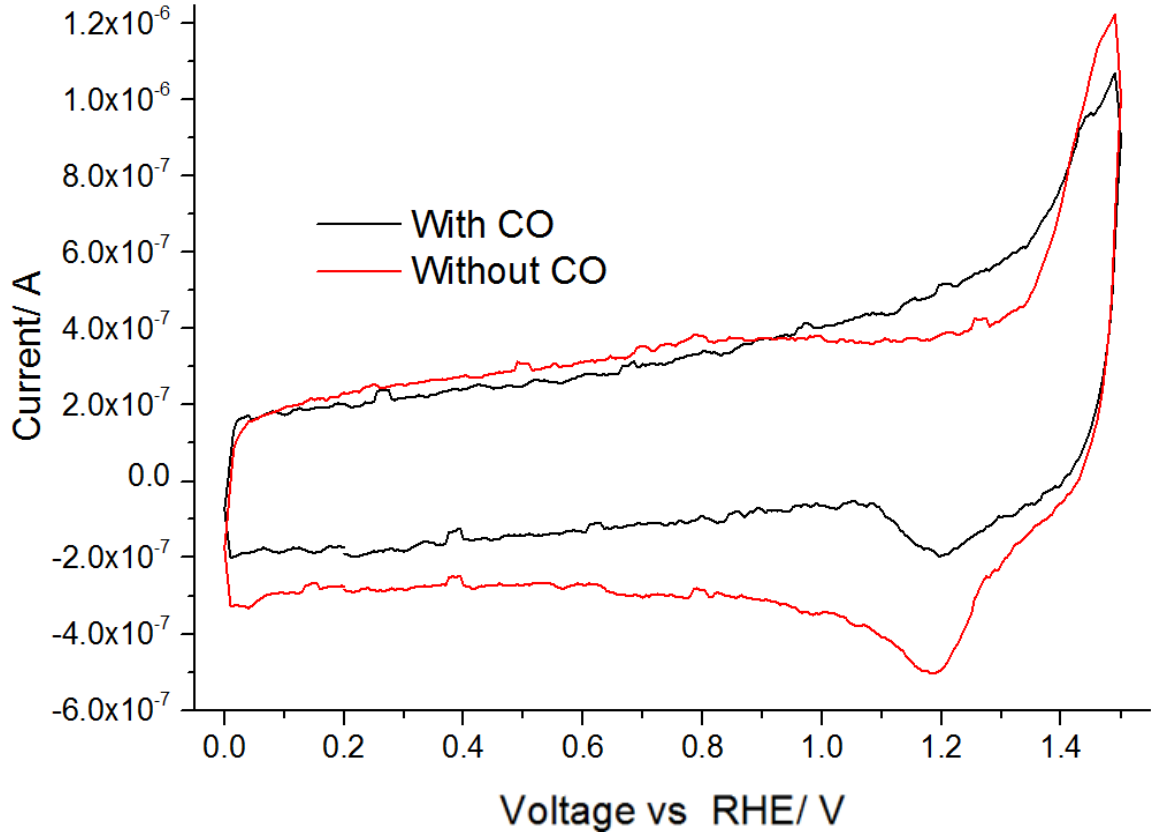

Figure 5.18 6.5 min initial Ti deposition sample CV scans. Scans have been smoothed to remove unnecessary noise. Shows scans with and without CO present. 0-1.5 V, Scan speed = 50 mV s^{1}, electrolyte = 0.1 M $HClO_4$

It can be seen that there is very little apparent effect caused by the introduction of CO to the electrolyte; possibly some slight inhibition of oxide formation but the characteristic CO oxidation peak is not present. It was considered that the sample was no longer viable, as it had been used for AFM imaging: this was proven when the sample preparation was repeated with identical conditions. This repeated sample was not imaged via AFM, due to concerns with exposure to atmosphere interfering with electrochemical experiments, as indicated above.

This sample was first scanned with a 0-1.1 V limit, and differs drastically from initial scans of earlier samples: a much clearer indication of surface activity is immediately present. These peaks are most likely to be due to the desorption and adsorption of electrolyte ClO_4^- ions, though they do not correspond as well as those seen with earlier CV data, notably the forward and backwards scans appear to have shifted apart from each other, possibly indicating an issue with the conductivity of the sample.

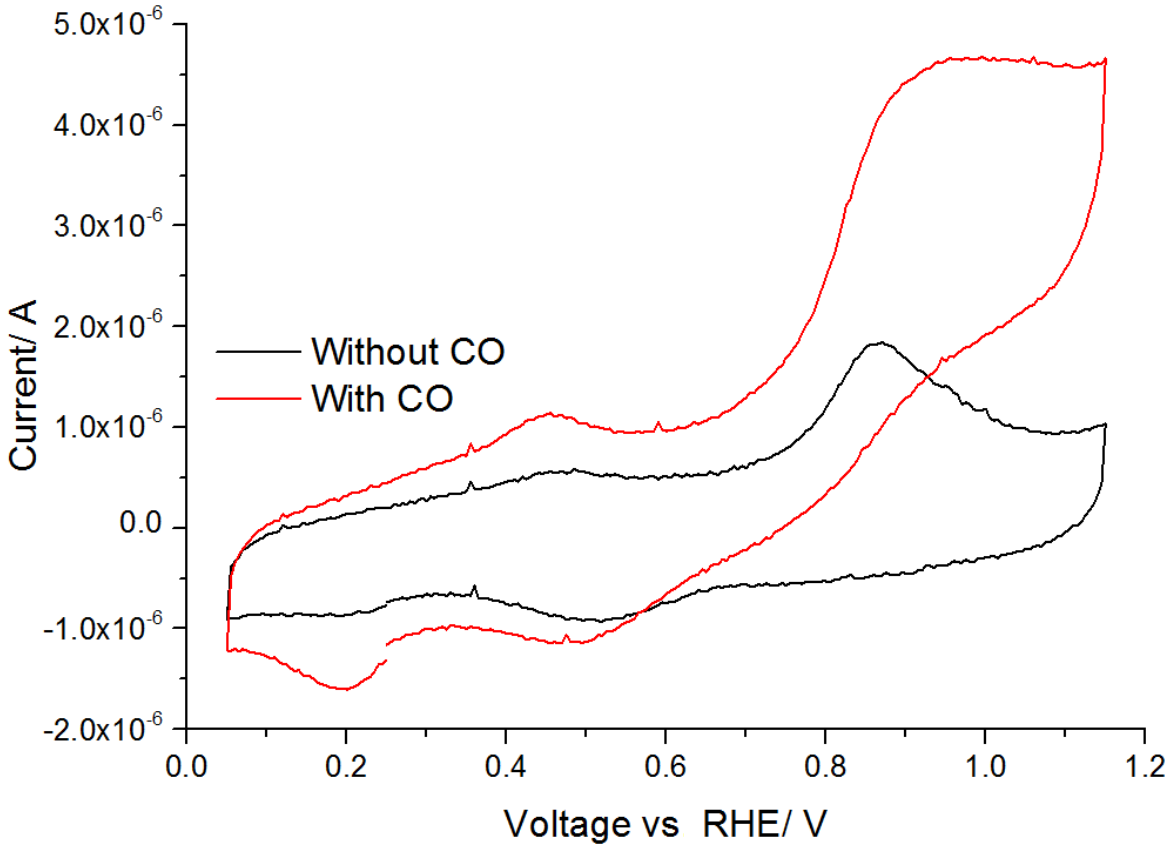

Figure 5.19 1st scan of repeated 6.5 min Ti sample with and without CO. 0-1.1 V, scan speed = 50 mV s^{1}, electrolyte = 0.1 M $HClO_4$

The addition of CO was also more effective than previously, indicating that a large period of exposure to atmosphere may have had a deleterious effect on the gold/glass substrates. Unfortunately, this is unlikely as similar issues were seen for tests on gold/glass where cleaning was performed immediately prior to electrochemical testing.

Evidence for a separate cause for this odd activity was seen when we consider a separate set of samples with identical synthesis conditions. These samples were initially synthesised with the belief that samples required as minimal time as exposed to atmosphere possible prior to electrochemical testing. However, it became apparent upon testing the first of these samples that the data collected for the clean gold/glass substrate as well as the supposedly over-exposed to atmosphere samples were more indicative of the usual response to testing than initially expected. It was decided, alongside a dwindling supply, that the gold/glass substrates would not be suitable for electrochemical testing of our inverse catalyst samples, as any data collected would be considered suspect, as well as lacking any demonstration of high-throughput production methodology. As such, more focus was put towards utilising the 10*10 arrays.

5.6 10*10 Electrochemical Arrays

Due to a number of issues, few samples were produced using the gold 10*10 arrays, and no significant data were collected with those that were. As such, a separate chip type was utilised for the final samples: 10*10 arrays identically arranged to the gold chips, but with ITO utilised as a replacement for gold, for both electrodes and the connecting tracks. Because of time constraints and issues with production of the arrays, only one sample was produced with these ITO chips.

200-250 nm gold was initially deposited on the ITO electrodes to act as the base for subsequent deposition of titanium. Ti deposition times between 6.25 and 8.5 minutes, with 15 second intervals were performed, allowing for the production of 10 electrode sets of particle densities. These limits were chosen to allow for greater comparison with the samples produced in Chapter 4, with 6.5, 7 and 8 minute deposition times giving titania coverages of 15.8, 28.8 and 68.0 %, respectively. These correspond well with the coverages seen in the Au(111) crystal samples, where a maximum coverage of 63.1 % was tested, as well as allowing for investigation into higher and lower coverages.

This sample performed considerably closer to that expected for the CO oxidation on gold, as seen in Figure 5.20 (only first forward scans are shown for ease of viewing) with what appears to be a trend similar to that of the Au(111) samples.

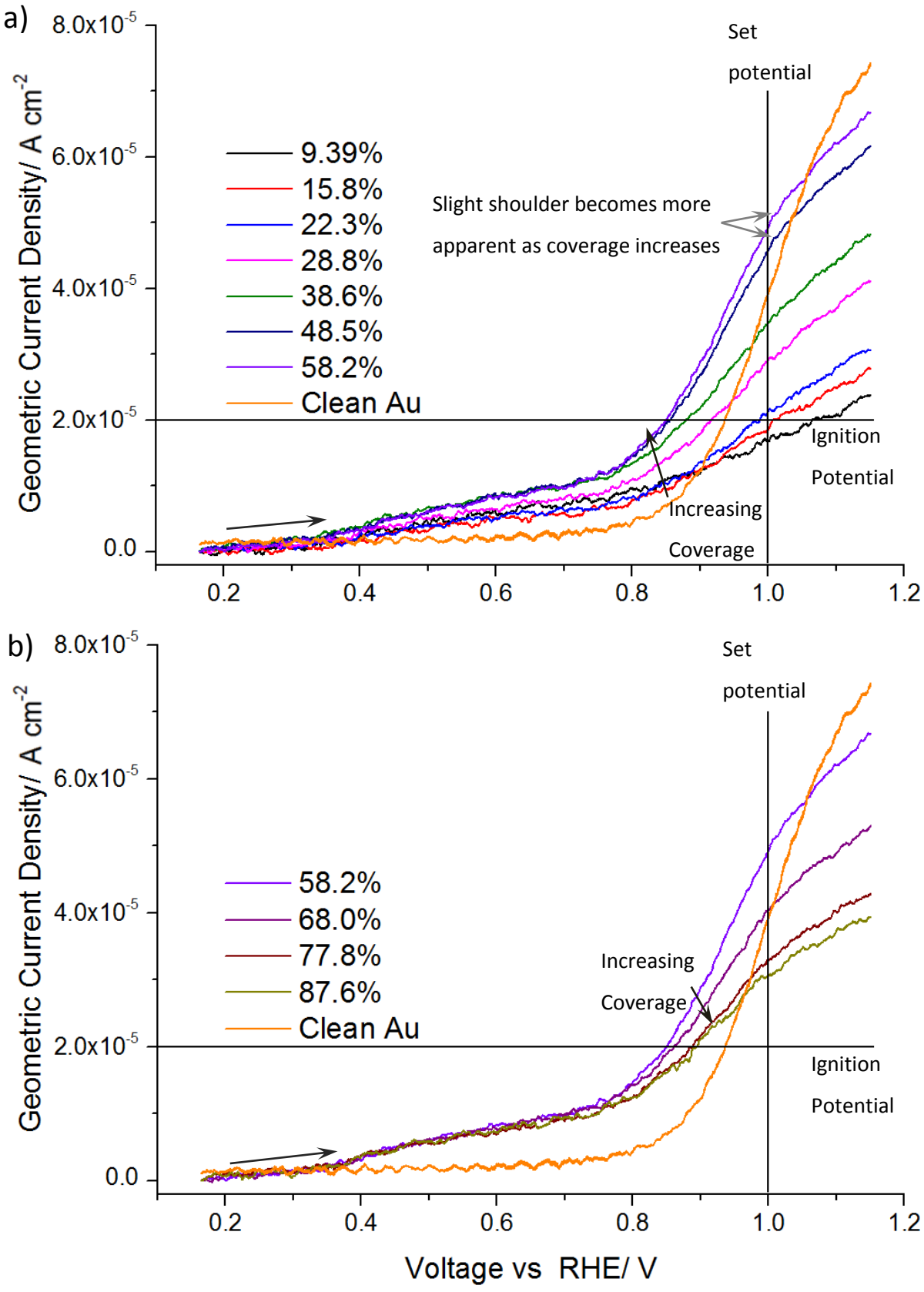

Figure 5.20 1st Forward scan of CO oxidation for ITO array sample alongside clean Au. a) First 7 particle coverages indicating increasing activity, b) peak activity and subsequent decrease for final 3 coverages. Percentage refers to titania surface coverage. 0.15-1.15 V vs RHE, Scan speed = 50 mV s^1, electrolyte = 0.1 M $HClO_4$

The CVs have been split so as to give a clearer illustration of the effect of increasing titania coverage on the CO oxidation. As the coverage is increased, the activity increases until ~58.2 % coverage is reached, with a shoulder becoming more prominent as indicated; the activity then decreases as the titania coverage is further increased past this point. It should be noted that the data collected here using the ITO chip are not as clean as would be ideal: issues with conductivity were prevalent in these chips. These issues were believed removed, though some concern remains that silicon removal was not consistent across pads and some variation in conductivity may still be present. Ideally, repetition of this sample would be performed to confirm the data collected above; however time constraints prevented further synthesis than this single sample. As such, whilst the data above does allow for investigation into the inverted catalyst system, further clarification is required before the conclusions reached here can be considered fully supported.

Despite these issues, a trend can be made out across the sample, though some degree of uncertainty is present. We can utilise these data in a similar manner as was performed for the Au(111) samples: first, we will compare the current seen at 1 V, chosen as it was considered to give the clearest indication of change in activity across the substrate, as well as to provide suitable comparison with previous data.

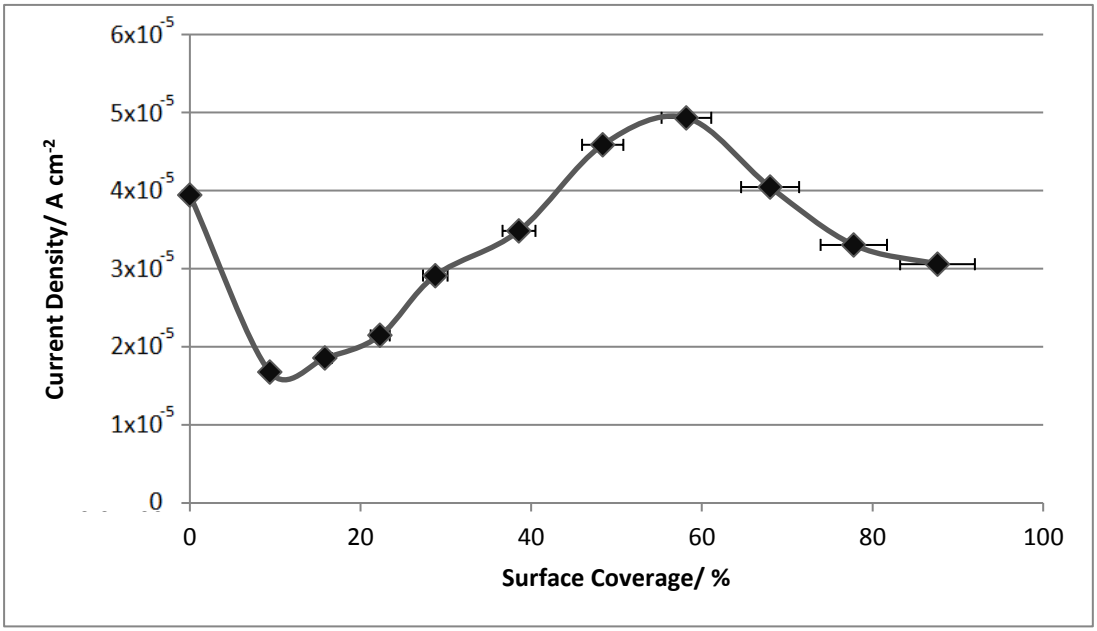

Figure 5.21 Current Density vs surface coverage for ITO array sample. Current values taken at 1 V.

An initial deactivation of the gold is seen with the addition of titania, as was present for the Au(111) supported samples, followed by increasing activity as the titania coverage increases, with a clear maximum in activity seen at ~58 % coverage, though whether the true peak position lies higher or lower than this is unknown without further investigating of intervening coverage values. This differs from the activity observed for the Au(111) supported samples, where the activity was still observed to be increasing at 63 % coverage, though a slight indication of the beginnings of a peak in activity were present.

Using the images in Figure 5.4, we can additionally estimate the particle separation values that correspond with this sample, giving us a better idea of the possible area affected by the particles on the surface. Figure 5.22 shows this comparison between current density and the estimated average particle separation values, with 1 V used once more as the set potential.

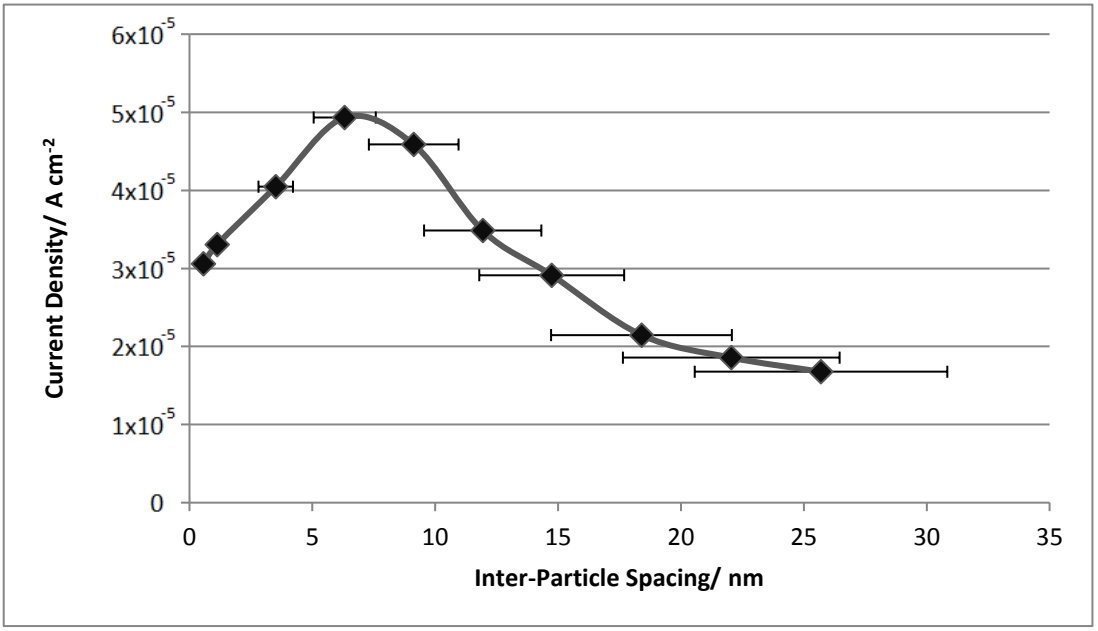

Figure 5.22 Current density vs inter-particle spacing for ITO array sample. Current values taken at 1V.

The peak in activity is once again clearly visible, though comparison with the Au(111) samples shows once more that the peak indicated here is at lower effective coverage levels than would be expected from the Au(111) supported titania samples previously tested, where the beginnings of the activity peak are indicated to be lower than ~4.7 nm separation, compared with 6.3 nm here, though this is most likely due to these values being for the geometric data. An interesting comparison comes from

observing the particle spacing for the Au(111) samples alongside those determined here: an average decrease of ~17 % in separation is seen for the ~11.5 nm particles compared with ~20 nm diameter seen for the samples here. Such a decrease in separation is not unexpected, as maintaining similar coverages with smaller particles requires a concurrent decrease in spacing: however, the observed decrease is about half what might be expected for such a change in particle size, though this may be due to the reasonably large degree of variation in particle size observed from AFM/STM imaging of our surfaces. However, despite this, with the data collected above, we can see that there is a clear trend in the activity of the particles with increasing activity as surface coverage increases, culminating in an activity peak appearing at ~6.3 nm.

This trend continues when we consider the ignition potential (with $2*10^{-5}$ A cm^{-2} as the set current density), leading to a similar peak in activity at ~58 % coverage. However, as with the set potential data, this trend differs significantly from that seen on the Au(111) samples; where the ignition potential remained reasonably constant prior to a significant negative shift as the coverage increased above 50 %, in addition to the potentials being considerably more negative than those seen here.

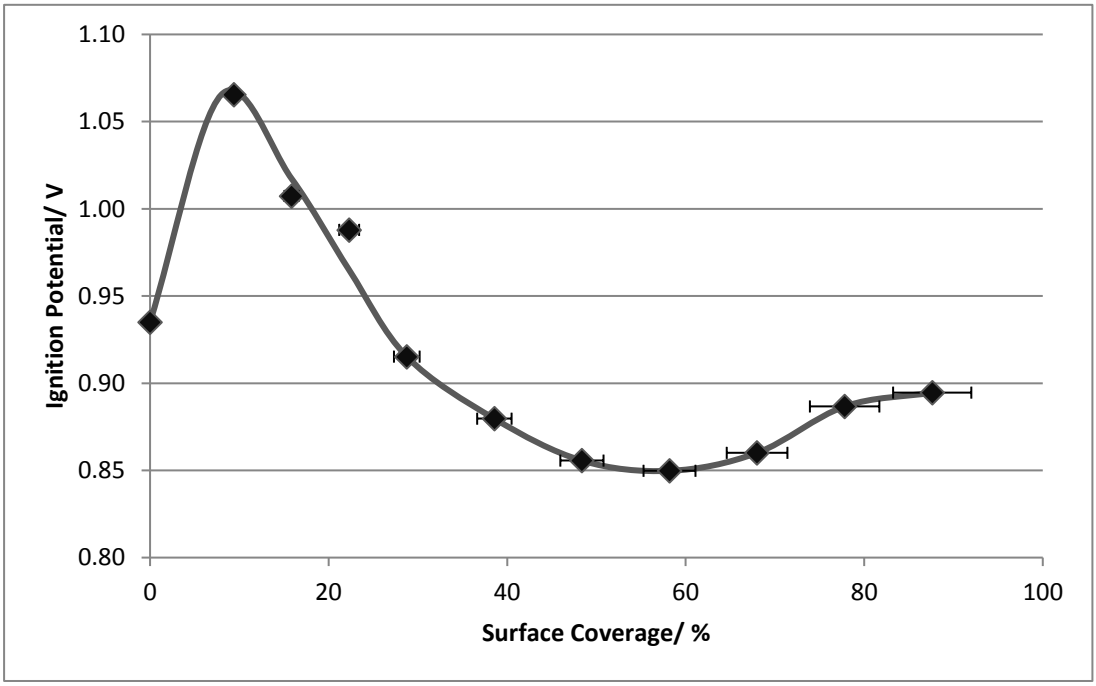

Figure 5.23 Ignition potential (potential (V vs. RHE) at which current density reaches $2.0x10^{-5}$ A cm^{-2}) vs Surface Coverage (%) for ITO array sample

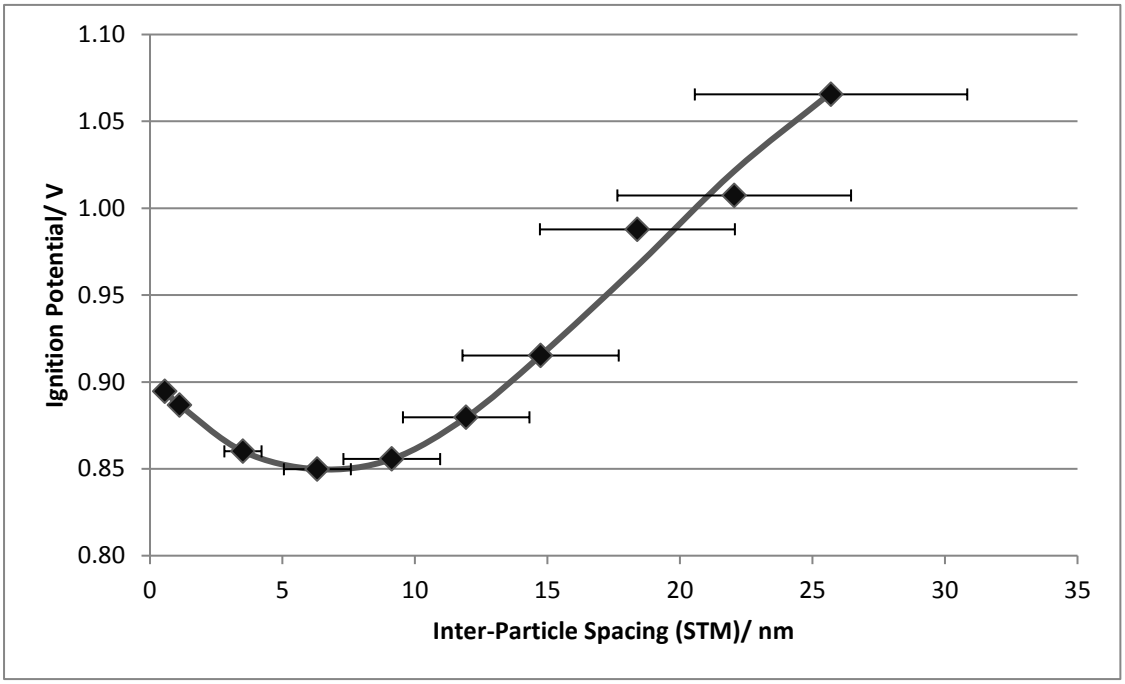

Figure 5.24 Ignition potential (V vs RHE) (potential at which current density reaches $2.0*10^{-5}$ A cm^{-2}) vs inter-particle Spacing (nm) for ITO array sample

Once again, an initial deactivation is seen with the addition of titania to the surface, followed by increasing activity as further titania is applied to the surface: however, this deactivation is less potent than that observed on the Au(111) supported samples, most likely due to differences in the nature of sites on the polycrystalline gold used as the support here compared with the (111) surface, as well as the extent to which these sites are decorated by the titania.

Unfortunately, due to issues during scanning of this sample, we cannot provide the specific current density values as calculated from the electrochemical data (specifically, the formation of oxide on the surface). However, with the AFM images of the titania modified surfaces, we can provide an less exact version by modifying the geometric area with our assumed titania coverage of the surface, thus determining a value for the specific area of gold remaining. This is not ideal for determination of the specific area, but as no other methods are available it will be sufficient for use here. The electrochemical data modified with these specific area values, alongside the clean gold, is shown below in Figure 5.25.

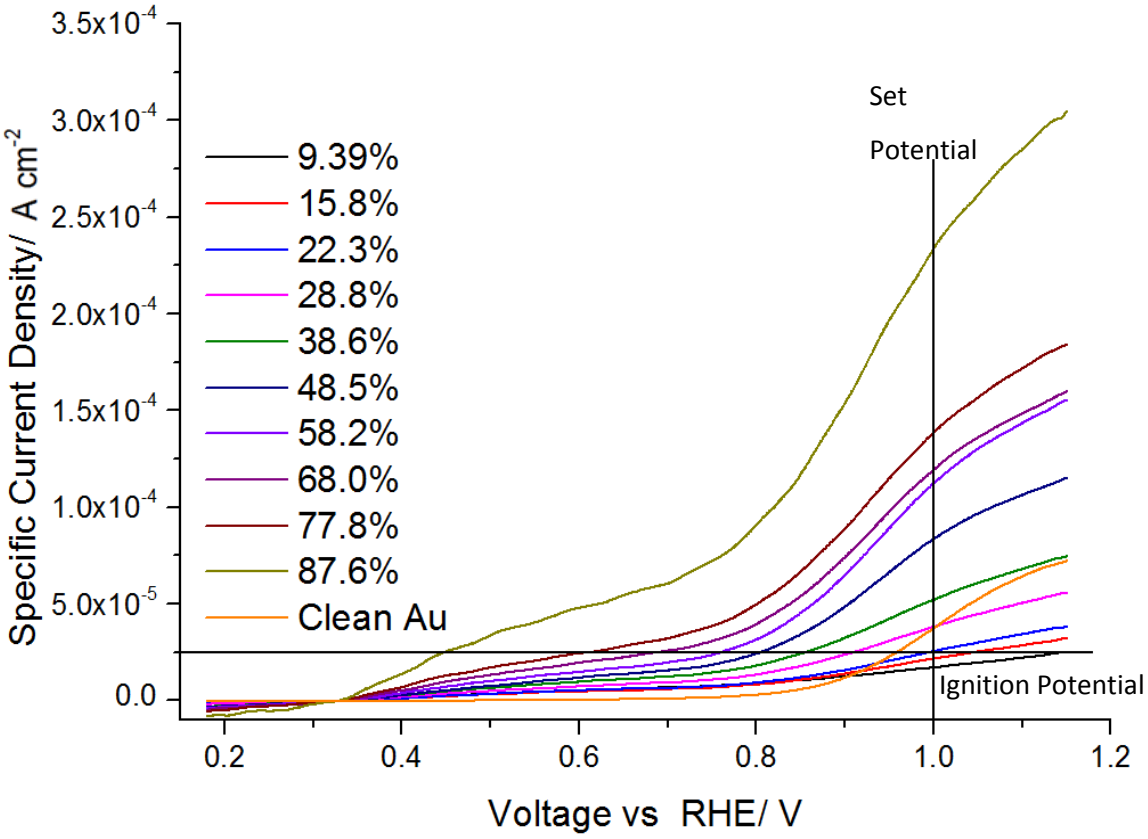

Figure 5.25 1st Forward scan of specific activity CO oxidation for ITO array sample alongside clean Au. Percentage refers to titania surface coverage. 0.15-1.15 V vs RHE, Scan speed = 50 Mv s^{1}, electrolyte = 0.1 M $HClO_4$

It can be seen that there is a very distinct change in the CV data when we consider the specific activity. Notably, there is no longer a decrease in activity with coverages above 58 %; whilst a shift in the activity peak to higher coverages is not unexpected considering we are focussing solely on the active gold in the system, we might have expected it to remain here. This is exemplified when we consider the current density at a set potential (1 V) in Figure 5.26.

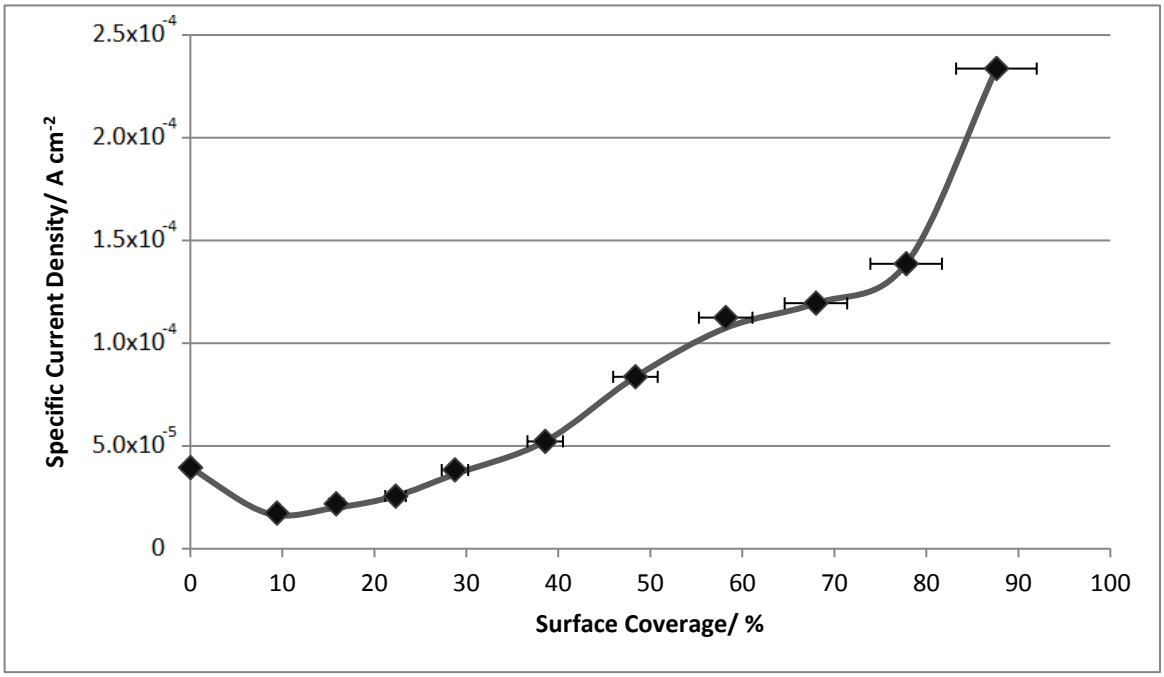

Figure 5.26 Specific current density vs surface coverage for ITO array sample. Current values taken at 1 V.

The initial deactivation of the surface with titania formation remains present for the specific activity data, with increasing activity as the surface is further covered. However, unlike what would be expected for this system, no peak in activity is seen at high coverage values; indeed, despite the apparent beginnings of what may be a peak in activity at ~70 % coverage, the current density suddenly increases past this point. A similar effect is observed when we consider the inter-particle spacing, with the decreasing activity gradient being interrupted by the higher coverage samples. Of interest is how these data correlates with those observed for the Au(111) supported samples produced in chapter 4: the progression of the specific current density is similar, but once again the deactivation of the surface appears less prevalent than seen for the Au(111) crystal, further supporting our supposition of differences in sites on the surface.

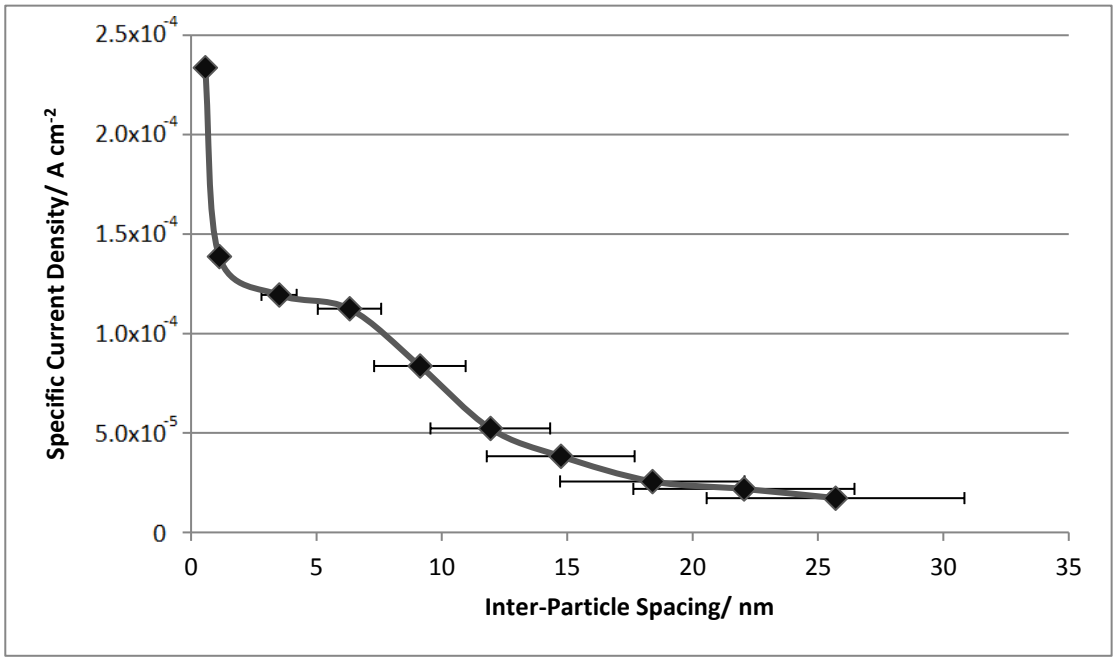

Figure 5.27 Specific current density vs inter-particle for ITO array sample. Current values taken at 1 V.

Such a severe change in the activity for the high coverage samples is very unexpected, as it would be thought that any changes should proceed in a relatively consistent manner, without such a drastic modification appearing. It is possible that the data are being affected by issues proceeding from the intrinsic limitation from considering the current density at a set voltage; notably that as current density increases, the increasing contribution of mass transport will impede our understanding of the surface kinetics.

Such a consideration also provides our reasoning behind expecting an activity peak; eventually the improvement to activity of the gold provided by addition of titania to the surface (whether via reactant spill-over or Ti-Au interface sites) will reach a saturation point where further addition of titania only removes active gold without activating further gold. At this point, it is worth considering why the activity may be acting in such an unexpected manner: the most likely cause is that our estimates for the coverage/inter-particle spacing of the surface do not properly represent the actual surface conditions, as we only possess images for the 6.5, 7 and 8 minute depositions (15.8, 22.3 and 68.0 % coverages, respectively) on the gold/glass substrates with other values extrapolated from them. As such, we must expect errors in the considered coverage, though these are most likely fairly minimal except for the coverages estimated above 68 %, where such errors

are most prevalent: as the limit for agglomeration of particles is unknown to us, any estimates for the surface coverage at this level are suspect, and as such are most likely not suitable for use by us here.

With this in mind, if we eliminate the specific data for coverages above 68 %, where our confidence in the accuracy of the actual coverage is severely reduced, a very distinctive pattern emerges: an onset of activity is formed, with a reducing gradient at higher coverage levels.

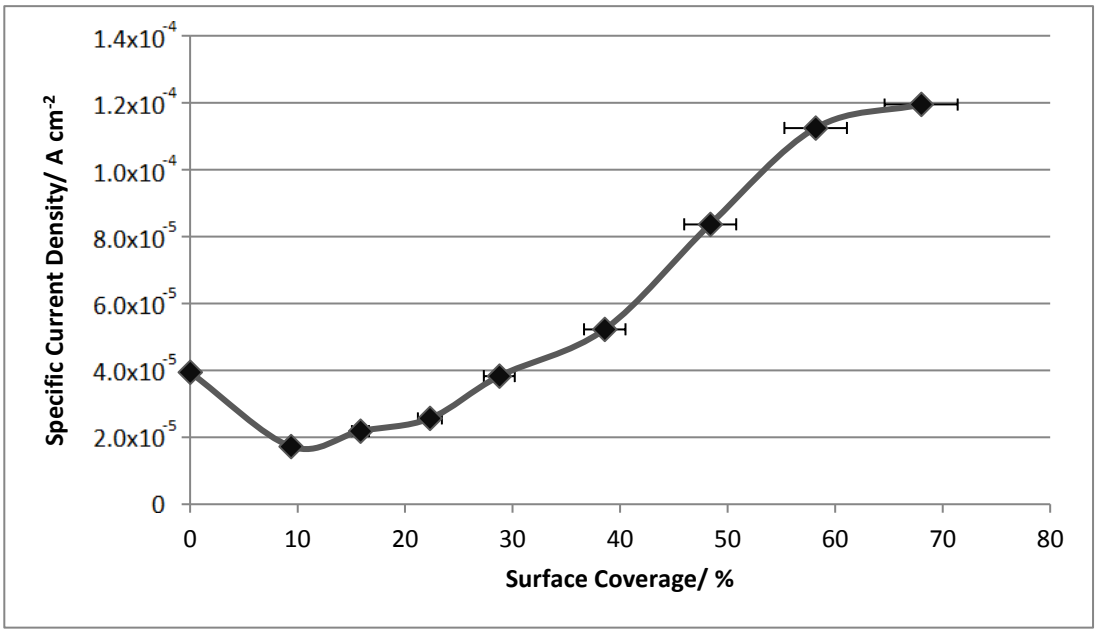

Figure 5.28 Specific current density vs surface coverage for ITO array sample excluding coverages above 68 %. Current values taken at 1 V.

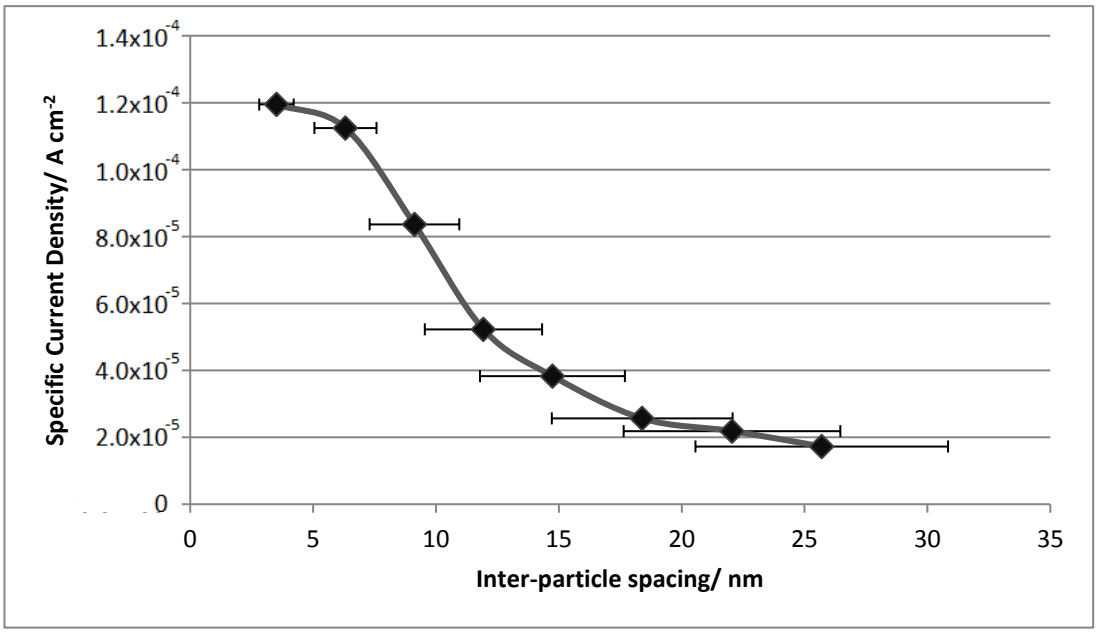

Figure 5.29 Specific current density vs inter-particle spacing for ITO array sample excluding coverages above 68 %. Current values taken at 1 V.

Once again, we must consider that we are limited by mass transport considerations for the high current densities and thus these data must be appraised with this in mind: despite what appears to be the beginnings of an activity peak, without removal of mass transport limitations we cannot declare whether this is an accurate representation of the activity progression with further titania formation.

At this point, we must consider the Ignition potential for the specific activity, where mass transport limitations are of less concern: the initial deactivation with the addition of titania remains, as would be expected given the previous data. However, the gradient for the ignition potential as the titania coverage is increased from this point is very consistent, with no indication of a plateau being reached, or even beginning, as would be expected for this system.

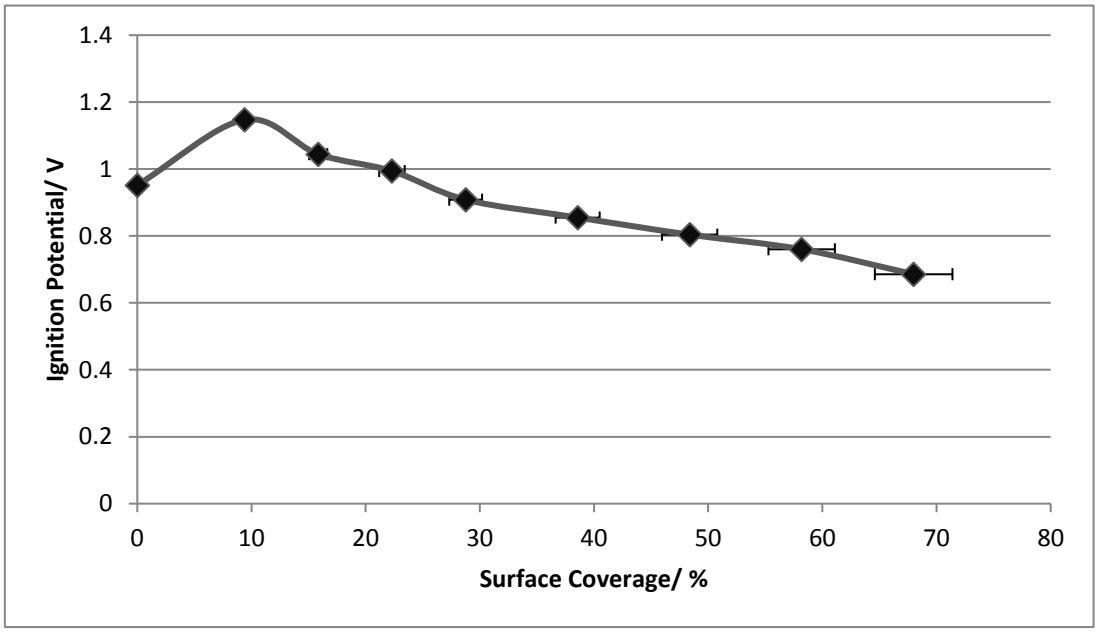

Figure 5.30 Ignition potential (potential (V vs RHE) at which current density reaches $2.5*10^{-5}$ A cm^{-2}) vs surface coverage (%) for Specific activity ITO array sample.

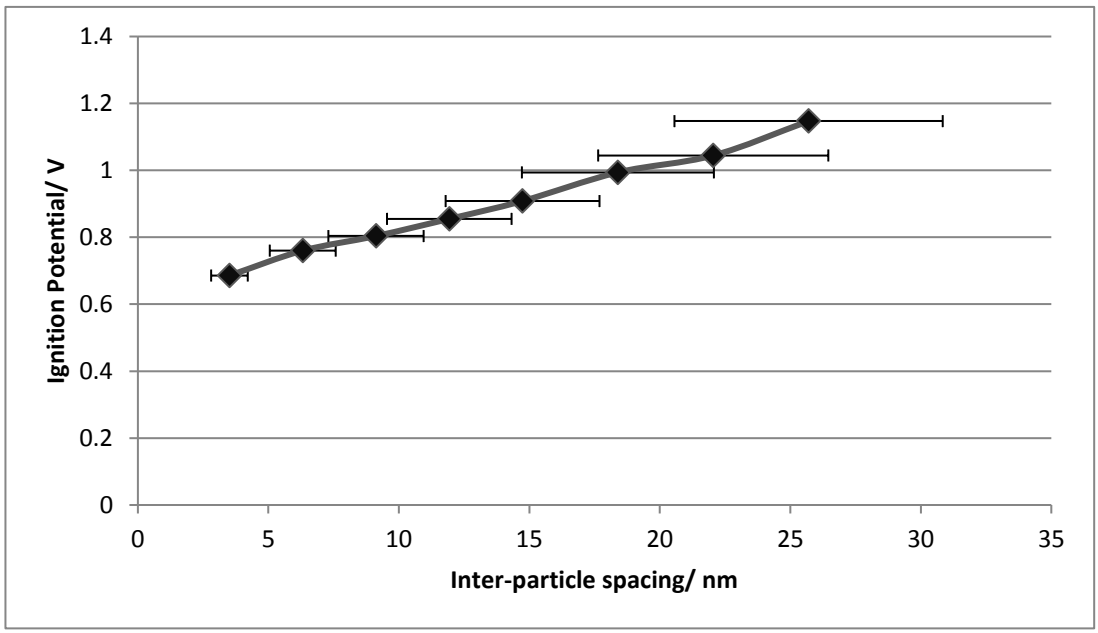

Figure 5.31 Ignition potential (V vs RHE) (potential at which current density reaches $2.5*10^{-5}$ A cm^{-2}) vs inter-particle spacing (nm) for Specific activity ITO array sample

This lack of any indication for a plateau in the ignition potential is somewhat unexpected; however, this may be an artefact of the fact that we must consider such a low current density to include the lower coverage samples, and the beginnings of such a plateau becomes visible if slightly higher current density values are utilised. As such, we may consider that the activity is indeed reaching a plateau, which falls in line with what is expected for these two mechanisms.

A peak in activity is expected to appear for the specific data, as once all gold on the surface is activated, further deposition of titania on the surface should give a decreased relative activity, as active gold is effectively removed from the surface. This activity peak should, however, appear at lower coverage levels for the geometric data due to a similar deactivation of the surface occurring at high coverage levels, but with two sources responsible: the intrinsic removal of active gold described above for the specific system remains, but for the geometric data this is also compounded by a decreasing ratio of active gold to total surface area, which also leads to an effective decrease in observed activity. This also explains why the observed peak in geometric activity appears at lower coverage levels compared with the Au(111) crystal samples where only the specific activity of the system was considered.

With the data for coverages above 75 % discounted due to concerns over the accuracy of the estimated titania coverage/spacing, we can see a distinct onset in activity, with the beginnings of what may be a peak in activity appearing, allowing us to conclude that it is indeed reactant spill-over or Ti-Au interface sites responsible for the improved activity observed for the titania modified gold system, particularly with the observed initial disruption of activity. However, the data displayed by us here do not allow for us to distinguish which of these is truly responsible, and further work is required to determine this, as described below.

5.7 Conclusions and further Work

In this chapter we have described the deposition of titania nanoparticles onto the surface of glass supported gold films and both gold and ITO based 10*10 Electrochemical chip arrays utilising the Potapenko *et al*.[73] alloy technique. Investigation into the structure of these particles was performed via AFM imaging of the gold/glass surface, showing particles of ~20±3 nm in diameter across all samples. These were larger than those produced previously on the Au(111) crystal (thought to be brought about from longer anneal and oxidation times) with indication that the same triangular/hexagonal shapes are present, though it proved to be considerably more difficult to obtain clear AFM images of the particles at the lowest scan areas.

XPS was performed alongside early samples for the determination of the process by which the titanium is deposited, alloyed and oxidised on the gold/glass substrates to give titania nanoparticles. A positive shift of ~3 eV was observed for the Au $4f_{7/2}$ and $4f_{5/2}$ peaks during deposition and alloying, attributed to variations in the ratio of alloyed Ti-Au[130], followed by a return to metallic gold upon oxidation of the system. The presence of oxygen was found during initial deposition of titanium, indicating slight contamination of the source material, but upon oxidation, all Ti was converted to Ti^{4+}, indicating no contamination of the titania and, alongside the corresponding O data, the titania present during final synthesis was in the form of TiO_2. Comparison of the XPS data to AFM also indicated a slight loss of titanium to the gold bulk during alloying.

Subsequent electrochemical testing of these samples proved difficult, as no suitable data were collected with the gold/glass or gold 10*10 substrates, with only a single ITO

10*10 array giving any suitable data. The ITO array also proved less than ideal, as the data collected varied somewhat; however, a trend was observed in the geometric data indicating that the CO oxidation activity peaks at a titania coverage of ~58%, before decreasing with further titania formation, tallying with the predicted behaviour for titania modified gold surfaces for both the spill-over and Interface site methodologies. When we consider the specific activity, no such peak in activity is initially observed, with coverages greater than 77 % showing a sudden increase in activity where eventual deactivation would instead be expected. This, however, was considered to be an artefact of the method by which the specific area of gold was determined; as the particles formed on the surface of the ITO array sample were never directly measured, the calculated coverage values via the gold/glass substrates must be considered as a useful guideline, but not necessarily completely accurate to the conditions of the surface, especially for coverages above 70 %, where agglomeration becomes a serious consideration. If these coverages are discounted, a distinct onset in activity is observed, with the beginnings of what may be a peak in activity appearing after this initial deactivation. This, in turn, supports that reactant spill-over or Ti-Au interface sites are responsible for the increased activity observed in CO oxidation, though does not allow for us to distinguish between the two.

Useful comparison can also be made with the Au(111) crystal supported samples. Firstly, the deactivation of the gold with the addition of titania to the surface remains present for both: however, this deactivation appears to be less prominent for the ITO supported samples, with the deactivation overcome before titania coverages of 30 % are reached, compared with the Au(111) where significant improvements to the CO oxidation are only observed at coverages above 50 %. This was attributed to the blocking of the formation of more active CO at edge sites,[115,126] due to the preferential initial formation of the titania particles at such positions on the Au(111) crystal and indicates that the nature of the sites, or the extent to which titania decorates them, differs significantly for samples produced on the polycrystalline gold supported samples, as is to be expected.

Secondly, the observed peak in activity occurs at lower coverages for the geometric data, further supporting spill-over/interface sites as responsible for the increased CO oxidation activity in this system. It should be noted that the gradient for activity with titania coverage is considerably shallower for the ITO based sample: this may also be a

consequence of the differing initial surface structure, and thus differences in the activity of initial CO bound to the surface.

It should be stressed that the data collected from the ITO array are considerably less refined than would be ideal, notably in that our estimates for the coverage come from samples produced on the gold/glass substrates, which were considerably more likely to be in the form of Au(111) during our depositions, compared to the sample produced on the ITO array, where the deposited gold is polycrystalline and thus may influence the exact form of the deposited particles on the surface. Attempts were made to image the gold array via AFM, but these images proved significantly difficult to obtain, and imaging of the ITO based samples was not possible due to equipment concerns. This may be responsible for some of the observed differences in our data, but does not detract from their use as a guide for future investigations into the inverse catalyst system.

In consideration of such future investigations, first, a deeper examination must be made into samples produced utilising the ITO arrays to clarify the form of titania on these samples, allowing more significant consideration of changes in particle spacing and coverage progression, as well as providing greater clarity on the position of any peak in the specific activity. This will in turn allow for the electrochemical behaviour of the TiO_x/Au to be linked with surface conditions more closely, providing further insight into the active mechanism for the improved CO oxidation activity. As discussed in chapter 4, a study of the changes brought about from modifying particle size would add further information in this regard: however, improvements to the imaging with the AFM system would be required to obtain a better understanding surface topography before this would be possible. Finally, the use of a RDE set-up would allow for mass transport limitations to be significantly reduced and provide further insights into the specific improvement method.

In summary, the data collected here support that titania particles of varying densities were produced, as well as confirmation that the dominant form of this titania was TiO_2. An indication of the effect of progression of TiO_2 coverage on gold for the oxidation of CO has been displayed, providing further evidence for either spill-over or Ti-Au interface sites being responsible for the increased activity observed in the titania modified gold system, but further work is required to determine which is truly responsible.

6 Final conclusions and further work

The alloy modified synthesis technique as described by Potapenko and Osgood[73] for the synthesis of titania nanoparticles on a gold substrate, has been used to investigate CO oxidation on Inverse electro-catalyst systems. Consistent triangular/elongated hexagon shapes were observed for these particles, exemplified by the images captured with STM (Figure 6.1).

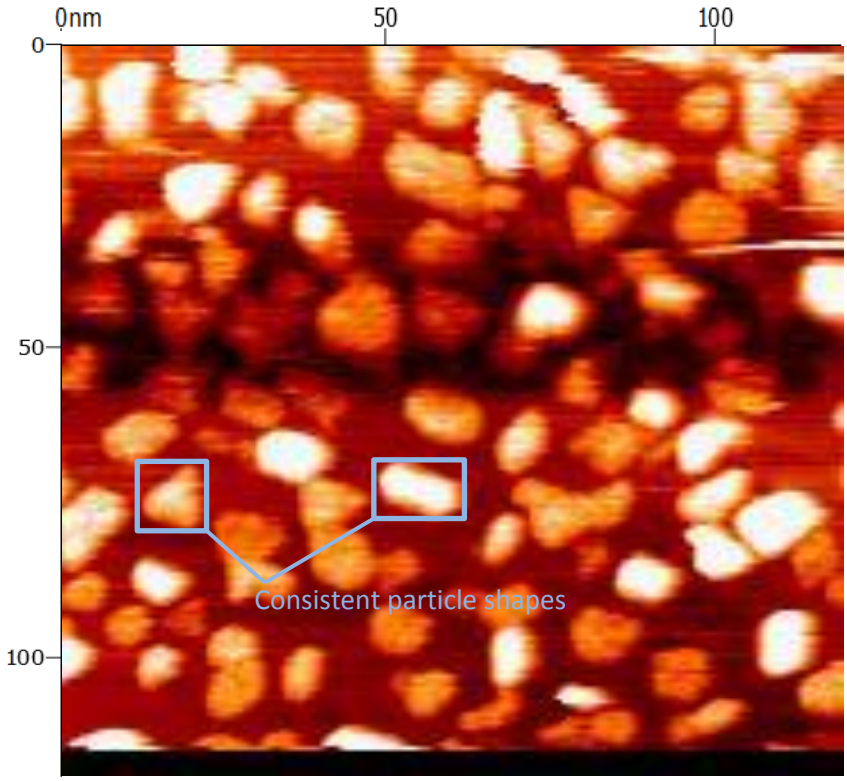

Figure 6.1 118*118 nm STM image of titania modified Au(111) surface. Constant current mode: tip voltage = 0.8 V, tunnelling current = 0.5 nA, Gain = 5.0 %. Distinctive hexagonal and triangular particles visible.

XPS data (Figure 6.2) collected for samples produced upon gold/glass substrates in the HT-PVD for the shows the progression of the Au 4f and Ti 2p peaks at the four main stages of this synthesis procedure: before/after deposition of Ti, the alloyed state and the final product post oxidation. Analysis indicates that the addition of titanium provided significant modification to the electronic states of both metals before and after alloying of the two elements. This appears to be follow the effect observed by Bzowski and Sham[130] for various alloyed states of Au and Ti where the Au 4f peaks experience a positive shift with the addition of Ti, with higher relative Ti levels giving larger shifts, though not to the

extent observed by us here. This indicates that in the samples synthesised by us here, the alloy formed titanium rich, signifying titanium remaining near the surface during the alloying step. The deposition of titanium on gold also has significant effect on the electronic structure of both elements, possibly due to the beginnings of alloying between the two during initial deposition. Finally, it was shown that once the full synthesis was completed, the titania particles formed on the gold surface consisted of pure TiO_2 with no apparent residue of unoxidised titania, as well as a return of the gold to its pre-deposition electronic state, indicating that whatever effect being provided by the metallic titanium has been removed upon its conversion to Ti^{4+}.

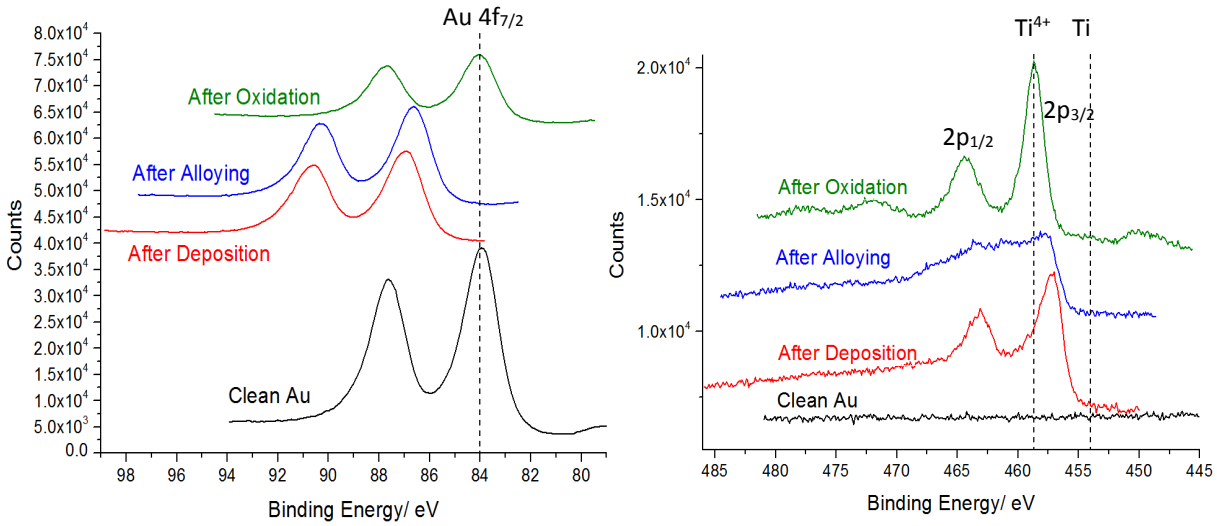

Figure 6.2 XPS Progression of Au 4f and Ti 2p peaks at the 4 main stages of sample synthesis. All peaks adjusted via respective C 1s peaks and spaced for ease of viewing, Mg filament, 10.5 kV.

Quantification of the XPS data also indicated a slight loss of titanium into the gold bulk during deposition/alloying, which was further supported by residual titanium being found in the Au(111) crystal used for experiments in the STM system after numerous series of Ti deposition and alloying, despite continual removal of titania from the crystal surface via Ar^+ sputtering between experiments.

Once the conditions for controlled formation of titania particles on the gold surface was established, a series of samples with varying titania densities was produced, using both high throughput on polycrystalline gold, and a singular production method on single crystal gold. This density was controlled via the initial level of titanium deposited upon gold; it was found that this provided a minimal effect upon the size of the particles

produced, with sizes remaining reasonably constant between samples produced in each system. However, it was observed that variation in the time spent alloying as well as the alloy temperature had distinctive effects on the size of these particles; for those produced in the STM system, where the alloying temperature was 850 K and the time spent reaching this temperature was very minimal, the average particle size was 11.5±2.5 nm, whereas in the HT-PVD, because of limits of temperature imposed by the substrates, the alloy temperature was reduced to 723 K and heating occurred at 25 K/min, giving average particles of 20±3 nm.

Electrochemical experiments were performed on samples produced in both these systems, in 0.1 M $HClO_4$ electrolyte. The data produced using the two substrates are shown below in Figure 6.3, with the percentage values referring to the coverage of the surface with titania.

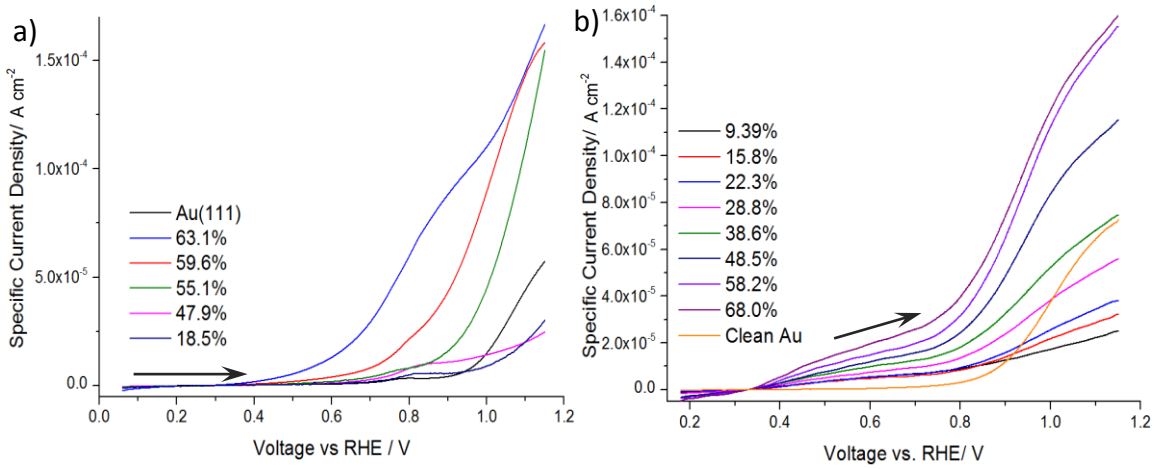

Figure 6.3 1st Forward scan of CO oxidation for samples synthesised on the Au(111) crystal (a) and the ITO 10*10 electrode array (b), alongside the respective clean Au data for Specific Current Density. Percentage refers to Titania surface coverage. 0-1.15 V, Scan speed = 50 Mv s^{-1}, electrolyte = 0.1 M $HClO_4$

It can be seen that there is a very distinct effect on the activity for the oxidation of CO for both inverse catalyst systems: a significant decrease is observed for the CO oxidation onset potential at higher titania coverage values, indicating a decreasing over-potential for the CO electro-oxidation, with the specific current density also showing significant increases. As stated, by having utilised such an inverse system compared to the

standard gold nanoparticles on titania, we have removed considerations such as quantum effects in the gold nanoparticles[31] (as gold is in the bulk state) or increasing relative levels of more highly active lower coordination gold atoms.[33,34] As such, we can confidently state that only Ti-Au interface sites or spill-over remain as possible methodologies behind the improvement to CO oxidation activity observed by us here, though distinguishing between the two is difficult. This supports work previously performed by Hayden *et al.*[32] where no evidence was found for spill-over of an oxidant being present, but activation of water at the Ti-Au interface sites was considered as the most likely explanation for the observed activity changes in the non-inverse system, which corresponds with our observations here.

An interesting effect that is noted for both inverse catalyst systems is that there is an initial deactivation of the gold with the addition of titania to the surface, with subsequent coverage of the surface providing an increase to the activity from that point. The exact positions at which the activity provided by the titania overcomes this differs between the Au(111) and ITO-Au supported samples, with coverages of greater than 30 % being more active for the ITO-Au, whereas no significant improvement is seen for the Au(111) supported samples until at least 50 % of the surface is covered. With observations of the progression of particle formation on the Au(111) crystal, where titania was shown to preferentially grow along terrace edges prior to forming elsewhere, it was concluded that the reason for this decrease in the initial observed activity was due to a disruption of higher activity CO that forms at such edge sites.[115,126] We cannot provide such conclusive evidence for the samples synthesised on polycrystalline gold, where numerous defects are likely present; this observed disruption must come either from the nature of the disturbed sites or the extent to which titania forms at them, with the only conclusion we can reach being that the CO oxidation is less disrupted by initial titania formation on the polycrystalline surface compared to the Au(111) crystal.

After this initial deactivation, there is clear indication of the effect of titania on the gold. By concentrating upon the specific activity data, we can track the level of active gold present in the system: as the titania coverage increases, the relative level of active gold increases, thus providing the improved activity observed. However, for both the spill-over and Ti-Au interface sites models, there will come a point at which an intrinsic deactivation of the surface will occur despite the benefits provided by the presence of titania on the

surface; as the surface becomes saturated with “activated” gold, further titania addition solely removes this gold from the system without increasing the activity of the remaining surface. For the two methods discussed methods for the improved activity, this intrinsic deactivation should occur at significantly different coverage values; for the spill-over method, it would be expected that deactivation would appear at considerably larger inter-particle spacing, and as such the intrinsic deactivation for this method should come at a lower titania coverage, compared with the Ti-Au interface site method, where the affected area per particle is considerably lower, and as such the activity peak should appear at higher coverages. The exact difference between these two methods for the coverage at which this deactivation occurs depends upon the extent that the spill-over area extends from the titania particles.

Such a difference was observed for the data collected by us here, particularly for the ITO supported samples where higher coverages were investigated. This is exemplified by consideration of the current density observed at 1.0 V_{RHE} for both systems (Figure 6.4).

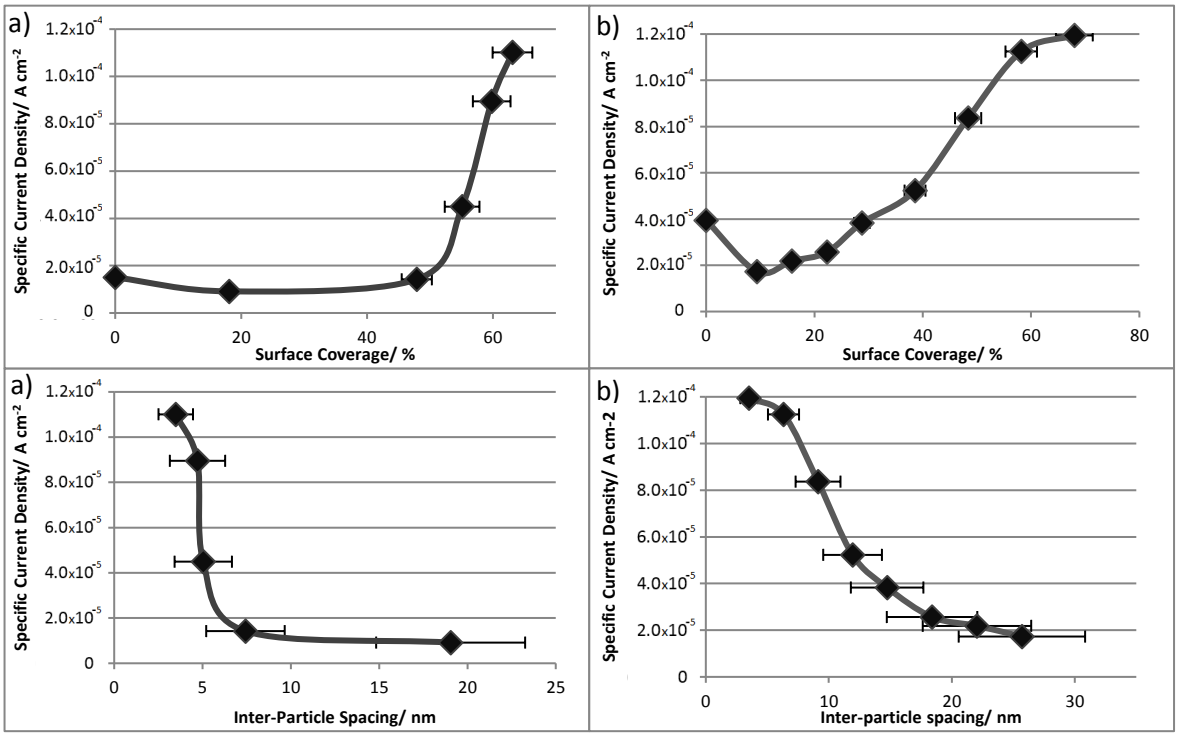

Figure 6.4 Comparisons of specific current density taken at 1.0 V_{RHE} for Au(111) (a) and ITO-Au (b) supported titania nanoparticles for both surface coverage and inter-particle spacing

It can be seen that for both an onset in activity is observed in the activity, with the beginnings of what may be a peak in activity at similar coverage/particle spacing values

showing. The indication of such a peak beginning lends support to the fact that it is spill-over rather than Ti-Au interface sites that is responsible for the observed activity increase to CO oxidation seen by titania modified gold, but without a full maximum being reached we cannot fully declare support.

The ignition potential for these two systems is less conclusive, with a much sharper decrease observed for the Au(111) supported samples above 50 % coverage, though this is most likely influenced by the considerably larger deactivation observed for the initial addition of titania to the surface seen than for the ITO-Au supported samples, with similar values determined for the higher coverage samples.

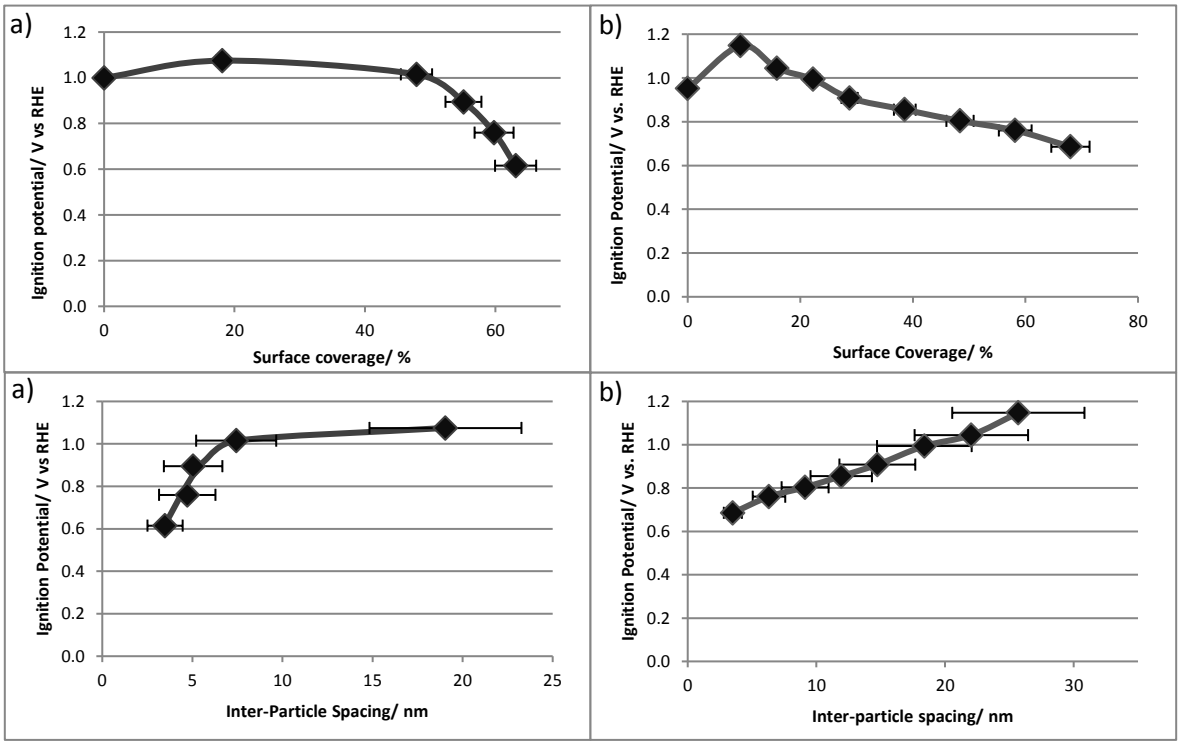

Figure 6.5 Comparisons of ignition potential for Au(111) (a) and ITO-Au (b) supported titania nanoparticles for both surface coverage and inter-particle spacing.

From Figure 6.5 there is a suggestion that the increase in activity appears to increase less steeply at coverages in the region of roughly 70 %, corresponding to an inter-particle spacing of ~3.0 -3.5 nm as the maximum density of titania particles possible before the intrinsic deactivation of the surface occurs. Because of this, we can consider that spill-over is more probable than Ti-Au interface sites as the method behind the increased activity observed for the titania modified gold system, though we cannot discount these interface sites without further investigation into the system.

However, at this point we must consider the limitations within the data collected by us here: the most notable of which is the fact that in the cells used for the determination of the electrochemical activity of our samples, mass transport becomes a serious limiting factor as the current density increases; most significantly the consideration of the replacement of CO to the surface. The peaks being observed in our activity may in fact be indicative of CO replenishment to the surface becoming the rate-determining step for the oxidation of CO, as the formation of hydroxide is provided for by the addition of increasing quantities of titania to the gold. As such, we cannot conclude with certainty that spill-over is truly responsible for the activity observed here, and reaction at the edge of the titania particles also provides a reasonable explanation of these results.

This leads us into deliberation of possible future work that would allow for such a determination to be made with greater clarity. The greatest of these would be the testing of such titania modified gold surfaces in an RDE environment, thus significantly reducing the contribution of mass transport to the system. By observing where the expected activity peak appears in such an experiment, which should be present due to the expected intrinsic deactivation of the surface at high coverages, the further evidence should be gleaned for which of the two methods is responsible for the observed activity.

Another possible angle of consideration comes from investigation of the modification observed when the size of these particles is varied whilst maintaining similar coverage levels: an increase in effective activity will be observed for the interface site method as the ratio of perimeter locations to particle diameter increases with decreasing particle size, thus providing a relative increase in active gold per area of titania. Modifying particle size has a less clear cut effect on spill-over, as the specific relationship between the area of titania to the provided spill-over area is unknown to us at this juncture. However, there are three possible outcomes that would result from such a modification: if the ratio of spill-over area to particle size increases, the observed activity will increase as more gold is activated; if this ratio is lowered, activity will decrease, and if the ratio remains constant, then so will the observed activity. Of these, two (constant and decreased activity with lower particle sizes) are distinct from the expected effect of decreased particle size on activity for the Interface sites method, and as such should provide further evidence for the responsible method.

7 References

1. Cook, B. D., Introduction to fuel cells and hydrogen technology. *Eng Sci Educ J* **2002,** *11* (6), 205-216.

2. Klaiber, T., Fuel cells for transport: Can the promise be fulfilled? Technical requirements and demands from customers. *J Power Sources* **1996,** *61* (1-2), 61-69.

3. Grove, W., On Voltaic Series and the Combination of Gases by Platinum. *Philosophers magazine and Journal of Science* **1839,** *3* (14), 127-130.

4. Panik, F., Fuel cells for vehicle applications in cars - bringing the future closer. *J Power Sources* **1998,** *71* (1-2), 36-38.

5. Dunwoody, D., Proton Exchange Membranes: The View Forward and Back. *Electrochemical Society Interface* **2005,** *14* (3), 37-39.

6. Chunzhi, H.; D., S.; B., G.; B., S., PEM Fuel Cell Catalysts: Cost, Performance, and Durability. *Electrochemical Society Interface* **2005,** *14* (3), 41-44.

7. Wu, Y. N.; Liao, S. J.; Su, H. N.; Dang, D.; Liu, B., Shortened Carbon Nanotubes as Enhanced Support for High-performance Platinum Catalysts. *Fuel Cells* **2010,** *10* (6), 920-925.

8. Norskov, J. K.; Rossmeisl, J.; Logadottir, A.; Lindqvist, L.; Kitchin, J. R.; Bligaard, T.; Jonsson, H., Origin of the overpotential for oxygen reduction at a fuel-cell cathode. *J Phys Chem B* **2004,** *108* (46), 17886-17892.

9. Gasteiger, H. A.; Panels, J. E.; Yan, S. G., Dependence of PEM fuel cell performance on catalyst loading. *J Power Sources* **2004,** *127* (1-2), 162-171.

10. Gasteiger, H. A.; Markovic, N.; Ross, P. N.; Cairns, E. J., Co Electrooxidation on Well-Characterized Pt-Ru Alloys. *J Phys Chem-Us* **1994,** *98* (2), 617-625.

11. Lopez-Salido, I.; Lim, D. C.; Dietsche, R.; Bertram, N.; Kim, Y. D., Electronic and geometric properties of Au nanoparticles on highly ordered pyrolytic graphite (HOPG) studied using X-ray Photoelectron Spectroscopy (XPS) and Scanning Tunneling Microscopy (STM). *J Phys Chem B* **2006,** *110* (3), 1128-1136.

12. Irawan, T.; Barke, I.; Hovel, H., Size-dependent morphology of gold clusters grown on nanostructured graphite. *Appl Phys a-Mater* **2005,** *80* (5), 929-935.

13. Guerin, S.; Hayden, B. E.; Lee, C. E.; Mormiche, C.; Owen, J. R.; Russell, A. E.; Theobald, B.; Thompsett, D., Combinatorial electrochemical screening of fuel cell electrocatalysts. *J Comb Chem* **2004,** *6* (1), 149-158.

14. Hayden, B. E., Particle Size and Support Effects in Electrocatalysis. *Accounts Chem Res* **2013**.

15. Bond, G. C., The Origins of Particle-Size Effects in Heterogeneous Catalysis. *Surf Sci* **1985,** *156* (Jun), 966-981.

16. Che, M.; Bennett, C. O., The Influence of Particle-Size on the Catalytic Properties of Supported Metals. *Adv Catal* **1989,** *36*, 55-172.

17. Bell, A. T., The impact of nanoscience on heterogeneous catalysis. *Science* **2003,** *299* (5613), 1688-1691.

18. Kintaichi, Y.; Hamada, H.; Tabata, M.; Sasaki, M.; Ito, T., Selective Reduction of Nitrogen-Oxides with Hydrocarbons over Solid Acid Catalysts in Oxygen-Rich Atmospheres. *Catal Lett* **1990,** *6* (2), 239-244.

19. Tauster, S. J.; Fung, S. C.; Garten, R. L., Strong Metal-Support Interactions - Group-8 Noble-Metals Supported on Tio2. *J Am Chem Soc* **1978,** *100* (1), 170-175.

20. Cant, N. W.; Hall, W. K., Catalytic Oxidation .4. Ethylene and Propylene Oxidation over Gold. *J Phys Chem-Us* **1971,** *75* (19), 2914-&.

21. Schwank, J., Catalytic Gold. *Gold Bull* **1983,** *16*, 103 - 110.

22. Schwank, J., Gold in Bimetallic catalysts. *Gold Bull* **1985,** *18*, 1-10.

23. Bond, G. C.; Thompson, D. T., Gold-catalysed oxidation of carbon monoxide. *Gold Bull* **2000,** *33* (2), 41-51.

24. Hammer, B.; Norskov, J. K., Why Gold Is the Noblest of All the Metals. *Nature* **1995,** *376* (6537), 238-240.

25. Haruta, M.; Kobayashi, T.; Sano, H.; Yamada, N., Novel Gold Catalysts for the Oxidation of Carbon-Monoxide at a Temperature Far Below 0-Degrees-C. *Chem Lett* **1987,** (2), 405-408.

26. Haruta, M.; Yamada, N.; Kobayashi, T.; Iijima, S., Gold Catalysts Prepared by Coprecipitation for Low-Temperature Oxidation of Hydrogen and of Carbon-Monoxide. *J Catal* **1989,** *115* (2), 301-309.

27. Haruta, M.; Tsubota, S.; Kobayashi, T.; Kageyama, H.; Genet, M. J.; Delmon, B., Low-Temperature Oxidation of CO over Gold Supported on Tio2, Alpha-Fe2o3, and Co3o4. *J Catal* **1993,** *144* (1), 175-192.

28. Haruta, M., Size- and support-dependency in the catalysis of gold. *Catal Today* **1997,** *36* (1), 153-166.

29. Tauster, S. J., Strong Metal-Support Interactions. *Accounts Chem Res* **1987,** *20* (11), 389-394.

30. Bamwenda, G. R.; Tsubota, S.; Nakamura, T.; Haruta, M., The influence of the preparation methods on the catalytic activity of platinum and gold supported on TiO2 for CO oxidation. *Catal Lett* **1997,** *44* (1-2), 83-87.

31. Valden, M.; Lai, X.; Goodman, D. W., Onset of catalytic activity of gold clusters on titania with the appearance of nonmetallic properties. *Science* **1998,** *281* (5383), 1647-1650.

32. Hayden, B. E.; Pletcher, D.; Rendall, M. E.; Suchsland, J. P., CO oxidation on gold in acidic environments: Particle size and substrate effects. *J Phys Chem C* **2007,** *111* (45), 17044-17051.

33. Lemire, C.; Meyer, R.; Shaikhutdinov, S.; Freund, H. J., Do quantum size effects control CO adsorption on gold nanoparticles? *Angew Chem Int Edit* **2004,** *43* (1), 118-121.

34. Mavrikakis, M.; Stoltze, P.; Norskov, J. K., Making gold less noble. *Catal Lett* **2000,** *64* (2-4), 101-106.

35. Bahn, S. R.; Lopez, N.; Norskov, J. K.; Jacobsen, K. W., Adsorption-induced restructuring of gold nanochains. *Phys Rev B* **2002,** *66* (8).

36. Valden, M.; Pak, S.; Lai, X.; Goodman, D. W., Structure sensitivity of CO oxidation over model Au/TiO2 catalysts. *Catal Lett* **1998,** *56* (1), 7-10.

37. Chen, M. S.; Goodman, D. W., The structure of catalytically active gold on titania. *Science* **2004,** *306* (5694), 252-255.

38. Xu, Y.; Mavrikakis, M., Adsorption and dissociation of O-2 on gold surfaces: Effect of steps and strain. *J Phys Chem B* **2003,** *107* (35), 9298-9307.

39. Okazawa, T.; Kohyama, M.; Kido, Y., Electronic properties of Au nano-particles supported on stoichiometric and reduced TiO2 (110) substrates. *Surf Sci* **2006,** *600* (19), 4430-4437.

40. Boccuzzi, F.; Chiorino, A.; Manzoli, M.; Lu, P.; Akita, T.; Ichikawa, S.; Haruta, M., Au/TiO2 nanosized samples: A catalytic, TEM, and FTIR study of the effect of calcination temperature on the CO oxidation. *J Catal* **2001,** *202* (2), 256-267.

41. Liu, H.; Kozlov, A. I.; Kozlova, A. P.; Shido, T.; Asakura, K.; Iwasawa, Y., Active oxygen species and mechanism for low-temperature CO oxidation reaction on a TiO2-supported Au catalyst prepared from Au(PPh3)(NO3) and As-precipitated titanium hydroxide. *J Catal* **1999,** *185* (2), 252-264.

42. Widmann, D.; Behm, R. J., Active Oxygen on a Au/TiO2 Catalyst: Formation, Stability, and CO Oxidation Activity. *Angew Chem Int Edit* **2011,** *50* (43), 10241-10245.

43. Grunwaldt, J. D.; Baiker, A., Gold/titania interfaces and their role in carbon monoxide oxidation. *J Phys Chem B* **1999,** *103* (6), 1002-1012.

44. Conner, W. C.; Falconer, J. L., Spillover in Heterogeneous Catalysis. *Chemical reviews* **1995,** *95* (3), 759-788.

45. Date, M.; Haruta, M., Moisture effect on CO oxidation over Au/TiO2 catalyst. *J Catal* **2001,** *201* (2), 221-224.

46. Date, M.; Ichihashi, Y.; Yamashita, T.; Chiorino, A.; Boccuzzi, F.; Haruta, A., Performance of Au/TiO2 catalyst under ambient conditions. *Catal Today* **2002,** *72* (1-2), 89-94.

47. Li, N. H.; Sun, S. G.; Chen, S. P., Studies on the role of oxidation states of the platinum surface in electrocatalytic oxidation of small primary alcohols. *J Electroanal Chem* **1997,** *430* (1-2), 57-67.

48. Date, M.; Okumura, M.; Tsubota, S.; Haruta, M., Vital role of moisture in the catalytic activity of supported gold nanoparticles. *Angew Chem Int Edit* **2004,** *43* (16), 2129-2132.

49. Guerin, S.; Hayden, B. E.; Pletcher, D.; Rendall, M. E.; Suchsland, J. P.; Williams, L. J., Combinatorial approach to the study of particle size effects in electrocatalysis: Synthesis of supported gold nanoparticles. *J Comb Chem* **2006,** *8* (5), 791-798.

50. Guerin, S.; Hayden, B. E.; Pletcher, D.; Rendall, M. E.; Suchsland, J. P., A combinatorial approach to the study of particle size effects on supported electrocatalysts: Oxygen reduction on gold. *J Comb Chem* **2006,** *8* (5), 679-686.

51. Kita, H.; Nakajima, H.; Hayashi, K., Electrochemical Oxidation of Co on Au in Alkaline-Solution. *J Electroanal Chem* **1985,** *190* (1-2), 141-156.

52. Kunimatsu, K.; Aramata, A.; Nakajima, H.; Kita, H., Infrared-Spectra of Carbon-Monoxide Adsorbed on a Smooth Gold Electrode .2. Emirs and Polarization-Modulated Irras Study of the Adsorbed Co Layer in Acidic and Alkaline-Solutions. *J Electroanal Chem* **1986,** *207* (1-2), 293-307.

53. Rodriguez, P.; Garcia-Araez, N.; Koper, M. T. M., Self-promotion mechanism for CO electrooxidation on gold. *Phys Chem Chem Phys* **2010,** *12* (32), 9373-9380.

54. Rodriguez, P.; Koverga, A. A.; Koper, M. T. M., Carbon Monoxide as a Promoter for its own Oxidation on a Gold Electrode. *Angew Chem Int Edit* **2010,** *49* (7), 1241-1243.

55. Rodriguez, J. A.; Hrbek, J., Inverse oxide/metal catalysts: A versatile approach for activity tests and mechanistic studies. *Surf Sci* **2010,** *604* (3-4), 241-244.

56. Cargnello, M.; Fornasiero, P.; Gorte, R. J., Opportunities for Tailoring Catalytic Properties Through Metal-Support Interactions. *Catal Lett* **2012,** *142* (9), 1043-1048.

57. Demmin, R. A.; Ko, C. S.; Gorte, R. J., Effect of Titania on the Chemisorption and Reaction Properties of Pt. *J Phys Chem-Us* **1985,** *89* (7), 1151-1154.

58. Rodriguez, J. A.; Ma, S.; Liu, P.; Hrbek, J.; Evans, J.; Perez, M., Activity of CeOx and TiOx nanoparticles grown on Au(111) in the water-gas shift reaction. *Science* **2007,** *318* (5857), 1757-1760.

59. Senanayake, S. D.; Stacchiola, D.; Evans, J.; Estrella, M.; Barrio, L.; Perez, M.; Hrbek, J.; Rodriguez, J. A., Probing the reaction intermediates for the water-gas shift over inverse CeOx/Au(111) catalysts. *J Catal* **2010,** *271* (2), 392-400.

60. Yan, T.; Redman, D. W.; Yu, W.-Y.; Flaherty, D. W.; Rodriguez, J. A.; Mullins, C. B., CO oxidation on inverse Fe2O3/Au(111) model catalysts. *J Catal* **2012,** *294*, 216-222.

61. Fujitani, T.; Nakamura, I., Mechanism and Active Sites of the Oxidation of CO over Au/TiO2. *Angew Chem Int Edit* **2011,** *50* (43), 10144-10147.

62. Hayden, B. E.; Pletcher, D.; Suchsland, J. P., Enhanced activity for electrocatalytic oxidation of carbon monoxide on titania-supported gold nanoparticles. *Angew Chem Int Edit* **2007,** *46* (19), 3530-3532.

63. Song, D.; Hrbek, J.; Osgood, R., Formation of TiO2 nanoparticles by reactive-layer-assisted deposition and characterization by XPS and STM. *Nano Lett* **2005,** *5* (7), 1327-1332.

64. Narasimhan, S.; Vanderbilt, D., Elastic stress domains and the herringbone reconstruction on Au(111). *Phys Rev Lett* **1992,** *69* (10), 1564-1567.

65. Vanhove, M. A.; Koestner, R. J.; Stair, P. C.; Biberian, J. P.; Kesmodel, L. L.; Bartos, I.; Somorjai, G. A., The Surface Reconstructions of the (100) Crystal Faces of Iridium, Platinum and Gold .1. Experimental-Observations and Possible Structural Models. *Surf Sci* **1981,** *103* (1), 189-217.

66. Barth, J. V.; Brune, H.; Ertl, G.; Behm, R. J., Scanning Tunneling Microscopy Observations on the Reconstructed Au(111) Surface - Atomic-Structure, Long-Range Superstructure, Rotational Domains, and Surface-Defects. *Phys Rev B* **1990,** *42* (15), 9307-9318.

67. Chado, I.; Padovani, S.; Scheurer, F.; Bucher, J. P., Controlled nucleation of Co clusters on Au(111): towards spin engineering. *Appl Surf Sci* **2000,** *164*, 42-47.

68. Biener, M. M.; Biener, J.; Schalek, R.; Friend, C. M., Growth of nanocrystalline MoO3 on Au(111) studied by in situ scanning tunneling microscopy. *J Chem Phys* **2004,** *121* (23), 12010-12016.

69. Chambliss, D. D.; Wilson, R. J.; Chiang, S., Nucleation of Ordered Ni Island Arrays on Au(111) by Surface-Lattice Dislocations. *Phys Rev Lett* **1991,** *66* (13), 1721-1724.

70. Carrozzo, P.; Tumino, F.; Passoni, M.; Bottani, C. E.; Casari, C. S.; Bassi, A. L., Growth and electronic properties of Ti nanoislands on Au(111). *Surf Sci* **2014,** *619*, 77-82.

71. Meyer, J. A.; Baikie, I. D.; Kopatzki, E.; Behm, R. J., Preferential island nucleation at the elbows of the Au(111) herringbone reconstruction through place exchange. *Surf Sci* **1996,** *365* (1), L647-L651.

72. Biener, J.; Farfan-Arribas, E.; Biener, M.; Friend, C. M.; Madix, R. J., Synthesis of TiO2 nanoparticles on the Au(111) surface. *J Chem Phys* **2005,** *123* (9).

73. Potapenko, D. V.; Osgood, R. M., Preparation of TiO2 Nanocrystallites by Oxidation of Ti-Au(111) Surface Alloy. *Nano Lett* **2009,** *9* (6), 2378-2383.

74. Murray, J. L., The Au-Ti (Go!d-Titanium) System. *Journal of Phase Equilibria* **1983,** *4* (3), 278 - 283.

75. Angersteinkozlowska, H.; Conway, B. E.; Hamelin, A.; Stoicoviciu, L., Elementary Steps of Electrochemical Oxidation of Single-Crystal Planes of Au .1. Chemical Basis of Processes Involving Geometry of Anions and the Electrode Surfaces. *Electrochim Acta* **1986,** *31* (8), 1051-1061.

76. Jerkiewicz, G., Surface Oxidation of Noble Metal Electrodes. In *Interfacial Chemistry*, Wieckowski, A., Ed. Marcel Dekker Inc., 1999.

77. Conway, B. E.; Barnett, B.; Angersteinkozlowska, H.; Tilak, B. V., A Surface-Electrochemical Basis for the Direct Logarithmic Growth Law for Initial-Stages of Extension of Anodic Oxide-Films Formed at Noble-Metals. *J Chem Phys* **1990,** *93* (11), 8361-8373.

78. Burke, L. D.; Nugent, P. F., The electrochemistry of gold: I The Redox Behaviour of the Metal in Aqueous Media. *Gold Bull* **1997,** *30* (2), 43-53.

79. Angersteinkozlowska, H.; Conway, B. E.; Hamelin, A.; Stoicoviciu, L., Elementary Steps of Electrochemical Oxidation of Single-Crystal Planes of Au .2. A Chemical and Structural Basis of Oxidation of the (111) Plane. *J Electroanal Chem* **1987,** *228* (1-2), 429-453.

80. Edens, G. J.; Hamelin, A.; Weaver, M. J., Mechanism of carbon monoxide electrooxidation on monocrystalline gold surfaces: Identification of a hydroxycarbonyl intermediate. *J Phys Chem-Us* **1996,** *100* (6), 2322-2329.

81. Herrero, E.; Feliu, J. M.; Blais, S.; Radovic-Hrapovic, Z.; Jerkiewicz, G., Temperature dependence of CO chemisorption and its oxidative desorption on the Pt(111) electrode. *Langmuir* **2000,** *16* (11), 4779-4783.

82. Rodriguez, P.; Garcia-Araez, N.; Koverga, A.; Frank, S.; Koper, M. T. M., CO Electroxidation on Gold in Alkaline Media: A Combined Electrochemical, Spectroscopic, and DFT Study. *Langmuir* **2010,** *26* (14), 12425-12432.

83. Sun, S. G.; Cai, W. B.; Wan, L. J.; Osawa, M., Infrared absorption enhancement for CO adsorbed on Au films in perchloric acid solutions and effects of surface structure studied by cyclic voltammetry, scanning tunneling microscopy, and surface-enhanced IR spectroscopy. *J Phys Chem B* **1999,** *103* (13), 2460-2466.

84. Rodriguez, P.; Plana, D.; Fermin, D. J.; Koper, M. T. M., New insights into the catalytic activity of gold nanoparticles for CO oxidation in electrochemical media. *J Catal* **2014,** *311*, 182-189.

85. Rodriguez, P.; Plana, D.; Fermin, D. J.; Koper, M. T. M., Supporting Information for New insights into the catalytic activity of gold nanoparticles for CO oxidation in electrochemical media. *J Catal* **2014,** *311*, 182-189.

86. Guerin, S.; Hayden, B. E., Physical vapor deposition method for the high-throughput synthesis of solid-state material libraries. *J Comb Chem* **2006,** *8* (1), 66-73.

87. Williams, L. J. Electrocatalysis of model Titania supported Platinum. University of Southampton, 2009.

88. Binnig, G.; Quate, C. F.; Gerber, C., Atomic Force Microscope. *Phys Rev Lett* **1986,** *56* (9), 930-933.

89. Binnig, G.; Rohrer, H.; Gerber, C.; Weibel, E., Tunneling through a Controllable Vacuum Gap. *Appl Phys Lett* **1982,** *40* (2), 178-180.

90. Ernst, S. Optimisation of the preparation process for tips used in scanning tunneling microscopy. Technische Universitat Dresden, 2006.

91. Chen, C. J., *Introduction to Scanning Tunneling Microscopy*. Oxford University Press: 2008; p 26.

92. Wiesendanger, R., *Scanning Probe Microscopy and Spectroscopy*. Cambridge University Press: 1994.

93. Binnig, G.; Gerber, C.; Stoll, E.; Albrecht, T. R.; Quate, C. F., Atomic Resolution with Atomic Force Microscope. *Europhys Lett* **1987,** *3* (12), 1281-1286.

94. Meyer, G.; Amer, N. M., Novel Optical Approach to Atomic Force Microscopy. *Appl Phys Lett* **1988,** *53* (12), 1045-1047.

95. Naeem, R. Lennard-Jones Potential. http://chem.libretexts.org/Core/Physical_Chemistry/Physical_Properties_of_Matter/Atomic_and_Molecular_Properties/Intermolecular_Forces/Specific_Interactions/Lennard-Jones_Potential (accessed 14/08/2016).

96. Leggett, G. J., Scanning Probe Microscopy. In *Surface Analysis The Principle Techniques*, Vickerman, J. C.; Gilmore, I. S., Eds. John Wiley and Sons: 2009; pp 479-562.

97. Davisson, C.; Germer, L. H., Diffraction of Electrons by a crystal of Nickel. *The Physical Review* **1927,** *30* (6), 35.

98. Melmed, A. J., The Art and Science and Other Aspects of Making Sharp Tips. *J Vac Sci Technol B* **1991,** *9* (2), 601-608.

99. Bryant, P. J.; Kim, H. S.; Zheng, Y. C.; Yang, R., Technique for Shaping Scanning Tunneling Microscope Tips. *Rev Sci Instrum* **1987,** *58* (6), 1115-1115.

100. Tahmasebipour, G.; Hojjat, Y.; Ahmadi, V.; Abdullah, A., Effect of Fabrication Process Parameters on the Apex-Radius of STM Tungsten Nanotip. *Scanning* **2009,** *31* (2), 65-74.

101. Oliva, A. I.; Romero G, A.; Peña, J. L.; Anguiano, E.; Aguilar, M., Electrochemical preparation of tungsten tips for a scanning tunneling microscope. *Rev Sci Instrum* **1996,** *67* (5), 1917.

102. Collins, A. M., Making Wire Tips for Scanning Tunnelling Microscopy. In *Nanotechnology Cookbook: Practical, Reliable and Jargon Free Experimental Procedures*, Elsevier: 2012; pp 233-255.

103. Ratner, B. D.; Castner, D. G., Electron Spectroscopy for Chemical Analysis. In *Surface Analysis The Principle Techniques*, 2nd ed.; Vickerman, J. C.; Gilmore, I. S., Eds. John Wiley and Sons: 2009; pp 47-113.

104. Siegbahn, K.; Nordling, C.; Fahlman, A.; Nordberg, R.; Hamrin, K.; Hedman, J.; Johansson, G.; Bergmark, T.; Karlsson, S.-E.; Lindgren., I.; Lindberg, B., ESCA - Atomic, Molecular and Solid State Structure Studied by Means of Electron Spectroscopy. *Nova Acta Regiae Soc. Sci. Upsal. Series IV* **1967,** *20*.

105. Woodruff, D. P.; Delchar, T. A., *Modern Techniques of Surface Science*. Cambridge University Press: 1994.

106. Hertz, H., Ueber einen Einfluss des ultravioletten Lichtes auf die electrische Entladung. *annalen der physik* **1887,** *267* (8), 983-1000.

107. Rutherford, E., The Structure of the Atom. *Philosophical magazine* **1914,** *27* (6), 488-498.

108. Koopmans, T., Über die Zuordnung von Wellenfunktionen und Eigenwerten zu den Einzelnen Elektronen Eines Atoms. *Physica* **1934,** *1* (1-6), 104-113.

109. Harten, U.; Lahee, A. M.; Toennies, J. P.; Woll, C., Observation of a Soliton Reconstruction of Au(111) by High-Resolution Helium-Atom Diffraction. *Phys Rev Lett* **1985,** *54* (24), 2619-2622.

110. Biener, M. M.; Biener, J.; Friend, C. M., Sulfur-induced mobilization of Au surface atoms on Au(111) studied by real-time STM. *Surf Sci* **2007,** *601* (7), 1659-1667.

111. Potapenko, D. V.; Li, Z. S.; Lou, Y.; Guo, Y.; Osgood, R. M., 2-Propanol reactivity on in situ prepared Au(1 1 1)-supported TiO2 nanocrystals. *J Catal* **2013,** *297*, 281-288.

112. Cohen, P. I.; Petrich, G. S.; Pukite, P. R.; Whaley, G. J.; Arrott, A. S., Birth Death Models of Epitaxy .1. Diffraction Oscillations from Low Index Surfaces. *Surf Sci* **1989,** *216* (1-2), 222-248.

113. Hamelin, A., Cyclic voltammetry at gold single-crystal surfaces .1. Behaviour at low-index faces. *J Electroanal Chem* **1996,** *407* (1-2), 1-11.

114. Schneeweiss, M. A.; Kolb, D. M.; Liu, D. Z.; Mandler, D., Anodic oxidation of Au(111). *Can J Chem* **1997,** *75* (11), 1703-1709.

115. Shue, C. H.; Yang, L. Y. O.; Yau, S. L.; Itaya, K., In-situ scanning tunneling microscopy of carbon monoxide adsorbed on Au(111) electrode. *Langmuir* **2005,** *21* (5), 1942-1948.

116. Blizanac, B. B.; Arenz, M.; Ross, P. N.; Markovic, N. M., Surface electrochemistry of CO on reconstructed gold single crystal surfaces studied by infrared reflection absorption spectroscopy and rotating disk electrode. *J Am Chem Soc* **2004,** *126* (32), 10130-10141.

117. Rodriguez, P.; Koper, M. T. M., Electrocatalysis on gold. *Phys Chem Chem Phys* **2014,** *16* (27), 13583-13594.

118. Kolb, D. M.; Schneider, J., Surface Reconstruction in Electrochemistry - Au(100)-(5x20), Au(111)-(1x23) and Au(110)-(1x2). *Electrochim Acta* **1986,** *31* (8), 929-936.

119. Gibbs, T. K.; Mccallum, C.; Pletcher, D., Oxidation of Carbon-Monoxide at Platinum and Gold Metallized Membrane Electrodes. *Electrochim Acta* **1977,** *22* (5), 525-530.

120. Hamelin, A., Note on the Behavior of the (111) Gold Face in Electrolytic Solutions. *J Electroanal Chem* **1986,** *210* (2), 303-309.

121. Arenz, M.; Mayrhofer, K. J. J.; Stamenkovic, V.; Blizanac, B. B.; Tomoyuki, T.; Ross, P. N.; Markovic, N. M., The effect of the particle size on the kinetics of CO electrooxidation on high surface area Pt catalysts. *J Am Chem Soc* **2005,** *127* (18), 6819-6829.

122. Chen, D. J.; Allison, T. C.; Tong, Y. Y. J., Mechanistic Insights into Electro-Oxidation of Solution CO on the Polycrystalline Gold Surface as Seen by in Situ IR Spectroscopy. *J Phys Chem C* **2016,** *120* (29), 16132-16139.

123. Suchsland, J. P. Particle Size and Substrate Effects in Electrocatalysis. University of Southampton, 2007.

124. Piccolo, L.; Loffreda, D.; Aires, F. J. C. S.; Deranlot, C.; Jugnet, Y.; Sautet, P.; Bertolini, J. C., The adsorption of CO on Au(111) at elevated pressures studied by STM, RAIRS and DFT calculations. *Surf Sci* **2004,** *566*, 995-1000.

125. Kim, J.; Samano, E.; Koel, B. E., CO adsorption and reaction on clean and oxygen-covered Au(211) surfaces. *J Phys Chem B* **2006,** *110* (35), 17512-17517.

126. Wang, J.; McEntee, M.; Tang, W. J.; Neurock, M.; Baddorf, A. P.; Maksymovych, P.; Yates, J. T., Formation, Migration, and Reactivity of Au-CO Complexes on Gold Surfaces. *J Am Chem Soc* **2016,** *138* (5), 1518-1526.

127. Haiss, W.; Lackey, D.; Sass, J. K.; Besocke, K. H., Atomic Resolution Scanning Tunneling Microscopy Images of Au(111) Surfaces in Air and Polar Organic-Solvents. *J Chem Phys* **1991,** *95* (3), 2193-2196.

128. www.arrandee.com. (accessed 06-01-2017).

129. Wagner, C. D., Auger and Photoelectron Energies and the Auger Parameters: A Data Set. In *Practical Surface Analysis by Auger and X-ray Photoelectron Spectroscopy*, Briggs, D.; Seah, M. P., Eds. John Wiley and Sons: 1983; pp 477-504.

130. Bzowski, A.; Sham, T. K., Electronic-Structure of Au-Ti Intermetallics. *Journal of Vacuum Science & Technology a-Vacuum Surfaces and Films* **1993,** *11* (4), 2153-2157.

131. Godfroid, T.; Gouttebaron, R.; Dauchot, J. P.; Leclere, P.; Lazzaroni, R.; Hecq, M., Growth of ultrathin Ti films deposited on SnO2 by magnetron sputtering. *Thin Solid Films* **2003,** *437* (1-2), 57-62.

132. Pouilleau, J.; Devilliers, D.; Garrido, F.; DurandVidal, S., Structure and composition of passive titanium oxide films. *Mat Sci Eng B-Solid* **1997,** *47* (3), 235-243.

133. McCafferty, E.; Wightman, J. P., An X-ray photoelectron spectroscopy sputter profile study of the native air-formed oxide film on titanium. *Appl Surf Sci* **1999,** *143* (1-4), 92-100.

134. Seah, M. P., Quantification of AES and XPS. In *Practical Surface Analysis by Auger and X-Ray Photoelectron Spectroscopy*, Briggs, D.; Seah, M. P., Eds. John Wiley and Sons: 1983.